



THE UNIVERSITY OF  
**WAIKATO**  
*Te Whare Wānanga o Waikato*

Research Commons

<http://researchcommons.waikato.ac.nz/>

## Research Commons at the University of Waikato

### Copyright Statement:

The digital copy of this thesis is protected by the Copyright Act 1994 (New Zealand).

The thesis may be consulted by you, provided you comply with the provisions of the Act and the following conditions of use:

- Any use you make of these documents or images must be for research or private study purposes only, and you may not make them available to any other person.
- Authors control the copyright of their thesis. You will recognise the author's right to be identified as the author of the thesis, and due acknowledgement will be made to the author where appropriate.
- You will obtain the author's permission before publishing any material from the thesis.

**The Formulation of Titanium - based Metal  
Feedstocks and the Fabrication of Parts using the  
Powder Injection Moulding Process.**

A thesis submitted in fulfilment of the requirements for the degree  
of

**Doctor of Philosophy**

in

**Materials and Process Engineering.**

by

**Paul D. Ewart**



**The University of Waikato**

Hamilton, New Zealand.

2015

©

## **Abstract**

Development of a profitable titanium industry for New Zealand will not come about without innovative technologies. Plastic injection moulding has long held a place in NZ manufacturing to produce large quantities of complex parts and holds the key to such innovation.

Titanium metal parts were fabricated by injection moulding titanium based metal powder feedstock followed by a debinding process and subsequent sintering. The fabrication process in its entirety was investigated in four distinct steps. Feedstock formulation involved combining the metal powders with various carrier components. Injection moulding enabled the shaping of the feedstock into geometries approximating the final part. Debinding being the process whereby the carrier/binder system is removed from the part to create a powder compact retaining the required geometry. Sintering being the final step where the metal powders are consolidated into a fully dense metal part of net shape.

The feedstock binder consisted of water soluble polyethylene glycol that reduced feedstock viscosity, improved particle wetting, aided greenpart shape retention and eliminated toxic solvents in debinding. Carnauba wax and bees wax aided dispersion, lubricated particles, were safe to handle and better for the environment (than petroleum waxes). Their low melt temperatures aided removal during thermal debinding and supported residue elimination.

By optimising the ratio of water soluble, wax and polyolefin binder components (3: 2: 1 respectively) for melt flow and pellet formation, greenparts defect free with uniform particle distribution were made. The optimal binder system proved suitable for titanium alloy and irregular shape pure titanium powders (hydride-de-hydride). Increasing powder loading ( $w_p = (0.60 \text{ to } 0.65)$ ) had no appreciable effect on viscosity while enabling feedstock with good uniformity and pellet formation. Dimensional change was not affected by uniformity of the feedstock however molecular weight, volume and dispersion of binder components affected interparticular distances.

Low processing temperatures reduced disruption to part geometry, benefitted particle bonding and helped retain handling strength.

The use of low temperatures for thermal debinding ( $t = 250\text{ }^{\circ}\text{C}$ ) enabled removal of the binder below the temperatures that facilitate interstitial diffusion and oxide/carbide formation, although part thickness, mass and overall volume effected the processing time. A strong correlation was seen between handling strength of the greenparts and defects, such as non-uniform density distribution and cracking after sintering.

Sintering was essential to produce the final part and showed that a binder free brownpart was not the only criteria for eliminating impurities. The furnace atmosphere must remain free from contamination to eliminate transfer back to the parts. This was addressed using an argon sweep gas, however, the design and efficacy of the system was considered inadequate. Decomposition products need to be removed quickly from the furnace as they evolve before impurities from the sweep gas diffuse back into the parts during the extended duration at sinter temperatures ( $t = 1300\text{ }^{\circ}\text{C}$ ).

The combination of an optimised titanium feedstock and the use of a low temperature thermal debinding technique produced a consolidated MIM part of relatively large dimensions. The parts were seen to have uniform microstructure throughout the cross-section with density comparable to that of MIM standards. In difference to the literature, a high powder loading ( $\phi_p = 0.65$ ) of HDH powders was used and shown to be readily mouldable. The higher powder loading also eliminate separation defects and shape distortions evident using lower amounts of powder.

### **Keywords**

Binder, feedstock, injection moulding, low temperature debinding, MIM, powder metallurgy, rheology, titanium.

## **Supporting academic works**

Paul Ewart, Deliang Zhang, Kim Pickering and Brian Gabbitas. *Metal injection moulding of titanium alloy powders; towards a titanium industry for New Zealand. A review supported by preliminary research findings.* A presentation at the SMNZI Materials Conference 10 - 11 December 2009, The University of Waikato, Hamilton, NZ.

Paul Ewart, Deliang Zhang, Kim Pickering and Brian Gabbitas. *Research on Metal Injection Moulding of Titanium Alloy Powders; towards a Titanium Industry for New Zealand.* A reviewed paper published in Proceedings of: SMNZI Materials Conference 2009.

Jorge Ortegon, Ernesto Zarazua, Sreenath Kodedala, Seokyoung Ahn, Paul Ewart and Deliang Zhang. *Metal injection moulding of titanium alloy powders; effects of binder composition on green part quality and the handling strength of the brown part following debinding.* A poster in the Hispanic Engineers Science and Technology Conference (HESTEC), The University of Texas Pan American, Edinburg, Texas. Sept. 26 - Oct. 2, 2010.

Jorge Ortegon, Ernesto Zarazua, Sreenath Kodedala, Seokyoung Ahn, Paul Ewart and Deliang Zhang. *3D Filling Analysis of Multi-Scale Metallic Implant Parts Promoting Osseointegration by PIM.* A poster in the Hispanic Engineers Science and Technology Conference (HESTEC), The University of Texas Pan American, Edinburg, Texas. Sept. 26 - Oct. 2, 2010.

Paul Ewart, Seokyoung Ahn, and Deliang Zhang. *Injection moulding titanium powders; feedstock homogeneity and handling strength.* A presentation at the MIM2011 March 14-16, Conference, Lake Buena Vista (Orlando), Florida. 2011

Paul Ewart, Seokyoung Ahn, Deliang Zhang and Seong Jin Park. *Encapsulation of titanium powders during binder removal from a metal injection moulded part*. A presentation at the PowderMet2011, International Conference on Powder Metallurgy & Particulate Materials May 18–21, San Francisco, California. 2011.

Paul Ewart, Seokyoung Ahn, Deliang Zhang, Seong Jin Park and Randall M. German. *Powder Injection Molding of Multi-scale Titanium Parts - Micro Features and Surface Modification*. Poster, PowderMet2011, International Conference on Powder Metallurgy & Particulate Materials May 18–21, San Francisco, California 2011.

Paul Ewart, Seokyoung Ahn, and Deliang Zhang. *Injection moulding titanium powders; feedstock compounding, homogeneity and handling strength*. A paper publication in Powder Injection Moulding International. Vol. 5 No.2 June 2011.

Paul Ewart, Seokyoung Ahn, and Deliang Zhang. *Removal of the Water Soluble Binder Component from Titanium Green Parts Produced by MIM*. Powder Processing, Consolidation and Metallurgy of Titanium, Conference. 5 - 7 December Brisbane Australia 2011.

Paul Ewart. *Metal Powder Injection Moulding; Research to Commercialisation*. Presentation to WaiCAM industry symposium. University of Waikato, Hamilton, NZ. December 2011.

Paul Ewart. *Metal Powder Injection Moulding, Research and Industry. A review and assessment of MIM as a commercial process and barriers to successful fabrication*. A report presented as condition of the Trade and Investment Research Scholarship 2010. January 2012.

Paul Ewart, Deliang Zhang and Seokyoung Ahn. *Removal of the Water Soluble Binder Components from Titanium and Titanium Alloy Powder Compacts Produced by MIM*. A paper reviewed and

published in Key Engineering Materials Vol. 520, Powder Metallurgy of Titanium. Editor Ma Qian, 2012.

Paul Ewart, Deliang Zhang and Seokyoung Ahn. The Effect of Low Temperature Thermal Debinding on MIM Titanium Parts. Parent Document: Proceedings of the 2012 Powder Metallurgy World Congress & Exhibition. 2012.

Paul Ewart, Johan Verbeek and Gabbitas, B. *Identification of Key Parameters for Injection Moulding Titanium Metals*. A presentation at the NZ Conference of Chemical and Materials Engineering. Auckland, NZ, 25 - 26 November 2013.

Paul Ewart, Johan Verbeek and Seokyoung Ahn. *A comparison of titanium MIM parts produced using various furnace conditions*. A presentation at the International Titanium Powder Processing, Consolidation and Metallurgy Conference. Hamilton, New Zealand, 2 - 4 December 2013.

## **Acknowledgements**

Besides all I have learnt during the PhD journey I now know that without the love and support of my wife and daughters this thesis would not have been possible.

I also acknowledge the enduring support of;

Johan Verbeek as my Chief Supervisor.

Hilda Chikwanda (UoP, South Africa) and Thomas Ebel (HZG, Germany) who as my examiners provided critical review and recommendations for the final manuscript.

Seokyoung Ahn my research advisor (US/Korea), Co-Supervisors Brian Gabbitas and Kim Pickering, and Past-Supervisor Deliang Zhang.

Technical and administrative support from the faculty and wider University, support with many funding applications from the Scholarships office and the moral fortitude to continue from my friends and fellow researchers.

Research funding from ENGCONS, Fulbright NZ, MFAT, UoW, UTPA and WaiCAM.

The industry support of ProMould Custom Moulding Ltd, SGS Hamilton Ltd, and TiDA Ltd.

Thanks also to Gods' grace.

## Contents

|   |       |
|---|-------|
| Abstract .....  | i     |
| Keywords.....   | ii    |
| Supporting academic works.....                            | iii   |
| Acknowledgements .....                                    | vi    |
| Contents .....  | vii   |
| List of Figures.....                                      | xii   |
| List of Tables .....                                      | xx    |
| List of Symbols/units .....                               | xxiii |
| List of Nomenclature.....                                 | xxiv  |
| Chapter One: Introduction .....                           | 1     |
| Chapter Two: Literature review.....                       | 5     |
| 2.1.    The feedstock used for MIM .....                  | 8     |
| 2.1.1.    The binder systems of MIM feedstock.....        | 10    |
| 2.1.2.    Metal powders used in MIM .....                 | 13    |
| 2.1.3.    Mixing of MIM feedstock .....                   | 17    |
| 2.2.    The injection moulding process.....               | 24    |
| 2.3.    Debinding processes for binder removal.....       | 27    |
| 2.3.1.    Solubility and solution debinding methods ..... | 32    |

|   |   |    |
|---|---|----|
| 2.3.2.  | Thermal debinding methods .....                   | 34 |
| 2.3.3.  | Combined solvent/ thermal debinding methods ..... | 38 |
| 2.3.4.  | Single step catalytic debinding methods.....      | 39 |
| 2.4.  | Consolidation through sintering.....              | 40 |
| 2.5.  | Summary .....                                     | 45 |
| Chapter Three: Injection moulding titanium based metal with a polymer binder system ..... |   | 47 |
| 3.1.  | Experimental.....                                 | 48 |
| 3.1.1.  | Materials .....                                   | 48 |
| 3.1.2.  | Equipment .....                                   | 50 |
| 3.1.3.  | Methodology .....                                 | 54 |
| 3.2.  | Results and discussion.....                       | 58 |
| 3.2.1.  | Thermal assessment and mixing.....                | 59 |
| 3.2.2.  | Moulding.....                                     | 70 |
| 3.2.3.  | Debinding.....                                    | 71 |
| 3.2.4.  | Sintering .....                                   | 75 |
| 3.3.  | Conclusions.....                                  | 81 |
| Chapter Four: A wax based binder for titanium based MIM .....                             |   | 82 |
| 4.1.  | Experimental.....                                 | 83 |
| 4.1.1.  | Materials .....                                   | 83 |
| 4.1.2.  | Equipment .....                                   | 84 |
| 4.1.3.  | Methodology .....                                 | 84 |

|  |                              |     |
|--|------------------------------|-----|
| 4.2.   | Results and discussion ..... | 88  |
| 4.2.1.   | The binder .....             | 88  |
| 4.2.2.   | The feedstock .....          | 90  |
| 4.2.3.   | Moulding .....               | 92  |
| 4.2.4.   | Debinding.....               | 96  |
| 4.2.5.   | Sintering .....              | 101 |
| 4.3.   | Conclusions.....             | 105 |
| Chapter Five: Feedstock formulation .....                      |                              | 106 |
| 5.1  | Experimental.....            | 107 |
| 5.1.1  | Materials .....              | 107 |
| 5.1.2  | Equipment .....              | 107 |
| 5.1.3  | Methodology .....            | 111 |
| 5.2  | Results and discussion.....  | 117 |
| 5.2.1  | The binder components .....  | 117 |
| 5.2.2  | Feedstock melt flow .....    | 119 |
| 5.2.3  | Thermal assessment.....      | 131 |
| 5.2.4  | Moulding.....                | 136 |
| 5.2.5  | Debinding.....               | 138 |
| 5.2.6  | Sintering .....              | 142 |
| 5.3  | Conclusions.....             | 149 |
| Chapter Six: Mixing assessment and particle interactions ..... |                              | 150 |
| 6.1.   | Experimental.....            | 150 |

|  |   |     |
|--|---|-----|
| 6.1.1.                                   | Materials .....                                     | 150 |
| 6.1.2.                                   | Equipment .....                                     | 151 |
| 6.1.3.                                   | Methodology .....                                   | 154 |
| 6.2.                                     | Results and discussion .....                        | 157 |
| 6.2.1.                                   | Compounding and uniformity .....                    | 157 |
| 6.2.2.                                   | Press moulding.....                                 | 160 |
| 6.2.3.                                   | Debinding.....                                      | 163 |
| 6.2.4.                                   | Particulate interactions and compact handling ..... | 165 |
| 6.2.5.                                   | Injection moulding and part processing. ....        | 166 |
| 6.2.6.                                   | Debinding.....                                      | 170 |
| 6.2.7.                                   | Sintering .....                                     | 172 |
| 6.3.                                     | Conclusions.....                                    | 178 |
| Chapter Seven: Summary and solution..... |   | 180 |
| 7.1.                                     | Experimental.....                                   | 180 |
| 7.1.1.                                   | Materials .....                                     | 180 |
| 7.1.2.                                   | Equipment .....                                     | 181 |
| 7.1.3.                                   | Methodology .....                                   | 182 |
| 7.2.                                     | Results and discussion .....                        | 183 |
| 7.2.1.                                   | Feedstock melt flow .....                           | 183 |
| 7.2.2.                                   | Debinding.....                                      | 185 |
| 7.2.3.                                   | Sintering .....                                     | 190 |
| 7.3.                                     | Conclusions.....                                    | 195 |

|   |     |
|---|-----|
| Chapter Eight: Conclusion and recommendations ..... | 197 |
| References:.....                                    | 201 |

## List of Figures

|   |    |
|---|----|
| Figure 1: Viscosity values for particle distribution [70] (Reproduced by permission, © Malvern Instruments). .....                              | 14 |
| Figure 2: Optimum dispersity showed low viscosity for constant solid loading [71]. (Reproduced by permission, © Malvern Instruments). .....     | 15 |
| Figure 3: Mixing rotors, a) sigma, b) banbury, c) cam and d) Roller blade (courtesy Rheometer Services Inc.). .....                             | 18 |
| Figure 4: Flow front profile showing slip layers for MIM feedstock. ....  | 19 |
| Figure 5: Dispersion viscosity master curve [72] for mono-dispersed spherical particles. ....   | 23 |
| Figure 6: Shear rate effect on viscosity for increasing particulate fraction [86] (Image © Malvern Instruments, reproduced by permission). .... | 24 |
| Figure 7: Debinding furnaces (a) solvent debinder, (b) catalytic debinder, (c) thermal debinder (courtesy Claus Joens, Elnik Systems). ....     | 29 |
| Figure 8: Theoretical solvent paths during solvent debinding. ....  | 31 |
| Figure 9: TGA plot showing binder weight loss in air. ....  | 36 |
| Figure 10: (a) MIM 3000 batch furnace (courtesy Claus Joens, Elnik Systems). (b) CM 300 continuous furnace (permission CM Furnaces Inc.). ....  | 41 |
| Figure 11: Particles coalesce during sintering at temperatures (50 to 80) % of melt temperatures. a) initially two particles ( $r_0$ ) have     |    |

point contact, b) a neck ( $x$ ) forms at the point of contact, c) a grain boundary forms and the neck continues to grow, d) surface and bulk transport mechanisms form a single entity, e) one single sphere remains ( $r_f \approx 2.52r_0$ ). ..... 42

Figure 12: Three sphere model depicting atomic transport during sintering [158] (reuse by permission Taylor and Francis, Rightslink CCC.). ..... 43

Figure 13: Internal pore size is determined by furnace pressure, surface energy, and diffusivity of gases within the pore..... 44

Figure 14: The batch mixer used to compound feedstock..... 50

Figure 15: Screw configuration of the TSE16 extruder. .... 50

Figure 16: The mould tool comprised fixed and moving inserts and the moulded acetabular cup with hidden detail. .... 51

Figure 17: The basic solvent debinder cycled heated solvent from the reservoir to the green parts to remove the soluble component. .... 52

Figure 18: The thermal debinding kettle with programmable heating allows binder to be removed with the aid of a sweep gas. 52

Figure 19: Sample SDT curves showing tabled selection points... 54

Figure 20: Sample mixing torque curves showing tabled data points. .... 55

Figure 21: Thermal debinding temperature profile. .... 56

Figure 22: Cup cross section showing image sample location..... 57

Figure 23: CW under different thermal conditions a)  $\beta = 5 \text{ }^\circ\text{C}/\text{min}$  in air, b)  $\beta = 20 \text{ }^\circ\text{C}/\text{min}$  in air and c)  $\beta = 5 \text{ }^\circ\text{C}/\text{min}$  in argon. .... 59

|  |    |
|--|----|
| Figure 24: Optical image of a) extruded binder showing segregated components on cooling and b) binder mixed during cool down....                 | 60 |
| Figure 25: Heat energy input for given heating rates. a) $\beta = 5$ C/min and b) $\beta = 20$ C/min.....  | 61 |
| Figure 26: TGA and DTA curves for the binder ( $\beta = 20$ °C/min)...   | 63 |
| Figure 27: Heterogeneity of Ti-6Al-4V feedstock on the micro-scale.<br>.....   | 65 |
| Figure 28: Torque evolution curves for Ti-6Al-4V feedstock with varying powder loading.....  | 66 |
| Figure 29: DTA and TGA curves showing thermal decomposition of the binder in air relative to powder loading of the feedstocks. ....              | 68 |
| Figure 30: (a) The moulded greenpart, after solvent debinding becomes (b) the greypart. ....   | 70 |
| Figure 31: Sintered parts (a, b) III, (c, d) VII with surface defects, distortion and cracks and (e, f) V with blistering.....                   | 75 |
| Figure 32: SEM of FS3 (VII) sample a) fracture surface b) polished surface and FS3 (V) sample c) fracture surface d) polished surface.<br>.....  | 77 |
| Figure 33: Part VII samples etched with Kroll reagent, a) inside section b) centre section and c) outer section (Figure 22). ....                | 78 |
| Figure 34: Part V sample sectioned and etched with Kroll reagent, a) inside section b) centre section and c) outer section (Figure 22).<br>..... | 79 |
| Figure 35: Density distribution assessment by pieces.....  | 85 |
| Figure 36: Thermal debinding temperature profile. ....   | 86 |

|  |     |
|--|-----|
| Figure 37:DTA curve showing the low intensity peak of LLDPE in comparison to the SA. ....  | 89  |
| Figure 38: FS5 greenparts; a) a digital image and radiographs ( $E = 100$ kV, $t = 30$ s) showing b) cracks and c) separation..... | 93  |
| Figure 39: Changing X-Ray energy to focus at; a) top of part, b) middle of part and c) bottom of part. ....                        | 94  |
| Figure 40: Average pycnomic density from top to base of greenpart. ....  | 95  |
| Figure 41: The general feedstock flow path into the mould cavity.  | 96  |
| Figure 42: FS5 cup part at different stages of processing, a) greenpart, b) greypart and c) after brownpart. ....                  | 97  |
| Figure 43: The greenpart a), SD b) 3 h, c) 6 h, d) 9 h, TD only e) and combined f) 3 h SD - TD, g) 6 h SD - TD and h) 9 h SD - TD. | 99  |
| Figure 44: Part surface after (a) solvent and thermal debind and (b) thermal debind only with residual layer.....                  | 100 |
| Figure 45: Images of the sintered part a) outside cup, b) inside cup and c) the radiograph showing through cup.....                | 101 |
| Figure 46: SEM image of the sintered outer surface, a) polished to show coalescence and b) the fracture surface. ....              | 102 |
| Figure 47: Part etched with Kroll reagent showing a) equiaxed alpha grain structure and b) grain boundaries and impurities. .      | 104 |
| Figure 48: Extrusion capillary set up showing melt flow direction. ....  | 108 |
| Figure 49: Capillary rheometer tester construction schematic [182]. ....   | 109 |

|   |     |
|---|-----|
| Figure 50: Modified convection oven used for low temperature thermal debinding with the aid of a sweep gas.....                                 | 110 |
| Figure 51: Thermal debinding temperature time profile. ....   | 115 |
| Figure 52: Mixing torque plots for the feedstock formulations ...   | 120 |
| Figure 53: Workdone by the screw on the feedstock formulations. ....  | 124 |
| Figure 54: Specific mechanical energy plot for the feedstock with varying component ratios. ....  | 125 |
| Figure 55: Viscosity relative to (L/D) ratio with power law trend. ....   | 126 |
| Figure 56: Raw viscosity data from extrusion capillary testing with no account for end effects or slip. ....                                    | 127 |
| Figure 57: Greenpart model showing section changes.....   | 128 |
| Figure 58: Raw viscosity data from capillary rheometer testing with no account for end effects or slip. ....                                    | 129 |
| Figure 59: Corrected viscosity and shear rate data for all feedstock. ....  | 130 |
| Figure 60: Corrected viscosity and shear rate for all feedstocks.   | 131 |
| Figure 61: TGA curves showing progressive weight loss changes debinding progressed ( $\beta = 5 \text{ }^\circ\text{C}/\text{min}$ , air). .... | 133 |
| Figure 62: TGA weight loss for low temperature thermal debinding shows limiting loss value in relation to total sample mass. ....               | 134 |
| Figure 63: a) Green part image b) defect free and uniform density distribution seen in radiograph. ....   | 136 |
| Figure 64: Binder level during solvent debinding ( $t = 250 \text{ }^\circ\text{C}$ ). ...  | 138 |

|   |     |
|---|-----|
| Figure 65: SEM images from green parts after solvent debinding showing, a) pore channels and b) bridging. ....                            | 139 |
| Figure 66: Binder level during low temperature thermal debinding. ....  | 141 |
| Figure 67: TGA curves show the remaining binder level is below the theoretical value and indicative weight gain value due to oxides. .... | 142 |
| Figure 68: The part seen as a) greenpart, b) greypart, c) brownpart and d) fully sintered. ....   | 143 |
| Figure 69: SEM image and EDS locations for sintered part. ....  | 144 |
| Figure 70: XRD elemental map of the Ti64 shows oxides present. ....   | 145 |
| Figure 71: A uniform microstructure of an equiaxed alpha phase matrix and secondary phase a) inner b) centre and c) outer section. ....   | 147 |
| Figure 72. SEM image showing the secondary phase within the primary alpha phase titanium matrix. ....                                     | 148 |
| Figure 73: Aluminium pocket mould. ....   | 152 |
| Figure 74: Solid models of the Ti MIM greenparts. ....  | 153 |
| Figure 75: SEM micrographs of changes in feedstock appearance from increased extrusion mixing a) EM1, b) EM5 and c) EM10. ....            | 158 |
| Figure 76: Melt flow rate for extrusion mixed feedstock.....  | 159 |
| Figure 77: Surface of the green parts, a) EM1, b) EM4 and c) EM10. ....   | 160 |
| Figure 78: TMA expansion curves for moulded parts overtime, temperature profile also shown.....   | 162 |

|  |     |
|--|-----|
| Figure 79: Solvent debound a) EM1, b) EM4 and c) EM10, and solvent/ thermal debound d) EM1, e) EM4 and f) EM10, parts..                            | 164 |
| Figure 80: DMA plots from testing of greenpart (AM) and greypart (SD) specimens.....   | 165 |
| Figure 81: TMA plots for dimensional change during part heating. ....  | 167 |
| Figure 82: Ascending and descending heat flow curve of TiCP greenpart (AM), greypart (SD) and brownpart (TD). ....                                 | 168 |
| Figure 83: SEM images a) greenpart, b) greypart, c) brownpart.   | 169 |
| Figure 84: Binder removal by dissolution for the step part. ....   | 170 |
| Figure 85: TD step parts a) without defects and b) with defects.   | 171 |
| Figure 86: Thinpart a) green, b) brown, c) sintered and defects that remained during sintering d) thinpart and e) thickpart .....                  | 172 |
| Figure 87: SEM image from the outer surface of thinpart, a) bulk Ti and b) internal porosity. ....   | 173 |
| Figure 88: XRD map of the thin titanium part shows high oxygen and carbon levels. ....   | 174 |
| Figure 89: Microstructure of sintered Ti part etched with Kroll reagent, a) polished outer surface and b) polished internal surface. ....          | 175 |
| Figure 90: Cross section of thickpart etched with Kroll reagent.   | 176 |
| Figure 91: Defect seen after sintering only evident in the brownpart. ....   | 177 |
| Figure 92: Sintered Part a) without and b) with defects.....   | 178 |
| Figure 93: Corrected viscosity and shear rate for the Ti ( $\phi_P = 0.65$ ) and Ti64 ( $\phi_P = 0.6$ ) feedstock made with the same binder. .... | 184 |

|   |     |
|---|-----|
| Figure 94: The debinding mechanisms for solvent debinding changes as the level of binder changes. ....                              | 185 |
| Figure 95: TGA weight loss plot for low temperature thermal debinding shows thermal stability occurs sooner for the feedstock. .... | 187 |
| Figure 96: Debinding mechanisms for LTTD shown as pressure driven and concentration driven. ....                                    | 188 |
| Figure 97: Ti cup a) brownpart and b) as sintered.....  | 190 |
| Figure 98: Radiographs of fully sintered cups a) Ti ( $w_p = 0.65$ ) and b) Ti64 ( $w_p = 0.60$ ).....                              | 191 |
| Figure 99: SEM/EDS image of sintered Ti cup part section.....   | 192 |
| Figure 100: XRD line spectra for the sintered cup with carbides, nitrides and oxides of titanium identified.....                    | 193 |
| Figure 101: Microstructure of alpha phase Ti matrix with carbide and acicular formations a) inner b) centre and c) outer section.   | 194 |

## List of Tables

|   |     |
|---|-----|
| Table 1: Examples of widely used feedstock components*.....   | 6   |
| Table 2: Rotor style with shear rate achievable. ....   | 18  |
| Table 3: Suggested solvents for common polymers binders [122].  | 33  |
| Table 4: Thermal values from SDT for the binder and individual components ( $\beta = 20 \text{ }^\circ\text{C}/\text{min}$ , air). .... | 60  |
| Table 5: Comparative values of mixing torque and time for compounding the binder and powder to produce a feedstock. ....                | 67  |
| Table 6: Thermal values from SDT (air) for binder and feedstock.  | 69  |
| Table 7: Mass analysis of the injection moulded green parts. ....   | 70  |
| Table 8: Solvent debinding mass loss for green parts. ....  | 71  |
| Table 9: Mass loss values from thermal debinding the grey parts.  | 73  |
| Table 10: Total binder mass loss from combined treatments. ....   | 74  |
| Table 11: Standard, manufacturer specification and elemental composition by LECO. ....  | 80  |
| Table 12: Component reaction values from SDT ( $\beta = 5 \text{ }^\circ\text{C}/\text{min}$ )...                                       | 88  |
| Table 13: Component volume fractions for the feedstock.....   | 90  |
| Table 14: Temperature of thermal event for feedstock FS4 and FS5. ....  | 90  |
| Table 15: The average mass of greenparts, greyparts and brownparts, and the level of residual binder after processing. ....             | 98  |
| Table 16: Elemental levels ( $w_E$ (%)) by EDS. ....  | 103 |

|   |     |
|---|-----|
| Table 17: Standard composition, manufacturer specification and elemental levels by LECO analysis.....   | 103 |
| Table 18: Dimensions and process parameters of the capillary set.<br>.....  | 108 |
| Table 19: Binder formulation chart for volume ratio of components.<br>.....   | 111 |
| Table 20: Capillary rheometer load and die parameters. ....   | 114 |
| Table 21: Binder thermal event values from SDT ( $\beta = 5 \text{ }^\circ\text{C}/\text{min}$ ).<br>.....  | 118 |
| Table 22: Mixing torque and compounding duration ( $\phi_P = 0.6$ )...  | 121 |
| Table 23: Processing values from the extrusion capillary trials..   | 122 |
| Table 24: Temperature of thermal events from SDT for feedstock before and after debinding in air ( $\beta = 5 \text{ }^\circ\text{C}/\text{min}$ ).....       | 132 |
| Table 25: Key TGA data points from greypart and SD binder sample after low temperature thermal debinding ( $t = 250 \text{ }^\circ\text{C}$ in air).<br>..... | 135 |
| Table 26: Mass averages for greenpart (AM), greypart (SD), brownpart (TD) and sintered part (S). ....   | 137 |
| Table 27: Elemental levels ( $w_E$ (%)) measured by EDS.....  | 144 |
| Table 28: Elemental levels for titanium alloy (Ti64). ....  | 145 |
| Table 29: Indicative elemental levels ( $w_E$ (%)) of the titanium matrix and secondary phase from EDS analysis. ....   | 148 |
| Table 30: Critical dimensions of the greenparts (Figure 74).....  | 153 |
| Table 31: Thermal event values for the feedstock using SDT in air.<br>.....   | 157 |

|  |     |
|--|-----|
| Table 32: Dimensional change from TMA ( $\epsilon$ ) ( $t = (25 \text{ to } 50) \text{ }^\circ\text{C}$ )... | 167 |
| Table 33: Elemental values from EDS spectrum ( $w_E$ (%), Figure 87).<br>.....                               | 173 |
| Table 34: Shimadzu capillary rheometer load and die parameters.<br>.....                                     | 182 |
| Table 35: Mass averages for greenpart (AM), greypart (SD),<br>brownpart (TD) and sintered part (S). ....     | 184 |
| Table 36: Solvent debinding rate analysis. ....  | 186 |
| Table 37: TGA data for low temperature process ( $t = 250 \text{ }^\circ\text{C}$ in air).<br>.....          | 187 |
| Table 38: Thermal debinding rate analysis.....   | 189 |
| Table 39: Elemental levels for the powder and sintered part.....   | 192 |

## List of Symbols/units

$A$  – Cross-sectional area

$B$  - Binder

$D, d$  – Diameter

$E'$  - Storage modulus

$E$  - Electric potential  
difference, activation energy

$F$  – Force

$h$  – Height

$k_r$  – Rate coefficient

$L, l$  – Length

$m$  – Mass

$m$  - Magnification

$\dot{m}$  – Mass flow

$n$  – Frequency

$P$  – Powder

$p$  - Pressure

$t$  – Time, thickness

$t$  – Temperature

$V$  – Volume

$\dot{V}$  – Volume flow

$W$  – Wax, load

$\alpha$  – Coefficient of thermal  
expansion

$\beta$  – Heating rate

$\gamma$  - Shear rate

$\Delta x$  – Dimensional change

$\varepsilon$  – Direct strain, dimensional  
change

$\eta$  – Viscosity

$\theta$  – Angle of diffraction

$\rho$  – Density

$\sigma$  – Standard deviation, direct  
stress

$\tau$  – Shear stress

$\varphi$  - Volume fraction

$\omega$  – Rotational velocity

$w$  – Mass fraction

## List of Nomenclature

|   |   |
|---|---|
| A&D – Company name, brand name, product name      | DSC - Differential scanning calorimetry                       |
| ACME – Company name, brand name, product name     | DTA – Differential Thermal Analysis                           |
| AIP – Company name, brand name, product name      | EDS – Energy dispersive X-ray spectroscopy                    |
| ANSI - American National Standards Institute      | EM – Extrusion mixed  |
| AM – As moulded, greenpart                        | EPMA - European Powder Metallurgy Association                 |
| ASTM - American Society for Testing and Materials | EVA – Ethylene vinyl acetate                                  |
| BASF – Company name, brand name, product name     | FFD - Field of focus depth                                    |
| BCC – Basic centre cubic                          | FS – Feedstock  |
| BM – Batch mixer                                  | HCP – Hexagonal close packed                                  |
| BW – Bees wax                                     | HDH - Hydrogenation dehydrogenation                           |
| CCC – Copyright Clearance Centre                  | HDPE – High density polyethylene                              |
| CFT – Capillary flow test                         | HESTEC - Hispanic Engineers Science and Technology Conference |
| CM – Company name, brand name, product name       | HZG – Helmholtz - Zentrum Geesthacht                          |
| CW – Carnauba wax                                 | HIP - Hot iso-static press                                    |
| DMA – Dynamic multi-frequency mechanical analysis | ICO – Company name, brand name, product name                  |
| Dr Boy – Company name, brand name, product name   | L/D – Length with respect to diameter                         |

|  |  |
|--|--|
| LECO – Company name, brand name, product name                  | PMMA – Polymethylmethacrylate                      |
| LLDPE – Linear low density poly-ethylene                       | POM – Polyoxy-methylene                            |
| LTTD – Low temperature thermal debinding                       | PP – Polypropylene                                 |
| MFAT – Ministry of Foreign Affairs and Trade                   | PS – Polystyrene                                   |
| MFI - Melt flow index  | PTFE – Polytetrafluoroethylene                     |
| MFR - Mass flow rate   | PVA – Poly-vinyl acetate                           |
| MIM – Metal Injection Moulding                                 | PVB – Poly-vinyl butyrol                           |
| MUD - multifunctional utility diesel                           | PVAL – Poly-vinyl alcohol                          |
| MW - Molecular weight  | PW – Paraffin wax                                  |
| NZ – New Zealand   | RBW – Refined bees wax                             |
| PA - Polyacetal  | S - Sinterpart                                     |
| PBMA – Polybutylemethylacrylate                                | SA – Stearic acid                                  |
| PDS - Plasma Discharge Spherodisation                          | SD – Solvent debind, greypart                      |
| PEG – Polyethylene glycol                                      | SDT – Simultaneous differential thermometer        |
| PEG8 – PEG with MW of 8000                                     | SEM – Scanning electron microscope                 |
| PEG20 – PEG with MW 20000                                      | SGS – Company name                                 |
| PID – Proportional, integral, differential signal conditioning | SI - International System of Units                 |
| PIM – Powder injection moulding                                | SME – Specific mechanical energy                   |
| PM – Powder metallurgy   | SMNZI – Society of Metals New Zealand Incorporated |
|  | TA – Thermal Analysis                              |
|  | TD – Thermal debind, brownpart                     |

|  |  |
|--|--|
| TEM - Transmission electron microscope                     | US, USA – United States of America                                   |
| TGA – Thermo-gravimetric analysis                          | WaiCAM – Waikato Centre for Advanced Materials                       |
| Ti - Titanium  | UoP – The University of Pretoria                                     |
| Ti64 or Ti-6Al-4V – Titanium, aluminium and vanadium alloy | UoW – The University of Waikato                                      |
| TiCP – Commercially pure titanium                          | UTPA – The University of Texas-Pan American                          |
| TiDA – The Titanium Industry Development Association       | WD - Work done   |
| TMA – Thermo-mechanical analysis                           | X-Ray – Electromagnetic radiation (X signifies the radiation source) |
| TSE – Twinscrew extruder                                   | XRD - X-ray crystallographic diffraction                             |

## **Chapter One: Introduction**

The injection moulding process is not restricted to polymeric materials with injection moulding of particulate materials (PIM) originally acknowledged in the 1920s [1]. The early research leads to Schwartzwalder's 1938 patent for forming ceramic spark plugs used by General Motors [2, 3]. Metals were formed from particles, binders and thermal processing in the mid 1940s and in the 1970s Karl Zueger, Ray Weich and partners formed a company to commercialise their process in North America [4-7]. PIM technology was often considered too complicated with too many unknowns [8]. Critical aspects of the technology have since been enabled with improved process control, equipment development and technical expertise contributing to the process now well established for ferrous and copper metals [9].

Metal injection moulding (MIM) is a process for fabricating parts from metal powders. As a net shaping process it eliminates waste and the need to machine complex features as the powders are moulded to the required geometry with consolidation by sintering. It provides equal or better material properties to those of cast or wrought metals and can be used for practically any metal produced in particulate form.

In order to use the injection moulding process the flow properties of the powders must be modified. The high interparticle friction is reduced using a carrier (binder) that is removed prior to sintering. The combination of metal powder and binder is referred to as the feedstock and is the first key step in the MIM process.

Academic investigation into metal injection moulding (MIM) started about ten years ago within the Oceania region, with industry

development shortly after. Commercial activity has been underway four to five years with start-up companies in New Zealand (NZ) in the last three years. In NZ, barriers to commercial activity (technical expertise, suitability of equipment, process knowledge, customer expectations and licensing costs) are even greater than they were in Europe, Asia and the Americas thirty years ago [10]. This being due to a lack of expertise and the associated technologies from which MIM emerged, especially an established powder metallurgy industry. With regard to the manufacturing industry; this work endeavoured to identify and solve aspects of the MIM process in general that is restricting commercial practise in NZ.

This study investigated current limitations of the MIM process regarding the two most common commercial grades of titanium (Ti) based metals. Pure titanium (TiCP) and a titanium, aluminium and vanadium alloy (Ti-6Al-4V) used extensively in the aerospace, chemical and medical industries.

There are four key processing steps in MIM, the first is to produce a feedstock, the second to form (mould) the required geometry, the third to remove the binder (debind) and the final consolidation (sinter) step. The mechanical properties required for end use of the part determines the acceptable elemental composition where standard grades are not specified.

The homogeneity of the binder in the feedstock and the flow properties of the feedstock are important and aid mould filling during the injection moulding phase. A more critical requirement will be the uniform distribution of particles in the feedstock and after moulding. The particle to particle interactions are far more critical to final part quality than the particle to binder interactions.

The concept, common in the literature, that the particle to binder interface requires strong adhesive bonds was disputed. Individual

particles require binder encapsulation to reduce friction during moulding. When the particles come to rest the green part cools to its lowest energy state. In this state the particles should have clean contact with no entrapped binder. Although there is interdependence on these interactions it was proposed that the particle to binder interface should be weak.

The interparticle bonds that form during moulding are critical to final part quality. Expansion within the compact will affect the particle packing, especially where binder remains in the compact. Disruption to particle packing should therefore be eliminated by keeping the debinding temperatures as low as possible.

During thermal debinding, temperatures are often in excess of those at which titanium powders will uptake contaminants. This is mitigated by use of atmosphere control. The use of low temperature ( $t = 250\text{ }^{\circ}\text{C}$ ) would also ensure the mechanisms for contaminant uptake are not in play. These thermal controls will therefore provide a reduction in both contaminant uptake and reliance on atmosphere control, during sintering.

Presentation of the research supporting the abovementioned hypothesis is set out in the following chapters as an applied scientific investigation. The structure may be considered slightly untraditional but will be found invariant in overall content. The decision to use separate experimental sections was based on the varying locations at which the research was conducted and the wide range of instrumentation used. The International System of Units (SI) was consistently applied within the guidelines set out by the American National Standards Institute (ANSI) throughout [11].

Chapter Two reviewed the literature identifying the underpinning knowledge that enables MIM, and determines limiting factors for titanium. Chapters Three and Four were used to test and confirm

that base knowledge with scoping studies and defined the subsequent investigation.

Chapters Five and Six investigated the key processing steps of an optimised feedstock formulation and allowed extensive rheological and moulding assessment. Investigation of debinding mechanisms supported a unique thermal process to be trialled and its efficacy determined.

Chapter Seven as the final experimental work in this research saw a culmination of the previous results in an applied solution that was novel and addressed some important aspects to extend the current knowledge of titanium MIM. Chapter Eight summarised and concluded on the research findings that an improved understanding of the Ti MIM fabrication process had been presented to better enable NZ industry to uptake the technology.

## **Chapter Two: Literature review**

As recently as 1982 commercial metal injection moulding (MIM) was too complicated, it proved difficult to get right and had too many unknown processing variables [8]. The greatest barriers to commercial activity were availability of metal powders, lack of technical expertise, suitability of equipment, process knowledge, customer expectations and licensing agreement costs [10]. Critical aspects, such as process control and understanding of the fundamentals, have since been addressed by established providers. Although the process is now proven for ferrous and copper metals, it is still easy to get wrong [9]. Further to this; reactive metals' parts (aluminium, titanium, magnesium) are still considered by many not possible to produce using MIM. It can be agreed that reactive metals are extremely difficult to process and as such are not being utilised to the extent with which they could be [12]. Titanium is one such metal and the development for MIM requires a scientific approach and a depth of understanding of the process and quality systems, in a similar manner to the initial development of the MIM process in the 1980s and 1990s [13].

A process patented in 1958 was used to form feedstock pellets suitable for moulding finely divided powders using a binder that was removed by burnout at high temperature [14]. The most common binder combinations today contain thermoplastic polymers, paraffin waxes and functional additives [15-17]. Polymers provide plasticity and mechanical strength when blended and are generally the last component to be removed prior to sintering [1, 17]. Waxes improve flow properties, increase wettability and improve lubrication. When mixed with powders the feedstock is formed and addition of functional compounds enhance

wettability, help lubricate and maintain powder dispersion during mixing and moulding (Table 1) [15, 18]. There must be good flow with low viscosity, high viscosity feedstock makes moulding difficult, however large amounts of binder give low strength and may introduce greenpart deformations [19].

Table 1: Examples of widely used feedstock components\*.

|   |
|---|
| <b>Polymers</b>   |
| Polyethylene (PE), polypropylene (PP), polyacetal (PA), polyethylene vinyl acetate (EVA), polymethyl methacrylate (PMMA), polyvinyl acetate (PVA), polyvinyl butyrol (PVB), polystyrene (PS). |
| <b>Waxes</b>  |
| Paraffin, carnauba, natural bee, micro-crytalline, fatty acid, polyoxymethylene, montan, candelilla.  |
| <b>Functional</b>   |
| Lubricants, wetting agents and plasticizers i.e., stearic acid, butyric acid, di-ethylphalate, boric acid, oils, fatty alcohols.  |
| <b>Particulates</b>   |
| Most metals that form particulates i.e. carbon steels, nickel, stainless steel, precious metals, copper, tungsten, carbide, titanium, super alloys, alloys of most metals and custom blends.  |

\*Binders from organic compounds such as protein based agars and more recently bio-polymers are also in use.

Titanium (Ti) is found in at least 35 mineral forms, is the ninth most abundant element in the earths' crust and fourth most abundant metallic element [20, 21]. German considers three product categories for Ti MIM (cosmetic, structural and demanding) that may utilise different starting powders, mechanical properties and part finish as dictated by the quality required [22].

Ti metal has a good tensile strength ( $\sigma > 650$  MPa) and ductility (elongation to fracture  $> 20$  %), with a moderate density ( $\rho = 4.5$  g/cm<sup>3</sup>) giving excellent specific properties (aerospace industry) [23]. It has corrosion resistance (chemical industry) greater than stainless steels and is highly bio-compatible (medical and dental application) [22, 24-26]. When alloyed i.e. Ti-6Al-4V, Ti has even

more desirable properties, high tensile strength ( $\sigma > 1000$  MPa), high resistance to creep ( $t \sim 650$  °C) and high corrosion resistance [23]. Negative aspects that keep Ti from materials selection are associated with cost and, for many titanium alloys, poor machinability as well as poor fatigue properties [27-29]. Despite the above qualities, Ti is not well known and overlooked for many applications that it would suit.

Referred to as a metallic solvent Ti has a reactive nature (fine powder) and affinity for contamination from common elements when processed at elevated temperatures [30, 31]. Although MIM is increasingly being used to produce metal parts with complex geometries, less than 1% utilise Ti, and mostly as demonstration parts suggesting a dominant titanium process has yet to be found [22, 32-34].

The MIM process ensures titanium powders are in close proximity with potential contaminants, the binder system. It is therefore necessary to understand the mechanisms of particle adhesion and bond strength in the greenpart. MIM feedstocks rely on rheological data, thermal analysis, and metallurgical composition of the final part [35-37]. Ti is more difficult to process using MIM and requires control on the level of interstitial elements especially, carbon, hydrogen, nitrogen and oxygen which cause embrittlement [18, 38-40]. Typical feedstock powder loading is (50 to 70) %, with a mean particle size of  $< 45\mu\text{m}$ , although many products require  $< 20 \mu\text{m}$  and more recently  $< 10 \mu\text{m}$  is not uncommon [41-43]. Particle distribution and particle shape are shown to affect packing kinetics and debinding behaviour as well as shrinkage and final part density [17, 18, 38, 41, 44, 45]. The most commonly used binder components for Ti MIM as expressed in recent literature are multiphase compositions of polyethylene glycol, polypropylene, paraffin wax and stearic acid [46, 47].

## **2.1. The feedstock used for MIM**

The binder components combine and encase the particles allowing them to flow at similar temperatures and pressures as polymers. Thermoplastic materials melt over a wide range of temperatures. Above the softening point or glass transition temperature ( $T_g$ ) intermolecular forces between the polymer chains allow movement within the elastic region [48]. At the melting point ( $T_m$ ) thermal energy overcomes intermolecular forces, the lattice breaks down and the polymer becomes liquid [49]. At temperatures just below  $T_m$  is a softened state where application of a driving force overcomes resistance to flow and allows materials to be moulded and formed.

The individual binder components determine the behaviour of the feedstock. Interactions may involve diffusion of one component into another, dissolution of the components into one another or chemical reactions [50]. Therefore the formulation process often relies on rheological data and thermal analysis, but any effect on the metal composition must also be considered [35, 37, 51].

The viscosity at moulding temperatures require the feedstock melt to flow smoothly into the die without segregation, and viscosity to remain constant during temperature fluctuations [52]. Low viscosity binders ( $< 100 \text{ Pa s}$  at  $1000 \text{ s}^{-1}$ ) are considered suitable for mixing with metal particles and loadings considerably higher than traditionally filled polymers have shown no problems during moulding [52, 53]. Particle size distribution and particle shape affect packing kinetics, debinding behaviour, shrinkage and final part density [17, 18]. It is often reported that the amount of binder added to the powder should equal the void space between particles as an excess or deficiency may result in distortion or defect formation [1, 53].

Selection of binder components is based on a number of considerations. This includes the availability of processing equipment, regulatory constraints, safety concerns, the metal composition of the powders and the final application. The optimum solids loading is known to decrease as the particle size decreases and it has been suggested that 50 % might suit small particles ( $d = 0.1 \mu\text{m}$ ) [3]. Concerns yet to be addressed, include particle size dependent viscosity shifts with shear rate, powder-binder separation, and heating/cooling behaviour [3].

A binder has a number of functions and determines greenpart strength. It effects dispersion of the metal particles, compaction properties, chemical stability and debinding rate of the feedstock. When mixing the feedstock components the binder also provides capillary and viscous forces to wet the particles [49]. The binder creates a thin dense layer on the particles reducing the attraction forces between them (negligible increase in size) and reduces viscosity. A feedstock should provide good formability and enable the greenpart to easily separate from the metal die and retain part shape and strength. Nor should it leave carbon or decomposition residue after debinding and sintering.

Only a multi-component mixture provides the range of functions of a successful binder [1]. The components should be mutually or partially soluble with each other i.e. when a polymer is insoluble in wax, it agglomerates in the wax matrix [5]. As a result, the softening point of the binder will be close to that of the wax which may not be of benefit as most waxes have a narrow decomposition range [19]. However, if the components are soluble to each other, the softening point of the binder increases above that of wax [49]. Herranz concluded that compatibility between binder components is essential but only partial miscibility between components is beneficial to subsequent debinding [19].

Environmental factors should also be considered, binders and their components should not be harmful on the environment or production staff during mixing, moulding, or removal and should be passive towards the powders [5].

### **2.1.1. The binder systems of MIM feedstock**

The first patented binder systems documented in 1935 for alumina ceramics were also considered suitable for binding oxides of magnesium and titanium [2]. Thermosetting materials (Bakelite, glycerol-phthalic-anhydride, phenol formaldehyde, urea formaldehyde) were easy to debind and did not lead to thermal deformation. Thermoplastic resins (vinyl compounds, aluminium stearate, cellulose acetate and various waxes) were also used. Lubricants (stearic acid, oleic acid, palmitic acid) with low melting point were intended to migrate out to the mould walls to aid part release and enable formation of connected pores [2].

In 1944 Bellamy patented a binder for moulding metal parts and porous metal moulds using ferric hydroxide and ammonium chloride that formed a paste when mixed with water [4]. The process used a reducing atmosphere during heating to vapourise the chloride and reduce the hydroxide prior to sintering [4].

In 1954 Pitzer patented a pelletising process to improve the fluid properties of fine powders [14]. These were mixed with binders of hydrogenated oils (i.e. corn, peanut, cotton seed and vegetable), waxes, crude asphalts, ammonium compounds, metal salts and soaps. He also used natural and synthetic resins (wood rosin and low melt polymers) that were thermally removed in a calcination step [14].

A description of MIM was published in 1975 by Dreger and then Bangs and PIM technologies grew when Weich and Rivers applied for patents [54]. Rivers binder comprised methyl cellulose, glycerine, boric acid and water with thermal removal from the

compact (greenpart) included as part of the sinter cycle (1978) [55]. The Weich process was based on, cotton seed or soybean oil, polyglycols or poly-vinyls, polystyrene and polyethylene, with removal by one or a combination of solvent vapour, liquid solvent and thermal treatment (1980) [56]. Weich also developed a binder system of paraffin wax, carnauba wax and polypropylene [15, 57, 58]. These were followed by Billiet's system of polyethylene, polypropylene, polymethyl-methacrylate, carnauba wax, paraffin wax, benzoyl peroxide and cobalt blue (1987) [59]. After this point in time the dominant composition had been established with the majority of subsequent binders having a similar composition to the Weich system.

A range of binder components and their effects on the MIM process are given below showing some of the wide range of modifications possible and the complexity of the formulation process.

Kryachek reviewed binders and grouped them as thermoplastic resins, thermo-reactive resins, freezable binders and gelatinized systems [5]. Water-soluble binders were also considered important i.e. PEG, antipyrone, polymethylacrylate, SA, PVA, boric acid and gelatin. He also referred to binders based on waxes i.e. montan-ester and liquid paraffin, that accelerated removal and enabled high density sintered parts.

Benson et al. combined EVA, wax (Licomont), SA and EVA plasticiser specifically for titanium [60]. They found through rheology that powder loadings as high as 70 % could be achieved but depended on the particle size and shape.

Vyal et al. used oleic acid, wax and sugar syrup as the binders to investigate greenpart strength for copper and iron [61]. Addition of carboxymethyl cellulose and polyvinylacetate (PVA) increased greenpart strength and enabled cutting and drilling without

damage to the geometry but showed the effect differed for individual metals.

Shibo et al. produced feedstock specifically for Ti ( $\phi = 63$  % paraffin wax, 12 % PEG, 14 % LDPE, 10 % PP and 1 % SA) [62, 63]. Partially replacing LDPE with PP reduced ash content during thermal debinding and sintering. PEG also improved interaction between components and allowed more binder to be removed during solvent debinding.

Ferri et al. investigated the influence of the MIM process on the fatigue properties of Ti. A feedstock to 32 % binder (PE, paraffin and SA) was unable to match the properties seen for wrought material [16].

Chuankrerkkul et al combined PEG, PMMA and SA in a feedstock for tungsten hard metals and stainless steel to investigate void formation [64, 65]. The use of SA reduced the viscosity but had no appreciable effect on sintered density. It was seen that more voids formed when the SA increased past a certain ratio relative to the PEG.

Herranz et al produced a binder for bronze ( $\phi = 50$  % HDPE, 50 % PW) and found substitution of PEG for PW improved powder loading and debinding [42]. Initial investigation saw decreased densities coincided with the PEG. This was due to increased carbon levels in the sintering atmosphere and was eliminated by use of argon or by reducing residual carbon in the brownpart.

Ahn et al. used seven different feedstocks; wax/polymer based and one water-soluble agar binder system to determine the effect on moulding parameters [36]. Wax controlled viscosity, SA as surfactant and polymer as the minor component. The results were compared with simulation studies and found the reliance of binder and powder on rheology, pressure, temperature and velocity parameters was different.

### **2.1.2. Metal powders used in MIM**

Almost any metal that can be produced in a suitable powder form can be processed by MIM. Reactive metals such as aluminium, magnesium and titanium are considered exceptions because of their affinity to contamination by common elements and for aluminium the adherent oxide film present on the surface inhibits sintering [52]. Powders for Ti MIM are expensive with supply issues and control of the metal chemistry still problematic [26-28, 66-69]. Powder characteristics (particle size, size distribution, shape, surface morphology) influence the achievable powder fraction as they effect the interaction of the particles. Increasing average particle size reduces the number of contact points and increases the interparticle spaces. The shape and surface morphology will determine the ability of the particles in contact to move relative to each other. Particle shape is determined primarily by production method and is typically one of two; spherical powder which has desirable flow properties and irregular powder which enable better shape retention during post moulding operations [1]. Although variable effects due to pressure such as, distribution, gradients and temperature are not so important [44]. The selection of metal powders with respect to density, shape and size are more important for MIM than other PM processes.

These factors also effect the rheological properties of feedstock and therefore final product formation [38]. It has been shown that a change in particle size distribution can affect the viscosity and stability of particle suspensions [70]. A wide distribution creates more free space for particles to move and it is easier for the feedstock to flow, i.e. lower viscosity. Therefore, it should be possible to increase solids loading without increasing the viscosity (Figure 1) and also maintain system stability.

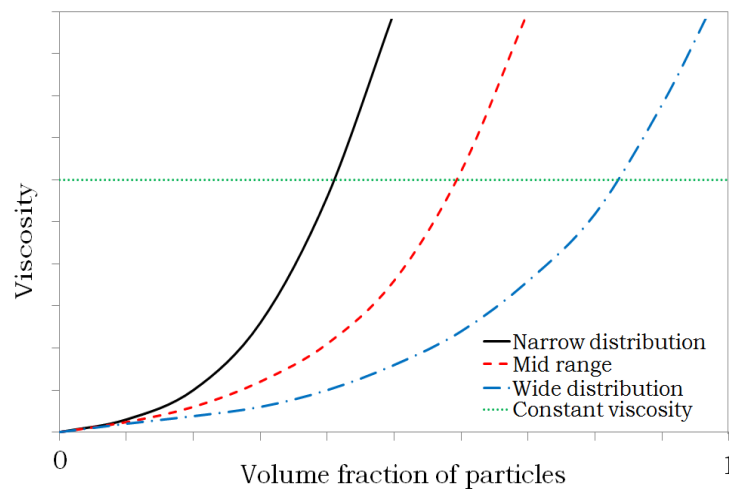


Figure 1: Viscosity values for particle distribution [70] (Reproduced by permission, © Malvern Instruments).

Figure 2 showed that a sample of relatively large particles with a small proportion of small particles may have a lower viscosity than a similar suspension of small particles or large particles alone. This is due to the combined effects of the number of particle-particle interactions, the particle size and polydispersity and will affect packing kinetics as well as debinding behaviour and have an effect on final part density [26, 69, 71-73].

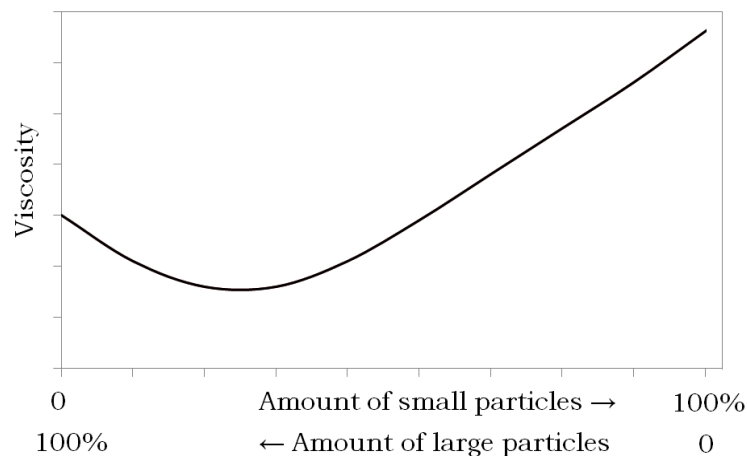


Figure 2: Optimum dispersity showed low viscosity for constant solid loading [71]. (Reproduced by permission, © Malvern Instruments).

The powder properties have a strong influence on the final MIM part with ideal particle size 30  $\mu\text{m}$  and preferably 10  $\mu\text{m}$ . Coarser powders or a mixture of coarse and fine powders are used to increase the powder loading or reduce porosity of the part [53]. The least active, coarser powders are balanced by close packing of finer powders which affect the permeability of the green part, as will the particle size [65, 74]. The use of coarser powders makes it possible to shorten the time for binder removal. Finer powders allow high surface purity and finish for an article [5] and greater deviation in process parameters during sintering.

Hydrogenation de-hydrogenation (HDH) powder has an irregular shape and lower production cost [26, 69]. This aids mechanical

interlocking and helps retain part shape once the binder has been removed. Spheroidisation of irregular particles, as a secondary process, has shown to improve density and flowability as well as benefit sintered products [38, 75]. Gas atomised powder are more expensive and their spherical shape can improve feedstock flow compared to irregular shape particles [26]. The regular shape can also benefit the debinding process, although they do not help with compaction of the powder [39]. Plasma Discharge Spherodisation (PDS) can produce metal, alloy and intermetallic powders with small mean particle size ( $d \approx 5 \mu\text{m}$ ), narrow size distribution and high purity [26, 41].

The European Powder Metallurgy Association (EPMA) has set concepts of best practice for MIM powders [52]. These factors enable reduced development time by creating parameters within which to begin investigations.

- clean particle surface for predictable binder interaction
- spherical particles improve flow properties (loss of geometry during debinding with reduced mechanical bonding)
- highest loading fraction possible i.e. high packing density
- no agglomeration, equiaxed particle shape with sufficient interparticle friction to avoid distortion after binder removal
- angle of repose  $> 55$  degrees, particle size  $< 20 \mu\text{m}$ , dense particles free of internal voids for rapid sintering
- tailor particle size distribution, mixture of lower cost large particles and higher cost small particles
- fine powders sinter more readily than coarse

### **2.1.3. Mixing of MIM feedstock**

To produce a homogenous MIM feedstock sufficient shear force and temperature is required during mixing, however the viscous nature of thermoplastic melts only allow for laminar flow [76]. The mechanisms may be considered as dispersive (extensive) leading to size reduction and distributive (intensive) for spatial redistribution [76]. The principle actions of feedstock compounding may be considered in the following five steps

- the particles are combined with the binder and loose particles, agglomerates and binder components disperse as air becomes displaced
- the binder components wet the particles and penetrate agglomerates which may form due to Van de Waals forces or surface tension of the binder
- the agglomerates breakdown as the aggregates break away and become wetted
- random flow allows dispersion of the particle aggregates and leads to uniform distribution
- spatial uniformity of the particle aggregates enables dispersion of binder components leading to stabilisation and uniform laminar flow

The feedstock mixing process begins with dry batching and blending at room temperature. It is typically completed with high shear at elevated temperature and pressure. Closed volume batch mixers are commonly used and range from measuring mixers (Brabender, ThermoHaake) to industrial rotor and planetary mixers. Various rotor configurations are used, depending on the torque and shear required for the formulation (Figure 3, Table 2).



Figure 3: Mixing rotors, a) sigma, b) banbury, c) cam and d) Roller blade (courtesy Rheometer Services Inc.).

Table 2: Rotor style with shear rate achievable.

|          | <b>Rotor type</b> | <b>Shear range</b> |
|----------|-------------------|--------------------|
| <b>a</b> | Sigma             | Low                |
| <b>b</b> | Banbury           | Medium             |
| <b>c</b> | Cam               | Medium             |
| <b>d</b> | Roller            | High               |

Viscosity of the feedstock is an important property and has often been considered to determine kinetic behaviour for the whole of the MIM process [75, 77-82]. Thermal properties such as conductivity and heat capacity are considered more important in MIM than in plastic injection moulding due to faster heat transfer. Even so, as recently as 2009, research on the effect of powder and binder on rheological and thermal characteristics was not common [36]. An increase in viscosity would be expected when increasing the

amount of the most viscous component of the binder. Stearic acid has shown to reduce intermolecular forces between polymer chains reducing the energy required to form slip bands therefore reducing apparent viscosity [64].

At higher temperatures the lower molecular weight (MW) polymer and wax thermally expand more than the metal, increasing the relative polymer content and lowering the viscosity [3]. Concentrated feedstock mixtures are shear thinning, where a decrease in viscosity is proportional to increasing shear rate. When mixing with high shear particles also align effectively lowering viscosity as shear rate increases [3]. Although the thermoplastic molecules are mobile about  $T_m$  they must remain below their degradation temperatures which will be well below the melting point for most metals [83].

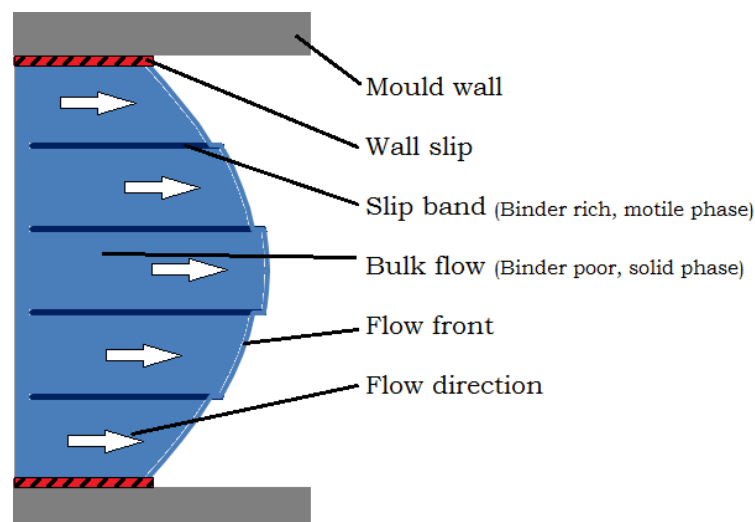


Figure 4: Flow front profile showing slip layers for MIM feedstock.

The relationship between particles, binder components, and mould walls (runners, gates and cavities) during moulding has received much attention. This is often explained as slip at the walls and slip bands within the bulk feedstock (Figure 4) where flow is dictated

by the solid (binder poor feedstock) and fluidic (motile binder) phases depending on the processing pressure, velocity and temperature [1, 51, 65, 84, 85]. Wall slip is due to cooling at the mould walls where the greatest temperature differential occurs. Slip bands are due to capillary forces and surface tension and represent the viscous forces acting within the feedstock [50]. The powder loading will alter the motility of the feedstock and may change with shear and geometry [86]. This would indicate that with successful formation of a part defects are still possible other than from porosity or non-uniform density distribution. Interaction between feedstock components has been modelled using mass conservation and differential flow to determine segregation during moulding and account for greenpart defects [84]. The binder is responsible for the liquid phase slip bands and metal powder the solid phase [65, 84].

Kwon and Ahn [85] used slip velocity and slip layers to represent the slip phenomena. In the slip velocity model, slip velocity was applied at the wall as a boundary condition. The slip layer model assumed the main flow region is occupied by feedstock as the bulk material and non-slip conditions are applied at the wall. Slip velocity and slip layer thickness as a function of shear stress at the mould wall was shown critical to the moulding process and must be controlled [85].

Chuankrerkkul et al. [64] considered shear thinning was due to reduced friction among binder components (release of polymer chain entanglement), and friction between powder and binder system (particle alignment with streamlines) at high shear rates. Shear thinning means viscosity drops with increasing shear rate, which is preferred for cavity filling with less energy required for complicated geometry, but may cause powder–binder separation where high shear rate gradients occur [36].

Viscosity data without slip correction depends on the diameter of the capillary die; the larger the diameter, the greater the viscosity. Data determined from capillary rheometry cannot cover low shear rate range required to precisely measure yield stress at the moulding temperatures [51]. Also the viscosity of a binder system is much lower than that of the feedstock and suggests that investigation of the binder only will have little or no bearing on the behaviour of feedstock.

Kwon and Ahn used a capillary rheometer to characterize slip with dies of (0.76, 1.27, 1.52) mm diameter and L/D ratios of (66.7, 60.0, 66.7) respectively [85]. To obtain temperature dependence data collection was performed at different temperatures ( $t = (80, 90, 100) ^\circ\text{C}$ ). The L/D ratios were considered large enough with no correction for pressure losses needed [85]. Melt flow is caused by the pressure differential from one end of the tube to the other with entry and exit effects considered negligible where the L/D ratio is high enough. Chabra and Richardson considered that for non-Newtonian flow behaviour capillaries of  $L/D \geq 120$  for purely viscous fluids and  $L/D \geq 200$  for two phase systems are required [87]. Although Kwon and Ahn did conclude that viscosity data obtained from a single capillary die of any diameter cannot predict even the simplest pipe flow without slip correction [51, 85]. Capillaries are considered to be restricted to measuring steady state functions of shear stress and shear rate behaviour for time independent fluids [87].

Rheology investigation is not so advanced for metallic blends with the most often referenced investigations of viscosity for solid particulate systems dedicated to ‘Einstein’s relative viscosity equation’ [88, 89];

$$\frac{\eta}{\eta_0} - 1 = C \cdot V_f \quad (1)$$

$\eta$  = viscosity of feedstock,  $\eta_0$  = viscosity of binder,  $V_f$  = particulate fraction and  $C$  = hydrodynamic flow coefficient of particulates ( $C \approx 2.5$  spheres).

Equation (1) deviates above  $V_f = 0.15$  so must be modified to suit MIM feedstock (50 to 70 %) [90]. Krieger-Dougherty type equations are used to produce master curves (Figure 5) for relative viscosity of feedstock as [72];

$$\frac{\eta}{\eta_0} = \left(1 - \frac{V_f}{V_{fm}}\right)^{-C \cdot V_{fm}} \quad (2)$$

$V_{fm}$  is the maximum particulate fraction.

A modified Cross model for feedstock viscosity depends on shear rate and temperature, and accounts for the yield stress [91];

$$\eta = \frac{\eta_0}{1 + C(\eta_0 \dot{\gamma})^{1-n}} + \frac{\tau_y}{\dot{\gamma}} \quad (3)$$

$\eta_0$  = zero shear rate viscosity,  $n$  = power law exponent and  $C$  describes the transition region from Newtonian to non-Newtonian behaviour.

$$\eta_0 = B \exp\left(\frac{T_b}{T}\right) \quad (4)$$

$B$  = amplitude coefficient,  $T$  = temperature and  $T_b$  reference temperature.

The dispersion curve (Figure 5) shows viscosity change as a function of powder loading dependent on particle shape. In response to Einsteins hydrodynamic flow coefficient for spherical particles ( $C = 2.5$ ) Douglas' and Garboczi calculated a value for irregular particles ( $C \approx 3.5$ ) [92]. Therefore the optimal powder fraction of 0.74 for spherical particles reduces to 0.66 for irregular particles.

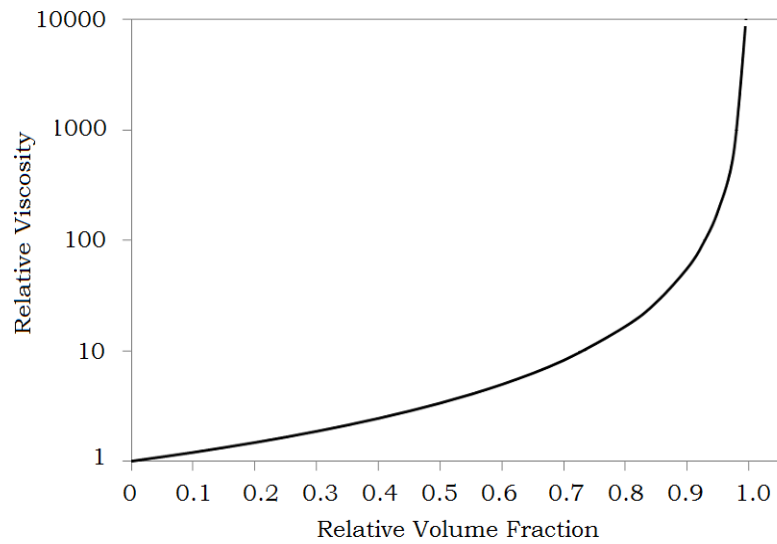


Figure 5: Dispersion viscosity master curve [72] for mono-dispersed spherical particles.

Evidence that viscosity is not linearly related to shear rate sees viscosity dropping as shear increases, from particle ordering (shear thinning), after which viscosity increases again (shear thickening), at the ideal powder loading values (Figure 6) [72].

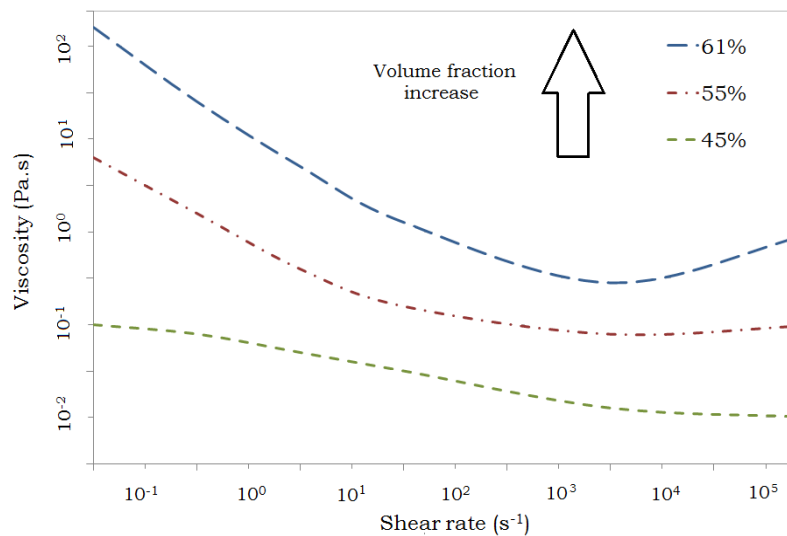


Figure 6: Shear rate effect on viscosity for increasing particulate fraction [86] (Image © Malvern Instruments, reproduced by permission).

## 2.2. The injection moulding process

The machines used for injection moulding of MIM feedstocks are essentially the same as those used in the plastics industry and deliver a homogeneous melt with uniform temperature and flow characteristics [51, 74, 93-98]. Correct sizing of the injection moulding machine is critical as accurate reproducible shot volume is essential for producing consistent parts. The process involves heating feedstock to its melt temperature and injecting a pre-set amount into a closed mould where the shape is formed and it is allowed to cool before removal.

Moulds may be designed with all the features possible for plastics (sliding bars, core pulls, unscrewing units, inserts) [52]. Surfaces

are polished for easy removal of the greenpart [94] and provide ideal conditions for moulding feedstock [37, 98, 99]. Flow paths need to be streamlined to eliminate material hang-up and degradation and high shear conditions avoided to maintain temperature control [95].

Defects that appear at any stage of MIM do not typically self repair, but manifest and exacerbate during subsequent processing [98, 100]. Unlike other manufacturing techniques a defective part will not be repairable. It is therefore beneficial to identify quality issues as early as possible [18, 100]. Post moulding defects are obvious when located on an external surface and may be caused by compaction and thermal shock during cooling, as well as impact or irregular shrinkage. Internal defects are harder to identify [101]. Cooling time is sensitive to a variety of energy related properties such as feedstock density, specific heat capacity, thermal heat conductivity, and ejection temperature. Other than that, part thickness, injection temperature and mould wall temperature are also significant parameters [74].

Basic rules important for manufacturing mould tools are;

- Gate location: it should be on the thickest section of the part, with unhindered flow into the rest of the cavity.
- Eject-ability: to assist greenpart release a parting line draft of  $(0.5 \text{ to } 2)^\circ$  is required.
- Material flow: sharp corners and edges to be avoided. Notch where  $90^\circ$  angles are needed. Uniform wall thickness or use a gradual transition.
- Flat Sides: provision of suitable surfaces for holding the part upright during sintering reduces distortion.

Greenpart quality improves as moulding reproducibility improves. The most essential parameters for this are the uniformity of the shot size, control of the screw position, constant injection pressures, and uniform temperature. Debinding and sintering also benefit from process control enabling uniform and consistent heating and cooling cycles.

The use of metal powders generally increase wear rate inside a moulding machine so hardened materials or surface hardening of the screw and barrel is needed for most feedstocks. For hard metals and ceramics, bimetal barrels and hardened screws are recommended [101].

The key function of a binder is to lubricate the particles so they are free to rotate and translate ( $t = (150 \text{ to } 200) \text{ } ^\circ\text{C}$ ) and enable the feedstock to be moulded into the required geometry. Due to flow and high moulding pressures, changes in the feedstock flow path could lead to a non-uniform density distribution. This is based on the particle morphology and particle to particle interactions. For conventional press forming, an HDH powder compact may be sufficiently consolidated, for handling, at pressures of 300 MPa through mechanical interlocking and limited deformation. For MIM the system pressures of the moulding machines are typically no more than 160 MPa [102]. Also pressure application for conventional powder press forming is bi-modal, while for MIM it is iso-static which effects compaction uniformity [103]. Flow however, is known to be affected by slip within the feedstock due to pressure acting on the powder and compression effects transferred to the binder, as well as cooling effects in the mould cavity [36, 51, 60, 65, 74, 85, 86].

Mould filling analysis has identified levels of significance for feedstock characteristics, processing parameters and part geometry [51, 74, 104]. Modelling of mould filling typically uses rheological models such as the modified Cross model, Carreau–Yasuda for

viscosity and physical models such as the Hele-Shaw approximation for heat transfer [105]. Tait and IKV models account for density variation in the feedstock and the cooling has been described using cycle average concepts [51, 91].

Overall it has been reported, that pressure and temperature related parameters were mostly sensitive to process conditions, geometry and feedstock properties, while flow related parameters were sensitive to process and geometry conditions [74]. Also, binder properties have been considered to play only a minor role in comparison to the feedstock properties [74]. For a given mould cavity configuration, packing and cooling time is most sensitive to the feedstock density, specific heat capacity, thermal conductivity and mould temperature, with maximum shear rate highly sensitive to filling time [97].

### **2.3. Debinding processes for binder removal**

The American Society for Testing and Materials (ASTM) defined thermal degradation as changes of physical, mechanical or electrical properties and thermal decomposition as a chemical change [106]. In this work the term degradation will refer to change in material properties that are reversible while decomposition will refer to those changes that are irreversible and substantially alter the chemistry of the starting material. Also where air is used during thermal analysis the results will not provide the pure thermal degradation or decomposition data that would be obtained under inert conditions [107].

The removal of organic binders and lubricants from titanium and titanium alloy powder compacts was referred to in the patent granted to Facaros and the General Electric Company in 1975 [108]. The initial removal method for the powder compacts involved thermal burnout that produced carbides, nitrides and hydrides. This affected the final metal composition which for reactive metals was detrimental. Their patented solvent extraction method became essential to the success of the MIM process one year later [55, 56].

It is known that single-component binders are difficult to extract without causing defects or loss of part shape. Multi-component binder system and hence multi-process debinding cycles are therefore used to enable progressive removal. It is also apparent that, while thermal debinding cycles are better designed based on TGA analysis, there has not been a lot of investigation on the solubility of binder systems and solution methods.

Removing the binder should be a gradual and controlled process to minimise the disruption to the particulate arrangement created during moulding [109]. Common removal techniques include solvent debinding, thermal debinding and catalytic debinding or a combination of these [1]. Although it is ideal to have zero residue after debinding, where it is present removal is often part of the sintering cycle [16, 19].

The solvent debinding process ultimately relies on solubility of the binder [108]. With many feedstocks produced from multiple components, consideration of miscibility and reactivity is also required [16, 18, 19, 39, 42, 110]. Selective removal of the individual binder components should also be possible where the correct solvent is identified. The amount of binder removed is a critical precursor to sintering, it is dictated by the binder system and may require specialised equipment (Figure 7) [111]. The debinding parameters are also dictated by the binder system and its interaction with the particles [75, 112, 113].

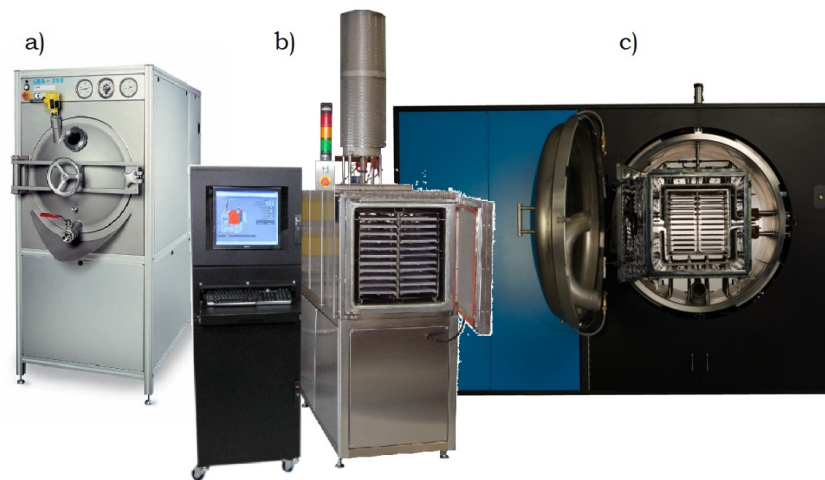


Figure 7: Debinding furnaces (a) solvent debinder, (b) catalytic debinder, (c) thermal debinder (courtesy Claus Joens, Elnik Systems).

The mechanisms that drive debinding are complex and just as the particles effect feedstock flow they also effect the debinding rate, large average particle size should enable a fast debinding rate [114]. Interconnected pore channels are created as a function of the inter-particle spaces and, so small average particle size may restrict the flow of diluent binder as the inter-particle distance is also small.

The mechanism of progressive binder removal enables the primary (lower MW) component to be removed first (by transport out of the interstices) to partially open pores [49]. The secondary (higher MW) binder components, stay in the moulded parts to 'lock' powder in position, retaining the shape of the compact. To aid the retention of compact shape, a capillary attractive force has to be exerted on the particle by the wetting of the particles with the residual binder. Subsequently, opening of the pore channels allows for removing the higher MW components and relieves the stresses associated with such movement [115]. At higher temperature the secondary binder evaporates and escapes through the open pores, without generating an internal vapour pressure. Pre-sintering shrinkage may occur as a result of binder removal, resulting in partial welding of the particle contact points. As a result, defects due to distortion and residual thermal stress are minimized [49].

The ability of a solvent to dissolve and remove binder from a greenpart is governed by permeability of the feedstock. The ability of the solvent to permeate the greenpart surface is dependent not only on the physical nature of the binder components but also on chemical interaction between the components. Figure 8 shows models of binder dissolution where the particle/binder interface will either increase or decrease the dissolution rate about the particles [114, 116]. Considering these models, removal dependency will be reliant on particle surface reactivity and interaction with the binder system [75, 112, 113].

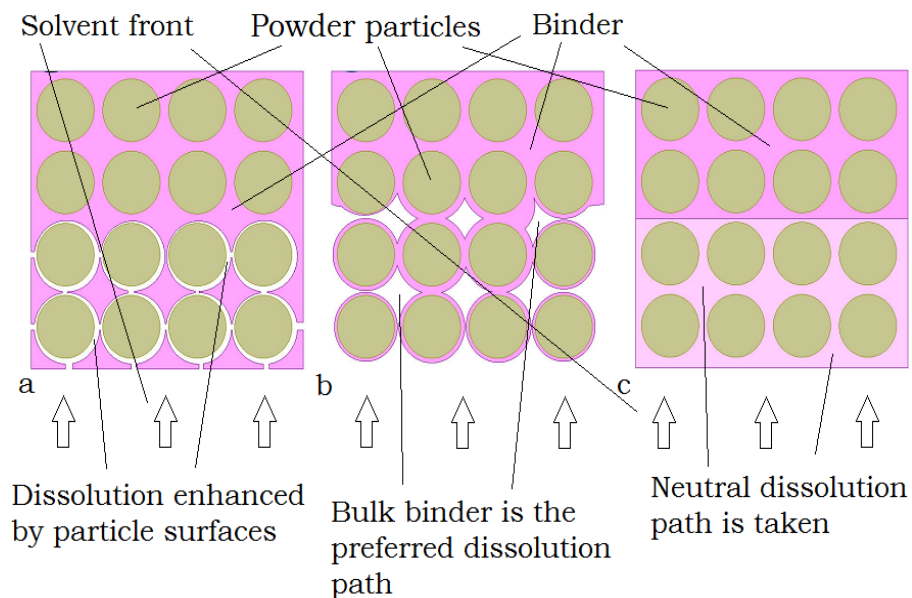


Figure 8: Theoretical solvent paths during solvent debinding.

### **2.3.1. Solubility and solution debinding methods**

Solution debinding is typically done with solvent vapour where the greenparts are in contact with the vapours or a liquid bath with full immersion of the parts in the solvent. The solvents are not restricted and may be any fluid able to dissolve the targeted binder component allowing removal from the part. Water may be used as a solvent where components are water soluble but, typical solvents may be pure organic liquids or solutions of organic liquids. Inflammable or toxic solvents require special handling to ensure operator safety and all equipment must be safe for the purpose.

The ability of a solvent to dissolve any given binder component from its solid form and leach it from the part will be governed by the permeability of the feedstock in the greenpart form [117, 118]. As the solvent permeates into the part it breaks chemical bonds that form the solid phase of the targeted binder component, and the diluted molecules disperse, via a micro-porous network [39, 112, 119, 120]. The ratio of solvent to solute (concentration gradient) starts high and as the solid phase disperses the concentration gradient decreases and the ability of the solvent to leach the binder will decrease [17, 121].

ASTM D5226 identifies standard methods and solvents for dissolving polymers [122] including those in Table 3.

Table 3: Suggested solvents for common polymers binders [122].

|  |
|--|
| <b>Ethylene/vinyl acetate (EVA)</b>  |
| Benzene, toluene, chloroform, methanol, carbon tetrachloride/ethanol, dichloroethylene/ethanol @ 20:80, chlorobenzene, ethanol/water, n-butanol/water, allyl alcohol, 2,4-dimethyl-3-pentanol, benzyl alcohol, tetrahydrofurfuryl alcohol, tetrahydrofuran, di-methyltetrahydrofuran, dioxane, glycol ethers, glycol ether esters, acetone, methyl ethyl ketone, acetic acid, lower aliphatic acids, vinyl acetate, acetals, acetonitrile, nitromethane, N,Ndimethylformamide, dimethyl sulfoxide, 1,2,4-trichlorobenzene @ 135°C. |
| <b>HDPE</b>  |
| Aliphatic, cycloaliphatic, and aromatic hydrocarbons, halogenated aliphatic, cycloaliphatic, and aromatic hydrocarbons, higher aliphatic esters and ketones, di-n-amyl ether. > 80 °C  |
| <b>LDPE/ LLDPE</b>   |
| As above > 50 °C   |
| <b>PP</b>  |
| Atactic hydrocarbons and chlorinated hydrocarbons at room temperature, isoamyl acetate, diethyl ether. Isotactic trichlorobenzene, xylenes, decahydronaphthalene > 135 °C.   |
| <b>Poly-vinyl alcohol (PVAL)</b>   |
| Glycols (hot), glycerol (hot), piperazine, methylenediamine, formamide, N,Ndimethylformamide, dimethyl sulfoxide (hot), water, hexamethyltrisphosphoramidate, tetrahydrofuran.   |
| <b>Poly-vinyl butural (PVB)</b>  |
| Acetalization 70 %-alcohols, cyclohexanone, ethyl acetate, ethyl glycol acetate. Acetalization 77 %-methylene chloride, alcohols, acetone, methyl ethyl ketone cyclohexanone, lower esters. Acetalization 83 %-methylene chloride, alcohols, ketones, lower esters.  |

Solubility kinetics for debinding green parts are strongly related to both permeability and formation of open pores (capillaries) [39, 120]. The formation of the open pores should occur from the outer surface through to the centre of the part. The following paragraphs show details of investigations for solvent debinding and the advantages of the various approaches.

Kryachek investigated a thermoplastic binder of polymer, paraffin wax (PW) and PVA, and compared it to a water-soluble binder ( $w_b =$

88 % PEG, 10 % PMMA 2 % SA) [5]. The thermoplastic binder was debound in 28 hours ( $\phi_p = 65\%$ ,  $t = 6$  mm) while the water soluble binder was debound in 3 h ( $\phi_p = 46\%$ ,  $t = 60$  °C). He concluded that water soluble binder was preferred, with no reaction of contaminants and a lower energy cost to remove.

Bakan et al. binder used combinations of varying MW PEG and found the debinding time reduced with reduced higher MW PEG. It was also found that contrary to expectation viscosity did not change [123, 124].

Chuankrerkkul et al. found that mixing duration effected the debinding [64]. Stainless steel parts made with a PEG feedstock ( $\phi_p = 52\%$ ) that were debound in water ( $t = 60$  °C,  $t = 6$  h). The feedstock mixed for 15 min lost less PEG ( $w_b = 91\%$ ) than those mixed for 60 min ( $w_b = 96\%$ ).

### **2.3.2. Thermal debinding methods**

Thermoplastic polymers and waxes have a similar response to increasing temperature. The initial softening as the intermolecular bonding forces are overcome is followed by transition to a liquid/melt phase ( $t = (40$  to  $100)$  °C waxes,  $(90$  to  $180)$  °C polymers). They then begin to thermally degrade ( $t = (100$  to  $300)$  °C) until the molecules form a gaseous phase [125]. The final response ( $t = (180$  to  $500)$  °C) is decomposition where the molecules breakdown to form gases (i.e. CO, CO<sub>2</sub>) or volatile units of their starting elements (i.e. C, H, N, O) and evaporate [126]. Where the units are not small enough to evaporate, they form carbon compounds (ash) and complex residues of non-volatile molecular units.

Thermal debinding generally involves a series of thermal steps over a given time to remove the binder components. Removal from the greenpart (or greypart) should not affect particle packing, part geometry or structural integrity. Thermal processes are typically energy intensive, slow and somewhat costly, with risk of part

distortion, however, it is still widely used. Froes reported that thermoplastic binders thermally depolymerise to their starting monomers but this is known to only occur for a select number of polymers (i.e. PMMA) [30]. Regardless of the method of debinding, any residual binder can introduce impurities into Ti MIM parts at temperatures as low as 260 °C [31, 127]. Therefore, as the polymer breaks down to its starting monomer or other molecule smaller than the initial component it must be removed before further decomposition occurs.

Thermal debinding can be done in any oven or furnace. To ensure purity of the debinding atmosphere it is common to use a sweep gas (air, inert or other) that uniformly passes over and around the parts before venting externally to special filters or recycling system.

For the majority of binders reported by Kryachek little effect on carbon content was seen due to residual binder [5]. The exception being stearic acid (SA), where carbon concentration increased as specimen thickness increased. Thermal debinding cycles are designed based on TGA results. However, high heating rates can produce cracks in parts, and the use of small samples cannot account for thermal constraints associated with whole parts or thick sections [19].

Thermal analysis using differential thermal analysis (DTA), differential scanning calorimetry (DSC) and thermal gravimetric analysis (TGA) is often used for MIM [15, 75, 128, 129]. The data is considered essential in determining decomposition parameters of binders by allowing optimised thermal profiles to be found. Thermal analysis in general is affected by changes in sample mass and heating rate [130-132]. Increasing heating rate increases sensitivity while decreasing heating rate increases resolution [133]. Rapid ramp rates ( $\beta > 10$  °C/min) may distort TGA results as completely thermal mechanisms overshadow slower atmospheric related mechanisms. However, low rates ( $\beta < 1$  °C/min) are not

practical so rates between ( $\beta = (2 \text{ to } 5) \text{ }^\circ\text{C}/\text{min}$ ) may be used [134]. The correct thermal technique also allow blends to be appropriately analysed [135].

A typical TGA plot shows the weight loss (Figure 9), for a preset thermal profile, with the curve showing distinct rate changes leading to the point where maximum decomposition takes place. The rate changes are depicted by the straight lines in Figure 9 as [135];

- 1 melt phase of binder and loss of highly volatile parts
- 2 decomposition of medium volatility parts
- 3 decomposition of low volatility parts
- 4 combustion with formation of elemental compounds (oxide, carbide ...)

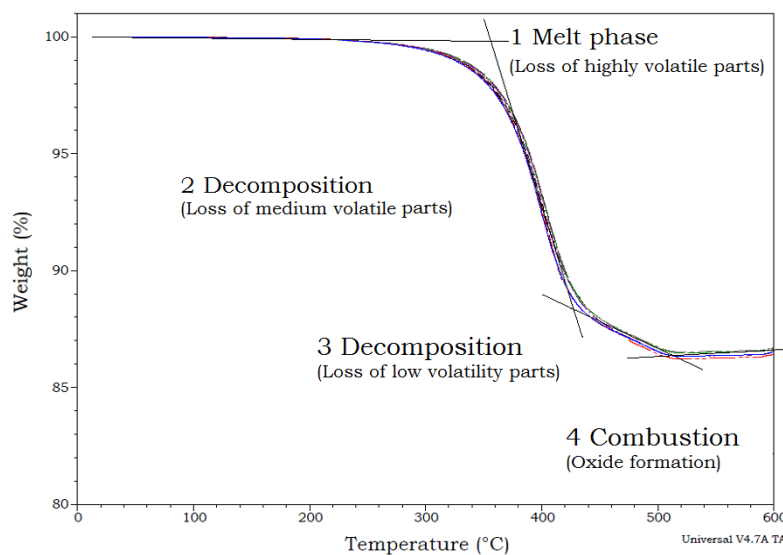


Figure 9: TGA plot showing binder weight loss in air.

Discrepancies within thermal analysis data could lead to false thermal profiles being proposed for MIM production [134].

Especially where, the heating rate is considerably different from that used in later processing, the mass of each component differs or the processing atmosphere changes. This was mitigated by Park et.al by creating master curves for decomposition from plots for three heating rates [75]. They included maximum rate of weight loss, apparent activation energies, calculated ratio parameters and specific rate constants for the binder. Grohowski and Straus used a series of isothermal plots to predict optimisation for thermal debinding and found that data from one feedstock cannot be directly applied even to a similar system [134].

Optimising the atmosphere during TD is also seen as binder dependant with vacuum, sweep gas and positive pressures often used [136-138]. High vacuum hampers thermal transfer so partial vacuum is more effective and can be done at lower temperatures although the choice of binder has been considered of greater importance for reducing residues than the atmosphere [139].

The TD profiles for stainless steel feedstocks of polymer and wax binder are dependent on the binder components and any initial debinding [134, 136, 137, 139]. Heating rates are typically (1 to 5) °C/min with isothermal regions set to coincide with activation temperatures for the binder components. The final temperatures are generally (475 to 600) °C to allow for complete decomposition and may include pre-sintering ( $t = 700$  to  $900$  °C). The debinding atmosphere also has a wide range to consider with differing pressure and composition seen. Typically a sweep gas is used (hydrogen, nitrogen, argon and mixtures of the same) and pressures range from positive pressure to full vacuum.

The approach for titanium is similar to ferrous metals however as a reactive metal the atmosphere has shown to be restricted although there is a wider range of binder components. The use of argon flow gas under positive pressure or partial vacuum are by far the most

widely used thermal debinding atmosphere presented in literature for titanium [12, 24, 26, 29, 39, 111, 127, 138, 140-148].

Based on molecular structure, some binder components will perform better than others. Growhowski and Strauss discussed the thermal debinding process in relation to the amount of residue resulting from binder components [126]. PE, PS and PP are often used because random chain scission readily forms volatile fractions, minimising residue [149]. Also PS, PMMA PBMA and POM were shown to leave minimal residue, from a combination of depolymerisation and random chain scission. Although it has been suggested that co-reactivity between binder components, and decomposition products, may lead to grafted copolymers that influence binder behaviour [149].

### **2.3.3. Combined solvent/ thermal debinding methods**

A dual solvent/ thermal debinding process is often used to better control the binder removal. As previously mentioned SD typically removes lower molecular weight binder components. Under ideal conditions solvent debinding creates a network of open pores throughout the moulded green part. The pore structure will aid removal of the larger binder molecules during TD thereby reducing disruption to the particle arrangement. For titanium, an inert or vacuum atmosphere needs to be used to minimise any possible reactions due to its reactivity [126, 127, 139]. Any elemental uptake acceptable during a thermal process is dependent on the starting composition of the powders used and the target composition of the finished part [127, 150].

Examples of dual debinding for Ti MIM includes the investigations previously mentioned and the following summary [151]. First stage, SD mainly use hydrocarbon solvents that extract wax (ethanol, heptane, hexane,  $t = 40$  to  $60$  °C,  $t = 4$  to  $24$  h). The duration was shown dependent on the part size which was typically small test

bars and thin sections. Second stage, TD uses similar heating rates and temperatures as stainless steels. The sweep gas composition used for titanium being limited to argon with or without partial vacuum. There is little distinction shown between TD for titanium or its alloys and the final temperatures used (300 to 600) °C coincide with the decomposition temperatures of thermoplastic binders. Pre-sintering may also be part of a TD cycle at temperatures (750 to 850) °C [62]. It is also reported that the TD may be completed as part of the sinter cycle [152].

#### **2.3.4. Single step catalytic debinding methods**

The catalytic approach is considered to be a very rapid debinding process compared to solvent or thermal processes. The parts are set in a closed vessel and catalytic vapours are pumped through the chamber and across the parts and are then exhausted from the vessel. Where the catalytic vapour contacts the parts a chemical reaction takes place (depolymerisation) and the binder rapidly breaks down to its monomers. The volatile molecules mix with the catalytic vapours and are then removed as the exhaust [101]. The theory is that the binder vaporises without having to undergo a liquid phase, thus reducing the debinding time significantly [1].

A reported disadvantage of catalytic systems is expense of the specialist equipment to handle the hazardous decomposition by-products i.e. formaldehyde, and means of eliminating the toxic exhaust gases. The hazards are overcome when handled correctly and by using appropriate equipment, i.e. Figure 7 b). The BASF Catamold® polyacetal binder system uses catalytic debinding and is reported as the most widely used system in commercial use. It uses a gaseous nitric or oxalic acid catalyst that depolymerises poly-acetal to gaseous constituents that leave the greenpart without producing any residue [101].

## **2.4. Consolidation through sintering**

Sintering of particulate compacts is a well established process. The density of parts prepared by injection moulding and sintering is generally considered to be higher than for parts prepared by traditional pressing and sintering, with strengths close to that of cast and rolled metal [5]. As the final consolidation phase, the brown compact is heated to a temperature typically (70 to 80) % of the melt temperature of the metal being formed. The high surface energy of fine MIM particulates ( $d < 40 \mu\text{m}$ ), compared to coarse, press and sinter powders ( $d > 75 \mu\text{m}$ ), enable the particles of the brown parts to coalesce, up to densities of 99 % theoretical values [101, 111].

Special furnaces are used for processing MIM parts, although it is often successful in conventional vacuum furnaces provided with adequate thermal control [111]. Volumetric shrinkage during sintering will be significant at (30 to 60) % and depends on binder composition, powder loading, thermal expansion coefficients, brownpart porosity, and uniformity of cooling [5]. Slower heating may control shrinkage and the furnace atmosphere will help prevent contamination. It is also known that mechanical properties of titanium metals are influenced by impurities (carbon, hydrogen) [39].

Two basic sinter furnace configurations are batch (Figure 10 (a)) and continuous (Figure 10 (b)) [111]. The batch furnace is a closed system with capacity limited to the physical dimension inside the furnace chamber that requires loading and unloading for each sintering profile. The continuous furnace operates a conveyer system; the parts, arranged on trays, pass through the furnace at the required rate to achieve the appropriate sinter conditions.



Figure 10: (a) MIM 3000 batch furnace (courtesy Claus Joens, Elnik Systems). (b) CM 300 continuous furnace (permission CM Furnaces Inc.).

Spark plasma sintering, induction sintering and microwave sintering are other processes currently under investigation. They have shown to be effective for the consolidation of Ti powder compacts [153-155]. Similar densities for (Ti, Ti-6Al-4V) powder compacts sintered by conventional means have been reported using reduced heating temperatures and reduced process times [156]. Although lower heating rates are often selected for MIM brownparts to reduce likelihood of cracks in parts [19].

The kinetics of particle coalescence is explained using the two-sphere sintering model in Figure 11 [157].

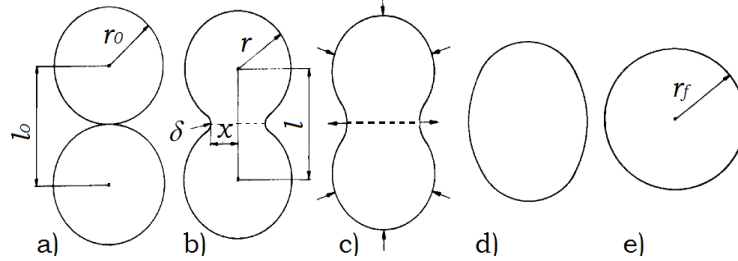


Figure 11: Particles coalesce during sintering at temperatures (50 to 80) % of melt temperatures. a) initially two particles ( $r_0$ ) have point contact, b) a neck ( $x$ ) forms at the point of contact, c) a grain boundary forms and the neck continues to grow, d) surface and bulk transport mechanisms form a single entity, e) one single sphere remains ( $r_f \approx 2.52r_0$ ).

Neck growth can be calculated from;

$$\left(\frac{x}{r}\right)^n = \frac{Bt}{(2r)^m} \tag{5}$$

$x$  = size of neck,  $r$  = particle radius,  $t$  = time,  $n$  &  $m$  from tables [143].

$$B = B_0 \exp\left(-\frac{Q}{kT}\right) \tag{6}$$

$Q$  = sintering activation energy,  $k$  = Boltzmanns' constant,  $T$  = absolute temperature, equations for  $B_0$  from tables [143].

Lineal shrinkage;

$$\frac{\Delta l}{l} = \left(\frac{x}{4r}\right)^2$$

(7)

$$l = 2r$$

Volume reduction;

$$\frac{dV_s}{dt} = \frac{\gamma_{sv}\Omega D_v}{kT8r^3}$$

(8)

$V_s$  = sintered volume,  $\gamma_{sv}$  = surface energy,  $\Omega$  = atomic volume,  $D_v$  = volume diffusivity

The model (Figure 12) simplifies the atomic transport taking place at high temperature, first at particle surfaces then, as they form, grain boundaries, followed by diffusion within the solid [158].

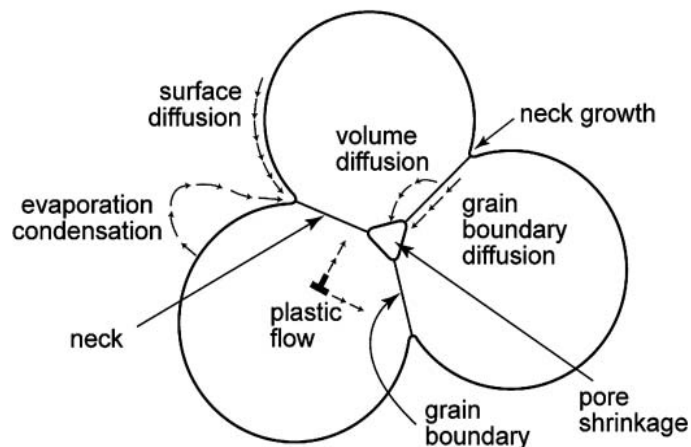


Figure 12: Three sphere model depicting atomic transport during sintering [158] (reuse by permission Taylor and Francis, Rightslink CCC.).

When applying the two-sphere model to multiple spheres, i.e. within a powder compact, neck growth and boundary formation enables channels to form at particle boundaries. The initial mechanism for coalescence is driven from the sinter atmosphere and the surface energies of the particles. As the necks form ( $\rho > 75\%$ ) transport of the atoms from within the particles becomes the main driving mechanism. Sintering slows; the channels close ( $\rho > 85\%$ ) and become pores (Figure 13).

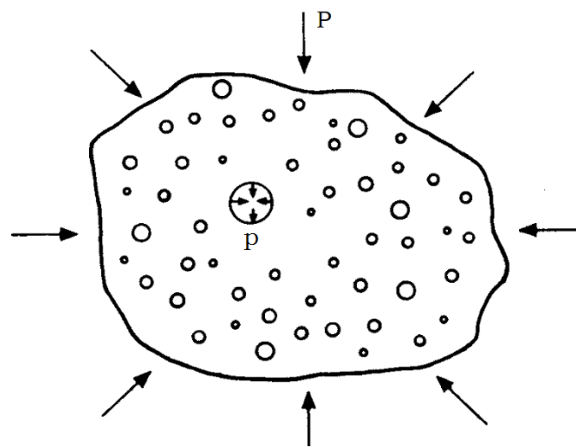


Figure 13: Internal pore size is determined by furnace pressure, surface energy, and diffusivity of gases within the pore.

In the final stage the pores shift (diffuse) to grain boundaries, and join other pores, reducing the overall energy of the system ( $\rho > 92\%$ ). Grain growth occurs as bulk transport slows and the driving mechanism returns to surface energies and grain boundary transport [158]. This is balanced by pressure within individual pores (Figure 13) that restrict the compact from attaining full density. When diffusion to grain boundaries and grain growth allow pore-boundary separation occurs and a pore left within a grain is less likely be removed by further processing [157].

Established PM press and sinter methods simplify the selection of thermal parameters for sintering MIM compacts. However, residual

binders from incomplete debinding ensure that the MIM sinter process has specific criteria outside of traditional sinter methods. During MIM sintering, it is usual to control the atmosphere to ensure the final part is free from decomposition products of the binder i.e. interstitial elements oxygen, carbon, hydrogen and nitrogen [12]. Control of the sinter atmosphere is enabled much the same as for TD, by the use of gases (nitrogen, hydrogen or argon), to purge the furnace of air and any remaining decomposition products [159]. Sub-ambient pressures are also used in conjunction with gases to sweep decomposition products from parts [126, 134, 139]. Alternatively vacuum is used to exclude air and enhance consolidation as well as help achieve low interstitial levels for titanium and magnesium [140, 146].

During sintering MIM parts can attain densities of (92 to 99) % of the theoretical values depending on the starting powders and sintering profile (temperature, hold time). To achieve greater density parts may be processed using a hot iso-static press (HIP). During a HIP cycle parts are heated to approach sintering temperature and the pressure is increased until internal porosity is removed with values reported up to 99.9 %.

## **2.5. Summary**

It has been shown from the literature presented here that there is a knowledge gap between metal injection moulding (MIM) as an established manufacturing process and its use for the fabrication of titanium (Ti). The moulding process for Ti MIM requires the same rheological considerations as conventional MIM with the tool design having distinct requirements not seen for polymer processing. Disruption to particle arrangement of the moulded greenpart is detrimental to the final product.

Thermoplastic binder components contain the very elements (C, O, N, H) that must be controlled to meet industry standards for Ti metals. Principles of controlling elemental levels identified for Ti but seldom applied to commercial endeavours include, elimination of binder residues and reduction of processing temperatures. In support of this, commonly investigated binders for Ti MIM (polyethylene glycol, polypropylene, paraffin wax, stearic acid) have shown to produce negligible residues. Greater control during Ti MIM debinding is required to ensure residues that introduce impurities are not present in the brownpart at temperatures above 260 °C. Although the sinter process is critical to successful parts fabrication, defects introduced during prior processing will remain in the part.

For many Ti MIM is considered too hard and although standard MIM processing equipment is suitable the number of variants identified is evidence that a dominant approach has yet to be identified.

## **Chapter Three: Injection moulding titanium based metal with a polymer binder system**

Metal injection moulding (MIM) is an established fabrication process. Metal powders are mixed with a thermoplastic binder to form a feedstock that can be moulded into complex shapes (green parts). Following moulding the binder is removed (debinding) and the powders are consolidated (sintered) to form the final part.

Problems associated with MIM techniques arise from inconsistent particle and density distribution as well as binder contamination. For titanium (Ti) MIM there are also reactivity issues associated with an affinity for oxygen, carbon and nitrogen which greatly affect mechanical properties.

Binder systems are grouped as polymeric, wax or water soluble based on the major constituent. PEG, CW and LLDPE have been identified as suitable MIM binder components and have also been used successfully to produce titanium parts [1, 137, 160-162].

Thermal stability is a measure of a material's response to heating over a range of temperatures without the influence of oxygen, while thermo-oxidative stability is a measure of a material's response to heating over a range of temperatures in an atmosphere containing oxygen. DTA and TGA provide information on softening, melting and decomposition, and are widely used to determine processing parameters for feedstock mixing, injection moulding, debinding and sintering. The ability to correlate this data to MIM debinding should enable greater control over final part quality. Subsequent processing, however, may change the chemistry of the components due to interactions with the debinding environment. Therefore, analysis of the individual components will only be relevant for the

mixing process. Further analysis will be needed to adequately investigate the binder at each processing step. Low heating rates should minimise disruption to the particle arrangement within the greenpart during debinding and help control the outflow of decomposition products [1, 99, 163].

This work was undertaken as a scoping exercise to gain an understanding of Ti MIM processing. The approach was to enable a broad empirical investigation of a subject that spans three distinct fields of study; polymers, solution chemistry and powder metallurgy. A more in-depth study was based on these findings and presented in later chapters.

Firstly binder components were identified from literature and determination of their thermal response in relation to MIM was achieved. Further to this, the relationships between the feedstock and part moulding were investigated. This was followed by an assessment of the solvent debinding (SD) and thermal debinding (TD) processes and their relationship. Finally the effects of moulding, debinding and sintering on defect formation and elemental composition of sintered Ti MIM parts was assessed.

### **3.1. Experimental**

#### **3.1.1. Materials**

The feedstock components:

- COTENE™ 3901 linear low density polyethylene copolymer (LLDPE) with a melt flow index (MFI) of 4.0 g/10min. The annealed density was 0.905 g/cm<sup>3</sup>, it had a softening point (Vicat) of 83 °C and was supplied by ICO Courtenay, NZ.
- Carbowax™ 8000 polyethylene glycol (PEG8) with a melting/freezing point of  $t = (55 \text{ to } 62) \text{ } ^\circ\text{C}$ . The density was 1.11

g/cm<sup>3</sup>, the water solubility was 700 g/L @ 20 °C and it was supplied by Union Chemicals Limited, Auckland, NZ.

- Copernica cerifera carnauba wax (CW) with a melting/freezing point of  $t = (81 \text{ to } 86) \text{ } ^\circ\text{C}$  and a density of 0.97 g/cm<sup>3</sup> was supplied by Go Native New Zealand.
- Titanium 6Al - 4V alloy (Ti64) powder produced by the hydride de-hydride (HDH) process [26]. The particles had irregular shape and passed through a 100 mesh sieve ( $d < 149 \text{ } \mu\text{m}$ ,  $w_E = (\text{C } 0.02, \text{H } 0.039, \text{N } 0.18, \text{O } 0.5)\%$ ). It was supplied by Xi'an Lilin International Trade Co., China.

HDH powders are formed by hydrogen embrittlement at elevated temperature that transforms titanium to titanium hydride (TiH<sub>2</sub>) to reduce ductility and sensitivity to oxygen. The TiH<sub>2</sub> is crushed to produce the fine TiH<sub>2</sub> powders that then undergo a de-hydrating process whereby the hydrogen is liberated and the powders return to the required elemental composition.

Where these chemicals are also used in subsequent chapters they will be referred back to this section for the specific details.

### 3.1.2. Equipment

Feedstock mixing was done with a batch mixer designed by the author and built at the University of Waikato (BM1). It had a Kistler torque sensor ( $\tau = (0 \text{ to } 100) \text{ N}\cdot\text{m}$ ) and a temperature controlled mixing chamber ( $t = (25 \text{ to } 250) \text{ }^\circ\text{C}$ ,  $V = 154 \text{ cm}^3$ , Figure 14). The counter rotating roller rotors ( $V = 45 \text{ cm}^3$ ) had 2:3 speed differential ( $\omega = (0 \text{ to } 80) \text{ r/min}$ ).

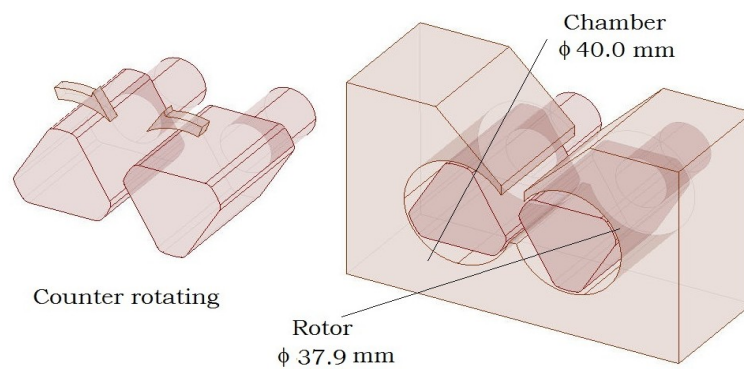


Figure 14: The batch mixer used to compound feedstock.

A ThermoPrism co-rotating twin screw extruder (TSE16) was also used for mixing and pellet formation. It had co-rotating twin screws (Figure 15) and temperature control over four heating zones ( $D = 16 \text{ mm}$ ,  $L/D = 24$ ,  $\omega = (0 \text{ to } 250) \text{ r/min}$ ,  $t = (25 \text{ to } 300) \text{ }^\circ\text{C}$ ).

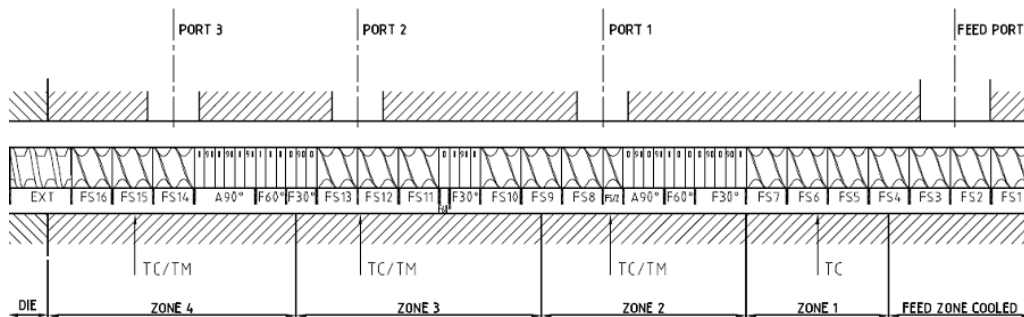


Figure 15: Screw configuration of the TSE16 extruder.

Moulding of samples was done using an injection moulder (Dr Boy 50T2) with a 38 mm reciprocating screw ( $L/D = 15$ ,  $\omega = (0 \text{ to } 300)$  r/min), a maximum clamping load of  $F = 500$  kN and maximum injection pressure  $p = 1300$  bar. Heating control ( $t = (25 \text{ to } 300)$  °C) was over three heating zones.

The mould tool was designed by the author and built (ADF Engineering, NZ) to produce the acetabular cup ( $V = 40.4$  cm<sup>3</sup>, Figure 16). The tool had cooling channels, automatic ejection and removable sprue.

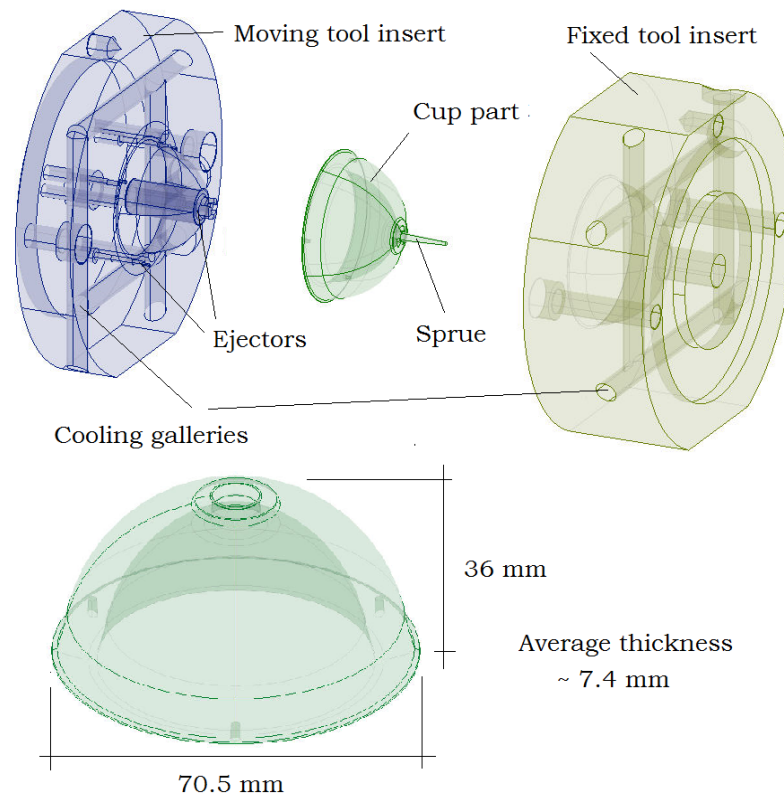


Figure 16: The mould tool comprised fixed and moving inserts and the moulded acetabular cup with hidden detail.

Debinding was done using both solvent debinding (SD) and thermal debinding (TD) techniques. For SD an apparatus was designed and built by the author (SD1). Solvent was pumped from a heated reservoir ( $V = 4$  L,  $\dot{V} < 5.0$  L/min,  $t = (25 \text{ to } 80)$  °C) to a

dissolution tank ( $V = 0.5$  L), holding the greenparts, and returned to the reservoir (Figure 17). The TD kit was designed and built by the author (TD1). It had a heated (PID controlled,  $t = (25$  to  $600)$  °C) steel kettle ( $V = 15$  L) with an inlet for sweep gas ( $\dot{V} < 20$  L/min) and an outlet for removing volatile waste gases (Figure 18).

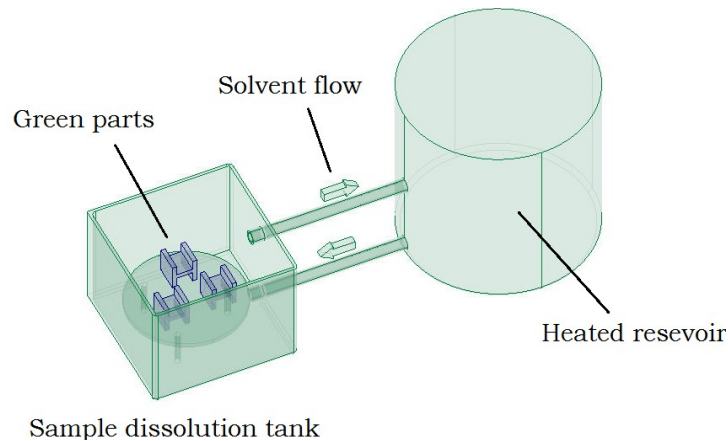


Figure 17: The basic solvent debinder cycled heated solvent from the reservoir to the green parts to remove the soluble component.

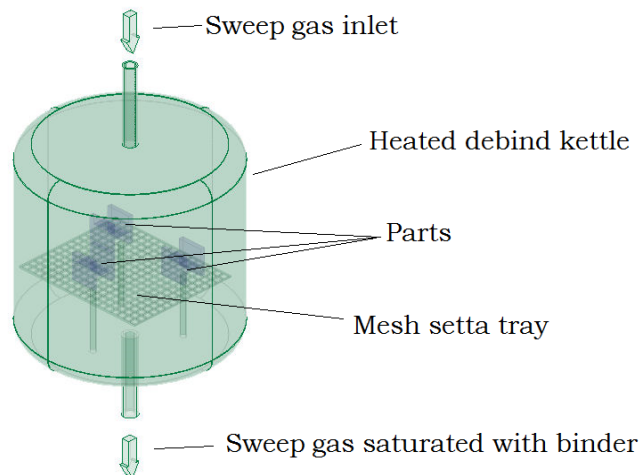


Figure 18: The thermal debinding kettle with programmable heating allows binder to be removed with the aid of a sweep gas.

Sintering was done using a cylindrical hot zone ( $t = (25$  to  $1500)$  °C) molybdenum furnace ( $V = 1.5$  L) with argon atmosphere control

(American Iso Press CPSI SL-1). A vacuum sinter furnace was also used (Mellen Graphite BG25). It consisted of a graphite furnace box ( $V = 8$  L) with argon purge system and computer controlled heating ( $t = (25 \text{ to } 1800) \text{ }^\circ\text{C}$ ,  $p > 1 \times 10^{-4}$  MPa).

Differential thermal analysis (DTA) and thermal gravimetric analysis (TGA) were completed using the simultaneous scanning differential thermometer (TA instruments SDT2960). The instrument capable of programmed heating cycles and atmosphere control using gas purge ( $\beta = (0.1 \text{ to } 200) \text{ }^\circ\text{C}/\text{min}$ ,  $t = (25 \text{ to } 1300) \text{ }^\circ\text{C}$ ). DTA was used to analyse phase changes through measuring the temperature difference between a sample and an inert reference material. TGA determined change in mass of a substance as a function of temperature during the same heating cycle.

Elemental levels (O, N, H) of the metal were measured using inert gas fusion-infrared absorbance (LECO TCH600). A sample combusted in flowing argon gas produces a gas stream that is compared against known reference values to quantify the level in the sample. Carbon and other elements (Ti, V, Al, Si) were also identified. This was done using the X-ray diffraction spectrometry (EDS) capability of the Hitachi (S-4700) field emission scanning electron microscope (SEM).

Structural analysis was done using the Hitachi (S-4700) field emission scanning electron microscope (SEM) with good image resolution (1.5 nm @ 15 kV) and magnification ( $M = (30 \text{ to } 500,000)$ ). Optical light microscopy ( $M = (6 \text{ to } 400)$ ) was used for digital images (Olympus BX60 and Wild M3B).

Density measurements were made using a pycnometer (Quantachrome Ultra-pycnometer 1000) with nitrogen gas. The instrument used Archimedes' principle of gas displacement and Boyles' law of gas expansion to determine density values. Pressure

changes before and after sample placement determines the volume which in conjunction with the sample mass give the density.

Where the equipments detailed above are also used in subsequent chapters, specific details where relevant will also apply.

### 3.1.3. Methodology

The binder components LLDPE, PEG8 and CW were individually analysed by SDT to determine their comparative thermal response.

The binder formulated of LLDPE, PEG8 and CW was mixed and analysed using SDT. Equal volumes of each component were used based on theoretical densities. The analysis was to determine how thermal response was affected by component interactions. Sample DTA and TGA curves are shown in Figure 19 with location of specified data points marked.

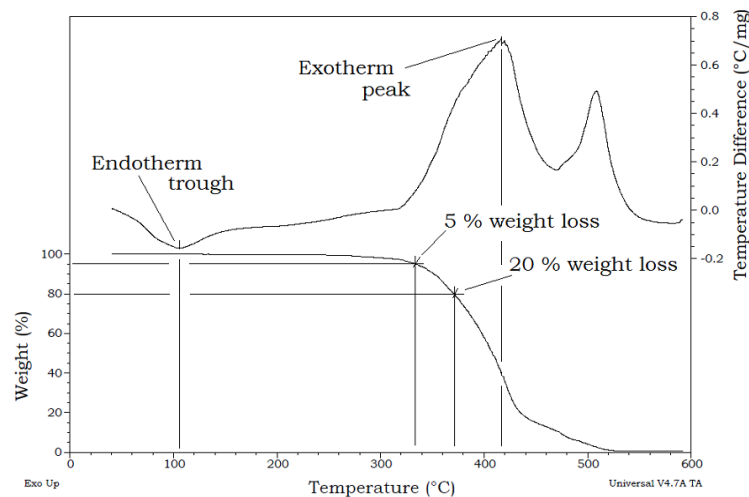


Figure 19: Sample SDT curves showing tabled selection points.

To determine how thermal response of the binder was affected by interactions with the powder the components were batch mixed and analysed using SDT. The binder components were first mixed together before blending in the powder to produce the feedstock ( $\varphi_B$

= 0.5). This was followed by incrementally adding powder to the feedstock to produce ( $\varphi_B = 0.6$ ) and then ( $\varphi_B = 0.7$ ) compounds.

Mixing to achieve a uniform distribution of the feedstock components was done using the batch mixer (BM1, Figure 14). Data from the torque sensor was used to determine a) time to reach maximum torque relative to the steady state torque, b) time from peak torque to steady state, c) the change in torque during time b), and d) torque approaching steady state (Figure 20).

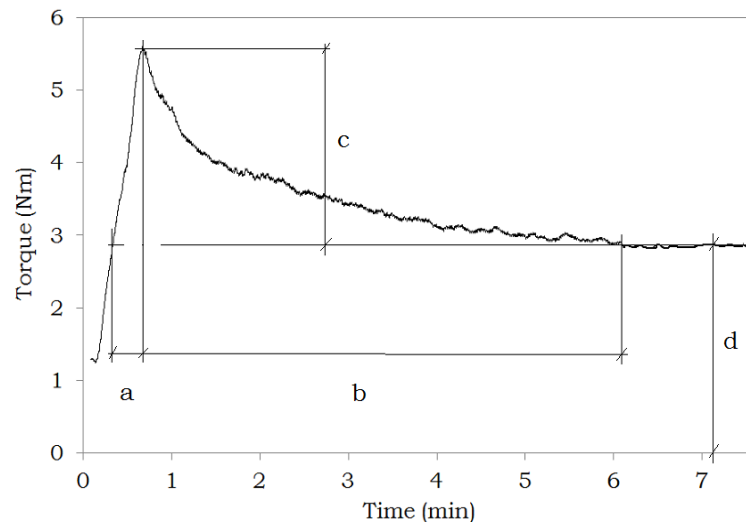


Figure 20: Sample mixing torque curves showing tabled data points.

The batch mixed feedstock was crushed and extruded through a 6 mm strand die to produce granules of uniform section. The feedstock granules were then injection moulded ( $t = (130 - 150) ^\circ\text{C}$ ,  $p_i = 700$  bar) to produce the acetabular greenparts (Figure 16).

Debinding trials were done using either the SD process or the TD process, or both. The volume ratio of the binder formulation (1:1:1) equated to mass fractions of (37.0, 32.5, 30.5) % for PEG8, CW and LLDPE respectively. Therefore, 37 % should be the maximum mass of binder removal possible with SD and 63 % the maximum binder

removal possible through TD. After SD and TD the parts are referred to as greyparts and brown parts respectively.

Solvent debinding involved placing the greenparts in the dissolution tank (SD1) where they were submerged in water ( $t = 60$  °C). The water circulated over the parts creating a washing effect to remove the diluted PEG as it migrated to the part surface. Parts were removed from the tank at (5, 10, 24) h, dried and weighed to determine mass loss.

Thermal debinding involved a four segment temperature profile based on the SDT results (Figure 21). Segment one was controlled heating ( $\beta = 3$  °C/min) to the decomposition onset temperature. Segment two used controlled heating ( $\beta = 1$  °C/min) to the temperature at which 20 % decomposition occurred. Segment three was an isothermal hold period ( $t = (0.5, 6.0, 10.0)$  h), followed by segment four cooling to room temperature. Air flow of ( $\dot{V} = 0.5$  L/min) was maintained to aid removal of the decomposition products. After TD the brownparts were weighed and the mass loss relative to total binder was calculated.

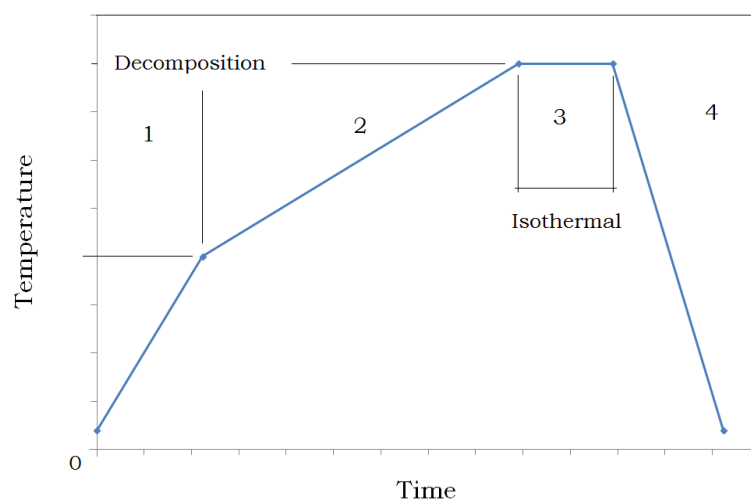


Figure 21: Thermal debinding temperature profile.

Only brownparts with five percent or less residue were taken to the sinter process to avoid damage to the furnace. Residue removal and sintering were done under inert atmosphere to eliminate oxidation of the powder. The brownparts were sintered using two furnace conditions to establish an understanding of the relationship between residue removal and particle consolidation at sinter temperatures. The first furnace profile was controlled heating ( $\beta = 5 \text{ }^\circ\text{C}/\text{min}$  to  $t = 600 \text{ }^\circ\text{C}$ ) with an isothermal period ( $t = 60 \text{ min}$ ), followed by controlled heating ( $\beta = 10 \text{ }^\circ\text{C}/\text{min}$  to  $t = 1250 \text{ }^\circ\text{C}$ ) with an isothermal period ( $t = 60 \text{ min}$ ) to sinter in a static argon atmosphere (AIP furnace). The second furnace profile was controlled heating ( $\beta = 4.5 \text{ }^\circ\text{C}/\text{min}$  to  $t = 800 \text{ }^\circ\text{C}$ ) followed by ( $\beta = 6 \text{ }^\circ\text{C}/\text{min}$  to  $t = 1250 \text{ }^\circ\text{C}$ ) and an isothermal period ( $t = 180 \text{ min}$ ) in a vacuum atmosphere to sinter ( $p = 3.0 \times 10^{-4} \text{ mbar}$ , Mellen furnace).

The sintered cups were inspected on the surfaces and sectioned parts analysed using SEM and optical microscopy. An etching reagent was used to expose the microstructure of cut and polished samples. The samples were submersed ( $t = 1 \text{ min}$ ) in Krolls reagent (100 mL distilled water, 2 mL HF, 4 mL HNO<sub>3</sub>) before rinsing in distilled water followed by rinsing in alcohol and drying. Samples treated with Krolls' reagent to reveal the micro-structure were taken from across the cup section as depicted in Figure 22.

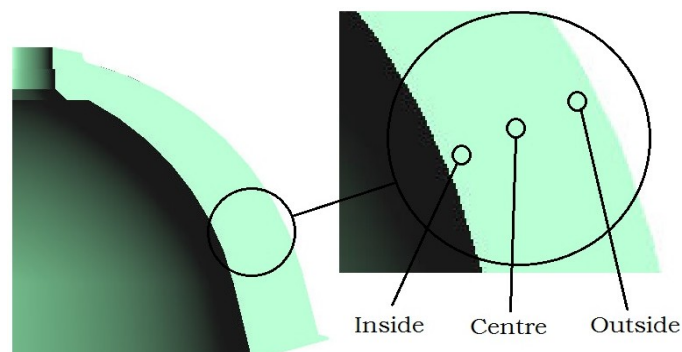


Figure 22: Cup cross section showing image sample location.

Oxygen, hydrogen and nitrogen levels were determined using the inert gas fusion-infrared absorbance method (LECO TCH600).

### **3.2. Results and discussion**

Overall the function of this binder was threefold; to improve flow properties of the powder (CW), enhance binder/powder wettability and promote particle dispersion (PEG8), and provide strength to the moulded green compact (LLDPE). The literature refers to the strength component as the 'backbone' and the final component to be removed prior to sintering, however, the ratio of binder components with relation to their function is not well documented in the literature. In this work an equal functional importance was given to each of the binder components by formulating the binder based on the volumetric ratio of 1:1:1 (LLDPE, PEG8, CW).

### 3.2.1. Thermal assessment and mixing

#### 3.2.1.1. The binder

Changing the heating rate and atmosphere of analysis caused changes in the measured TGA and DTA response for the binder components (Figure 23, Table 4). The changes were seen as shifts in the temperature of the endothermic and exothermic peaks, and the onset of weight loss as well as changes to the intensity. Heating rates and atmospheric conditions of analysis can of course be set to values to be replicated during processing. However, combining components, varying composition, overall mass and reactivity also influence the results. Therefore selection of processing parameters based on individual binder components is not accurate and there needs to be analysis of both mixed binder components and the feedstock to determine component interactions. Thermo-oxidative analysis (Table 4) showed where all components reached or passed their melt point ( $t = 115\text{ }^{\circ}\text{C}$ ) therefore mixing above this temperature should ensure the components were in the melt state.

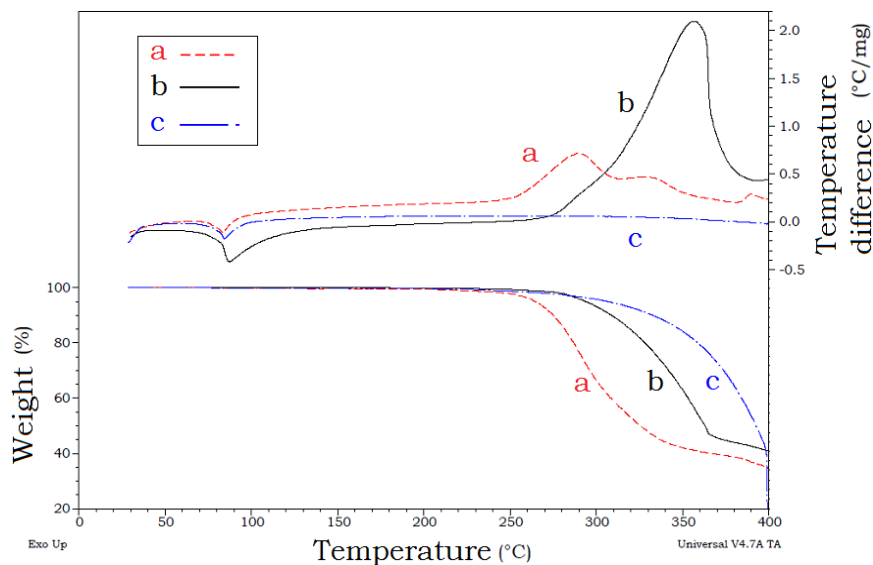


Figure 23: CW under different thermal conditions a)  $\beta = 5\text{ }^{\circ}\text{C}/\text{min}$  in air, b)  $\beta = 20\text{ }^{\circ}\text{C}/\text{min}$  in air and c)  $\beta = 5\text{ }^{\circ}\text{C}/\text{min}$  in argon.

Table 4: Thermal values from SDT for the binder and individual components ( $\beta = 20 \text{ }^\circ\text{C}/\text{min}$ , air).

|        | Endotherm ( $^\circ\text{C}$ ) | Exotherm ( $^\circ\text{C}$ ) |     | Weight loss ( $^\circ\text{C}$ ) |      |
|--------|--------------------------------|-------------------------------|-----|----------------------------------|------|
|        |                                | 1                             | 2   | 5 %                              | 20 % |
| PEG8   | 70                             | 260                           | 325 | 220                              | 262  |
| CW     | 85                             | 295                           | 355 | 265                              | 330  |
| LLDPE  | 115                            | 295                           | 420 | 295                              | 385  |
| Binder | 105                            | 300                           | 420 | 335                              | 370  |

Segregation occurred between the polymer and wax after the extrusion and cooling (Figure 24 a). The segregation was due to the difference in melt temperature of the components (Table 4), the short mixing time and the low miscibility of the components. It was possible to produce a homogeneous mix by continued mixing during the cool down period after the initial mixing temperature ( $t = 145 \text{ }^\circ\text{C}$ ) was reached (Figure 24 b).

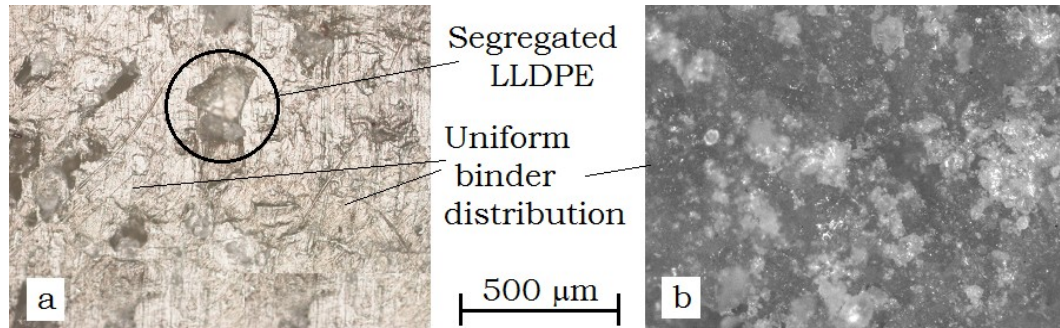


Figure 24: Optical image of a) extruded binder showing segregated components on cooling and b) binder mixed during cool down.

It is considered that a DTA peak is at its maximum intensity at the same temperature at which the TGA reaction rate is at maximum. Changing the heating rate, however, alters the thermal response in relation to the activation energy of the binder components. This is seen for phase transformations (melting and volatilisation) and chemical reactions (evaporation, crystallization, decomposition)

during processing and analysis. This is explained by considering the heat energy input determined by the heating rate and the heating duration. As shown in Figure 25 the heat energy input, signified by the areas under the temperature time graph, ( $\beta = 5$  °C/min) is equal ( $\beta = 20$  °C/min) but is reached in half the time.

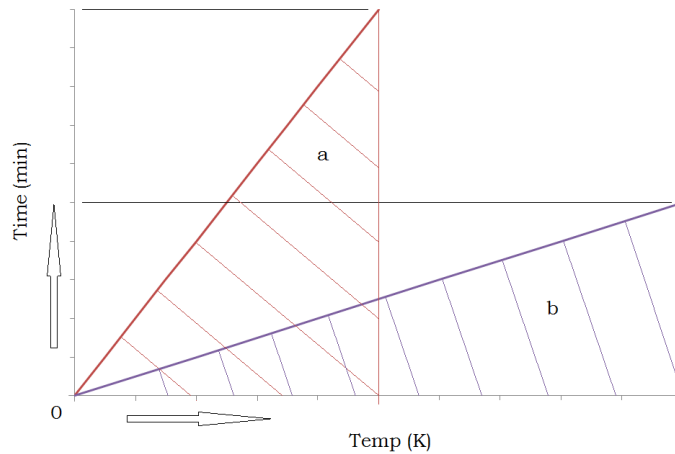


Figure 25: Heat energy input for given heating rates. a)  $\beta = 5$  C/min and b)  $\beta = 20$  C/min.

The activation energy for a given thermal reaction is generally not constant and the temperature at which the value is reached shifts relative to the heating rate [107]. This is shown with the rate constant ( $k$ ) for thermal reactions expressed as a function of temperature with the Arrhenius equation:

$$k = Ae^{(-E/RT)} \quad (9)$$

$A$  is the pre-exponential factor ( $\text{sec}^{-1}$ ),  $E$  activation energy (J/mole),  $R$  the gas constant (8.314 J/mole K) and  $T$  is thermodynamic temperature (K).

Kinetic reaction studies to determine thermodynamic states produced the equation for constant heating rate TGA [131]:

$$\frac{d\alpha}{dt} = k(1 - \alpha)^n \quad (10)$$

$d\alpha/dt$  is the rate of mass loss,  $\alpha$  is the fraction of material reacted,  $n$  is the reaction order.

Flynn and Wall revised this and proposed a constant heating method widely cited when describing decomposition and first order kinetics [131, 164-166]. For a constant heating rate and assuming a first order reaction ( $n = 1$ ), the rate expression becomes:

$$-E = \left(\frac{-R}{b}\right) \frac{d \ln \beta}{d(1/t)} \quad (11)$$

With  $b$  a constant ( $n=1$ ),  $\beta$  is the heating rate ( $^{\circ}\text{C}/\text{min}$ ) and  $t$  the temperature of weight loss ( $^{\circ}\text{C}$ )

This also shows that increasing the heating rate ( $\beta$ ) will reduce the activation temperature ( $t$ ) for the given activation energy ( $E$ ). It can also be considered that segregation of the binder components following extrusion can be explained by considering the activation energies of the individual components to be occurring at different points. Regardless of the association of the decomposition equations only interaction of the binder components will determine the behaviour of the binder once it is mixed.

It is considered that thermoplastic polymers thermally decompose by reactions causing molecular rearrangement and scission [107]. Molecular rearrangement sees a loss of a small number of the intermolecular forces holding the chains together [167]. This will not rapidly affect the polymer as the main mechanism determining mechanical properties is entanglement of the chains. These chain breaks can be physically or thermally induced or the result of impurities within the polymer and produce loss of mechanical properties but negligible changes in mass (Figure 26, stage 1).

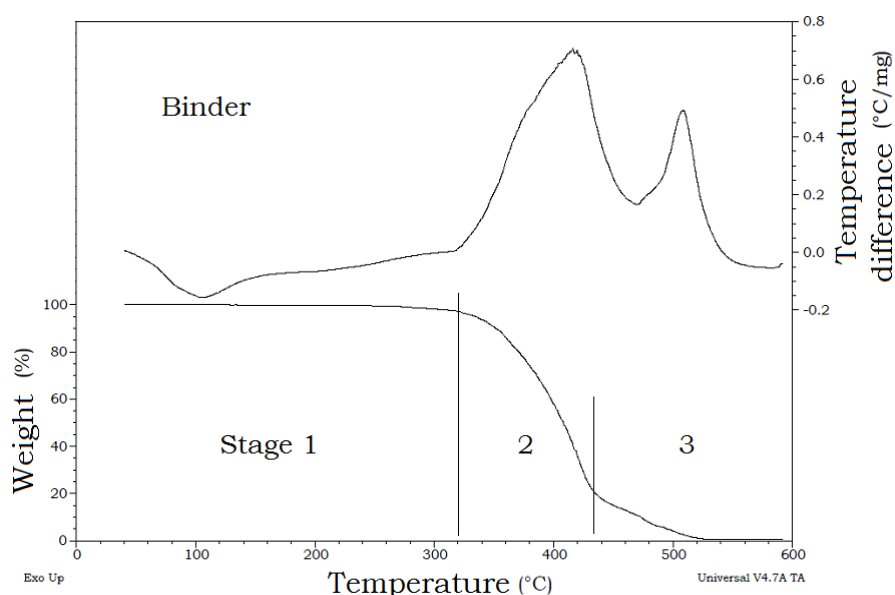


Figure 26: TGA and DTA curves for the binder ( $\beta = 20 \text{ }^\circ\text{C}/\text{min}$ ).

Scission has been shown to occur by two mechanisms chain scission and random scission [107]. Chain scission sees the repeat unit maintained but the chain length reduces forming radicals that depolymerise to produce monomers. This rapid depropagation is often referred to as unzipping (Figure 26, stage 2). Random scission does not maintain the repeat unit but tends to fracture the polymer chains producing radicals that are low molecular weight fragments or oligomers. A third decomposition mechanism is that of

thermal reaction where new species are formed along the polymer chains. These reactions typically transform polymer to soot or other stable carbonaceous forms (Figure 26, stage 3). The rate of decomposition however is determined by the repeat unit, which is the arrangement of the organic chains (C, H, N, O), that make up the polymer.

TGA of the binder (Figure 26) showed three main stages of weight loss. Stage one was within temperatures used for polymer processing and generally enables low energy molecular rearrangement. Mass loss was slow and due to release of water vapour and residual solvents of polymerisation. During stage one the binder softens, melts and forms a viscous liquid phase [168].

Stage two had the highest rate of mass loss and is considered to be the range at which depolymerisation occurs. Mass loss is attributed to chain scission that increases with the rapid formation of volatile components or free radicals which may be complex species of the starting monomer [107]. Volatile components form as the input energy increases together with a phase change as the liquid begins to vapourise [1]. These volatilised components readily leave the residue from the surface and are carried out of the furnace area in the purge stream.

In the third stage, the remaining and often higher MW molecules decompose to form carbon dioxide and carbon monoxide gases that readily disperse with the purge stream from the SDT. Where residual binder remains as soot or carbonaceous ash it is detrimental to MIM as it becomes trapped in the brownpart and will contaminate the Ti during sintering [18].

One aspect that supports the selection of binder components is the form any residual binder takes during thermal processing and the level that remains as impurities [126]. The TGA curve (Figure 26) showed zero mass after the analysis an indicator of zero or negligible residue ( $t = 520\text{ }^{\circ}\text{C}$ ), this was also confirmed by a clean sample crucible.

### 3.2.1.2. The feedstock

Binder and Ti-6Al-4V powder was mixed using the twin screw extruder ( $t = 145\text{ }^{\circ}\text{C}$ ) to form a uniform strand. Varying powder loadings ( $\varphi_B = (0.5, 0.6, 0.7)$ ) were achieved and the strands were sampled for visual and thermal analysis. A homogeneous structure was observed with both the naked eye and optical microscopy at low magnification. Higher magnification ( $m \approx 100$ , Figure 27) showed heterogeneity with distinct phases of Ti-6Al-4V and binder, as would be expected.

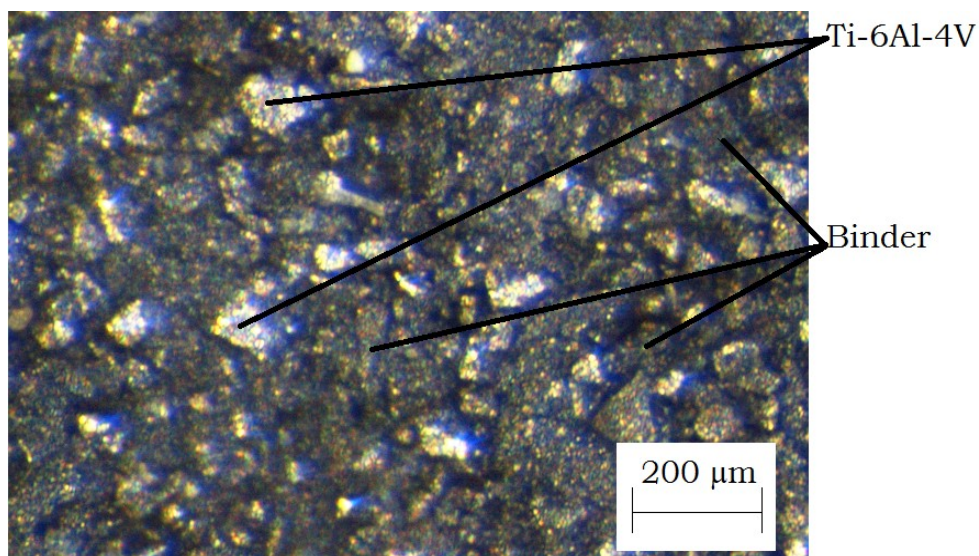


Figure 27: Heterogeneity of Ti-6Al-4V feedstock on the micro-scale.

Literature indicated that mixing duration has a significant effect on the uniformity of feedstock and influences segregation within greenparts [19, 39, 42]. Compounding times of 5 min to 8 h are reported, however high shear rates and long mixing time may cause thermal or shear induced degradation [19, 42, 110, 169].

Mixing with the BM1 recorded torque evolution curves (Figure 28). The feedstock was mixed in three steps, with the powder loading increased at each step. The binder components were loaded and compounded ( $t = 145\text{ }^{\circ}\text{C}$ ). Torque increased as the Ti64 powder was loaded and friction remained high until the shear action distributed the powder throughout the binder ( $\phi_B = 0.5, 0.6, 0.7$ ).

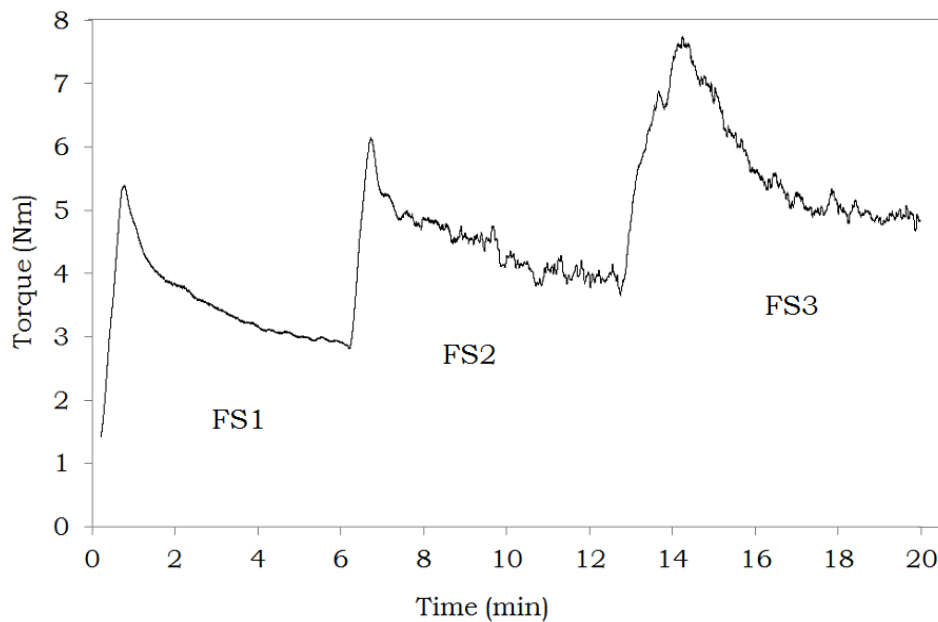


Figure 28: Torque evolution curves for Ti-6Al-4V feedstock with varying powder loading.

The results indicated that mixing time was crucial to producing a homogenous feedstock. A minimum of (4 to 5) min (Table 5) was needed to reach steady state indicated by a levelling of the torque curve (Figure 28) and therefore a shorter residence time than this is unlikely to be sufficient [170]. Extrusion of the binder and Ti-6Al-4V powder did not show segregation of the binder (Figure 27). Efficacy of the twinscrew extrusion mixer and the total residence time ( $t \approx 5$  min) ensured uniformity of the feedstock was achieved.

Table 5: Comparative values of mixing torque and time for compounding the binder and powder to produce a feedstock.

|     | Powder fraction | a   | b   | c   | d   | max. |
|-----|-----------------|-----|-----|-----|-----|------|
|     |                 | min |     | Nm  |     |      |
| FS1 | 0.5             | 0.4 | 5.0 | 2.6 | 2.9 | 5.5  |
| FS2 | 0.6             | 0.4 | 4.2 | 2.3 | 4.0 | 6.3  |
| FS3 | 0.7             | 1.2 | 3.3 | 2.8 | 5.0 | 7.8  |

TGA of the feedstock was used to determine the powder loading fraction by decomposition of the binder in air. After the binder was totally decomposed ( $t \approx 500 \text{ }^\circ\text{C}$ ) a slight increase in mass may indicate oxide forming on the Ti64 powder (Figure 29). The minimum weight after the final exotherm gave values (FS1, FS2, FS3) of  $\omega_B = (82.4, 87.8, 92.2) \%$  respectively, which were  $\sim 1 \%$  greater than the formulated values.

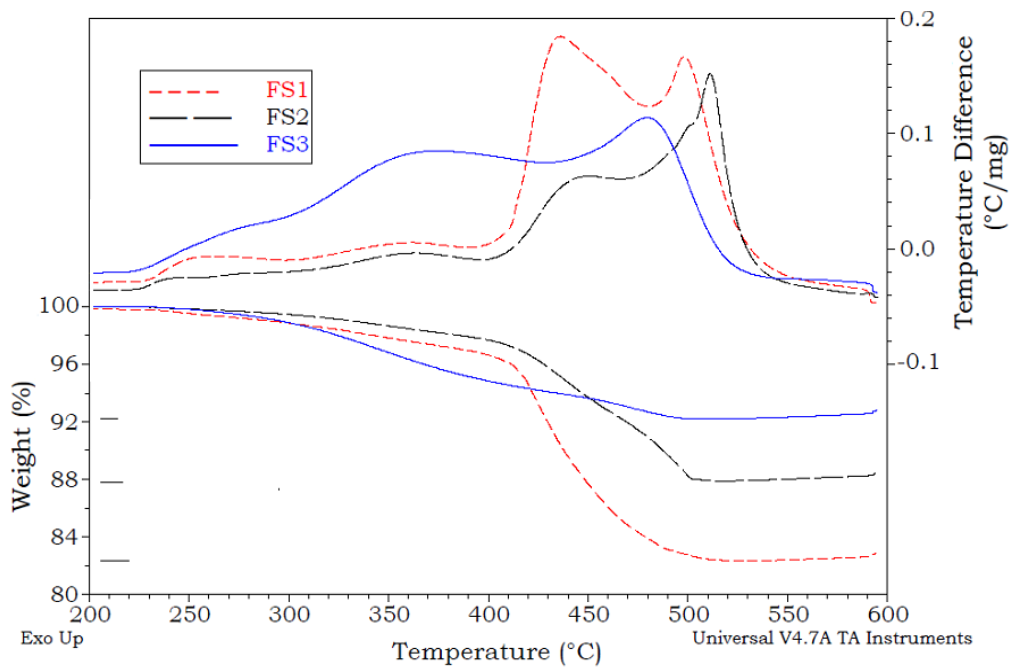


Figure 29: DTA and TGA curves showing thermal decomposition of the binder in air relative to powder loading of the feedstocks.

The binder DTA showed two exothermic peaks (Figure 26) which were also present in FS(1 to 3) although much less prominent and at lower temperatures (Figure 29, Table 6). Shibo et al. proposed that PEG bonds well with metal powders and enabled greater adhesion of other components [63]. This would explain this result with the PEG producing stronger bonds in the feedstock that require more energy for decomposition. This is also supported by a statement made by Tam et al. that miscibility between binder components will enable a shift in exothermic reaction temperatures [49]. This means that combined (binder & feedstock), exothermic temperatures would be higher than the individual wax component and lower than the individual polymer components. Although, it did not determine the level of miscibility or which, if any, components had greatest effect.

Table 6: Thermal values from SDT (air) for binder and feedstock.

| °C  | Endotherm | Exotherm |     | Decomposition (%) |     |
|-----|-----------|----------|-----|-------------------|-----|
|     |           | 1        | 2   | 5                 | 20  |
| B1  | 105       | 300      | 420 | 335               | 370 |
| FS1 | 90        | 360      | 445 | 275               | 380 |
| FS2 | 90        | 360      | 455 | 270               | 350 |
| FS3 | 90        | 380      | 460 | 250               | 300 |

The above results showed greater thermal stability ( $t < 600$  °C) of the feedstock over the binder from addition of the titanium powder. This did not however, wholly reflect the MIM process as the PEG will be removed from the parts before thermal debinding.

### 3.2.2. Moulding

Feedstocks FS(1 to 3) were injection moulded ( $t = 145\text{ }^{\circ}\text{C}$ ,  $p_i = 70$  bar) forming acetabular cups (Figure 16). There were no processing difficulties, and the greenparts appeared defect free (Figure 30 a) although the fine edge of the cup could be easily damaged.

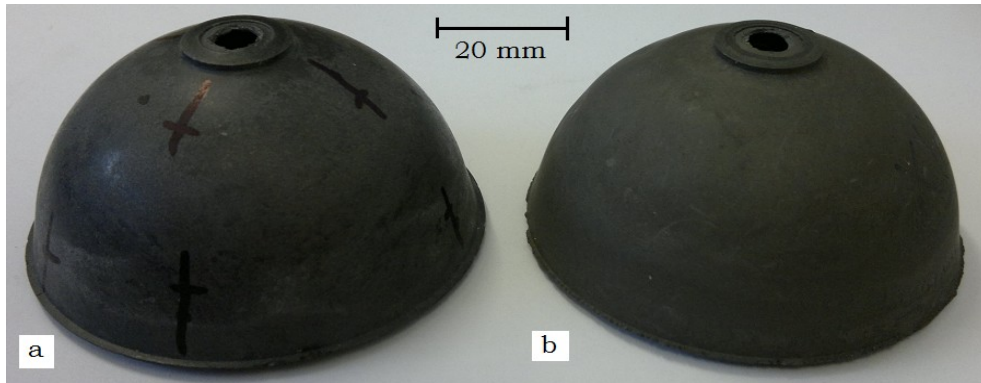


Figure 30: (a) The moulded greenpart, after solvent debinding becomes (b) the greypart.

Theoretical masses of the parts were calculated from mould cavity volume, component density and formulation ratio, the actual mass was measured by weighing. Deviation between the theoretical mass and the actual mass (Table 7) suggested that powder wetting may not have been sufficient to enable full consolidation, resulting in some porosity in the green part. There was no trend for deviation with the increasing powder loading.

Table 7: Mass analysis of the injection moulded green parts.

| g   | Theoretical mass | Mass average ( $\sigma$ ) | Deviation % |
|-----|------------------|---------------------------|-------------|
| FS1 | 110.57           | 107.30 (1.28)             | 3.0         |
| FS2 | 124.53           | 115.83 (0.17)             | 7.0         |
| FS3 | 138.49           | 131.53 (0.50)             | 5.0         |

### 3.2.3. Debinding

The binder must be removed to ensure that the final metal composition is consistent with the starting powder. This is referred to as the debinding phase of the MIM process. Each debinding step was targeted to a single component of the binder system. Solvent debinding (SD) targeted the water soluble fraction (PEG8) while thermal debinding (TD) targeted CW and LLDPE. Residues need to be removed early in the sintering phase before pore channels close and final consolidation takes place.

The scoping experiments presented here only represent a small number of debinding treatments and debinding of the FS1 part was not completed. The high level of binder did not allow sufficient particle interaction and shape distortion occurred as the binder was removed.

#### 3.2.3.1. Solvent debinding

Distilled water ( $t = 50\text{ }^{\circ}\text{C}$ ) was circulated over the greenparts during SD using varied debinding times for each part Table 8. The temperature was below the melt temperature of PEG8 (Table 4), ensuring removal was a dissolution process and not thermal.

Table 8: Solvent debinding mass loss for green parts.

| Green Part | #   | $m_{\text{Green}}$ | Duration (h) | $m_{\text{L}}(\%)$ |
|------------|-----|--------------------|--------------|--------------------|
| FS2        | I   | 116.0              | 5.0          | *                  |
|            | II  | 115.9              | 10.0         | 14.5               |
|            | III | 115.6              | 24.0         | 40.0               |
| FS3        | IV  | 121.5              | 5.0          | *                  |
|            | VI  | 132.0              | 10.0         | 12.0               |
|            | VII | 131.6              | 24.0         | 27.0               |

\* Mass loss was not recorded for this experiment.

After solvent debinding the parts, referred to as greyparts were dried and weighed to determine the weight loss using the following formula.

$$m_{L(\%)} = \left( \frac{m_{Green} - m_{Grey}}{m_{Green} \times \omega_B} \right) \frac{100}{1} \quad (12)$$

$m_{L(\%)}$  = mass loss (%) of total binder,  $m_{Green}$  = mass (g) of greenpart,  $m_{Grey}$  = mass (g) of grey part,  $\omega_B$  = mass fraction of binder in greenpart.

Increasing the dissolution time increased the amount of binder removed confirming that the removal mechanism is dependent on the interaction of the greenpart and water. Two main driving forces can be considered here; the solute differential between the greenpart and the solvent, and diffusion of the solvent within the network of pores. Lower mass loss with increased powder loading was likely due to a combination of the two mechanisms.

Solvent debinding (t = 24 h) removed 40 % of the binder mass from the greenpart. In the solid phase there is a definite boundary between the binder and particles [171]. This is further defined during solvent debinding where the solvent surrounds the PEG molecules allowing them to become motile [172]. Hydrophobic CW and LLDPE are hardly soluble, highly resistant to water and would prefer to aggregate when combined. This would suggest that when the binder solidified during the mixing process CW and LLDPE molecules became entrapped within the soluble phases. It also explains the excess mass loss as loss of insoluble components through entrainment during the solvent debinding process.

### 3.2.3.2. Thermal debinding

The thermal debinding process included two variables; isothermal temperature and dwell time. Increasing the isothermal temperature increased the mass loss for all parts (Table 9), however, as the greyparts underwent different SD treatment a comparison of the mass loss values between parts was difficult.

Table 9: Mass loss values from thermal debinding the grey parts.

| Green Part | #   | Temperature (°C) | Dwell time (h) | Mass loss (%) |
|------------|-----|------------------|----------------|---------------|
| FS2        | I   | 350              | 0.5            | 7.9           |
|            | III | 400              | 6.0            | 25.8          |
| FS3        | IV  | 350              | 0.5            | 18.6          |
|            | VI  | 400              | 6.0            | 48.2          |
|            | V*  | 350              | 10.0           | 38.9          |
|            | VII | 350              | 10.0           | 30.9          |

\* thermal debind of greenpart

When SD and TD were combined (for the same part) residual binder was less in samples with higher powder loading (Table 10). This was at odds with the SD results where a higher powder loading retarded the debinding process. This can be attributed to binder interaction with the particles by two means. Firstly, the debinding mechanism was improved by the higher powder surface area and subsequent increase in surface energy within the compact. Secondly, the higher powder loading improved thermal conductivity within the compact, thereby increasing the rate of debinding.

Table 10: Total binder mass loss from combined treatments.

| Green Part | #   | SD           | TD         |              | Mass loss (%) | Residue (%) |
|------------|-----|--------------|------------|--------------|---------------|-------------|
|            |     | Duration (h) | Temp. (°C) | Duration (h) |               |             |
| FS2        | I   | 5            | 350        | 0.5          | 7.9           | 12.0        |
|            | II  | 10           | N/A        |              | 14.5          | 11.2        |
|            | III | 24           | 400        | 6.0          | 66.1          | 4.4         |
| FS3        | IV  | 5            | 350        | 0.5          | 18.6          | 7.2         |
|            | V   | N/A          | 350        | 10.0         | 38.9          | 5.4         |
|            | VI  | 10           | 350        | 10.0         | 42.9          | 5.0         |
|            | VII | 24           | 400        | 6.0          | 75.7          | 2.1         |

Comparison of TD with the combined SD and TD treatment suggested that differences in mass loss were related to molecular interaction of the binder components. PEG was used to increase particle wettability and hence stronger bonds between CW, LLDPE and Ti would explain the greater resistance to leave the greenpart than the greypart. SD is considered the precursor to formation of the interconnected pores that are integral to the debinding process. Greater energy was required to overcome the bonds between the components as the resistance to flow of the PEG8 and the CW was greater than for the CW alone. Therefore, a greater mass loss was facilitated by combined debinding.

### 3.2.4. Sintering

All brownparts with less than 5 % residue were sintered at 1250 °C [62, 63]. Brownparts (III, VII) were sintered in the AIP furnace with a static argon atmosphere (1 h) and (V, VI) were sintered in the Mellen furnace in a vacuum ( $p = 2.0 \times 10^{-4}$  mbar,  $t = 3$  h).

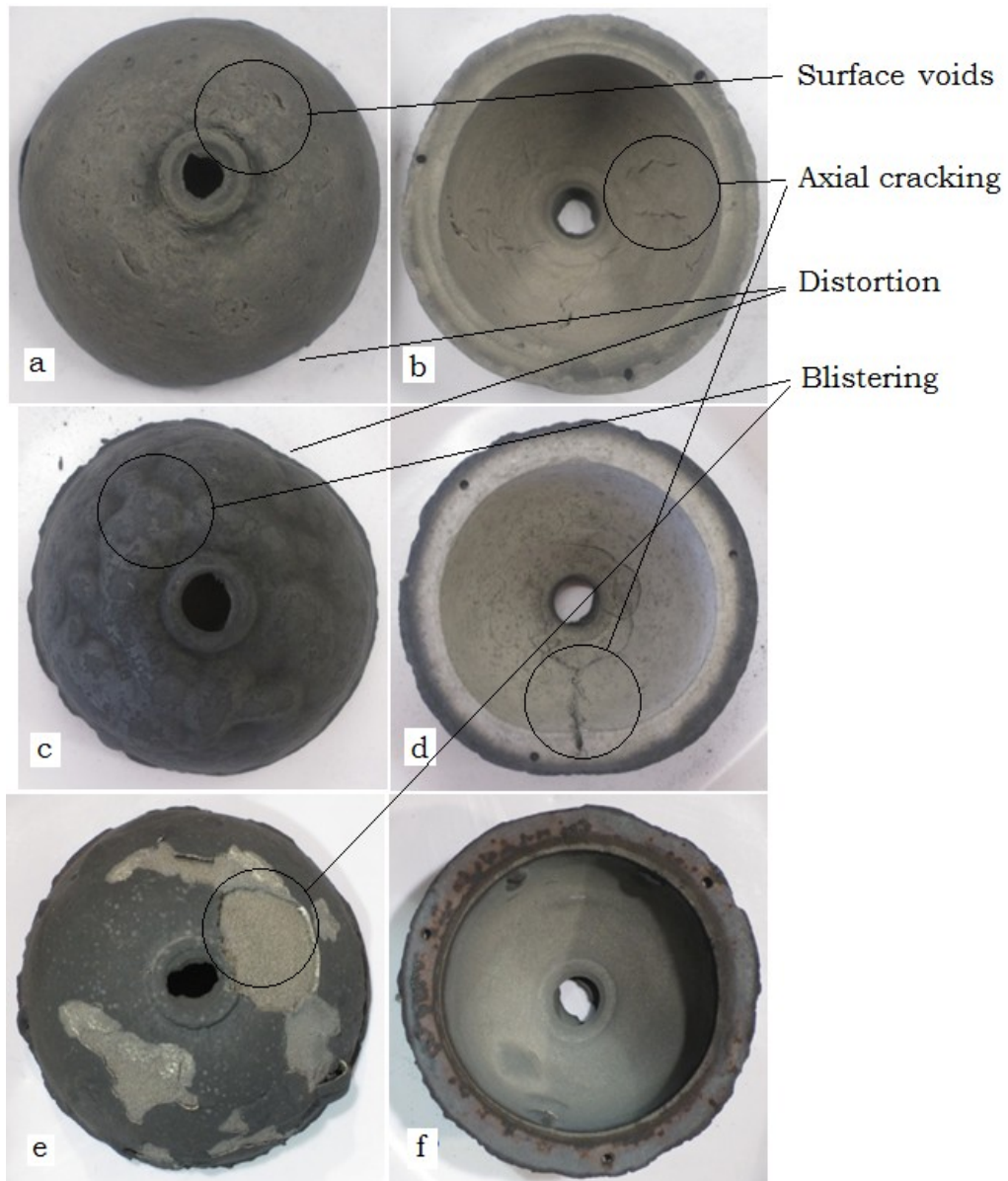


Figure 31: Sintered parts (a, b) III, (c, d) VII with surface defects, distortion and cracks and (e, f) V with blistering.

All parts (Figure 31) had axial cracking, shape distortion and surface defects that were not present in the brown state. Voids in the sintered part may be caused by gas vapours generated from excess residual binder in the brown part. Contamination may be from residual binder or existing furnace contamination forming elemental deposits on the part surfaces. The surface contamination (III) was easily removed by wire brushing (Figure 31 a) and the underlying titanium surface appeared clean. The axial crack (Figure 31 d) through the inner shell of FS3 (VI) may be caused by non-uniform shrinkage or moulding defects. Carbon formations on the outer surface of V & VII (Figure 31 (c, e)) were accompanied by separation blistering. Carbon deposits were not evident on the inner surface; but the appearance was different from the outer surface for both III and VII. The inner surface of part VII showed (Figure 31 d) a distinct oxide formation.

Part V (Figure 31 e & f) had no cracking or distortion but still had severe blistering on the outer surface and the colouring had less contrast from inside to outside. Blistering of the outer surface (Figure 31 c & e) can result from increased shear stress breaking the organic bonds during moulding causing feedstock separation, or slip causing non-uniform particle flow [74]. Powder and binder separation forms distinct layers that separate when the binder is removed and the weak particle bonds are lost. Blistering was not evident on the surface of part III. This can be attributed to both the internal furnace pressure during sintering and the higher level of binder retaining a uniform particle distribution.

Shape distortion was more evident with FS2 than the FS3. This was attributed to the lower powder loading and indicated that particle - particle interaction had an important role in the sintering phase. In line with literature these results suggested that powder loading between ( $\phi_B = 0.6$  and  $\phi_B = 0.70$ ) would reduce both the distortion (Part III) and the blistering (Part (V, VII)). Surface defects

and cracking must be minimised (Figure 31), however, without knowing at which part of the MIM process defects occur it will be difficult to determine a solution. For example, a crack that forms during moulding will not be repairable during debinding but a crack that forms due to thermal stresses while sintering can be avoided by altering the sintering conditions.

SEM images of the sintered parts showed partial coalescence of particles on the fracture surface (Figure 32) evidence of insufficient sintering. The polished surfaces showed porosity, when measured by pycnometer values were 7 % (V) and 9 % (VII). Vacuum sintering provided better conditions for sintering based on lower porosity than the static sintering, even with more residue to be removed (Table 10). Although the external surfaces of the parts showed high levels of contamination, the bulk metal is more critical.

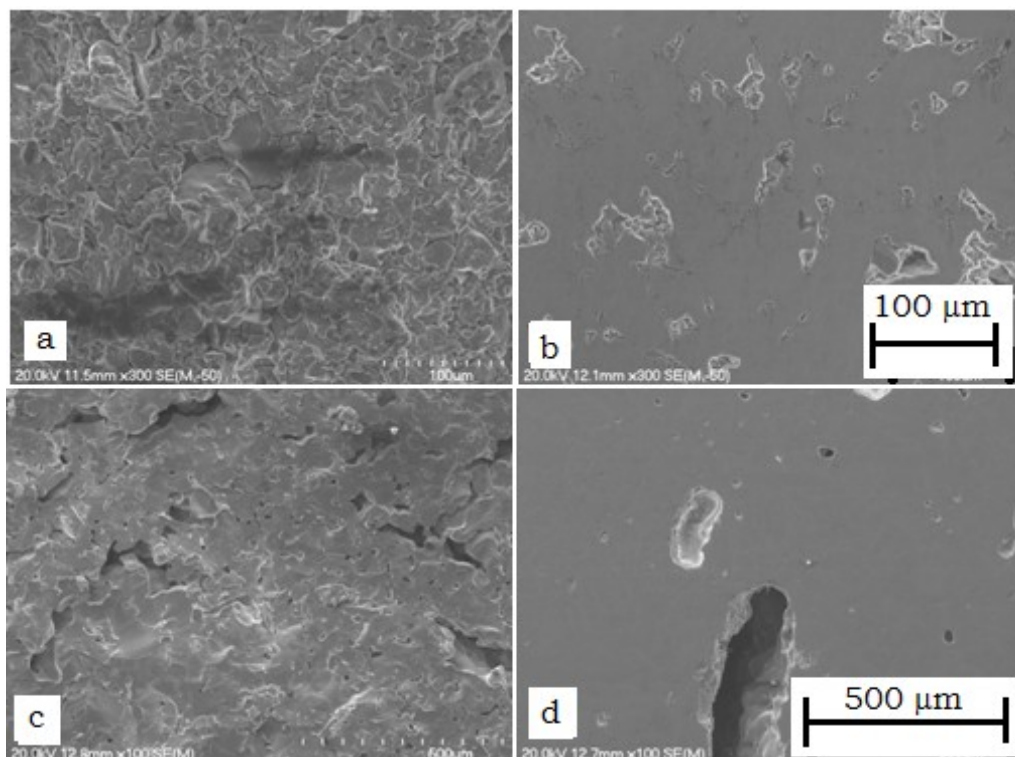


Figure 32: SEM of FS3 (VII) sample a) fracture surface b) polished surface and FS3 (V) sample c) fracture surface d) polished surface.

The sintered cup showed non-uniform microstructure across the section (Figure 33). Coarse grains of the light coloured alpha phase titanium formed inside of the cup (Figure 33 (a, b)). At the centre the grains were smaller with some beta phase titanium formed at the boundaries and entrapped carbon from binder residue between the particles (Figure 33 b). The outer section showed a high level of contamination with some beta phase lamella formations and little porosity (Figure 33 c). As expected the static furnace atmosphere during sintering did not allow removal of residual binder and resulted in a high level of surface contamination. This confirms the need to ensure the furnace itself is free of contamination during the sinter process.

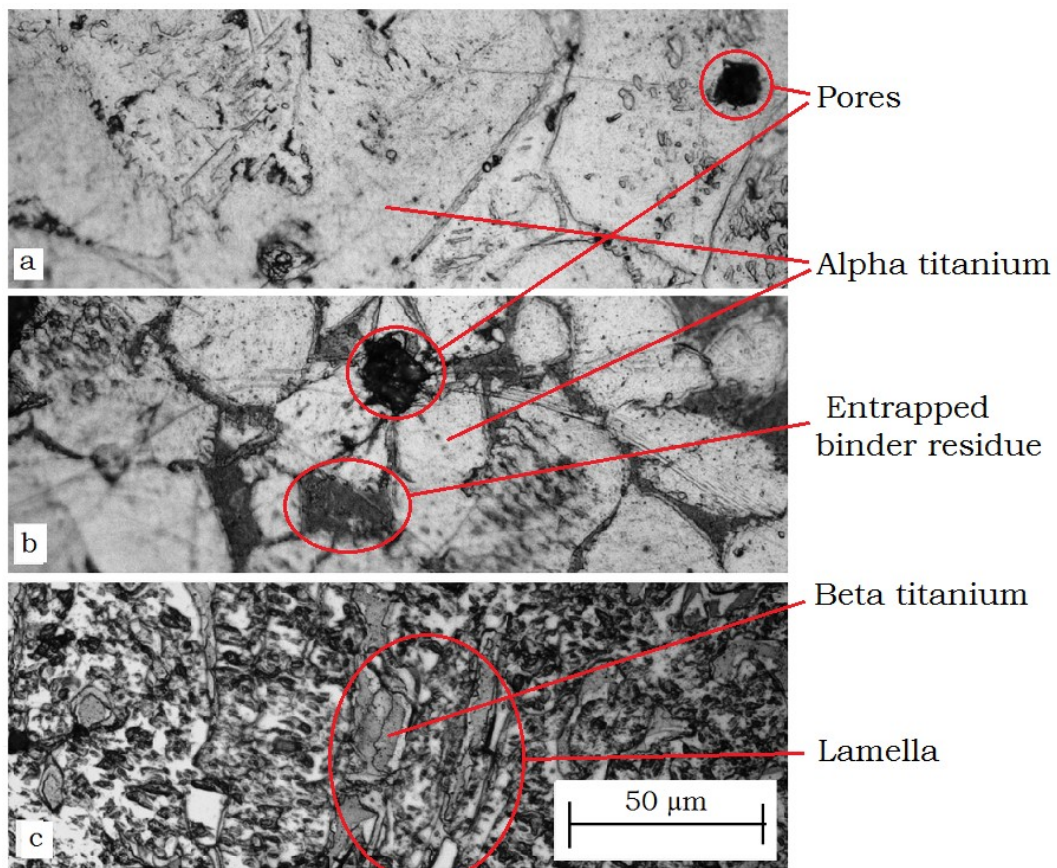


Figure 33: Part VII samples etched with Kroll reagent, a) inside section b) centre section and c) outer section (Figure 22).

The vacuum sintered parts showed non-uniformity throughout the cross section (Figure 34). There was a high level of contamination within the section but less than that seen with the static furnace. The inner section showed an alpha-beta structure with carbon deposits at the grain boundaries (Figure 34 a). The centre section had voids and a matrix of alpha phase titanium with some beta phase inclusions (Figure 34 b). The outer location had a more conventional alpha-beta structure with distinct lamella alpha phase within a beta phase matrix with a secondary dispersion of carbon inclusions at the surface (Figure 34 c). The use of a graphite furnace box will have contributed to the retention of the carbon.

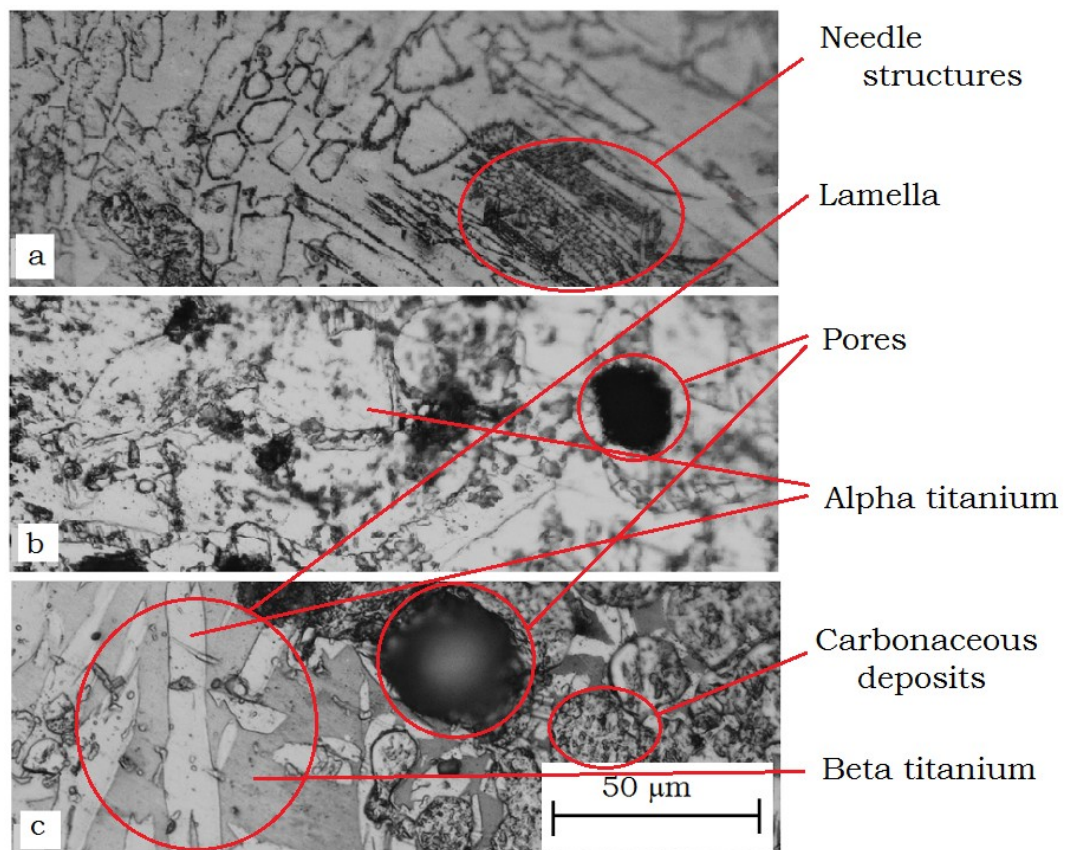


Figure 34: Part V sample sectioned and etched with Kroll reagent, a) inside section b) centre section and c) outer section (Figure 22).

ASTM prescribes upper limits of C, H, N and O (Table 11) to ensure consistency of mechanical properties of titanium [150, 173]. The values presented (Table 11) for the MIM samples exceed both the ASTM standard and manufacturer specifications. The elemental levels increased for all but hydrogen in the argon atmosphere. It is not clear why the nitrogen level increased in the argon sintered part and hydrogen in the vacuum sintered part. Carbon levels were not measured but were seen from the visible contamination and carbon formations to be high. The oxygen levels were also very high as indicated by LECO analysis (Table 11).

Table 11: Standard, manufacturer specification and elemental composition by LECO.

| $w_E$ (%)       |             | C    | H     | N    | O          |
|-----------------|-------------|------|-------|------|------------|
| ASTM B348 [173] | Standard    | 0.08 | 0.015 | 0.05 | 0.2        |
| Manufacturer    | As received | 0.02 | 0.039 | 0.18 | 0.5        |
| LECO            | Part V      | *    | 0.373 | 0.21 | $\geq 1.0$ |
|                 | Part VII    | *    | 0.021 | 0.52 | $\geq 1.0$ |

\* – not recorded.

The majority of defects formed during sintering. The physical defects may be attributed to feedstock formulation as well as moulding while shape distortion was more typical at low powder loading. Low density, or high porosity levels, is known to be caused from low sinter temperature, contamination within the furnace, disruption of particle to particle bonds and oxide formation on the particle surfaces [174]. Finally the elemental composition of the metal is linked to the sinter conditions and elimination of impurities and is known to be essential for achieving specified mechanical properties.

### **3.3. Conclusions**

Despite the limitations of this work it was found that success with part moulding does not ensure uniformity of the green parts. It was also shown that for this new binder system solvent debinding followed by thermal debinding enabled a higher level of binder removal than solvent or thermal debinding alone.

The processing atmosphere during sintering has been confirmed as critical to the final part. A low residue brownpart is not the sole criteria for limiting impurities in the final part. The sinter furnace atmosphere must also remain free from contamination to eliminate diffusion back into the parts at sinter temperatures.

The results also indicated that feedstock with a powder level between the lower ( $\phi_P = 0.6$ ) and higher ( $\phi_P = 0.7$ ) loading may reduce deformation and blistering of the sintered part.

## **Chapter Four: A wax based binder for titanium based MIM**

In the previous chapter the parts produced from a polymer based binder system showed high levels of surface contamination, macro defects and a non-uniform microstructure. In this chapter, those issues were addressed by evaluating the effect of wax as the major binder component in the feedstock. Wax being a common binder component for ferrous metals. It has a low molecular weight, a low melt temperature and is known to lubricate and improve dispersion within particulate flow systems. The binder system was based on a formulation previously used for the MIM of Ti-6Al-4V [100].

Thermo gravimetric and differential thermal analyses were used to assess the relationships of the binder, feedstock and moulded parts. Density distribution was assessed by density mapping greenparts. Non-uniformity and internal defects of the greenparts were identified by non-destructive inspection using X-ray radiography.

This was followed by an investigation of the efficacy of solvent and thermal debinding. Finally, the overall effect of moulding, debinding and sintering on defect formation and metal composition of sintered titanium parts was assessed.

## 4.1. Experimental

### 4.1.1. Materials

Materials previously specified:

- Linear low density polyethylene (LLDPE).

The materials introduced in this chapter:

- Icorene® PPCO14RM polypropylene copolymer (PP), with a melt flow index (MFI) of 13.0 g/10min. The annealed density was 0.90 g/cm<sup>3</sup>, it had a softening point (Vicat) of 85 °C and was supplied by ICO Courtenay, Auckland, NZ.
- Merck polyethylene glycol 20000 (PEG20), with melting/freezing points of (58 to 63) °C. The density was 1.20 g/cm<sup>3</sup> and it had a water solubility of 500 g/L @ 20 °C and was supplied by Merck Millipore, Auckland, NZ.
- Refined paraffin wax (PW) with a melting/freezing point of (61 to 66) °C and a density 0.97 g/cm<sup>3</sup>, was supplied by Ajax, New Zealand.
- Stearic acid (SA) of Unilab reagent grade, with a melting point 54 °C and a density 0.85 g /cm<sup>3</sup>, was supplied by Ajax, New Zealand.
- Titanium 6Al - 4V alloy powder (HDH Ti64) with irregular particle shape and interstitial levels of  $w_E = (0.039 \text{ (H)}, 0.50 \text{ (O)}, 0.18 \text{ (N)}) \%$ . The particles passed through 200 mesh sieves with an average particle size of < 74 μm and were supplied by Xi'an Lilin International Trade Co., China.

### **4.1.2. Equipment**

Equipment previously introduced:

The TSE16 twin screw extruder was used for capillary extrusion and to produce the feedstock pellets. Moulding of the samples was done in the Dr Boy 50T2 injection moulder with the acetabular cup mould. Solvent debinding (SD) was done using the SD1 kit ( $V = 0.5$  L). Thermal debinding (TD) with controlled atmosphere was done in the TD1 kettle and the Mellen BG25 vacuum furnace was used for sintering. Differential thermal analysis (DTA) and thermal gravimetric analysis (TGA) was done using the SDT2960. Oxygen, hydrogen and nitrogen levels were measured using the inert gas fusion-infrared absorbance method (LECO TCH600). Visual analysis was done using the Hitachi SEM and optical analysis used an Olympus BX60 and a Wild M3B microscope. The Quantachrome Ultra-pycnometer 1000 was used for density measurement.

The equipment introduced in this chapter:

A Philips G200/S power supply transformer coupled with an X-ray radiation source (FFD = 700 mm) was used for radiographic inspection courtesy of SGS Ltd, Hamilton, NZ. The FFD was the field of focus depth from the tungsten filament source to the sample table through an image aperture of 1.5 mm  $\times$  1.5 mm.

### **4.1.3. Methodology**

The binder components LLDPE, PEG20, PP, PW and SA were individually analysed using SDT to determine their comparative thermal response ( $t = (40 \text{ to } 400) \text{ }^\circ\text{C}$ ,  $\beta = 5 \text{ }^\circ\text{C}/\text{min}$ , Figure 19). The results were used to determine processing parameters for mixing and moulding of the feedstock.

The feedstock was mixed using the extruder (TSE16) and analysed using SDT. It was formulated by calculating the mass of each component based on the density required for the specified volume.

The binder ( $\varphi_B = 0.63$  (PW), 0.12 (PEG20), 0.14 (LLDPE), 0.10 (PP) and (0.01) SA) was blended with Ti64 ( $\varphi_P = 0.5, 0.6, 0.7$ ) [63]. SDT was used to determine how thermal response was affected by component interactions.

The feedstock was extruded through a strand die ( $\varnothing = 6$  mm) before breaking into uniform granules. Acetabular cup samples were moulded and referred to as greenparts (Figure 16). The moulding parameters were; barrel temperature ( $t = (155, 155, 140)$  °C), injection pressure ( $p = 700$  bar), screw speed ( $\omega = 100$  r/min) and mould temperature ( $t = 30$  °C).

Density distribution was assessed by cutting the acetabular cup into pieces (Figure 35) and measuring the piece density using the pycnometer with nitrogen gas as the pressure medium. Non-uniformity and internal defects of the greenparts were investigated using X-ray radiography.

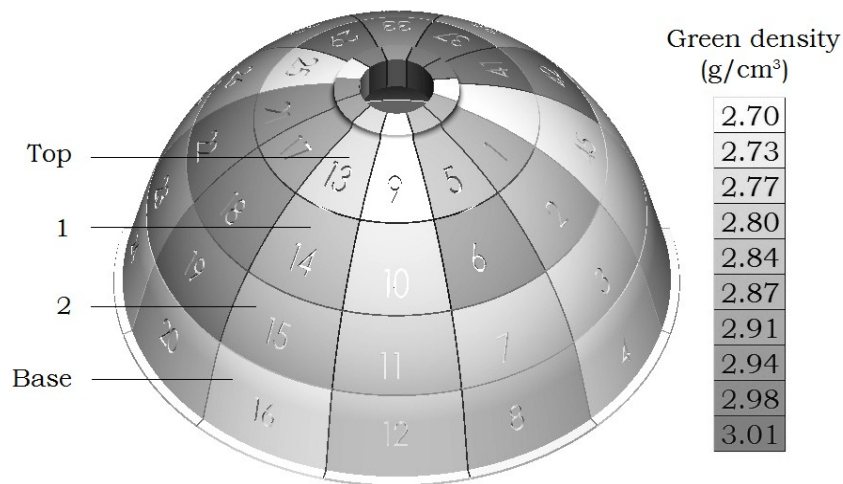


Figure 35: Density distribution assessment by pieces.

Debinding of the greenparts was done using solvent debinding (SD) followed by thermal debinding (TD) and by TD only.

SD involved submersion of the parts in the solvent debinding apparatus (Figure 17). The heptane and ethanol solution (8:2) was heated ( $t = 60\text{ }^{\circ}\text{C}$ ) and circulated at 5 L/min to slowly remove the wax and stearic acid ( $t = (0\text{ to }24)\text{ h}$ ). After solvent debinding and subsequent drying, the parts are referred to as greyparts.

During TD the greyparts were placed in the thermal debinding kit (Figure 18) and heated with a sweep gas to remove the volatile waste. The process involved a series temperature increases at the rates shown in Figure 36. Isothermal steps ( $t = (350, 420, 600)\text{ }^{\circ}\text{C}$ ) allowed for outflow of binder decomposition products and limited any disruption to the particle packing during removal. Air was used as the sweep gas ( $\dot{V} = 0.5\text{ L/min}$ ,  $t < 250\text{ }^{\circ}\text{C}$ ) before switching to argon ( $\dot{V} = 0.5\text{ L/min}$ ,  $t > 250\text{ }^{\circ}\text{C}$ ) to limit the potential for oxygen uptake.

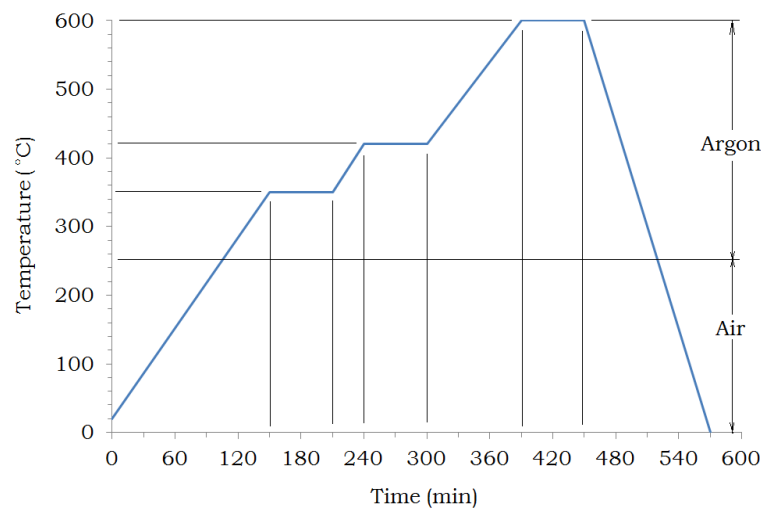


Figure 36: Thermal debinding temperature profile.

Sintering of the brownparts was done using the Mellen vacuum furnace. The parts were placed in the furnace and purged with

argon gas and a vacuum cycle to remove air. After two purge cycles the furnace was placed under vacuum ( $p = 3.0 \times 10^{-4}$  mbar) with two heating steps ( $\beta = 4.5$  °C/min to  $t = 800$  °C,  $\beta = 6$  °C/min to  $t = 1250$  °C) before the sinter temperature was reached and maintained ( $t = 1250$  °C,  $t = 180$  min). Natural furnace cooling took about 10 hours and the parts were removed at ambient temperature.

The overall effect of moulding, debinding and sintering on defect formation and metal composition of the sintered cups was assessed. They were inspected on the outer and inner surfaces as well as through the parts using radiography. The cups were sectioned and analysed using the optical microscope and SEM. EDS was used to determine surface chemistry and indicate comparative carbon levels. An etching reagent was used to expose the microstructure of cut and polished samples. The samples were submerged ( $t = 1$  min) in a Kroll reagent (100 mL distilled water, 2 mL HF and 4 mL HNO<sub>3</sub>) before rinsing in distilled water.

Oxygen, hydrogen and nitrogen levels were measured using the inert gas fusion-infrared absorbance method (LECO TCH600).

## 4.2. Results and discussion

### 4.2.1. The binder

Thermal analysis of binder components was found to be of limited value where the parameters used during subsequent processing differ. For this reason initial analysis of the components was intended to determine mixing conditions of the binder and feedstock only. The thermal events that were identified by melt (endothermic) and decomposition (exothermic) peaks (Figure 19), as well as TGA weight loss were summarised in Table 12. SDT data showed all components were in the melt state during mixing ( $t = 170\text{ }^{\circ}\text{C}$ , Table 12). TGA gave the decomposition (5 % weight loss) temperature of PEG20 ( $t = 187\text{ }^{\circ}\text{C}$ ) and SA ( $t = 205\text{ }^{\circ}\text{C}$ ) to be high enough as to not be affected by the process temperature.

Table 12: Component reaction values from SDT ( $\beta = 5\text{ }^{\circ}\text{C}/\text{min}$ ).

|       | Endotherm<br>( $^{\circ}\text{C}$ ) | Exotherm<br>( $^{\circ}\text{C}$ ) |     | Weight loss ( $^{\circ}\text{C}$ ) |     |       |
|-------|-------------------------------------|------------------------------------|-----|------------------------------------|-----|-------|
|       |                                     |                                    |     | air                                |     | argon |
|       |                                     | 1                                  | 2   | 5%                                 | 20% | 20%   |
| PEG20 | 68                                  | 260                                | N/A | 187                                | 218 | 385   |
| PW    | 58                                  | 230                                | 280 | 215                                | 241 | 250   |
| SA    | 63                                  | 230                                | 340 | 205                                | 232 | 240   |
| LLDPE | 110                                 | 270                                | 340 | 330                                | 383 | > 400 |
| PP    | 165                                 | 280                                | 350 | 275                                | 302 | > 400 |

The form of the endothermic peaks from DTA indicate the crystallinity of a sample and may also indicate phase segregation within a polymer or polymer blend [175]. Low definition peaks indicate mostly amorphous or low-crystallinity (30 %) structures (LLDPE), while distinct peaks indicate high-crystalline (80 %) structures (PEG20, PP, PW, SA, Figure 37) [176]. Where abrupt spikes are present in DTA curves it indicates a rapid or explosive thermal response which would not be suitable for a binder component. Crystallinity is known to be a function of the polymer

structure but it is also influenced by processing parameters such as heating and cooling rates, and shear deformation. Degree of crystallinity is not a clear indicator of thermal behaviour and during debinding the activation energy of low-crystallinity polymers may be the same as that of high-crystallinity polymers [167]. As above their melting points both low and high crystallinity polymers have similar random molecular structure.

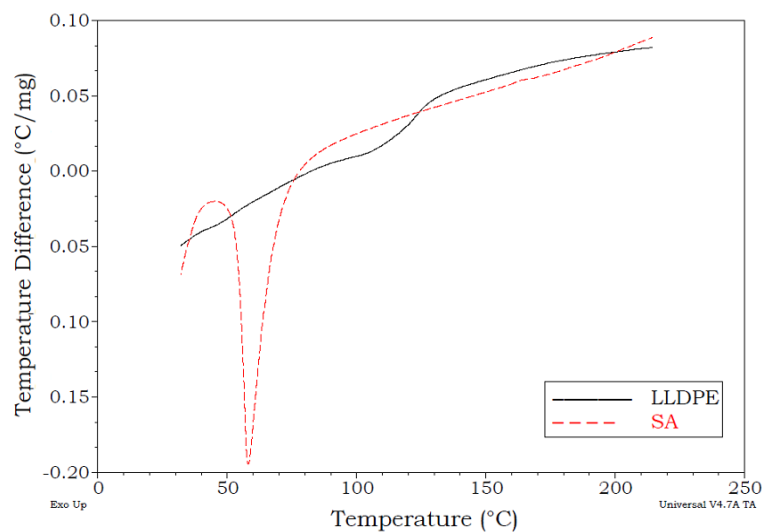


Figure 37:DTA curve showing the low intensity peak of LLDPE in comparison to the SA.

Decomposition of PEG20, LLDPE and PP was seen at lower temperatures (Table 12) in air than in argon (for 20 % weight loss). This is attributed to oxidation causing breaks in the polymer chains (scission) at temperatures below what they would generally be for thermal pyrolysis. Decomposition of the PW and SA showed little difference between air and argon confirming thermo-oxidative stability. During thermal processing the by-products, carbon and oxygen, must be removed with the sweep gas before combustion as CO and CO<sub>2</sub>. If this does not occur, carbonaceous residues or ash form which can be the precursor to formation of brittle carbides or remain as solid inclusions that hinder consolidation. Oxygen

readily becomes interstitial and will rapidly reduce ductility at levels above 0.4 %.

#### 4.2.2. The feedstock

The binder components and metal powder (Table 13) were combined before extrusion ( $t = 155$  °C) to form feedstock pellets ( $\phi_P = 0.5, 0.6$ ). The powder loading reported in the work of Shibo et.al. ( $\phi_P = 0.7$ ) for a similar binder [63] could not be replicated due to a lack of cohesion between the powder and binder.

Table 13: Component volume fractions for the feedstock.

|            | Binder ( $\phi_B$ ) |       |       |       |       | Ti64 ( $\phi_P$ ) |
|------------|---------------------|-------|-------|-------|-------|-------------------|
|            | LLDPE               | PP    | PEG20 | PW    | SA    |                   |
| Shibo [63] | 0.042               | 0.030 | 0.036 | 0.189 | 0.003 | 0.70              |
| FS4        | 0.070               | 0.050 | 0.060 | 0.315 | 0.005 | 0.50              |
| FS5        | 0.056               | 0.040 | 0.048 | 0.252 | 0.004 | 0.60              |

The feedstocks (FS4, FS5) had similar trends during heating ( $\beta = (5, 20)$  °C/min) (Table 14, Figure 19). The first thermal event ( $t = 60$  °C) was endothermic and showed the binder melted at a similar temperature to PEG20, PW and SA. The first and second exothermic events (Table 14) occurred at similar temperature to the PEG20, PW and SA. They collectively accounted for 76 % of the binder and had the major influence on the feedstock.

Table 14: Temperature of thermal event for feedstock FS4 and FS5.

|     |   | Endotherm (°C) | Exotherm (°C) |     | Weight loss (°C) |     |       |
|-----|---|----------------|---------------|-----|------------------|-----|-------|
|     |   |                | 1             | 2   | air              |     | argon |
|     |   |                |               |     | 5%               | 10% | 10%   |
| FS4 | a | 60             | 247           | 291 | 265              | 290 | 355   |
|     | b | 71             | 280           | 340 | 292              | 320 | N/A   |
| FS5 | a | 60             | 260           | 320 | 255              | 297 | 375   |
|     | b | 71             | 340           | 351 | 288              | 324 | N/A   |

For a and b,  $\beta = (5, 20)$  °C/min respectively.

There was a significant shift in the position of thermal events when the heating rate was increased ( $\beta = (5, 20) \text{ }^\circ\text{C}/\text{min}$ , Table 14). Thermal processes typically involve slow response times due to the transfer of heat energy into or out of a system. When heating rates are high the differential between an outer surface and centre of a part will be high. A low heating rate will therefore allow more uniform heat transfer throughout with a lower differential between the outer surface and the centre. Thermoplastic polymers typically have low thermal conductivities that will affect MIM parts during the debinding process as high heating rates create stress gradients throughout a part. Conversely, low heating rates could reach decomposition activation (energy) at lower than anticipated temperatures (Figure 25) and begin decomposition during the mixing, or moulding process.

Shibo et.al. [63] reported a similar MIM feedstock with a high powder loading ( $\phi_P = 0.7$ ). In this study ( $\phi_P = 0.7$ ) could not be obtained as mixing and extrusion was problematic and the extrudate did not form a cohesive strand. The powder used by Shibo et.al. was a blend (9:1) of spherical (gas atomised) and irregular shaped (HDH) powder. Spherical powder is known to have better flowability and to provide better formability at higher loading fractions. Irregular powders have greater compact strength from mechanical bonding and particle deformation. The powder used in this study was 100 % HDH powder (irregular shape).

### 4.2.3. Moulding

The feedstock moulded well, however, FS4 green parts easily cracked and failed to hold the moulded form. The green strength of the FS5 green parts was higher, although care was still needed to support the parts on ejection from the mould. While an optimised moulding cycle may rectify this (i.e. prolonged cooling time) only FS5 parts were selected for further investigation.

The average mass of the FS5 greenparts was 109.4 g ( $\sigma = 0.7$ ) with a density of 2.71 g/cm<sup>3</sup> or 89 % of the theoretical density of the feedstock as calculated from the design volume of the mould set ( $V = 40.4$  cm<sup>3</sup>). The design volume based on free volume addition of the individual components did not account for miscibility or changes in volume upon mixing [176]. The part volume measured by Archimedes principle ( $V = 39.0$  cm<sup>3</sup>) was 3.5 % lower than the tool cavity volume due to shrinkage of the part on cooling. The weight loss determined by TGA equated to a powder loading of 0.58, the density of the greenpart ( $\rho = 2.81$  g/cm<sup>3</sup>) was therefore 94 % of theoretical indicating internal defects (pores, cracks or cavities) accounted for 3.3 % of the actual part volume.

Radiographic imaging showed cracks (Figure 38 b) and separation layers (Figure 38 c) within some of the greenparts, but not equal to a 3.3 % volume differential. Separation between the particles and the binder may account for the difference and would not be seen as resolution of the radiographs was  $\geq 200 \mu\text{m}$ .

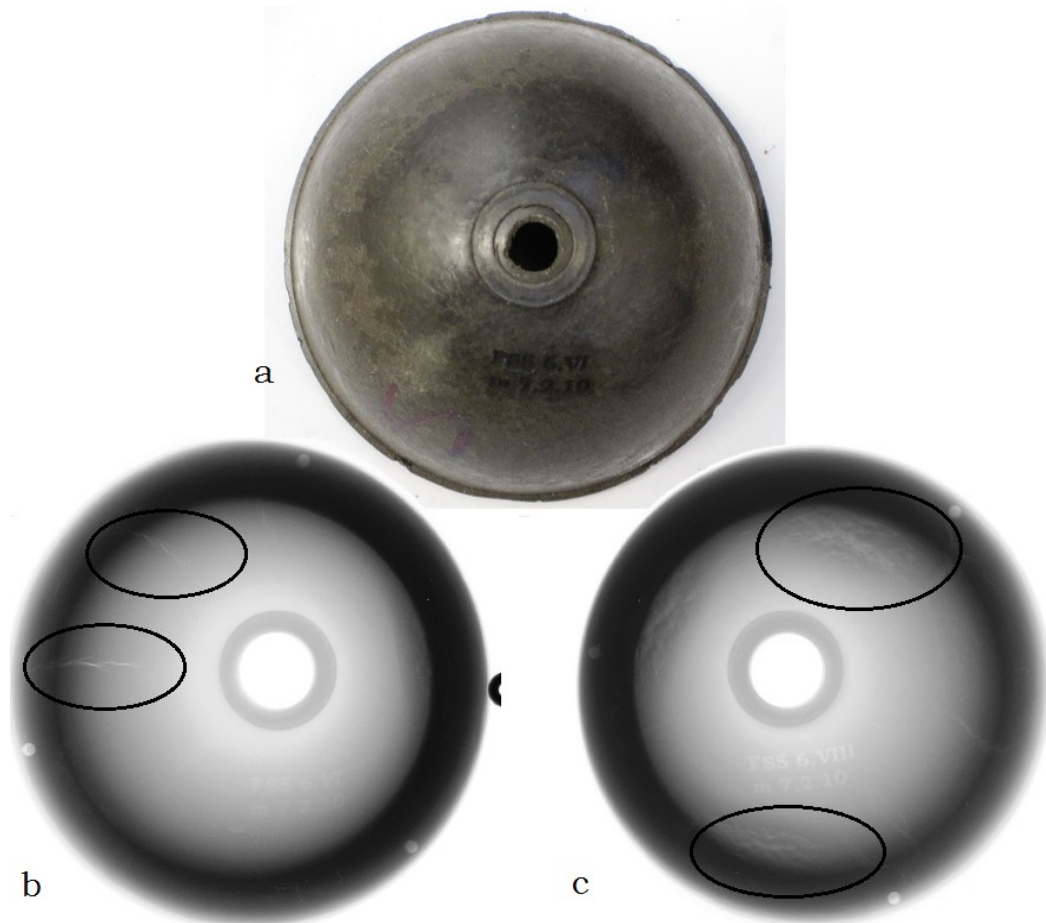


Figure 38: FS5 greenparts; a) a digital image and radiographs ( $E = 100 \text{ kV}$ ,  $t = 30 \text{ s}$ ) showing b) cracks and c) separation.

Further investigation of defects would require a layered approach to the imaging. The images in Figure 39 were obtained by changing the energy level of the X-ray, this allowed focusing on different horizontal planes throughout the part. Figure 39 a) focused near the top of the part ( $E = 80$  kV) and showed no clear defects. Figure 39 b) focused near mid part ( $E = 100$  kV) and showed a dimple, a fine crack and separation layers. Figure 39 c) focussed near the bottom of the part ( $E = 150$  kV) and showed further separation. Pores were not evident in this region.

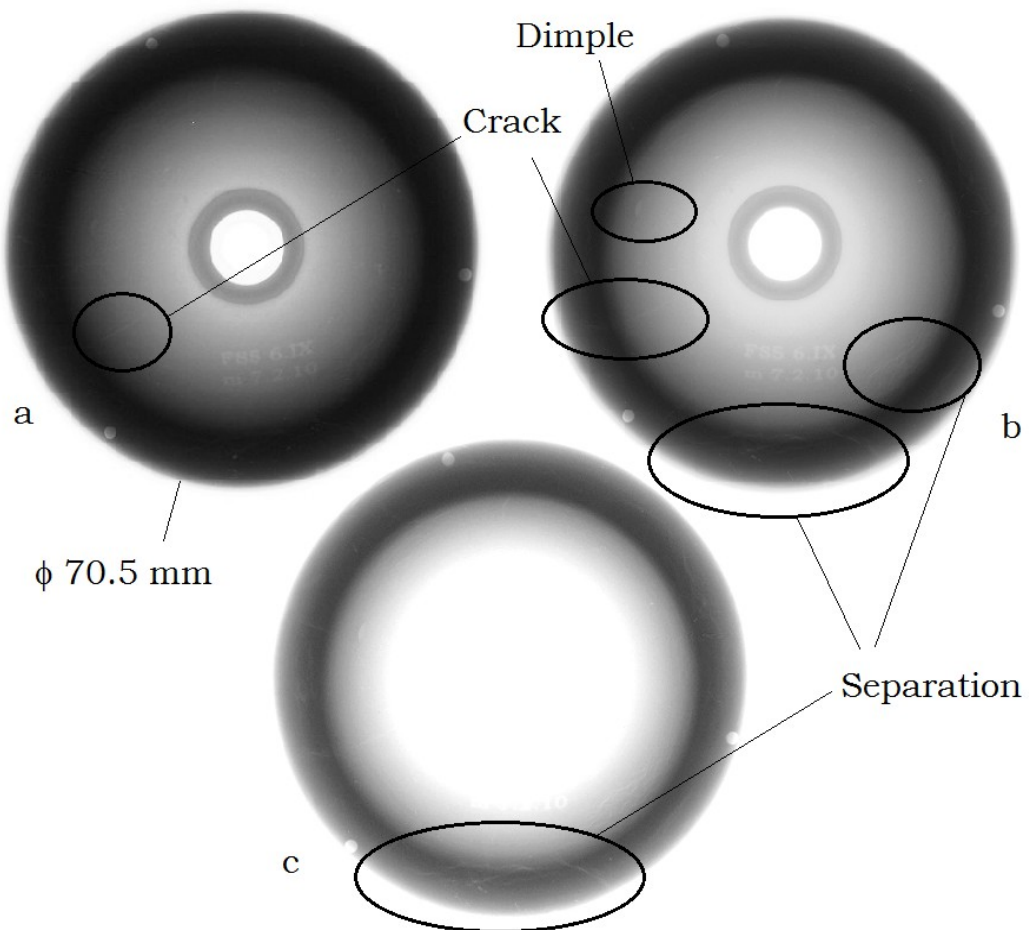


Figure 39: Changing X-Ray energy to focus at; a) top of part, b) middle of part and c) bottom of part.

Following this a green part was sectioned into pieces and to further investigate defect formation the piece density was measured using the pycnometer. The density values were presented as a density map using a 3D model of the part (Figure 35). The density map indicated that the density was not uniform about the top of the part. Average greenpart density decreased from the top of the part ( $\rho = 2.87 \text{ g/cm}^3$ ) to the base ( $\rho = 2.73 \text{ g/cm}^3$ , Figure 40). Packing gradients such as this will not be visible through radiography where part geometry has symmetrical thickness changes normal to the plane of view, such as this part. The average density value for the whole part also confirmed the value previously taken from TGA.

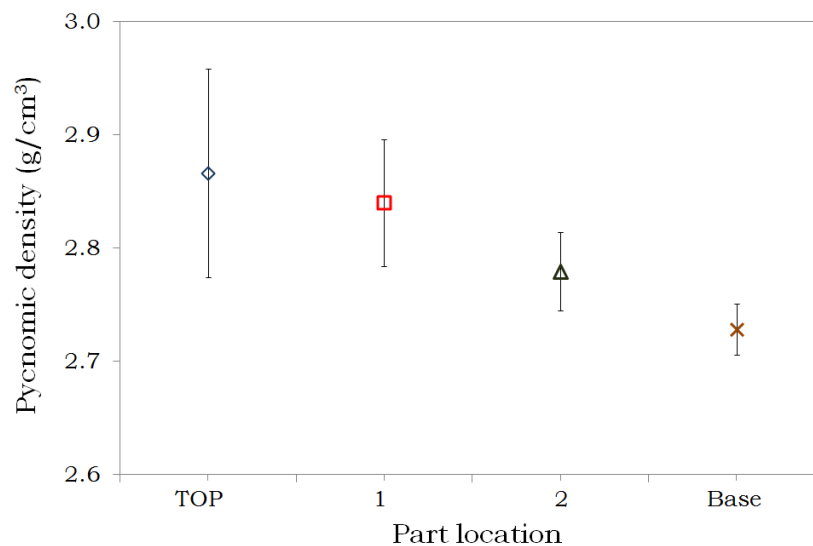


Figure 40: Average pycnomic density from top to base of greenpart.

Injection moulding involves a filling stage where the feedstock enters the cavity through the sprue and gate (Figure 41) at the preset injection speed. When the cavity is nearly filled a switchover to pressure control begins the packing stage. Pressure control compensates for shrinkage and ensures the cavity remains filled until freezing of the gate. The final cooling stage sees part pressure drop to ambient with no shrinkage possible once temperature also reaches ambient [177]. Although the cooling stage technically begun after the gate froze, the feedstock actually begun to cool once it left the heated nozzle ( $t = 155\text{ }^{\circ}\text{C}$ ) and entered the tool ( $t = 30\text{ }^{\circ}\text{C}$ ). This will account for the density gradient seen for the cup. The base of the cup cools sufficiently to resist the pressure of the packing stage and the top of the part underwent the greatest packing.

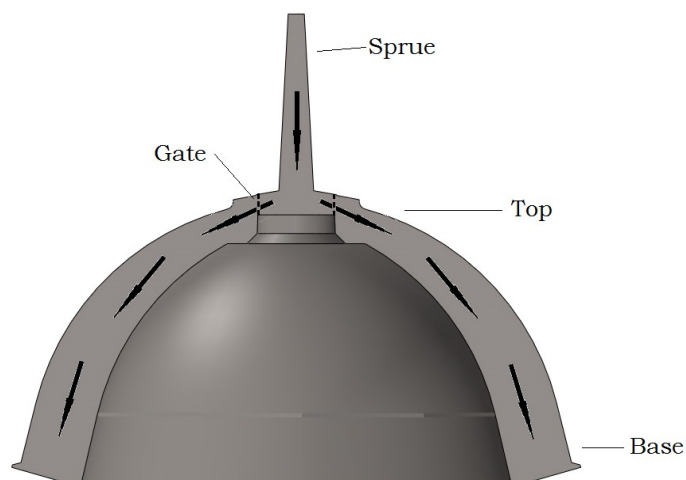


Figure 41: The general feedstock flow path into the mould cavity.

#### 4.2.4. Debinding

As for the previous chapter each debinding step targeted a specific component of the binder system. In this chapter SD targeted the wax (PW) and stearic acid (SA) while TD targeted the remaining components (PEG20, LLDPE, PP). The amount of binder removed

by SD was measured by weighing the parts after removal from the solvent ( $t = 24$  h) and drying ( $t = 60$  °C,  $t = 24$  h). The greyparts had lost 55 % ( $\sigma = 3.0$ ) of the total binder mass from a targeted 63 %. This was attributed to the debinding time, miscibility of components or PW & SA trapped by the non-soluble components [172]. After SD the greyparts showed flaking on the outer surface (Figure 42 b). Flaking is caused by separation during moulding as the low molecular weight binder segregates from the higher molecular weight polymer and powder in layers [36, 51, 60, 65, 74, 85, 86]. Handling strength of the parts after SD was good, however, some parts showed cracking (Figure 42 b) which was not apparent in the greenpart. These defects do not self repair during sintering as the distance between particles is too great.



Figure 42: FS5 cup part at different stages of processing, a) greenpart, b) greypart and c) after brownpart.

The TD removed 47 % ( $\sigma = 1.1$ ) of the binder from a targeted 37 % from a total time of 7 h above 250 °C. When combined with the SD value this was slightly more than the total amount of binder in the part (102 %) indicating loss of metal content. As a non-contact process, TD relied on thermal gradients (temperature and pressure) for extraction of the remaining binder as a volatile fraction. Powders could become dislodged during TD and flow out of the compact within a melt phase and conceivably with the sweep gas and decomposition products if the particles were fine enough. The

SD process relies on solvent contacting the greenpart which could erode the part surface also removing particles. The surface of the TD part (Figure 42 c) changed during TD, most noticeable was a fine carbonaceous layer and further definition that highlighted cracks. On closer inspection, it was observed that the compacts had no strength and were not easily handled. The TD temperature ( $t = 600\text{ }^{\circ}\text{C}$ ) was too low for pre-sintering ( $t > 700\text{ }^{\circ}\text{C}$ ) which would improve particle-particle bonding.

The average mass of the FS5 parts before and after each debinding step was measured (Table 15) and showed consistent mass loss, although the extreme fragility of the brownparts made weight measurement difficult.

Table 15: The average mass of greenparts, greyparts and brownparts, and the level of residual binder after processing.

| Mass g ( $\sigma$ ) |             |            |               |
|---------------------|-------------|------------|---------------|
| Greenpart           | Greypart    | Brownpart  | Residual      |
| 109.6 (0.4)         | 102.1 (0.8) | 95.5 (0.7) | - 0.2 % (0.4) |

An investigation of debinding was also done using small pieces cut from a greenpart ( $m_{ave.} = 2.2\text{ g}$ ). Complete binder removal was achieved from all pieces using SD followed by TD. Minimum duration SD ( $t = 3\text{ h}$ ) removed 66 % of the binder, however further increase of duration ( $t = (6, 9)\text{ h}$ ) only increased binder loss to 69 %. SD removed on average 68 % of the binder from the pieces, from a total of 75 % PW and PEG in the binder. From mass calculations TD removed the remaining binder, in agreement with the results for the full greenpart. This compared well to 64 % binder removed by SD and 99 % total binder removal from similar work where rectangular specimens ( $d \times w \times l = 6.38\text{ mm} \times 6.38\text{ mm} \times 48\text{ mm}$ ) and standard tensile bars were processed [62, 63].

Examination of the cross section and surface of the pieces showed progressive change as the binder was removed and particles become more distinguishable (Figure 43 a, b). SD of 6 h and 9 h (Figure 43 c, d) showed little difference from the 3 h treatment. This was expected as the difference in binder loss across all treatments was only 3 %.

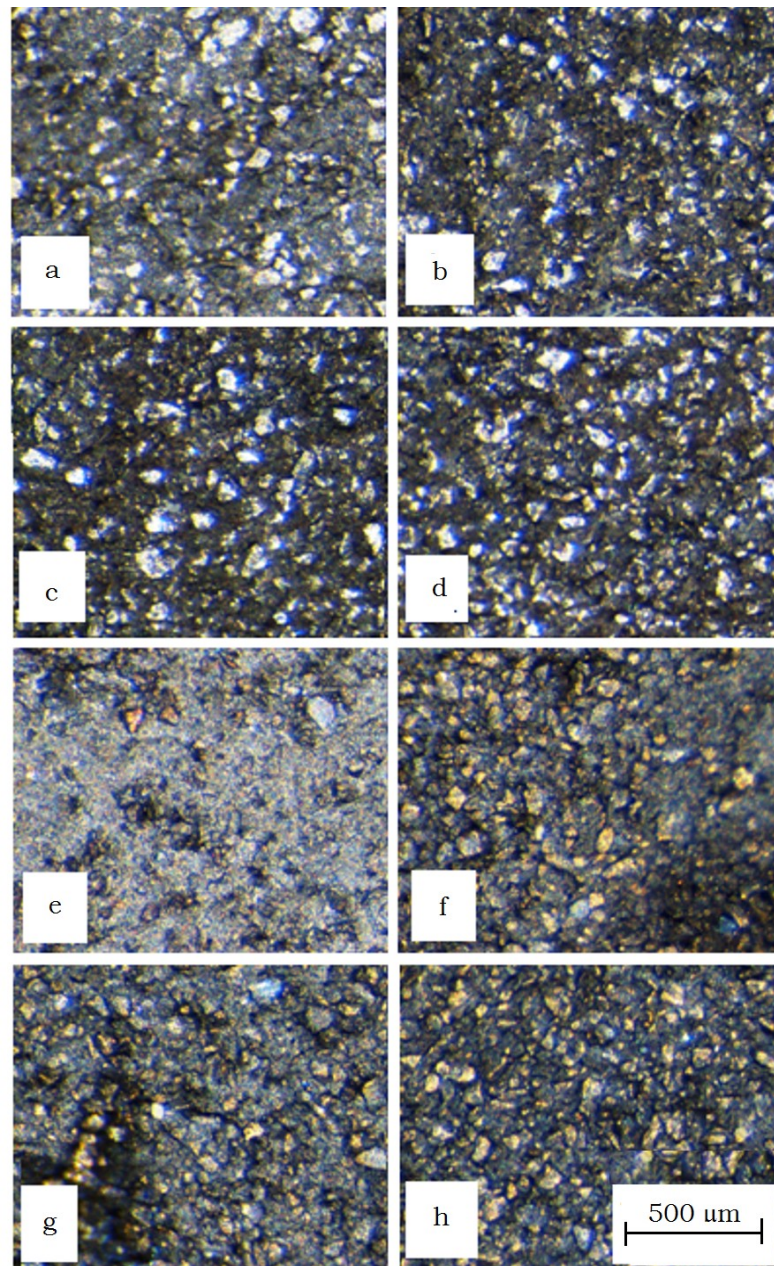


Figure 43: The greenpart a), SD b) 3 h, c) 6 h, d) 9 h, TD only e) and combined f) 3 h SD - TD, g) 6 h SD - TD and h) 9 h SD - TD.

Sample pieces subjected only to TD treatment (Figure 43 e, Figure 44 b) appeared no different from the green pieces (Figure 43 a). The particles still appeared embedded in binder which may confirm that the PEG improved interaction within the feedstock. This can be attributed to dispersion forces acting to maintain bonds between the binder and the particles. Pieces subjected to both SD and TD were noticeably different with clearly defined particles and distinct channel formation about the particles (Figure 44 a).

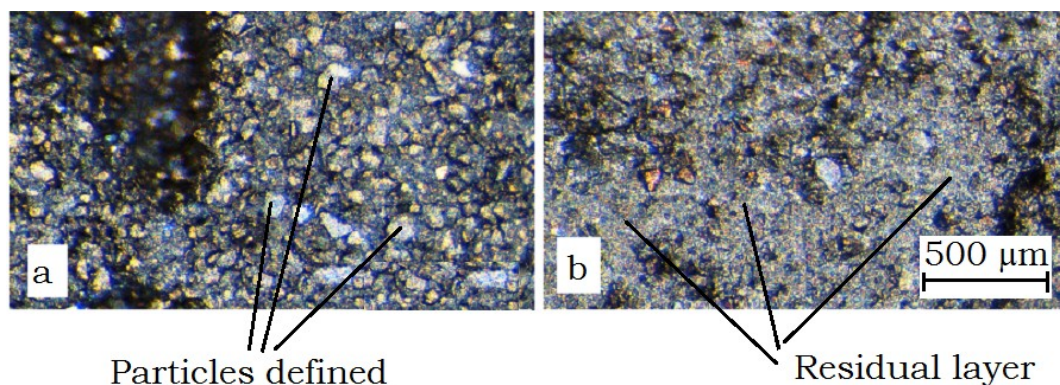


Figure 44: Part surface after (a) solvent and thermal debind and (b) thermal debind only with residual layer.

During TD the sweep gas constantly purged the kettle of the volatile binder gases (from waxes and polymers). If the volatile gases contact cooler surfaces before leaving the kettle they may condense [178]. Such condensed phases have been known to re-activate in later processing leading to carburisation at higher temperatures or during sintering [111, 179]. This may be due to the sweep gas flow rate being too low to remove decomposition products before they condense on the part surfaces and may account for the residual layer seen for TD only. Literature does tend to support the use of solvent debinding in conjunction with thermal debinding above thermal debinding alone, although it is reportedly sufficient for some commercial binder systems [180, 181].

As previously discussed, elements with molecules smaller than titanium (C, H, N, O) may diffuse interstitially. Therefore, where impurities are identified by visual examination, i.e. surfaces blackened from carbon or golden from nitrogen, parts will likely have levels in excess of those at which titanium will be useful. Eliminating contamination from binder decomposition products is especially important for reactive metals such as titanium [127]. It is, however, not until the brown part has become sintered that a true measure of the metal composition can be found.

#### 4.2.5. Sintering

The sintered parts had extensive radial and axial cracking (Figure 45). The radiograph of the part (Figure 45 c) also showed the extent and location of defects. Shibo et.al. [63] used the same sinter conditions to produce defect free Ti-6Al-4V test parts by MIM. This confirmed that particle shape, size and elemental composition had a great effect on the sinter result.

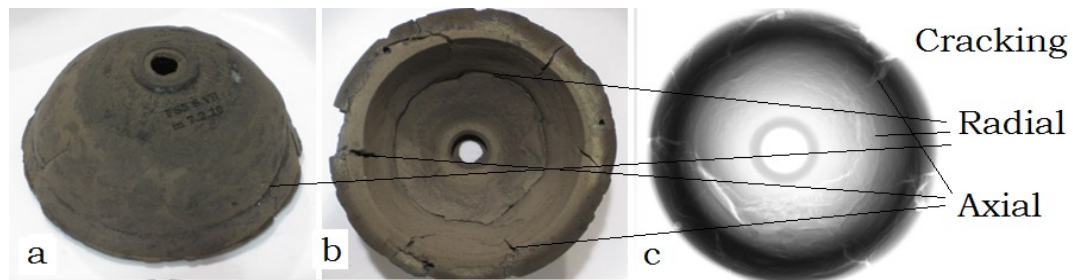


Figure 45: Images of the sintered part a) outside cup, b) inside cup and c) the radiograph showing through cup.

Radial cracks (Figure 45 a) form due to hoop stresses around the circumference of the part, while axial cracks (Figure 45 b) may be due to non-uniform shrinkage. The more likely cause of cracking is loss of the bonding strength between particles that formed by interaction with the binder during moulding that was lost through

TD. The brownpart handling strength was very low and indicated that any movement was going to be detrimental to the remaining particle bonds. Edge damage can be initiated during moulding due to separation and during removal from the mould as a result of the weakness of thin sections. Limitations of particulate size and shape have also been shown to hinder formation of fine edges.

Cracking around particle boundaries and porosity was evident through SEM (Figure 46 a). On closer inspection of the compact, (Figure 46 b) only partial coalescence was observed. The fracture surface (Figure 46 b) showed separation had occurred along particle boundaries, an indication that sinter conditions were not optimum for the brownparts. Particle distribution was uniform with some voids possibly due to thermal relaxation and coalescing.

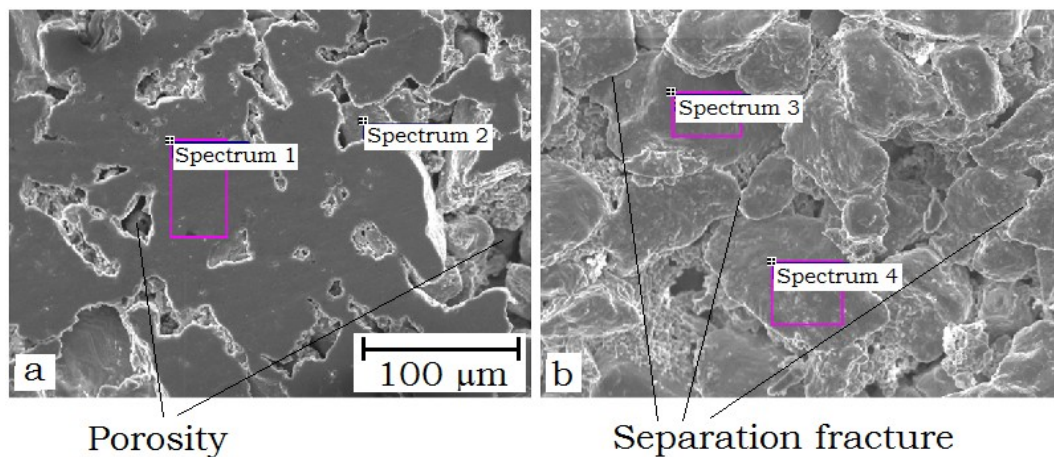


Figure 46: SEM image of the sintered outer surface, a) polished to show coalescence and b) the fracture surface.

From the EDS analysis it was seen that the metal composition was not uniform (Figure 46, Table 16). Although the bulk metal (Spectrum 1, 3) showed negligible carbon content other element levels exceeded the ASTM standard values (Table 17). The cavities (Spectrum 2) and some particle surfaces (Spectrum 4) showed high levels of carbon, a direct result of binder residue combustion and carbide formation.

Table 16: Elemental levels ( $w_E$  (%)) by EDS.

|            | C           | Al          | Ti    | V           |
|------------|-------------|-------------|-------|-------------|
| Spectrum 1 | $\approx 0$ | 7.24        | 88.77 | 3.98        |
| Spectrum 2 | 14.43       | $\approx 0$ | 85.57 | $\approx 0$ |
| Spectrum 3 | $\approx 0$ | 3.28        | 92.90 | 3.82        |
| Spectrum 4 | 5.39        | 5.37        | 85.37 | 3.88        |

Table 17: Standard composition, manufacturer specification and elemental levels by LECO analysis.

| $w_E$ (%)       |             | C    | H     | N    | O          |
|-----------------|-------------|------|-------|------|------------|
| ASTM B348 [173] | Standard    | 0.08 | 0.015 | 0.05 | 0.2        |
| Manufacturer    | As received | 0.02 | 0.039 | 0.18 | 0.5        |
| LECO            | FS5         | N/A  | 0.028 | 0.12 | $\geq 1.0$ |

The density of the sintered cups as measured using the Archimedes principle was low and averaged only 71 % of the theoretical sintered value. Optical images (Figure 47 a) showed the internal porosity in the sintered samples. Despite the open porous structure, the part was still very strong and handling did not damage the parts. Porosity and contamination within the particles (Figure 47 b) was consistent with the SEM images and excess carbon identified from the EDS analysis. Both carbon which forms carbides and oxygen which forms oxides restricts diffusion of the titanium and so hindering particle coalescence.

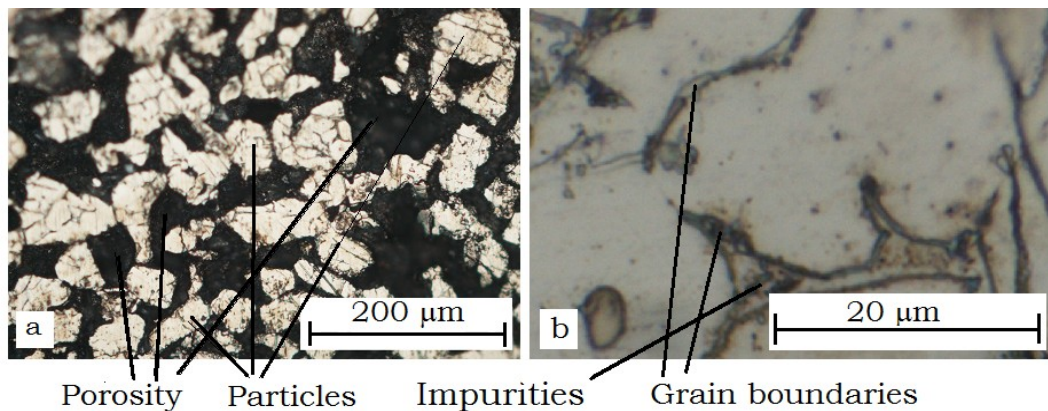


Figure 47: Part etched with Kroll reagent showing a) equiaxed alpha grain structure and b) grain boundaries and impurities.

The outside surface showed less porosity than the centre of the sintered sample (Figure 46 a, Figure 47 a) with the overall level of porosity evidence of poor consolidation. This can be attributed to less contamination of the part surfaces and may indicate a residual gradient that increased to a maximum at some point within the cross section. The cleaner outer surface would coalesce more readily with less carbide/oxide formation at the particle boundaries. The sintered part (Table 16) did show good metal composition although a high level of carbon was detected about the particles. There was an indication of variable levels of aluminium

with the high carbon levels attributed to a combination of residual binder levels and ineffective furnace conditions.

### **4.3. Conclusions**

The use of a wax based binder with its high volume content and low melt temperature had a negative effect on the greenpart strength. Thermal analysis of the feedstock using DTA showed that the low MW components that accounted for over 75 % of the binder volume had the greatest effect on feedstock melt temperature.

Radiography was suitable for identifying the cracks and separation in the greenpart but could not discern density distribution. This was done using a mapping technique which identified a density gradient decreasing from the top of the part to the base and was attributed to feedstock cooling during the filling and packing stages of moulding. Deficiencies within the feedstock such as low powder wetting and binder segregation were also factors.

In agreement with the previous binder, using solvent debinding followed by thermal debinding reduced the residual binder level compared to thermal debinding only. There was also a strong correlation seen between low handling strength within the greenpart and low density and cracking of the part after sintering.

## **Chapter Five: Feedstock formulation**

Chapters (Three & Four) discussed the behaviour of known binder components when mixed with titanium alloy powder. The results confirmed low powder loading produced weak parts susceptible to deformation. High powder loading may prove difficult to mould and produce defects due to inconsistent flow. Weak greenparts resulted from the main binder component having low strength. It was seen that low sintered part density with high porosity occurred due to particles in the brownpart not having the required proximity for coalescence during sintering. It also corresponded to low greenpart strength from moulding and particle disruption during debinding.

To address these deficiencies new feedstock formulations were proposed and an empirical selection process was used to determine the optimum formulation for processability. Particle dispersion, moulding uniformity and greenpart strength was also monitored.

As stated in the literature, diffusion of elemental residues occurs rapidly in titanium powders above 400 °C and even temperatures as low as 260 °C [31, 32, 127]. While such contamination has shown to be controllable using controlled atmosphere it is extremely difficult and it was proposed in this work to use a temperature below the lower diffusion limit ( $t = 260$  °C). The purpose of the low temperature thermal debinding was to remove the majority of binder before subjecting the parts to higher temperatures. This will have the added benefit of reducing disruption to the particle arrangement due to the higher expansion rates of the targeted binder components [109]. It was also proposed that increasing the range of molecular weights of the three main

functional binder components (PEG, polymer and wax) would support the efficacy of low temperature thermal debinding.

## **5.1 Experimental**

### **5.1.1 Materials**

Materials previously specified:

- Linear low density polyethylene (LLDPE) and Polypropylene (PP).
- Polyethylene glycol 8000 (PEG8) and Polyethylene glycol 20000 (PEG20).
- Carnauba wax (CW).
- Ti - 6Al - 4V powder (Ti64, 200 mesh).

Materials introduced in this chapter:

- White beeswax (BW) with a melting point of 60 °C and a density of 0.97 g /cm<sup>3</sup> that was supplied by Go Native New Zealand.

### **5.1.2 Equipment**

Equipment previously introduced:

The batch mixer was used for feedstock mixing (BM1). The TSE16 twin screw extruder was used for capillary extrusion and to produce the feedstock pellets. Moulding of the samples was done with the Dr Boy 50T2 injection moulder and the acetabular cup mould. Solvent debinding (SD) was done using the SD2 debinding kit ( $V = 21$  L). Differential thermal analysis (DTA) and thermal gravimetric analysis (TGA) was done using the SDT2960. Oxygen, hydrogen and nitrogen levels were measured using the inert gas fusion-infrared absorbance method (LECO TCH600). Microstructural analysis was done using the Hitachi SEM as well

as Olympus BX60 and Wild M3B optical microscopes. The Quantachrome Ultra-pycnometer 1000 was used for density measurement. The Philips G200/S instrument was used for through sample radiographic inspection (Courtesy SGS Ltd. Hamilton).

The equipment introduced in this chapter:

An extrusion capillary set designed and made by the author to enable comparative measurement of feedstock flow variations (Figure 48, Table 18). The round capillaries were adapted to connect to the TSE16 extruder and heated lengthwise.

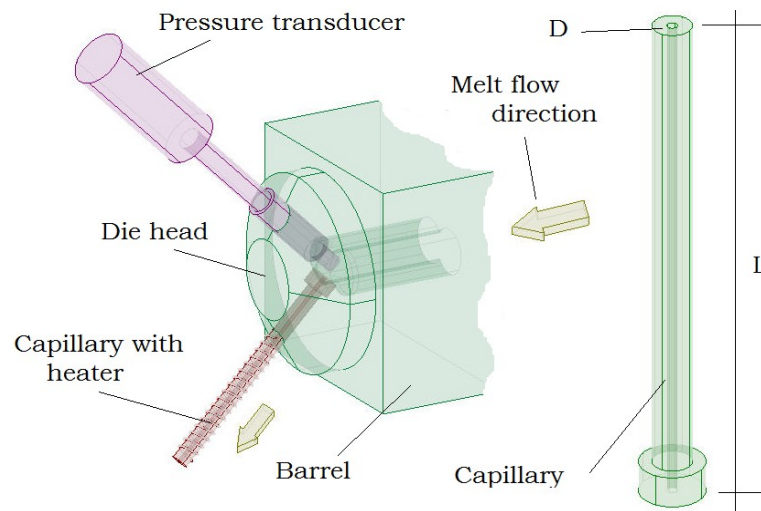


Figure 48: Extrusion capillary set up showing melt flow direction.

Table 18: Dimensions and process parameters of the capillary set.

| Capillary | Dimensions |        |     | Extrusion parameters |        |
|-----------|------------|--------|-----|----------------------|--------|
|           | D (mm)     | L (mm) | L/D | $\Omega$ (r/min)     | T (°C) |
| A         | 3.2        | 96     | 30  | 100                  | 120    |
| B         | 1.6        | 80     | 50  |                      |        |
| C         | 1.6        | 160    | 100 |                      |        |

Further testing was done using the Shimadzu CFT-500D flowtester capillary rheometer (Figure 49) with version 3.02 of the Shimadzu CFT application software [182]. The unit had electrical heating ( $t = (30 \text{ to } 400) \text{ }^\circ\text{C}$ ), with pressure control ( $p = (0.49 \text{ to } 49.03) \text{ MPa}$ ) and a wide viscosity measurement range ( $\eta = (8 \times 10^{-1} \text{ to } 1 \times 10^6) \text{ Pa}\cdot\text{s}$ ).

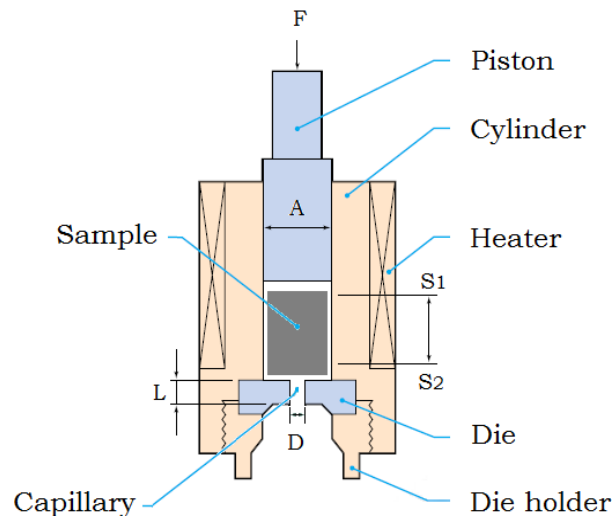


Figure 49: Capillary rheometer tester construction schematic [182].

Thermal debinding (TD) was done using a Contherm 2000 series electronically controlled mechanical convection oven (TD2). It had a 200 L capacity, variable temperature control ( $t = (25 \text{ to } 300) \text{ } ^\circ\text{C}$ ) and was coupled to compressed argon and air for atmosphere control (Figure 50).

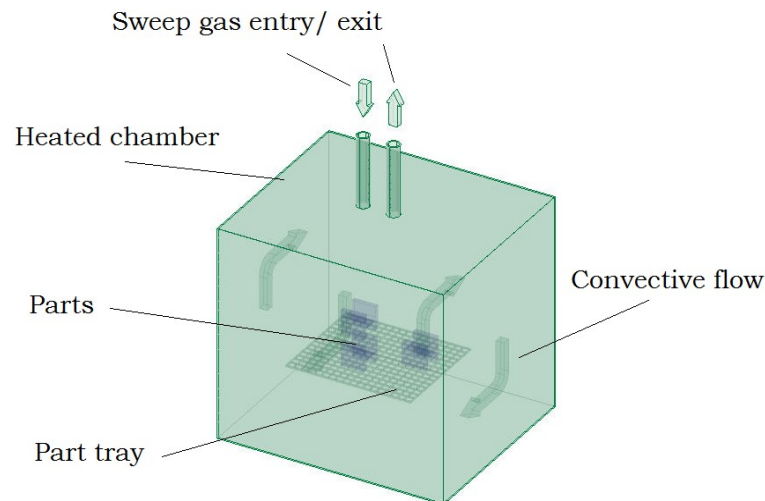


Figure 50: Modified convection oven used for low temperature thermal debinding with the aid of a sweep gas.

Sintering was done using an ACME high temperature vacuum sinter furnace (Model ZSJ-35/35/70). It was fully programmable with a de-wax system and controlled argon atmosphere ( $V = 85 \text{ l}$ ,  $p = 2 \times 10^{-3} \text{ mbar}$ ,  $t = (25 \text{ to } 1600) \text{ } ^\circ\text{C}$ ).

The ZEISS (EVOMA25) scanning electron microscope (SEM) with SmartSEM software and X-ray diffraction spectrometry (EDS) capability was used to enable microstructural analyses. With a working distance of 6 mm, a motorized 5 axis stage and an acceleration Voltage ( $V = (0.2 \text{ to } 30) \text{ kV}$ ) that allowed a wide magnification range ( $m = (5 \text{ to } 1,000,000)$ ).

Elemental analysis was done using the Panalytical Empyrean series 2 XRD instrument (XRD). It was equipped with the Hyscope

software for peak determination using the standard metal materials data base.

Mass and density were measured using a A&D electronic balance (EJ-410) with serial interface and automatic density determination. It had a 410 g capacity and 0.01g resolution. Specific gravity was automatically calculated from comparison of the sample weight in air to that of the sample immersed in liquid.

### 5.1.3 Methodology

Six binders were formulated using the component ratios shown in Table 19. The intention was to reduce polymer content and minimise the later formation of residues with high thermal resistance, while maintaining the integrity of the greenpart.

Table 19: Binder formulation chart for volume ratio of components.

| FS | Wax |    | Water-soluble |      | Polymer |    |
|----|-----|----|---------------|------|---------|----|
|    | CW  | BW | PEG20         | PEG8 | LLDPE   | PP |
| 1  | 1   | 1  | 1             | 1    | 1       | 1  |
| 2  | 1   | 1  | 2             | 2    | 1       | 1  |
| 3  | 2   | 2  | 1             | 1    | 1       | 1  |
| 4  | 2   | 2  | 2             | 2    | 1       | 1  |
| 5  | 3   | 3  | 2             | 2    | 1       | 1  |
| 6  | 2   | 2  | 3             | 3    | 1       | 1  |

The BW, CW, LLDPE, PEG8, PEG20 and PP were analysed individually, using DTA and TGA and the resulting data used to determine appropriate mixing conditions.

The binder components for each formulation were weighed into a plastic bag along with the Ti64 powder ( $\phi_P = 0.6$ ) and hand mixed ( $t = 2$  min). Compounding was done in the batch mixer (BM1) using high shear roller blades ( $V = 76$  cm<sup>3</sup>). The mixer was preheated ( $t = 120$  °C) and batched components slowly added to the mixing chamber ( $\omega = 50$  r/min). The temperature was increased to 170 °C

for 10 min to ensure all components had melted but remained below the degradation point of wax and PEG. Heating was then shut off and the mixer ran until the temperature was below 60 °C (melt temp for BW). The compounded formulations were granulated into a consistent size feedstock.

The torque and time data was recorded and tabled in line with Figure 20. The shear rate at the rotor was determined ( $\dot{\gamma} = 94.5 \text{ s}^{-1}$ ) using the following equation and compared during analysis:

$$\dot{\gamma} = \frac{\pi \times d}{60 \times h} \times \omega \quad (13)$$

$\dot{\gamma}$  = shear rate ( $\text{s}^{-1}$ ),  $d$  = rotor diameter (37.9 mm),  $h$  = distance between rotor and wall (1.05 mm),  $\omega$  = speed of rotor (50 r/min).

Measurement of the processability was made using the extrusion capillaries (A to C) and process parameters given in Table 18. Each feedstock was extruded and the extrudate was collected at one minute intervals and weighed. During extrusion the monitored processing variables were: screw load torque ( $T$ ), capillary entry pressure ( $p$ ) and extrudate mass flow rate ( $\dot{m}$ ). The shear rate at the wall for the extrusion capillaries was determined as:

$$\dot{\gamma}_a = \frac{32 \times Q}{\pi \times D} \quad (14)$$

$Q$  = volumetric flow ( $\text{mm}^3/\text{s}$ ),  $D$  = diameter of capillary (mm).

Comparison of the processing variables was made for each feedstock by plotting the work done on the screw (WD), the mechanical energy transfer (SME) and the apparent viscosity ( $\eta_a$ ), with respect to each capillary. The values were calculated using the respective formulae with relation to the L/D ratio of the capillaries, the shear stress and shear rate [183, 184]:

$$WD = 2 \times \pi \times N \times T \quad (15)$$

Workdone (WD) J/s, Screw speed ( $N$ ) r/s, Screw torque (T) Nm

$$SME = \frac{P_{motor}}{T_{max} \times N_{max}} \times \frac{T \times N}{\dot{m}} \quad (16)$$

$P_{motor} = 1250$  W,  $T_{max} = 24$  Nm,  $N_{max} = 1.67$  r/s

$$\eta_a = \frac{\tau_a}{\dot{\gamma}_a} \quad (17)$$

With:

$$\tau_a = \frac{p \times D}{4 \times L} \quad (18)$$

And:

$$\dot{\gamma}_a = \frac{32 \times Q}{\pi \times D} \quad (19)$$

Apparent viscosity ( $\eta_a$  (Pa.s)), apparent shear stress ( $\tau_a$  (Pa)), apparent shear rate ( $\dot{\gamma}_a$  (s<sup>-1</sup>)) and  $Q$  = volumetric flow (mm<sup>3</sup>/s).

Testing using the Shimadzu capillary rheometer compared the feedstock at different shear rate and shear stress. The feedstock ( $m = (2 \text{ to } 3) \text{ g}$ ) was loaded into the capillary cylinder for preheating ( $t = 170 \text{ }^\circ\text{C}$ ,  $t = 180 \text{ s}$ ) and extruded using the capillary dimensions and process loads in Table 20. The resulting data was collected with the Shimadzu CFT application software and viscosity corrections made using the Bagley plot method. Account for capillary entry and exit effects (or boundary effects) were made using multiple die configurations. The resulting data was used to produce master flow curves.

Table 20: Capillary rheometer load and die parameters.

| Capillary |        | Load F (N) |     |     |     |     |
|-----------|--------|------------|-----|-----|-----|-----|
| D (mm)    | L (mm) | 55         | 105 | 205 | 305 | 405 |
| 1.0       | 1.0    | *          | ✓   | ✓   | ✓   | ✓   |
|           | 2.0    |            |     |     |     |     |
|           | 10.0   |            |     |     |     |     |
| 2.0       | 2.0    | ✓          | ✓   | *   | ✓   | ✓   |
|           | 5.0    | *          |     |     |     |     |
| 3.0       | 3.0    | *          | *   |     |     |     |

The selected binder feedstock formulation was batched, blended, mixed and extruded to form a uniform strand ( $m = 1500 \text{ g}$ ). The strand was broken into regular feedstock pellets and the fines were discarded. Thermal analysis using DTA and TGA was done as well as isothermal analysis to investigate the proposed low temperature thermal debinding conditions ( $t = 250 \text{ }^\circ\text{C}$ ).

Full acetabular cups were moulded and the greenparts were weighed and visually inspected. Comparison of theoretical and actual density values showed the level of component compatibility.

Debinding the greenparts was done in two steps. Solvent debinding in water ( $t = 50\text{ }^{\circ}\text{C}$ ,  $t = (0\text{ to }600)\text{ h}$ ) produced the greyparts. They were removed from the water at specified time intervals for drying ( $t = 50\text{ }^{\circ}\text{C}$ ,  $t = 24\text{ h}$ ) and weighed to determine binder mass loss.

Thermal debinding produced brownparts. The process involved three temperature increases ( $\beta = 1\text{ }^{\circ}\text{C}/\text{min}$ ) followed by three isothermals (Figure 51). The isothermals allowed for controlled removal of moisture, expansion of waxes ( $t = 100\text{ }^{\circ}\text{C}$ ,  $t = 1\text{ h}$ ) and expansion of polymers ( $t = 175\text{ }^{\circ}\text{C}$ ,  $t = 1\text{ h}$ ). The final isothermal ( $t = 250\text{ }^{\circ}\text{C}$ ,  $t = 100\text{ h}$ ) was to remove remaining binder before combustion. Part weights were recorded throughout the final isothermal period ( $t = (0, 4, 8, 16, 32, 64, 100)\text{ h}$ ) to determine the point at which mass change was no longer seen.

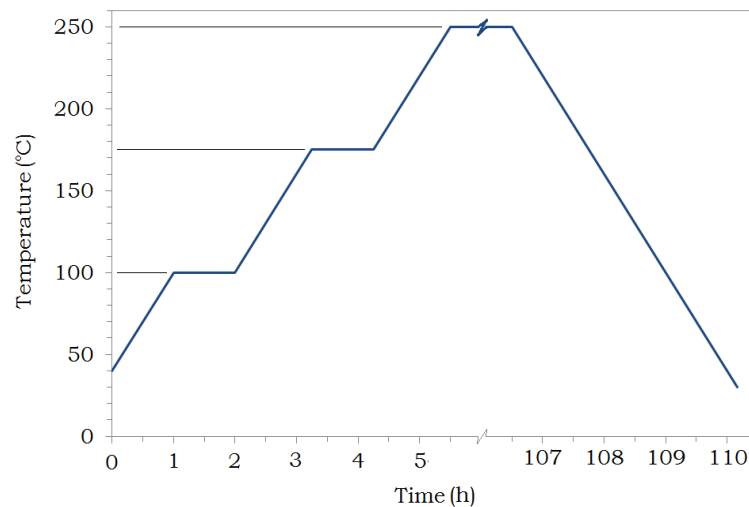


Figure 51: Thermal debinding temperature time profile.

Sintering of the brownparts was done in the ACME vacuum furnace. The brownparts were heated ( $\beta = 5\text{ }^{\circ}\text{C}/\text{min}$ ) with an isothermal period ( $t = 60\text{ min}$ ) at  $470\text{ }^{\circ}\text{C}$  followed by further heating to  $800\text{ }^{\circ}\text{C}$ , all under argon sweep gas ( $\dot{V} = 10.0\text{ L}/\text{min}$ ). This was followed by further heating at  $5\text{ }^{\circ}\text{C}/\text{min}$  and a final isothermal

period ( $t = 180$  min) under vacuum ( $t = 1350$  °C,  $p = 2.0 \times 10^{-3}$  mbar). Cooling was over three hours as a function of the temperature gradient between the sintered parts, the furnace chamber and the furnace cooling system. As a result the cooling rate slowed as the temperature in the furnace reduced ( $\beta = (15$  to  $3)$  °C/min).

The overall effect of moulding, debinding and sintering on defect formation and metal composition was assessed. The sintered cups were inspected on the outer and inner surfaces as well as through the parts. The cups were sectioned and parts analysed using the SEM ( $V = 20$  kV,  $m = (50, 250, 800)$ ) with EDS to determine local surface chemistry and carbon levels.

Through part sample examination was done using X-ray radiographic inspection ( $E = (80$  to  $150)$  kV,  $t = (5$  to  $30)$  s).

Sectioned parts were further analysed using the optical light microscope. An etching reagent (Kroll) exposed the microstructure of cut and polished samples. The samples were submersed for ( $t = 1$  min) in Kroll's reagent (100 mL distilled water, 2 mL HF, 4 mL HNO<sub>3</sub>) before rinsing in distilled water.

Sectioned and polished parts were analysed by XRD with power settings 45 kV at 40 mA through a copper electrode. Scanning from position (20 to 100) °2 $\theta$ , using a step size of 0.026 °2 $\theta$ , scan step time of 17.340 s in continuous scanning mode. Peak identification was done using the Highscope software.

Oxygen, hydrogen and nitrogen levels were checked using the inert gas fusion-infrared absorbance method (LECO TCH600, 3.1.2).

## **5.2 Results and discussion**

The functionality of the three main binder components previously introduced (PEG, polymer and wax) was enhanced by increasing the range of molecular weights of each in the binder formulation. During debinding the activation energy required for dissolution and thermal removal should lower and aid targeted component removal. PEG8 and PEG20 had solubilities of (700, 500) g/L respectively, therefore the PEG8 would theoretically be completely removed prior to the PEG20 during solvent debinding. The wax components (BW, CW) with melt temperatures of (60, 83) °C respectively will also present a flow differential during thermal debinding. The BW will become liquid and be removed ahead of the CW during thermal debinding. Similarly the polymers LLDPE and PP have a differential with respect to melt temperature and residue decomposition.

### **5.2.1 The binder components**

Each binder component was not only selected for a specific role in the feedstock but also with environmental and safety aspects in mind. PEG should reduce overall viscosity of the feedstock, improve particle wetting and aid shape retention after moulding. Being water soluble PEG will also eliminate the need for toxic solvents when debinding. Some water soluble binders may lead to adverse chemical reactions during processing with metals however, titanium has been shown to be inert [137].

The waxes aid dispersion, lubricate and improve feedstock flow during moulding. Naturally occurring waxes are safe to handle and the products of decomposition are safer for the environment than petroleum based materials [15, 60, 99, 185]. The low melt temperatures of waxes also aid in their removal during thermal debinding, which was especially important for the proposed low temperature thermal debinding. It is also important that the

binders decompose without leaving a residue before final sintering to eliminate contamination [18, 139, 141, 186].

The polymer provides strength to the greenpart and is the final binder component to be removed from the part prior to full sintering of the titanium brownpart.

From SDT analysis the endothermic peaks were used to determine the minimum mixing temperature of the binder. The TGA decomposition onset values correspond to maximum mixing temperatures (Table 21). The endotherms gave the minimum mixing temperature of 168 °C. Considering weight loss of 5 % to indicate onset of degradation the upper temperature was set by the PEG8 component ( $t_d = 185$  °C).

Table 21: Binder thermal event values from SDT ( $\beta = 5$  °C/min).

|       | Endotherm (°C) | Exotherm (°C) |     | Weight loss (°C) |      |
|-------|----------------|---------------|-----|------------------|------|
|       |                | 1             | 2   | 5 %              | 20 % |
| PEG8  | 62             | 230           | N/A | 185              | 208  |
| PEG20 | 68             | 260           | N/A | 187              | 220  |
| BWW   | 63             | 230           | 340 | 228              | 268  |
| CW    | 83             | 290           | 330 | 265              | 285  |
| LLDPE | 105            | 270           | 350 | 295              | 375  |
| PP    | 168            | 290           | 320 | 260              | 278  |

Decomposition onset and decomposition rate are important for thermal debinding, as gradual binder removal is required. The broad range of melt and decomposition temperatures (Table 21) will minimise disruption of the particles in the compact during TD [15, 75]. Although thermal analysis was in air only, it should be noted that the atmosphere type and pressure also affects the onset of decomposition, decomposition rate and the ability to completely remove the binder [139].

### **5.2.2 Feedstock melt flow**

The upper critical powder fraction for irregular shaped particles ( $\phi_p = (0.63 \text{ to } 0.66)$ ) is the point at which binder will no longer fill the spaces about the particles. The optimum loading is considered (2 to 5) % lower than this with excess binder necessary to support flow, but will depend on particle size and particle size distribution [1, 75, 92]. Higher metal fraction is ideal but still requires particle encapsulation to reduce viscosity with sufficient slip between the particles, mould walls and machine surfaces.

The literature does not agree on use of the torque rheometer to produce viscosity data due to the irregular three dimensional flow created by the rotor geometries [187]. However by using the relationship between the torque on the rotors and the feedstock response evaluation of the processing behaviour was possible, as defined by Figure 20 from Chapter Three [188].

The six binder formulations (FS(1 to 6) Table 19) were blended with HDH Ti-6Al-4V powder ( $\phi_P = 0.6$ ) and mixed using the torque rheometer. As seen in (Figure 52) the formulations required longer mixing times to reach levelling of the torque curve than the feedstock from Chapter Three (Figure 28, Table 5). This indicated more complex interactions between the components as a result of the range of molecular weights of the binder components. The mixing times were the same for all formulations with differences only for the maximum torque reached at the start of mixing and the minimum torque when mixing was stopped.

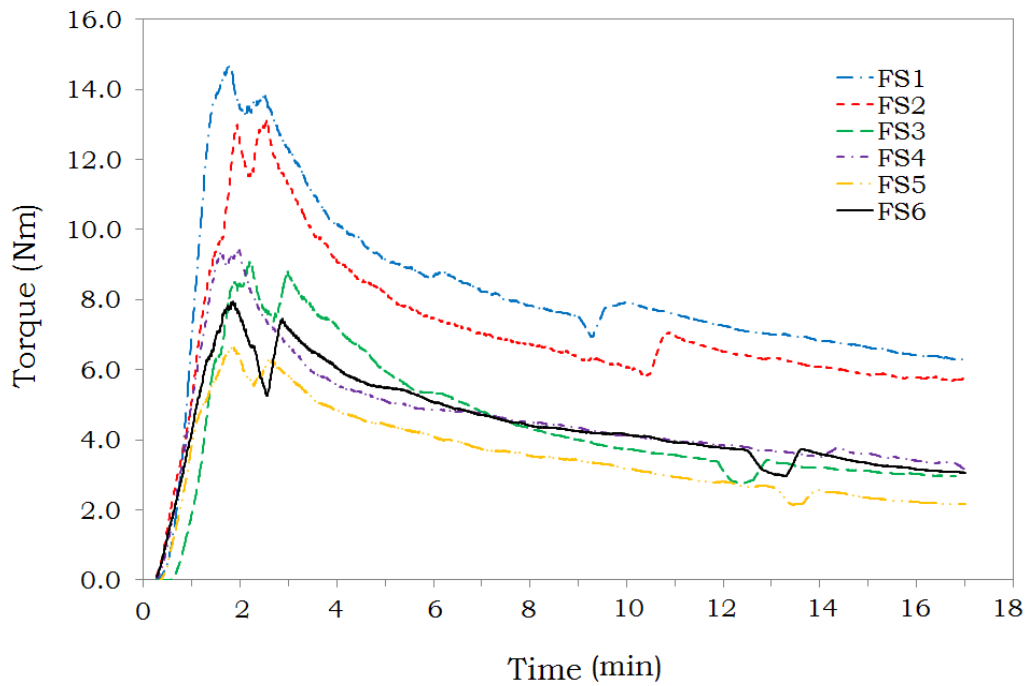


Figure 52: Mixing torque plots for the feedstock formulations

The feedstocks had the same Ti powder and the same powder loading as in Chapter Three but mixing duration (b) was longer by (2 to 4) times and a lower end torque (d) after mixing (Chp 3, Table 22). The feedstock with the lowest torque at end of mixing was FS5 then FS3 which both had the highest wax content ( $\phi_w = 50\%$ ).

Table 22: Mixing torque and compounding duration ( $\phi_P = 0.6$ ).

| FS    | Time (min) |      | Torque (Nm) |     |      |
|-------|------------|------|-------------|-----|------|
|       | a          | b    | c           | d   | max. |
| Chp 3 | 0.4        | 4.2  | 2.3         | 4.0 | 6.3  |
| 1     | 0.8        | 15.3 | 8.5         | 6.2 | 14.7 |
| 2     | 0.8        | 15.2 | 7.4         | 5.6 | 13.0 |
| 3     | 0.8        | 13.4 | 6.0         | 3.0 | 9.0  |
| 4     | 0.8        | 14.8 | 6.2         | 3.3 | 9.5  |
| 5     | 1.2        | 15.4 | 4.7         | 2.0 | 6.7  |
| 6     | 1.0        | 15.3 | 4.9         | 3.0 | 7.9  |

a) time to reach maximum torque (max.) relative to the steady state torque, b) time from peak torque to steady state, c) the change in torque during time b), and d) torque approaching steady state (Figure 24).

The mixing processes are well defined and readily related to theories of wetting, distribution, dispersion and homogenization [3, 50, 189], however with multi-component systems they overlap and the theories become difficult to apply [190]. The major influence on mixing rheology was the flow characteristics of the powder so by using the same powder and powder loading the effect of each binder was studied. The immiscible nature of the (Chp 3) binder system saw the predominant mechanism for mixing the feedstock to be distributive. The combination of heat and the shear forces of the mixing blades changed the binder components from their starting form of powders, granules and flakes, into increasingly smaller domains and redistributed them until uniformity was reached. The mixing mechanism for feedstock (1 to 6) began the same as (Chp 3), with wetting, distribution and homogenisation. Due to miscibility of similar components, when the domains were

sufficiently small dispersive forces and molecular diffusion occurred. The longer mixing times were attributed to diffusion, which is a slower process, due to the interaction of miscible molecular units and the osmotic pressures which are typically low. Dispersive mixing also ensured that non-uniform regions due to the binder components in their starting forms (particles, aggregates, agglomerates) within the bulk powder was minimised. The distributive forces are attributed to the insoluble titanium powders that were not subject to domain or phase changes.

The feedstocks (Table 18) were extruded through the capillaries with capillary pressure, screw torque and mass flow for a single pass presented (Table 23). Low pressure, low screw torque and high mass flow represented optimum moulding condition based on the energy required to process the feedstock into a suitable strand.

Table 23: Processing values from the extrusion capillary trials.

| FS | A           |              |                    | B           |              |                    | C           |              |                    |
|----|-------------|--------------|--------------------|-------------|--------------|--------------------|-------------|--------------|--------------------|
|    | $T$<br>(Nm) | $p$<br>(kPa) | $\dot{m}$<br>(g/s) | $T$<br>(Nm) | $p$<br>(kPa) | $\dot{m}$<br>(g/s) | $T$<br>(Nm) | $p$<br>(kPa) | $\dot{m}$<br>(g/s) |
| 1  | 6.00        | 700          | 0.10               | 8.64        | 2800         | 0.13               | 12.00       | 4900         | 0.11               |
| 2  | 5.76        | 700          | 0.22               | 7.20        | 2000         | 0.12               | 7.92        | 2300         | 0.09               |
| 3  | 5.52        | 900          | 0.21               | 6.72        | 1700         | 0.14               | 9.60        | 3200         | 0.21               |
| 4  | 6.48        | 600          | 0.17               | 6.00        | 1200         | 0.11               | 6.72        | 1200         | 0.10               |
| 5  | 5.76        | 600          | 0.16               | 5.76        | 1000         | 0.15               | 7.68        | 2000         | 0.16               |
| 6  | 5.52        | 500          | 0.18               | 6.00        | 1500         | 0.19               | 6.00        | 1400         | 0.09               |

$T$  = screw torque,  $p$  = capillary entry pressure,  $\dot{m}$  = mass flow.

The melt flow properties are not the only consideration; the feedstock must retain homogeneity of the binder and uniformity of particle distribution during moulding. Secondly, it must be formulated to enable gradual binder removal in subsequent debinding. The use of the capillary extrusion data allowed a comparative assessment of the melt flow characteristics. Varying the MW of the functional components of the binder allows a progressive and gradual binder removal based on the differences in melt temperature and weight loss values (Table 21) following solvent debinding.

Other criteria that required consideration included the form of the feedstock strand after extrusion. It is clear that liquids will have lower viscosity and flow more readily than a feedstock however, the ability to retain shape is critical. In a similar fashion to the wax based feedstock processed in Chapter Four, high wax content (FS5) had the lowest steady state mixing torque (Figure 52) but the extrudate strength was low and strand formation poor.

The extrudate data (Table 23) allowed comparisons to be made based on the influence of the different capillaries by three methods. The torsional work done by the screw in relation to the L/D ratio was mostly linear, but changing the component ratios affected the slope of the line (Eq (15), Figure 53). FS1 required more work to process while FS6 (higher PEG ratio) showed the lowest values in agreement with the ability of PEG to reduce the flow resistance within the feedstock.

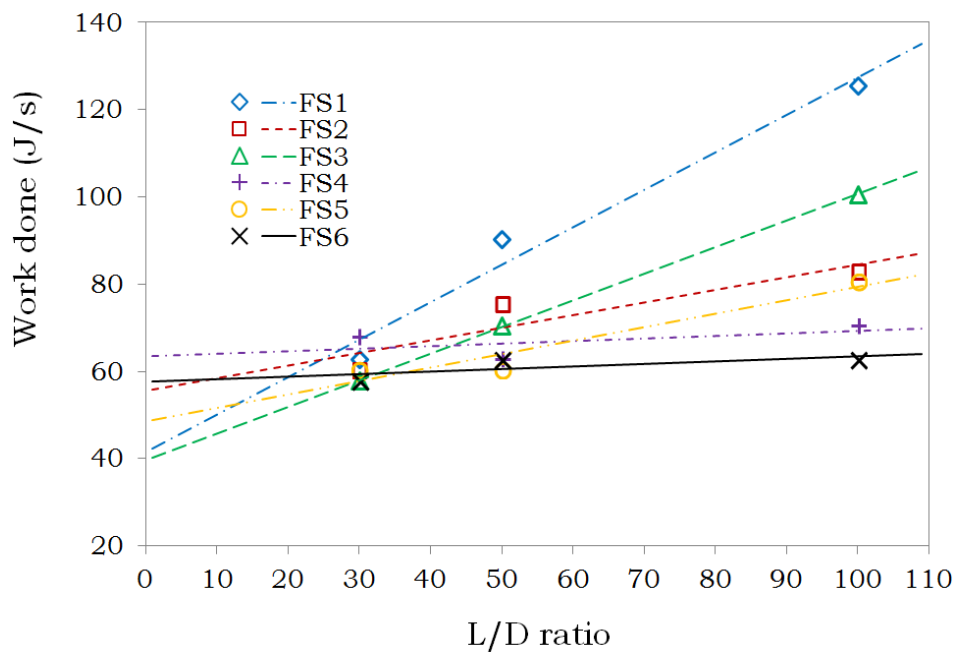


Figure 53: Workdone by the screw on the feedstock formulations.

To account for component interactions and mass flow rate of the feedstock during extrusion, the specific mechanical energy (SME) was determined (Eq (16)). SME describes the mechanical energy transferred to the feedstock during extrusion based on the ratio of the maximum output energy of the extruder to the energy input required to extrude the feedstock [191]. The SME values (Figure 54) with respect to the capillary L/D was based on data from Table 23.

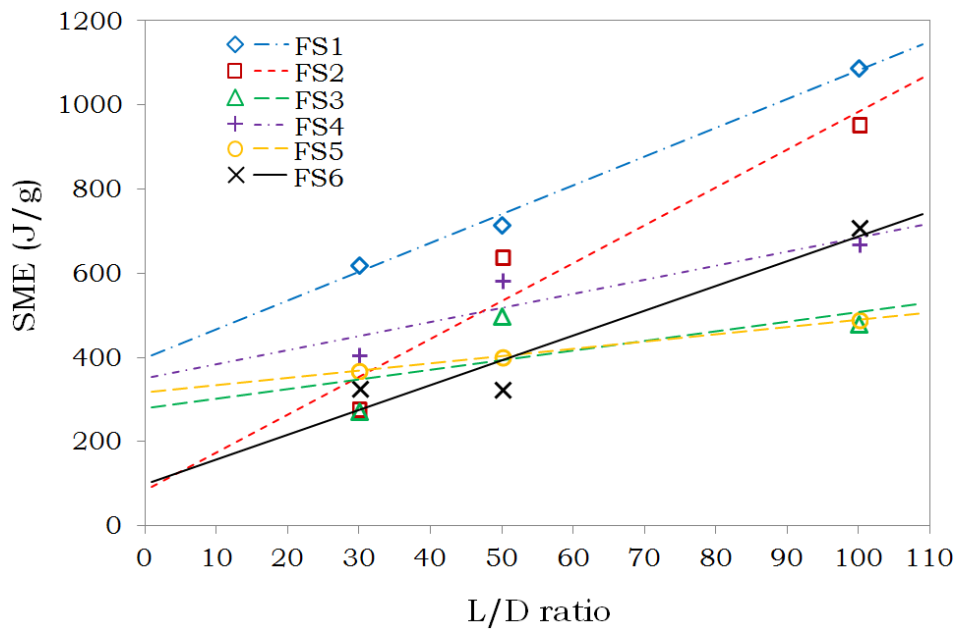


Figure 54: Specific mechanical energy plot for the feedstock with varying component ratios.

The SME plot provided similar results to the WD plot with the input energy trending down from FS(1 to 6). Lower SME was seen for FS6 in the (30, 50) L/D region while FS3 and FS5 were lower for the 100 L/D capillary. Both the SME and the work done correspond to flow resistance or apparent viscosity ( $\eta_a$  (Pa.s)) of the feedstock and showed that as the amount of PEG increased the energy to extrude reduced. This corresponds to an improvement in component interactions as PEG ensured the particles were well wetted thereby reducing the internal friction.

In order to ensure melt flow of the feedstocks was assessed in sufficient depth, account was taken of shear rate and subsequent shear stresses. The capillaries used were  $< 200$  L/D and so the results were not considered to be true shear stress and shear rate values. Therefore, only apparent values for shear stress and shear rate could be calculated with the viscosity values also apparent (Eq (17), Figure 55).

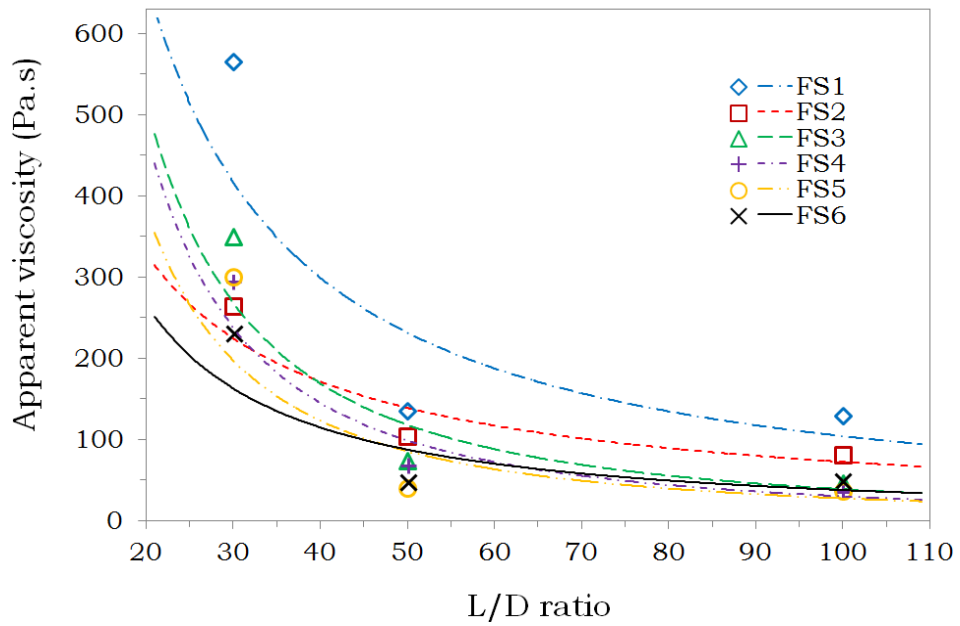


Figure 55: Viscosity relative to (L/D) ratio with power law trend.

The results were in agreement with literature showing the large diameter capillary having a higher viscosity because of a greater number of particle interactions. The approach taken here calculated the apparent shear rate for the three capillaries and used the values in place of the L/D values (Eq (19), Figure 56). Although there was no account for end effects, slip or temperature dependence the behaviour of the feedstock at the moulding temperature was considered critical. The results were similar to the WD and SME, FS1 showed the highest overall viscosity and FS6 the lowest. FS6 showed improved flow properties for this test compared to FS(2 to 5), due to the greater PEG content.

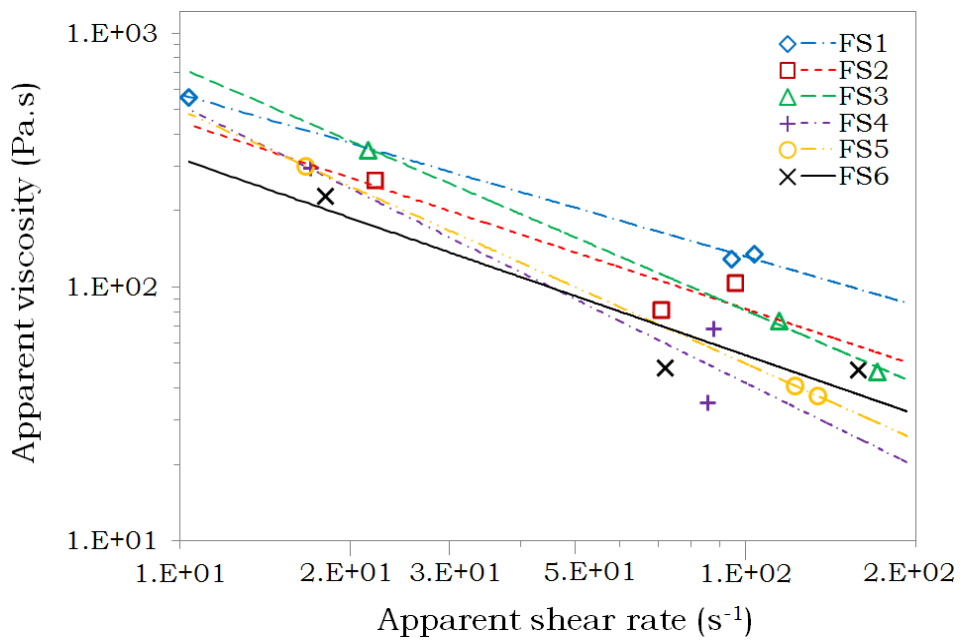


Figure 56: Raw viscosity data from extrusion capillary testing with no account for end effects or slip.

Capillary entrance and exit effects greatly affect viscosity data and master curves are considered the only way to characterise the flow properties [87]. Considering the injection moulding process has relatively short cross section to flow path ratios ( $\sim L/D$ ) (Figure 57), the applicability of this data was questioned. As seen for the cup part (Figure 57) the section changes from the point of injection through the sprue ( $A = (3.14 \text{ to } 14.56) \text{ mm}^2$ ,  $L \approx 22.0 \text{ mm}$ ), followed by a sprue to gate transition from ( $A = (14.56 \text{ to } 73.18) \text{ mm}^2$ ,  $L \approx 5.0 \text{ mm}$ ). This is followed by flow into the part body from the gate ( $A = (73.18 \text{ to } 1516.56) \text{ mm}^2$ ,  $L \approx 49.36 \text{ mm}$ ), and a final flow change from the maximum cross section to the end of the flow path ( $A = (1516.56 \text{ to } 0) \text{ mm}^2$ ,  $L \approx 2.61 \text{ mm}$ ).

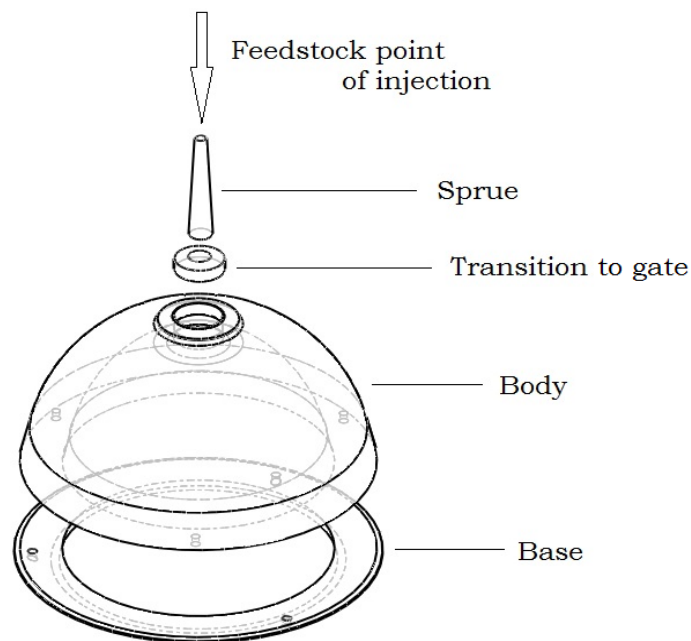


Figure 57: Greenpart model showing section changes.

To account for the greater range of shear rate and shear stress during moulding, the capillary rheometer was used. Each sample was weighed out and placed in the heated capillary barrel for pre-heating ( $t = 180 \text{ s}$ ) before the application of the load. Unlike the

screw extrusion capillary system, binder residue was seen on the plunger and die faces; also feedstock remained in the barrel after testing. This has also been attributed to low powder loading and was reduced by increasing the loading in the following chapter.

The data from the constant temperature testing gave the apparent viscosity and shear rate plots for all feedstocks (Figure 58). It was seen that all formulations showed shear-thinning behaviour over the given range of testing. FS6 showed the lowest zero shear rate viscosity and the highest shear rate sensitivity was for FS1. A distinct inversion point ( $\dot{\gamma}_a = 2000 \text{ s}^{-1}$ ) was seen due to the shear rate sensitivity at higher shear values.

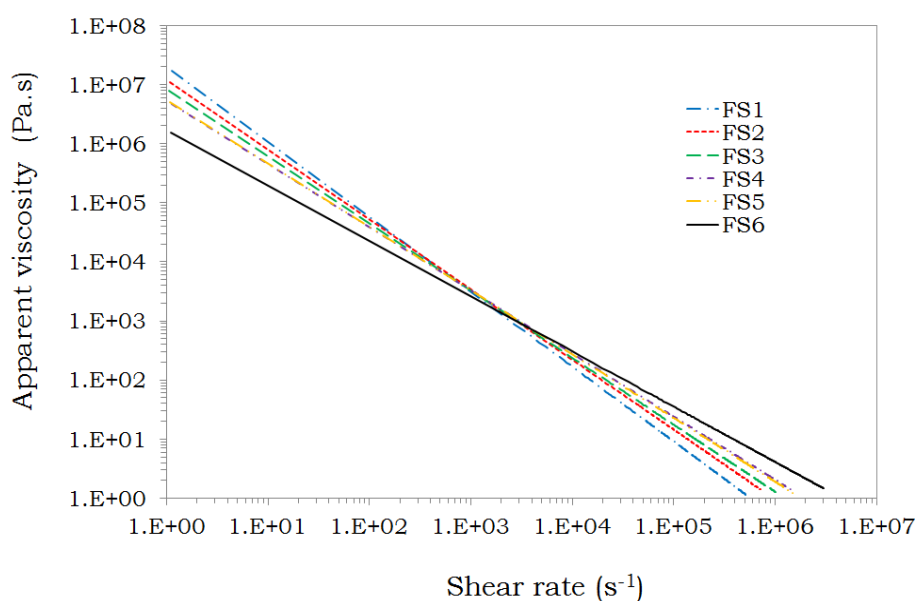


Figure 58: Raw viscosity data from capillary rheometer testing with no account for end effects or slip.

Correction for pressure losses (capillary end effects) and slip at the wall was made using the Shimadzu CFT software based on the test results with the different capillaries and extrusion pressures. The corrected values gave the true viscosity shear rate curves (Figure 59) with the trend lines extrapolated based on the power law. The

data point spread for the individual tests showed instabilities in testing as a result of the segregation during pre-heating and the inconsistencies shown to occur with irregular powders. FS2 showed the best fit of data with FS3 having the greatest shear rate sensitivity. FS5 and FS6 were similar and had the lowest zero shear viscosity values.

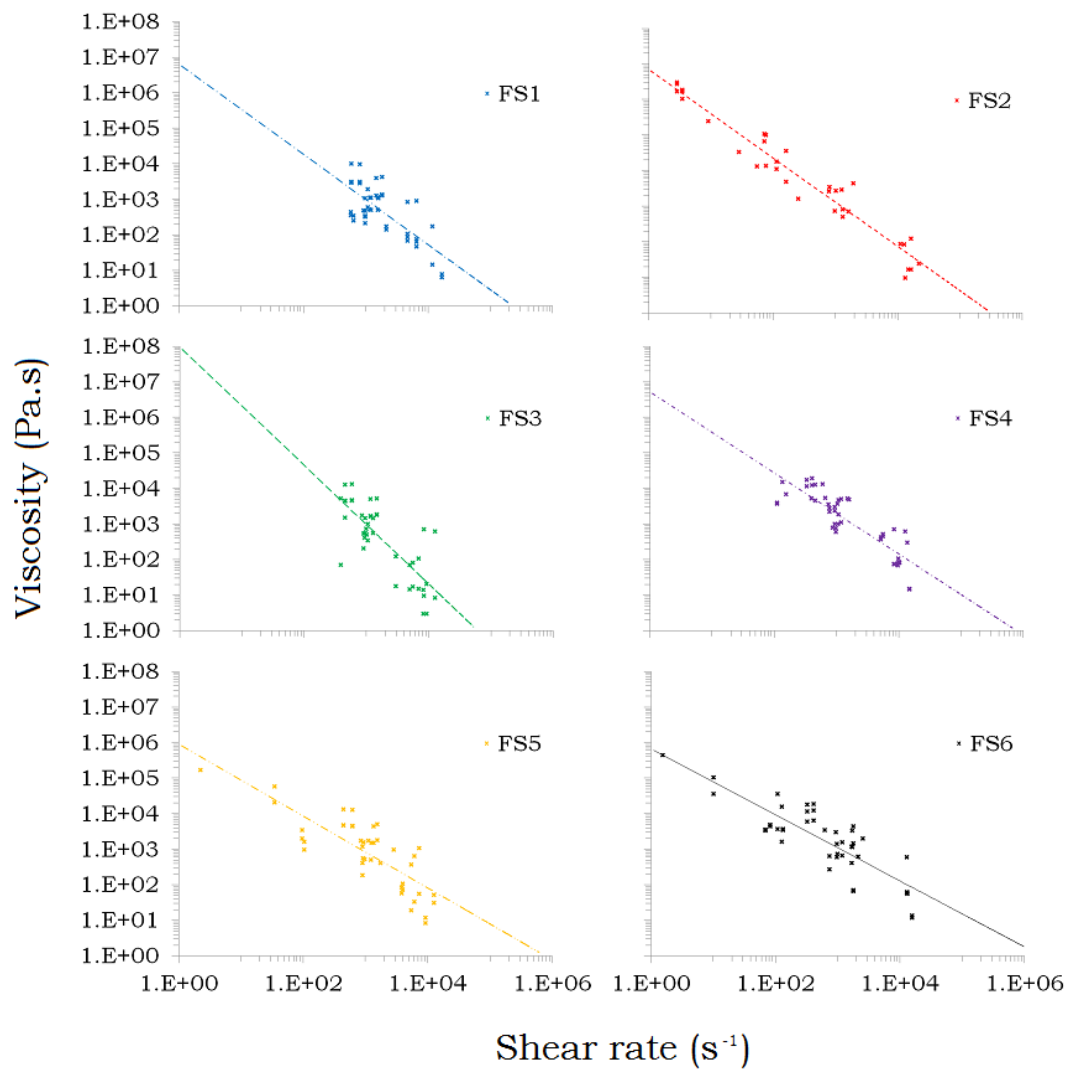


Figure 59: Corrected viscosity and shear rate data for all feedstock.

True viscosity and shear rate were compared (Figure 60) with similar flow behaviour seen for FS5 and FS6. The corrected data still showed inversion in the viscosity rankings due to shear sensitivity but was not as clearly defined as was the raw data. Considering the extrusion capillary and strand formation results, FS6 was a valid selection for the subsequent experiments.

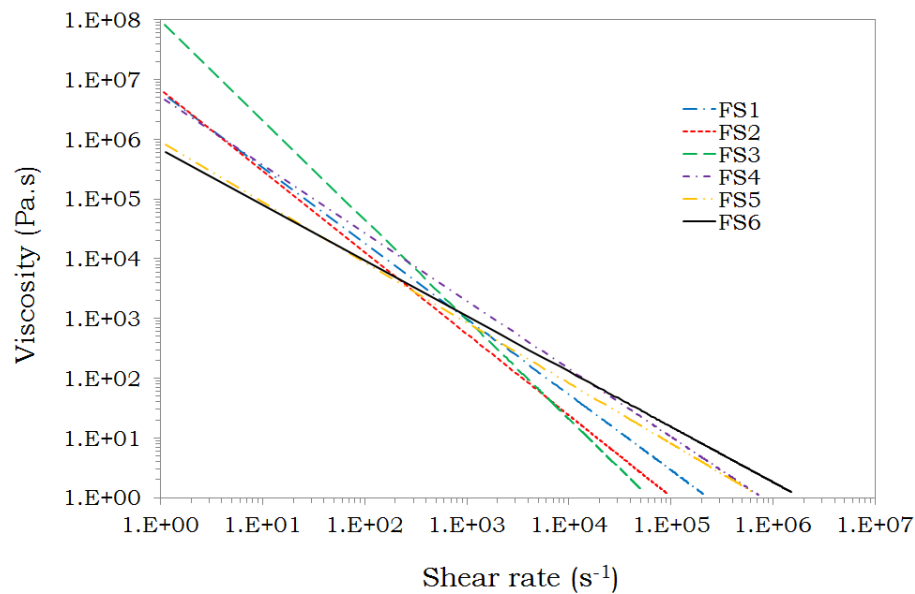


Figure 60: Corrected viscosity and shear rate for all feedstocks.

### 5.2.3 Thermal assessment

It is difficult to identify the most critical parameters for design of a feedstock system due to the broad range of process requirements [74]. However thermal stability is a critical parameter for the feedstock as it undergoes heating during mixing, moulding, debinding and final sintering [5, 75]. DTA showed that compared to the binder components with their individual endothermic peaks the feedstock produced only a single peak (Table 24). The endothermic peak produced for the combined binder components showed a synthesis as it broadened with a more controlled softening and melt phase indicated. The feedstock endotherm was followed with a

similarly broadened exothermic/decomposition response. The rate of decomposition from TGA for the individual components ranged from (1.00 to 5.66)  $\text{min}^{-1}$ . The green feedstock decomposition rate was 2.40  $\text{min}^{-1}$  and after removal of the PEG the grey feedstock decomposition rate was 3.03  $\text{min}^{-1}$ . This showed a tendency of the fast reaction rate components to decrease and the slow reaction rate components to increase when combined. Overall a slower reaction rate would cause the least disruption to the packing order of the particles. For example 5 % decomposition of the PEG8 occurred at 185 °C and for the PP occurred at 260 °C (Table 21) while for the feedstock (AM) it occurred at 252 °C (Table 24). In line with the previous binder systems the results directly supported the mixing and moulding phase of the process, as the binder components were sequentially removed.

Table 24: Temperature of thermal events from SDT for feedstock before and after debinding in air ( $\beta = 5 \text{ }^\circ\text{C}/\text{min}$ ).

|    | DTA events ( $^\circ\text{C}$ ) |          |     |     | TGA weight loss ( $^\circ\text{C}$ ) |      |       | Binder content (%) |
|----|---------------------------------|----------|-----|-----|--------------------------------------|------|-------|--------------------|
|    | Endotherm                       | Exotherm |     |     | 5 %                                  | 20 % | 100 % |                    |
|    |                                 | 1        | 2   | 3   |                                      |      |       |                    |
| AM | 65                              | 248      | 340 | 385 | 252                                  | 293  | 450   | 14.5               |
| SD | 80                              | 270      | 297 | 404 | 260                                  | 277  | 417   | 5.7                |
| TD | 80                              | 337      | 394 | 462 | 272                                  | 333  | 408   | 1.9                |

Another critical observation was the maximum weight loss values measured by TGA after each process step (Table 24). The theoretical mass of binder in the greenpart was 13.4 % ( $\varphi_P = 0.6$ ) where as the measured value was 14.5 % ( $\varphi_P = 0.58$ ). This indicated loss of powder or moisture absorbance during moulding, and was considered in greater detail later in the chapter.

Thermal response of the greenpart had little bearing on the greypart and as expected the thermal response changed with the level and composition of the binder. By considering the total binder

in each sample to be the limiting value (100 %) it was possible to monitor changes in response to the changing temperature (Table 24, Figure 61). Both melting point and 5 % weight loss temperature were seen to increase as the binder was removed where as the 20 % weight loss temperature decreased. This was attributed to the decomposition rate of the binder system being lower due to the compatibilising effect of PEG. Therefore once the PEG was removed the wax components reacted at a greater rate. This result showed that binder-particle bonding could be readily broken and removal of the binder at temperatures just above the decomposition onset temperatures was possible. The mass values however were influenced as in the Ti/ O phase diagram by the saturation levels of interstitial oxygen, ( $w_o \leq 5 \%$ ) and carbon compounds that readily form on powder surfaces above 370 °C. The density of oxides and carbides being higher than titanium will offset the TGA results where such formations occur.

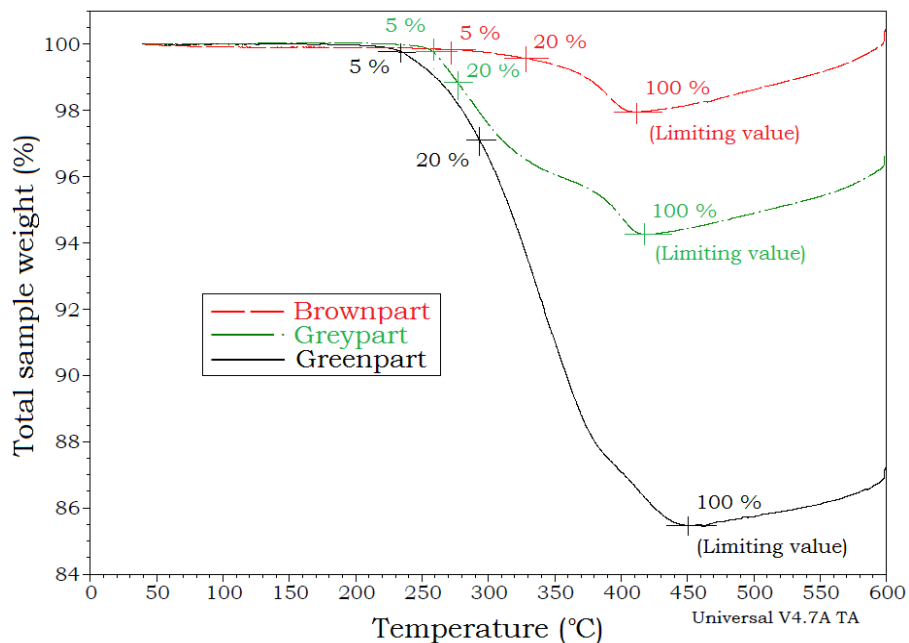


Figure 61: TGA curves showing progressive weight loss changes debinding progressed ( $\beta = 5 \text{ }^\circ\text{C}/\text{min}$ , air).

Investigation of low temperature thermal debinding (LTTD) began with TGA of the binder and feedstock (Figure 62). At these temperatures formation of oxides and carbides was not possible. Considering neither the wax nor the polymer content was reduced by SD (possible by entrapment within groups of water soluble molecules), the maximum possible residual binder in the greypart was the sum of the two ( $w_B = 6.94\%$ ). Unlike the binder only sample, that did not realise full decomposition, the binder mass in the greypart reached a steady level after 65 h.

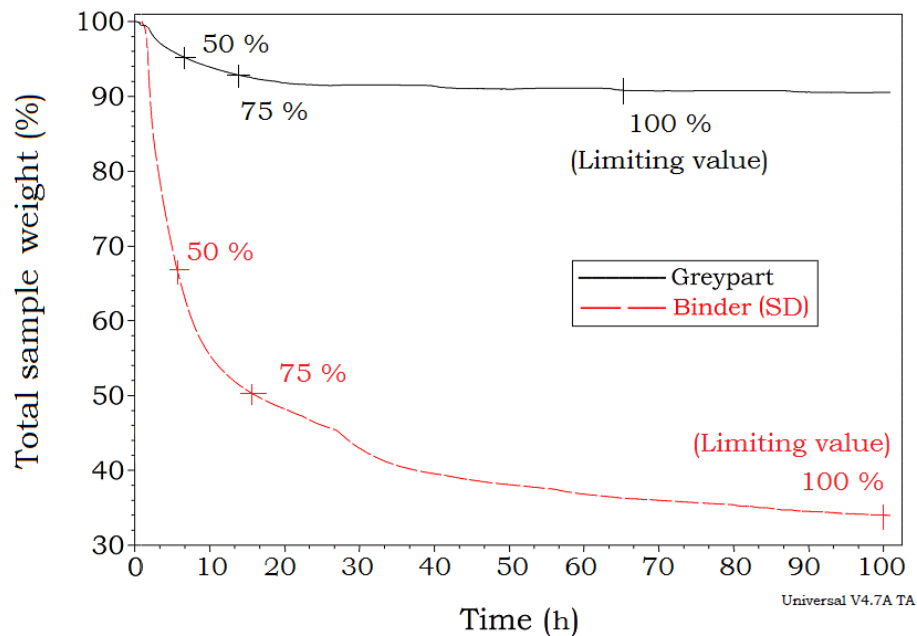


Figure 62: TGA weight loss for low temperature thermal debinding shows limiting loss value in relation to total sample mass.

This increased duration is explained by considering a combination of, the surface area of the binder directly exposed to the TD atmosphere and heat transfer through the sample. The binder (SD) sample with relatively large domains had low exposed surface area at any one time in relation to the mass of the binder and the thermal transfer was also low. For the greypart sample, due to the presence of the titanium particles, the heat transfer improved and the binder domains being smaller increased the exposed surface area.

It was seen that less than the theoretical wax component ( $w_w = 68.2\%$ ) was removed from the binder (SD) sample (Table 25). In contrast the greypart achieved a higher than theoretical ( $w_B = 6.7\%$ ) removal which was accounted for as there was incomplete removal of the PEG during solvent debinding.

Table 25: Key TGA data points from greypart and SD binder sample after low temperature thermal debinding ( $t = 250\text{ }^\circ\text{C}$  in air).

| Binder removal (%)     |             | 50   | 75   | 100  |
|------------------------|-------------|------|------|------|
| Time at isothermal (h) | Binder (SD) | 5.5  | 15.5 | 100  |
|                        | Greypart    | 6.7  | 13.7 | 65.2 |
| Weight (%)             | Binder (SD) | 33.0 | 50.0 | 66.0 |
|                        | Greypart    | 4.3  | 6.7  | 8.3  |

### 5.2.4 Moulding

The feedstock flowed well during moulding to form greenparts with no evidence of external (Figure 63 a) or internal (Figure 63 b) defects. Homogeneity is considered one of the most important requirements for MIM feedstock, however, due to immiscible binder components and insoluble solid particles this cannot be attained [1, 99]. More correctly, there needs to be uniform distribution of all components and therefore heterogeneity. The part mass as an indicator of homogeneity requires part to part volume to be consistent, although it may not be assumed that the particle distribution will be uniform.

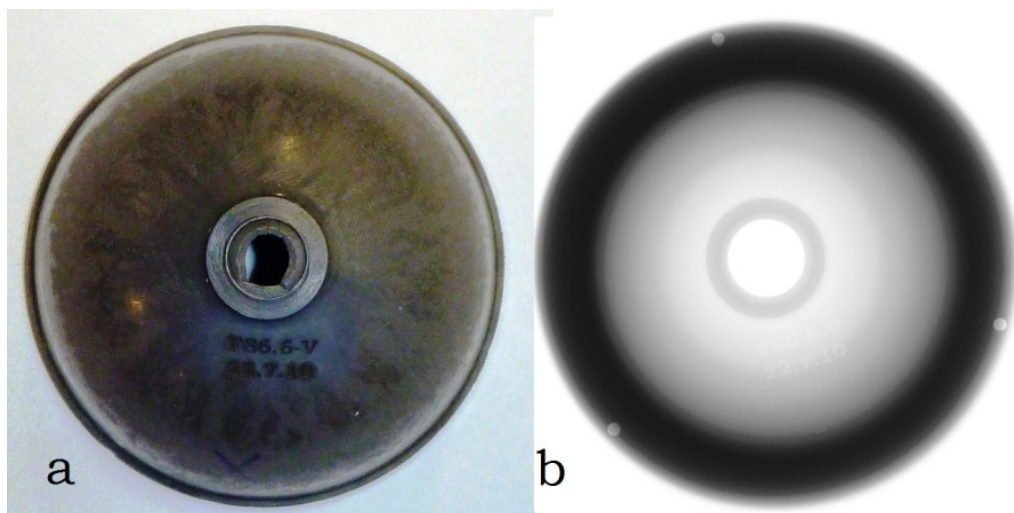


Figure 63: a) Green part image b) defect free and uniform density distribution seen in radiograph.

The average mass of the greenparts was lower ( $w_B = 6.7 \%$ ), and the density lower ( $\rho < 3.2 \%$ ), than the respective theoretical values (Table 26). The part volume ( $V = 38.82 \text{ cm}^3$ ) was also below the theoretical value ( $V = 40.4 \text{ cm}^3$ ). Thermal shrinkage and separation between particles were the main reason for the deviation with no evidence of further defects found.

Table 26: Mass averages for greenpart (AM), greypart (SD), brownpart (TD) and sintered part (S).

|                           |        | AM               | SD               | TD               | S                |
|---------------------------|--------|------------------|------------------|------------------|------------------|
| Mass g ( $\sigma$ )       | Theory | 124.81           | 115.81           | 110.57           | 108.14           |
|                           | Actual | 116.46<br>(0.86) | 108.18<br>(0.77) | 104.02<br>(0.52) | 102.80<br>(0.41) |
| Binder mass %             | Theory | 13.4             | 6.6              | 2.2              | 0                |
|                           | Actual | 15.0 – 15.5      | 5.7 – 6.0        | 2.0 – 2.2        | 0                |
| Density g/cm <sup>3</sup> | Theory | 3.1              | 2.9              | 2.7              | 4.4              |
|                           | Actual | 3.0              | 2.7              | 2.6              | 4.3              |

## 5.2.5 Debinding

### 5.2.5.1 Solvent dissolution

PEG targeted in the solvent debinding was removed (Figure 64) as water permeated into the part from the surface through to the core dissolving the PEG thereby forming a network of connected pores. The PEG concentration gradient between the greenpart and the (PEG free) circulating solvent drove dissolution and the PEG level in the parts reduced. In the final stages the diluted PEG molecules diffused via the micro-porous network in the part. The concentration reduced exponentially until it reached zero or the water reached the solubility limit and PEG removal was complete (Figure 64). By considering the limiting value from SD mass data the soluble fraction was determined. The rapid removal initially reduced the binder mass by 50 % ( $t = 34$  h) and 75 % ( $t = 135$  h), which was 6 % and 23 % of the total debinding time respectively.

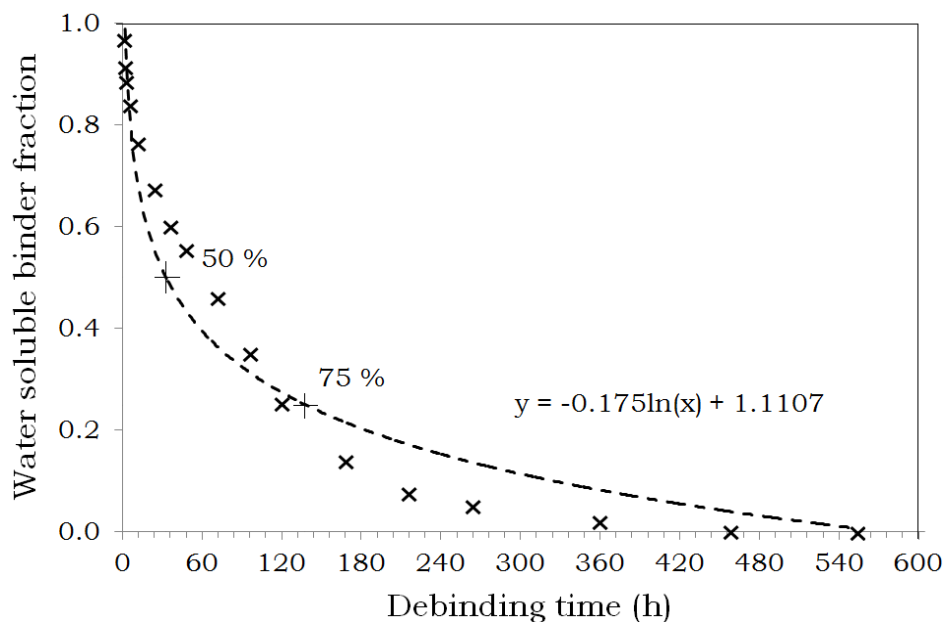


Figure 64: Binder level during solvent debinding ( $t = 250$  °C).

The initial mass ratio between the water (solvent) and the PEG/greenpart ( $m = 8.35 \text{ g}$ ) was  $\sim 260:1$ . At that ratio and considering a maximum dilution of PEG, a minimum of  $32 \text{ mg}$  ( $w_B = 0.38 \%$ ) could remain in the greypart. The average PEG removal was  $8.28 \text{ g}$ , which equated to  $70 \text{ mg}$  ( $w_B = 0.97 \%$ ) remaining in the greypart. Therefore while the plot suggested complete removal a low amount of PEG was present within non-soluble regions. If the non-polar and hydrophobic wax had a dominant effect on the binder dissolution the remaining PEG content would have been much higher. It was also seen that binder bridging between particles (Figure 65) occurred as interconnected pores ( $d = 1 \text{ to } 10 \mu\text{m}$ ) formed relative to the soluble binder.

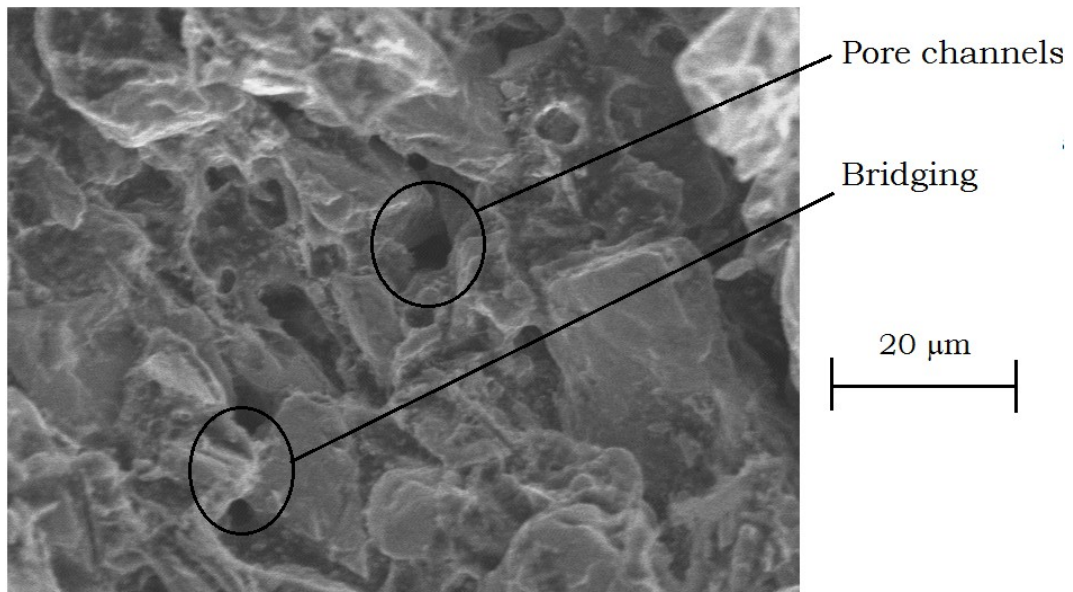


Figure 65: SEM images from green parts after solvent debinding showing, a) pore channels and b) bridging.

#### **5.2.5.2 Thermal debinding**

Thermal debinding is more complex than solvent debinding and relies on decomposition occurring in a controlled and complete manner. Phase transformations such as melting, evaporation and volatilisation, and chemical reactions (combustion) during heating should follow a preferential sequence based on a synergy of melt temperature, molecular size and mass. The mechanism of motility is predominantly influenced by pressure gradients, from expansion of the binder in the melt phase, vapour pressures from gases and finally concentration gradients between residues and the debinding atmosphere. Although higher temperatures would increase these gradients to produce superior binder removal, the use of LTTD was intended to reduce the potential uptake of contaminating elements.

TD ( $t = 250\text{ }^{\circ}\text{C}$ ) produced a similar data trend as SD (Figure 64, Figure 66) reducing the binder by 50 % ( $t = 4\text{ h}$ ) and 75 % ( $t = 20\text{ h}$ ) at 4 % and 20 % of the total debinding time respectively. The binder targeted by TD at only 67 % of the mass targeted during SD had a lower concentration gradient but with a lower duration the overall removal rate was higher. This was attributed in some respect to the network of connected pores created during SD and the mechanism determined during thermal analysis. Explained as a combination of the surface area of the binder directly exposed to the TD atmosphere and the through part heat transfer.

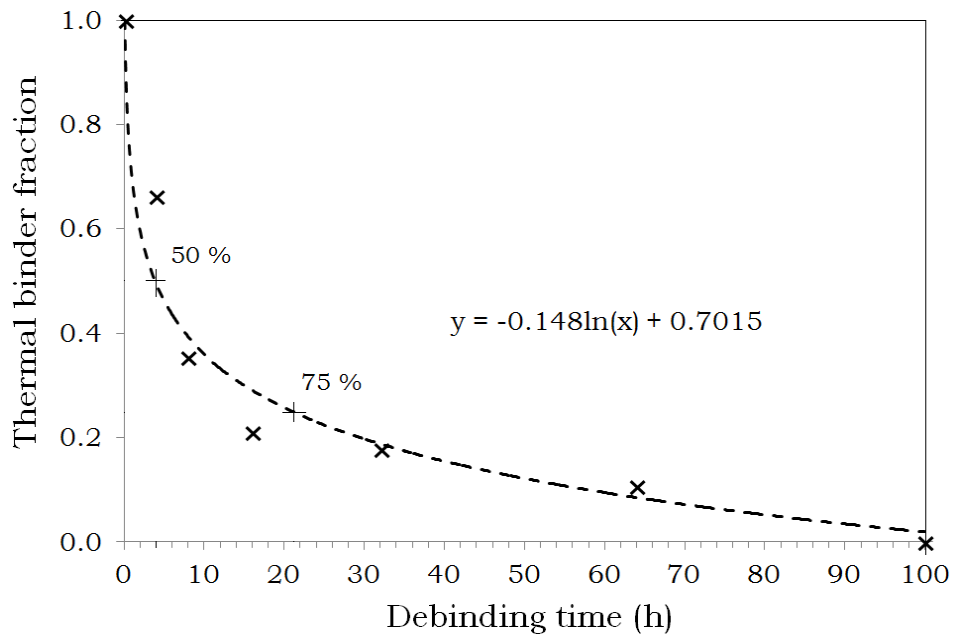


Figure 66: Binder level during low temperature thermal debinding.

The targeted binder components for the LTTD were the waxes and the theoretical values ( $w_B = (2.0 \text{ to } 2.2) \%$ ) determined by TGA confirmed this ( $w_B = 2.0 \%$ , Table 26, Figure 67). Potential oxide and carbide formation was accounted for with consideration for the increase in weight for the sintered sample at the corresponding temperature. These results confirmed that LTTD ( $t = 250 \text{ }^\circ\text{C}$ ) achieved removal of the binder components as required.

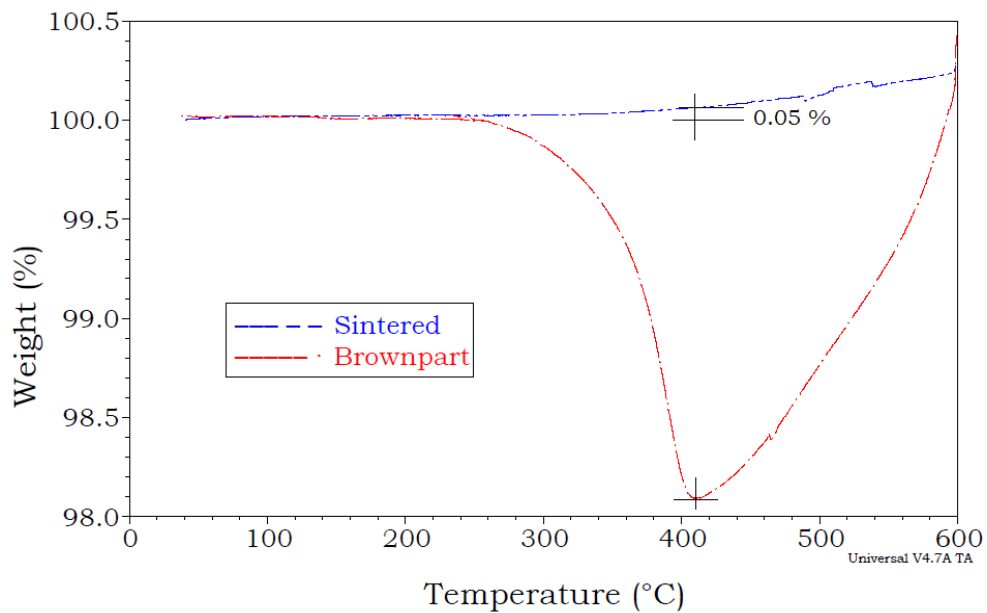


Figure 67: TGA curves show the remaining binder level is below the theoretical value and indicative weight gain value due to oxides.

### 5.2.6 Sintering

The combination of slow heating rates and the selected isothermal points up to the sintering temperature ( $t = 1300 \text{ }^\circ\text{C}$ ) enabled uniform heating of the part. This minimised distortion, removing moisture and helping retain integrity of particle packing and part shape. The mechanism of residue removal during sintering differed from that of TD. During TD pressure differentials from thermal expansion aided melt flow through the pore channels created

during SD. The volume of binder in the brown parts was low and therefore the remaining binder did not create the same capillary pressures. Here the mechanism changes from melt flow and liquid capillary action to a fluid (gaseous) state with motility relative to the concentration gradients between the compact and the furnace atmosphere.

The parts after sintering had good clean surfaces with a metallic appearance and a clear metallic ring when struck together (Figure 68 d). Despite no defects in the greenparts, greyparts or brownparts the sintered parts had surface blistering (Figure 68 d).

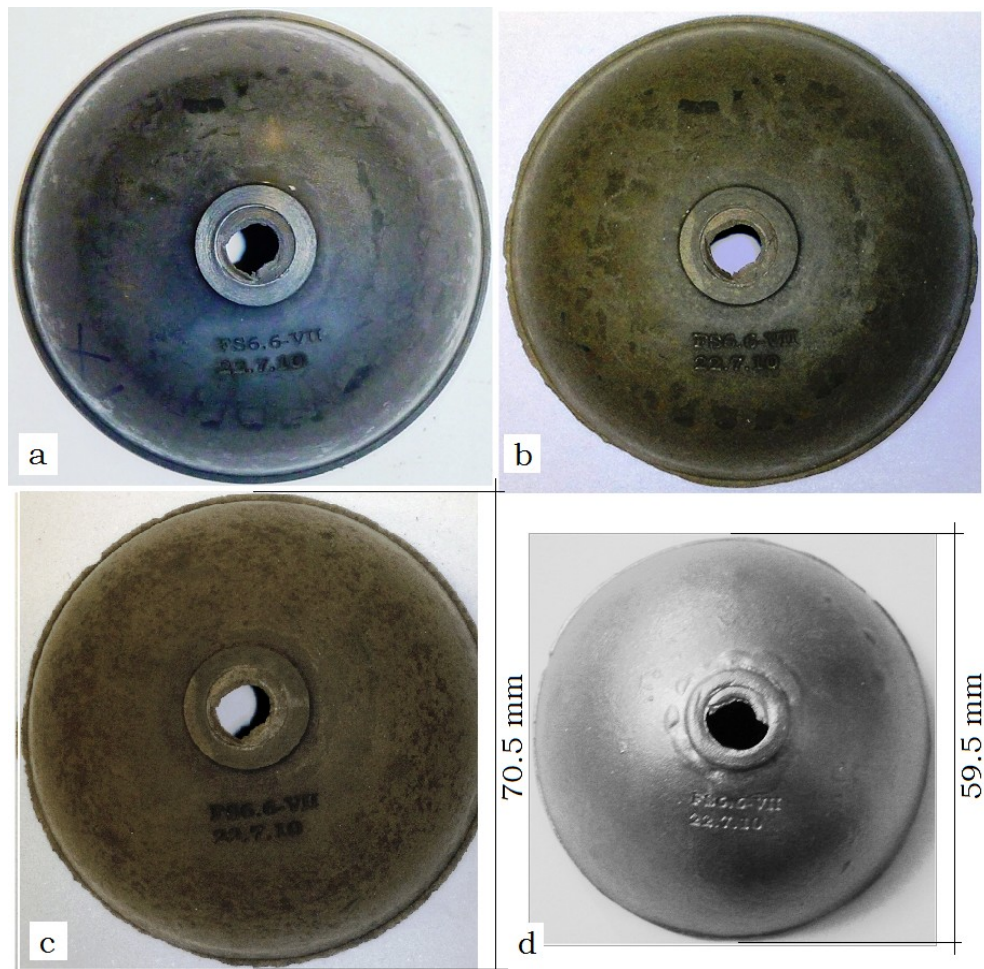


Figure 68: The part seen as a) greenpart, b) greypart, c) brownpart and d) fully sintered.

A section cut from the sintered part had many small pores (Figure 69) in line with the density measurement that gave a value at 96.4 % of theoretical ( $\rho = 4.29 \text{ g/cm}^3$ ). Accounting for the pores, it was seen from EDS results (Figure 69, Table 27) that high levels of carbon were on the surface of the pores. High carbon levels evidence of combustion of binder residues. The values obtained for the EDS map were determined from the area outlined by the box (Figure 69) where as the EDS point analysis was specific to the point selected. In this case the map select was used for the bulk metal where as the point select was used to identify the surface seen at the pore walls.

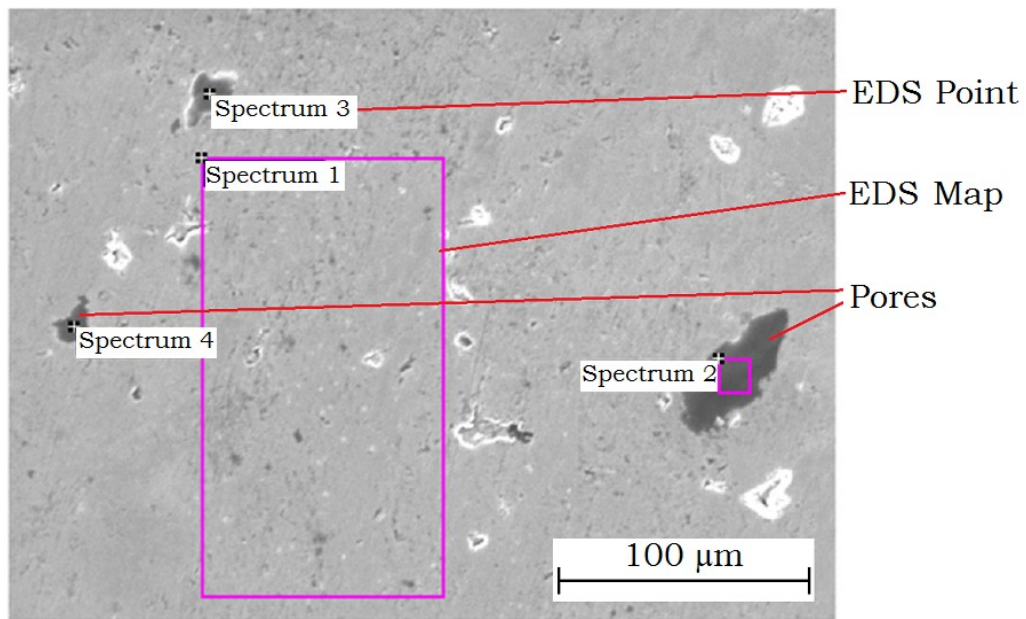


Figure 69: SEM image and EDS locations for sintered part.

Table 27: Elemental levels ( $w_E$  (%)) measured by EDS.

| Spectrum | C     | Al   | Ti    | V    |
|----------|-------|------|-------|------|
| 1        | 3.72  | 5.11 | 87.42 | 2.87 |
| 2        | 30.18 | 2.14 | 40.14 | 1.43 |
| 3        | 37.85 | 1.91 | 30.56 | 5.54 |
| 4        | 24.44 | 1.79 | 56.90 | 1.47 |

Elemental trace analysis was done to determine levels of hydrogen, nitrogen and oxygen using the LECO method. The levels (Table 28) for carbon and oxygen were well outside the ASTM values and greater than the as received powder. It was seen that the presence of hydrogen and nitrogen dropped appreciably possibly as a result of hydride and nitride formation.

Table 28: Elemental levels for titanium alloy (Ti64).

| $w_E$ (%)                          | C    | H     | N    | O          |
|------------------------------------|------|-------|------|------------|
| ASTM B348 [173]                    | 0.08 | 0.015 | 0.05 | 0.2        |
| As received powder (supplier data) | 0.02 | 0.039 | 0.18 | 0.5        |
| Sintered cup part (LECO)           | *    | 0.009 | 0.08 | $\geq 1.0$ |

\* not recorded.

The XRD analysis confirmed high oxygen levels but no peaks were detected for the carbon identified by EDS (Figure 70).

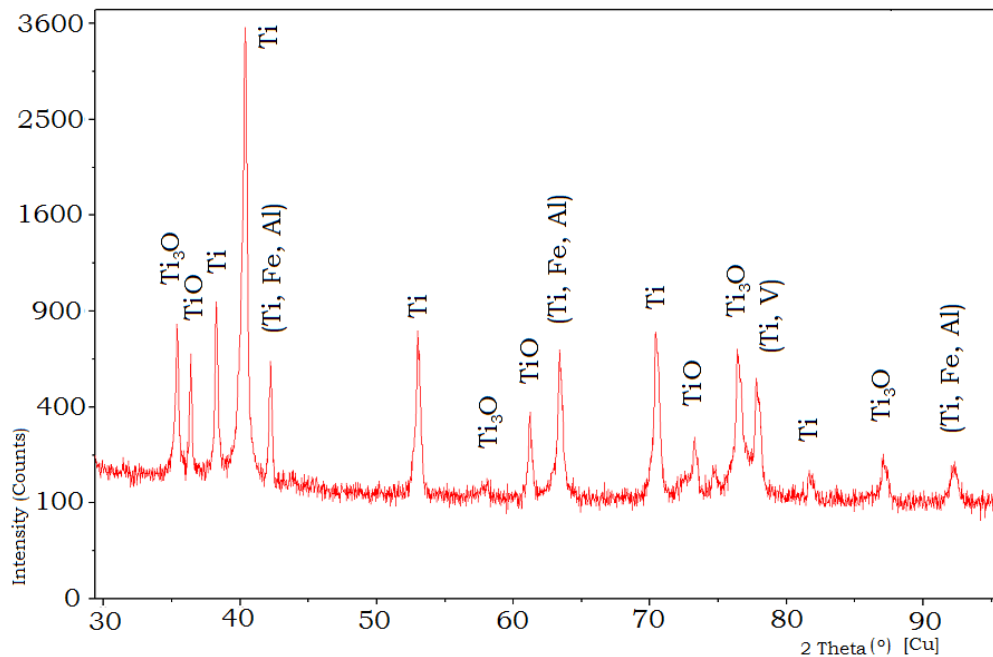


Figure 70: XRD elemental map of the Ti64 shows oxides present.

Binder residues will be composed of carbon, hydrogen, nitrogen and oxygen, the very elements which readily contaminate Ti powders at elevated temperature. Incomplete removal of the residues during the early stages of the sinter process means the particles coalesce and trap the residues within the solid part. Although the data collected from debinding indicated the binder had been sufficiently removed it is still the greatest source of contamination. Unlike the graphite or static furnace used in the previous chapters the ACME furnace was expected to have a marked improvement in atmosphere control.

Further investigation of the sintered part was done by etching with Kroll's reagent to reveal the microstructure. Ti-6Al-4V has an alpha-beta structure and will present two phases. At temperatures above 882 °C the typical alpha crystal structure (HCP) transforms to beta phase (BCC) and, providing the cooling rate will allow it, the alpha phase will return during cooling [192]. The presence of alpha stabilisers (aluminium, carbon, hydrogen, oxygen) increases the temperature at which the transformation occurs. The presence of beta stabilisers (molybdenum, niobium, vanadium) lowers the transformation temperature and may allow the beta phase to be stable at room temperature.

The microstructure showed through etching to be uniform across the sectioned part from the inner surface to the outer surface (Figure 71). A primary alpha titanium phase matrix of equiaxed grains ( $d = (10 \text{ to } 30) \mu\text{m}$ ) was produced with secondary phase inclusions about the grain boundaries. The microstructure was influenced by impurities and the formation of oxides/carbides which can impinge on grain growth and eliminate the typical laminar beta phase structures.

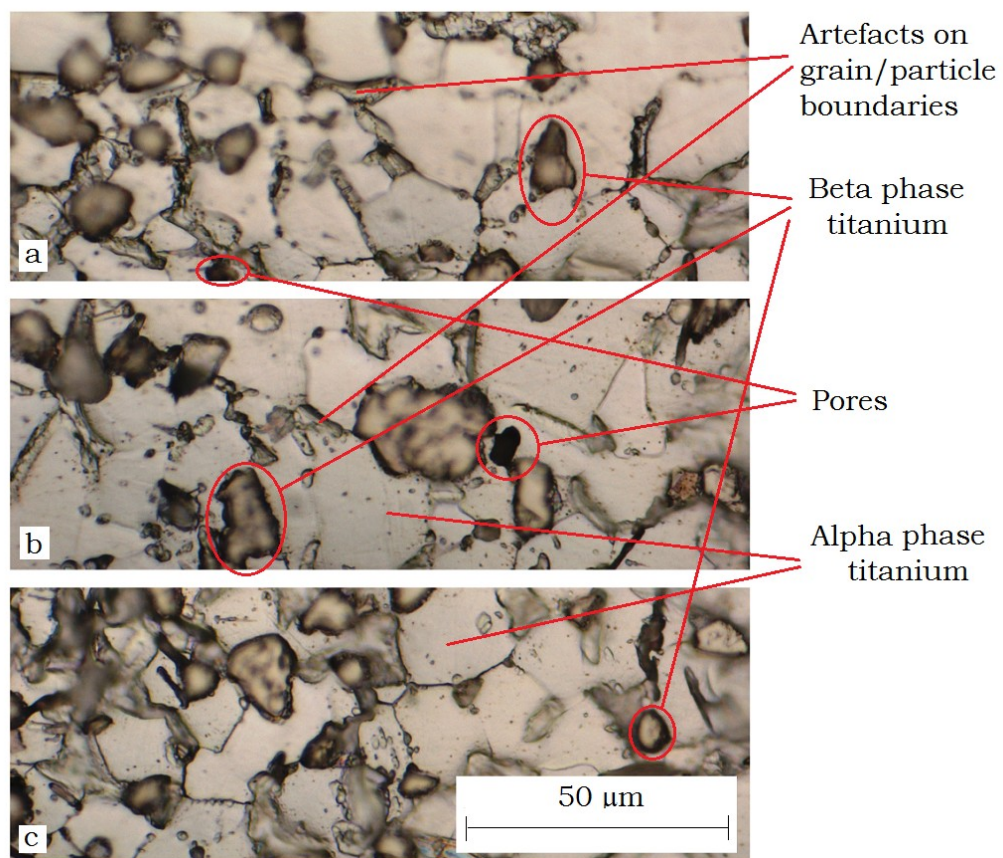


Figure 71: A uniform microstructure of an equiaxed alpha phase matrix and secondary phase a) inner b) centre and c) outer section.

Beta phase titanium as a secondary phase is known to give the Ti64 alloy its superior specific strength over pure titanium allowing it to be used for structural applications. The secondary titanium

phase (Figure 71, Figure 72) was shown from SEM and EDS (Table 29) to have elevated carbon content with no aluminium. Both aluminium and carbon, which are known as alpha stabilisers, impinge on the alpha to beta transformation of the titanium lattice structure. The XRD results (Figure 70) showed oxide presence but the detection of carbides is difficult. Without transmission electron microscopy (TEM) determination of the true lattice structure of the phase is difficult, however the loss of the aluminium and the presence of the vanadium, known to stabilise beta phase structures, it is likely a beta phase titanium with some carbide.

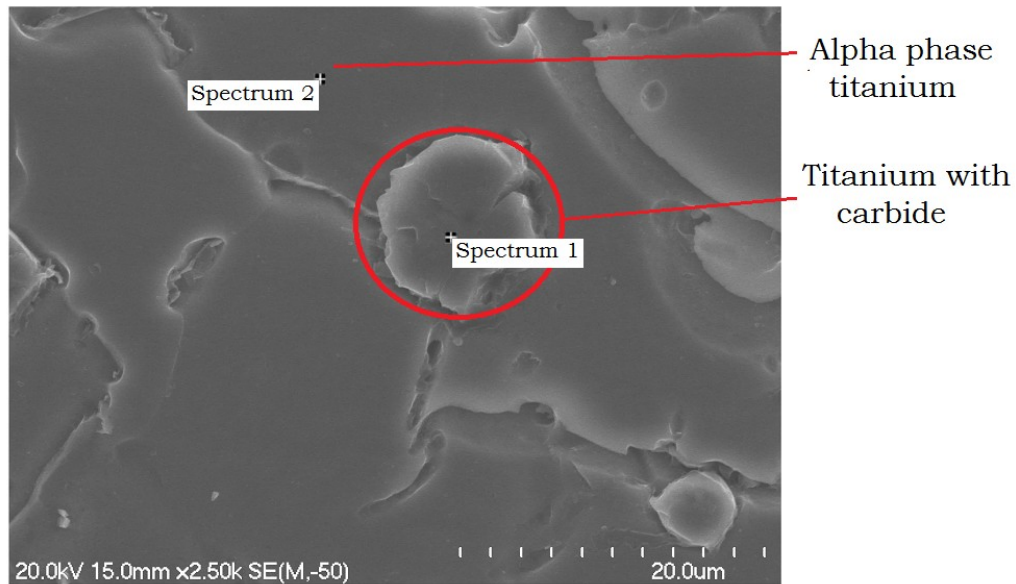


Figure 72. SEM image showing the secondary phase within the primary alpha phase titanium matrix.

Table 29: Indicative elemental levels ( $w_E$  (%)) of the titanium matrix and secondary phase from EDS analysis.

| Spectrum | Al   | C    | Ti    | V    |
|----------|------|------|-------|------|
| 1        | 0    | 8.22 | 93.03 | 0.75 |
| 2        | 4.08 | 2.72 | 90.14 | 2.76 |

Overall there were improvements of the microstructure seen for the sintered cup using the flow process optimised binder over the binder systems used in the previous chapters.

### **5.3 Conclusions**

The binder system of natural wax, water soluble PEG and polymers (2:3:1) was selected for titanium alloy MIM. By optimising the component ratios the mixing and moulding produced defect free greenparts with uniform particle distribution.

The use of different molecular weights of the binder components improved the efficacy of debinding and minimised disruption of the particle formation and part shape.

The use of low temperature thermal debinding enabled removal of the targeted wax binder below the temperatures known to facilitate impurity diffusion and oxide/carbide formation.

The combination of the optimised feedstock and LTDD produced a uniform microstructure throughout the part although oxide and carbide levels effected the alpha beta phase transformation.

## **Chapter Six: Mixing assessment and particle interactions**

The relationship between the binder components and feedstock melt flow behaviour was considered in the previous chapter. Interactions between the components were crucial with relation to subsequent moulding, debinding and final sintering. This chapter investigated the processing behaviour of the formulated binder (Chapter Five) after substitution with an unalloyed and finer titanium powder. This included mixing duration and its effect on homogeneity, mass flow, green part uniformity, and particle binder interaction. The handling performance of the greenparts, greyparts and brownparts were also considered as these are an important aspect of the shape retention. Sintering, as the final stage of MIM fabrication was investigated with relation to density uniformity, particle distribution and the resulting microstructure.

### **6.1. Experimental**

#### **6.1.1. Materials**

Materials previously specified:

- Linear low density polyethylene (LLDPE) and Polypropylene (PP).
- Polyethylene glycol 8000 (PEG8) and Polyethylene glycol 20000 (PEG20).
- Carnauba wax (CW).

The material introduced in this chapter:

- Refined beeswax (RBW, Strahl and Pitsch Inc. SP 422p) with a melting point 64 °C and density 0.97 g/cm<sup>3</sup> was supplied by Texas Drone, Texas, USA.
- Pure titanium (TiCP) hydride de-hydride irregular shape powder ( $w_E = (H = 0.042, O = 0.35, N = 0.23) \%$ ) that passed through a 325 mesh sieve ( $d < 45 \mu\text{m}$ ). It was supplied by specialty Metallurgical Products Co. Inc., Red Lion, PA, USA.

### **6.1.2. Equipment**

Equipment previously introduced:

Thermal debinding was done using the Contherm 2000 series convection oven (TD2). Sintering was done using the ACME high temperature sinter furnace (Model ZSJ-35/35/70). Elemental analysis was also done using the Panalytical Empyrean series 2 XRD with Hyscope software.

The equipment introduced in this chapter:

The ThermoLab co-rotating twin screw extruder (TSE) (USA lab digital) for feedstock mixing and pelletising ( $D = 16 \text{ mm}$  screws,  $L/D = 24$ ,  $\omega = (0 \text{ to } 250) \text{ r/min}$ ,  $t = (30 \text{ to } 300) \text{ }^\circ\text{C}$ ).

Feedstock melt flow was measured using the Tinius Olsen extrusion plastometer (melt indexer MP987). A deadweight piston plastometer it measured the extrusion rate of thermoplastic materials through an orifice ( $d = 2.1 \text{ mm}$ ,  $t = (30 \text{ to } 400) \text{ }^\circ\text{C}$ , deadweight  $W = 1050 \text{ g}$ ) [193].

Moulding of test samples was done using a Carver heated press (150 mm × 150 mm platen,  $W = (0 \text{ to } 10)$  ton and  $t = (30 \text{ to } 200)$  °C). The author made an aluminium plate with a machined pocket (40 mm × 40 mm × 3 mm) to be used as the mould (Figure 73).

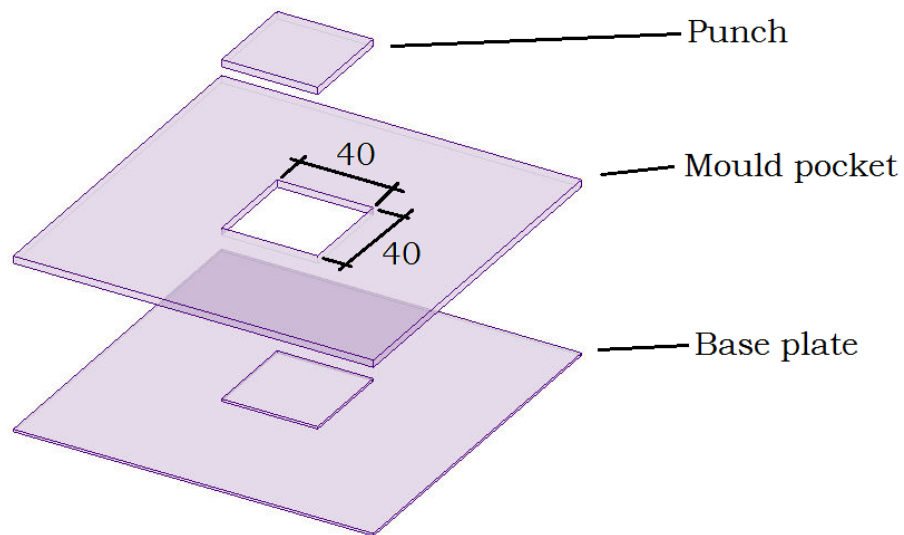


Figure 73: Aluminium pocket mould.

Injection moulding was done using a Dr Boy 35M fully hydraulic injection moulding machine. It had electronic control, a fully reciprocating 28mm screw and 350kN clamping pressure.

A multifunctional cavity in a MUD quick change tool system with a pocket bolster and interchangeable plastic (PTFE) inserts of varying geometries was designed by the author and used to mould the parts (Figure 74, Table 30).

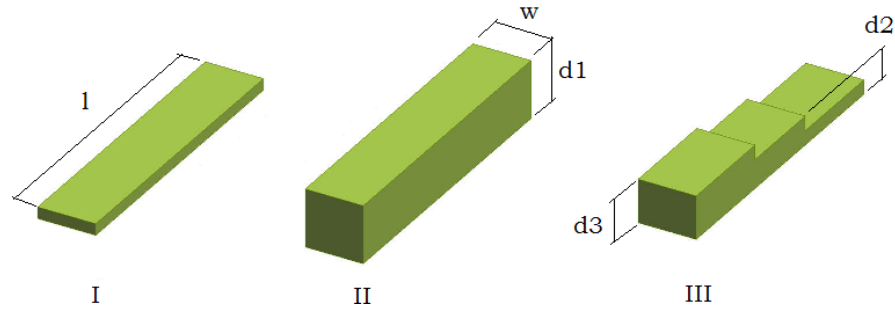


Figure 74: Solid models of the Ti MIM greenparts.

Table 30: Critical dimensions of the greenparts (Figure 74).

| Part |       | Loading | mm |   |    |     |    |
|------|-------|---------|----|---|----|-----|----|
|      |       |         | l  | w | d1 | d2  | d3 |
| I    | Thin  | 0.6     | 40 | 8 | 3  | N/A |    |
| II   | Thick |         |    |   | 8  |     |    |
| III  | Step  |         |    |   | 2  | 4   | 6  |

Debinding was done using both solvent and thermal processes.

A solvent debinding kit designed by the author and assembled at University of Texas – Pan American was used for the test samples (SD3). Solvent was cycled through a heated reservoir ( $t = 60\text{ }^{\circ}\text{C}$ ,  $V = 4\text{ L}$ ) to a dissolution tank holding the green parts (Figure 17).

Thermal debinding was done in a Binder convective drying oven (FED53,  $V = 53\text{ L}$ ,  $t = (30\text{ to }300)\text{ }^{\circ}\text{C}$ ) with a gas tight chamber and programmable PID temperature control (TD3). It was coupled to compressed argon and air for atmosphere control (Figure 50).

Thermal analysis was done using the following instruments.

TGA using the TA instruments Q500 ( $\beta < 100$  °C/min,  $t = (30$  to  $1000)$  °C).

The differential scanning calorimeter (DSC, TA instruments DSC 2920), with cooling system, measured differential heat flow between the sample and reference ( $t = (30$  to  $725)$  °C,  $\beta (0.1$  to  $20$  °C/min).

Thermal mechanical analysis (TMA, TA instruments TMA2940) was used to investigate expansion of the binder and feedstock components under controlled atmosphere ( $t = (30$  to  $1000)$  °C,  $\beta < 200$  °C/min).

Dynamic multi-frequency mechanical analysis (DMA, TA instruments DMA2980) was used to determine comparative values of storage modulus with a 3-point bending attachment.

Visual analysis was also done using an RJ Lee (Personal SEM) scanning electron microscope with Aspex image software.

### **6.1.3. Methodology**

Investigation of the mixing uniformity and effect on the melt flow for the TiCP feedstock was done using the thermo-lab twin screw extruder (TSE). The binder formulation (Table 19) and powder loading ( $\phi_P = 0.6$ ) from chapter five was retained.

The feedstock components were weighed into a bag and hand blended before being passed through the extruder ( $t = 170$  °C) and then granulated. Subsequently sample lots were passed back through the extruder and designated as EM(1 to 10) with respect to the number of extrusion mixes undertaken.

Each feedstock sample, EM(1 to 10), was tested in the extrusion plastometer to measure the extrusion rate. The plastometer was pre-heated ( $t = 170$  °C) and an amount of feedstock ( $m = 16$  g) was placed in the barrel for 6 min. After this time the dead weight ( $W =$

1050 g) and piston was used to extrude the sample feedstock through the orifice. The first sample was taken at ( $t = 60$  s) and then subsequently at ( $t = 30$  s) intervals until the piston had reached full stroke. The samples were weighed and the mass values recorded. The values for melt flow rate (g/10 min) were calculated and the averaged values for three runs were plotted.

Sample plates were press moulded in the Carver press using process parameters of temperature, pressure and time comparative to those for injection moulding ( $t = 170$  °C,  $p = 245$  MPa,  $t = 6$  min). The moulded plates were cut into test specimens for examination, thermal analysis and mechanical testing as required.

Debinding the test samples was done using both solvent and thermal treatment. Samples were placed in SD3 with circulating water for solvent debinding ( $t = 50$  °C,  $t = 24$  h), followed by oven drying ( $t = 50$  °C,  $t = 12$  h). Thermal debinding was done using the Binder convection oven, TD3, with a low thermal ramp rate ( $\beta = 1$  °C/min,  $t = (30 \text{ to } 250)$  °C) and an isothermal period of 4 h. A low cooling rate to ambient was also used ( $\beta = 1$  °C/min). A designation of SD for solvent debound and TD for thermal debound was used for the samples.

Comparative measurements of the particle binder interactions, before and after debinding, were made by 3-point bending in the DMA. The test was done using a slow heating rate, low temperature ( $\beta = 2$  °C/min,  $t = (30 \text{ to } 50)$  °C) and a single frequency ( $\eta = 1.0$  Hz). Each sample ( $l = 25$  mm,  $d = 6.5$  mm,  $t = 1.6$  mm) was tested with a support distance of 20 mm and amplitude of 5.0  $\mu\text{m}$ .

TMA was used to measure sample expansion. The samples ( $l = 8.0$  mm,  $d = 8.0$  mm,  $t = 1.6$  mm) were mounted and given a 10 N preload, followed by controlled heating ( $\beta = 2$  °C/min) to 50 °C with a 30 min isothermal period to measure dimensional change ( $\Delta t$ ).

Following the mixing analysis parts were injection moulded (Figure 74) using the Dr Boy 35M. The parts were debound and sintered using the same processing parameters used for the sample parts with extended duration for the thicker sections.

The brownparts were sintered using the ACME furnace. Initial heating with an isothermal period at 470 °C ( $\beta = 5$  °C/min,  $t = 60$  min) followed by further heating to 800 °C, all under argon sweep gas ( $\dot{V} = 10.0$  L/min). This was followed by further heat increase and a final isothermal period at sinter temperature under vacuum ( $5$  °C/min,  $t = 180$  min,  $t = 1350$  °C,  $p = 2.0 \times 10^{-3}$  mbar).

Sectioned and polished parts were analysed by XRD with power settings 45 kV at 40 mA through a copper electrode. Scanning from position (20 to 100) °2 $\theta$ , using a step size of 0.026 °2 $\theta$ , scan step time of 17.340 s in continuous scanning mode. Peak identification was done using the Highscope software.

## 6.2. Results and discussion

### 6.2.1. Compounding and uniformity

Changing the metal powder in the feedstock from Ti64 to pure titanium showed no appreciable change in the thermal response (Table 24, Table 31). The particle shapes were the same and therefore differences through changes in heat transfer and processing durations should be indicative of the particle size, surface areas and surface energies only.

Table 31: Thermal event values for the feedstock using SDT in air.

| Rate<br>(°C/min) | DTA events (°C) |          |     |     | TGA weight loss |              |             |
|------------------|-----------------|----------|-----|-----|-----------------|--------------|-------------|
|                  | Endotherm       | Exotherm |     |     | 5 %<br>(°C)     | 10 %<br>(°C) | Max.<br>(%) |
|                  |                 | 1        | 2   | 3   |                 |              |             |
| 5                | 65              | 245      | 345 | 400 | 315             | 350          | 15.0        |
| 20               | 85              | 280      | 405 | 455 | 355             | 390          | 15.5        |

The first feedstock extrusion was problematic due to high friction between particles and extruder surfaces. The dry particles needed to be encapsulated with the binder to reduce their resistance to flow. Although not investigated in this work this could be resolved with a two stage feed system that melts the binder components prior to slow feeding of the powder. Subsequent extrusion mixing reduced duration and increased mass flow ( $\dot{m} = (1.67 \text{ to } 3.33) \text{ g/min}$ ).

SEM images (Figure 75 a) showed the single pass feedstock had numerous hardly embedded particles on the surface and non-uniform distribution of the components. Particles were prevalent on the outer surface and therefore the low viscosity polymer at the centre. After five passes a reduction of surface particles was seen and a more uniformly distributed structure. The sample (Figure 75 c) after ten passes had no loose particles and the magnified image showed similar structure to the EM5 sample.

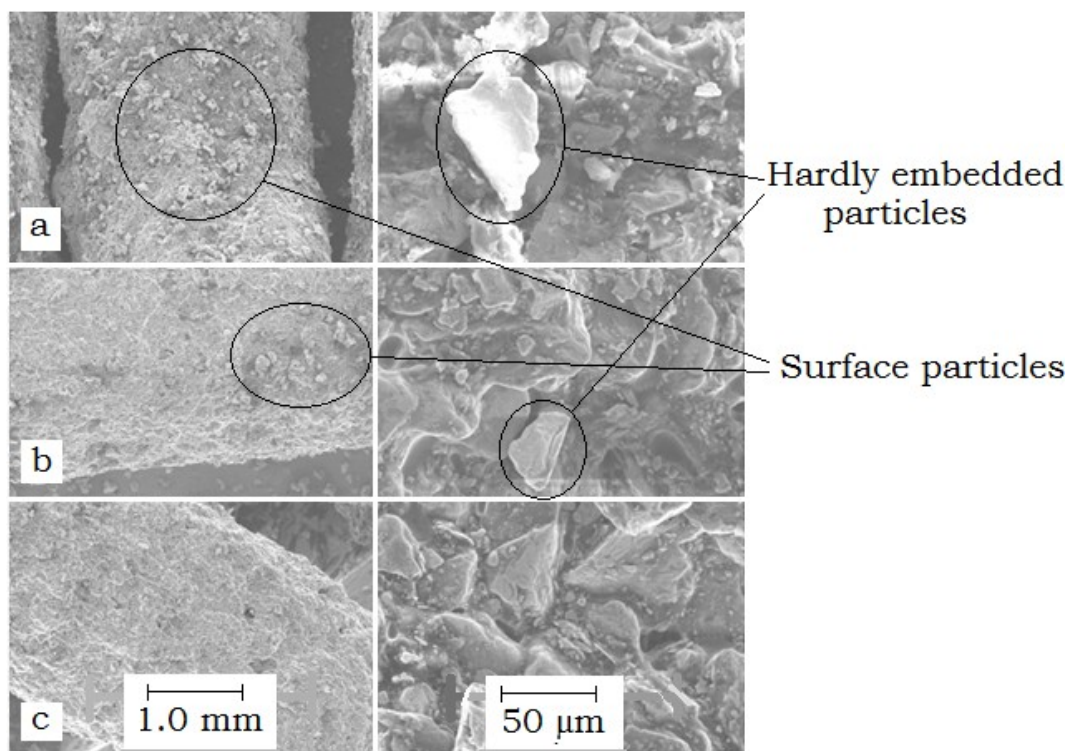


Figure 75: SEM micrographs of changes in feedstock appearance from increased extrusion mixing a) EM1, b) EM5 and c) EM10.

An increasing mass flow rate (MFR) was observed as the number of passes increased EM(1 to 4) (Figure 76). Interparticle friction was reduced by the distribution of the binder about the particles effectively encapsulating each one and reducing the pressures needed to enable flow. The MFR was at a steady state from EM(3 to 6), this is also the best processing region as flow stability will minimise the likelihood of moulding defects and distortion. What could not be ascertained was whether MFR would continue to decrease and therefore be attributed to shear degradation, and loss of the lower viscosity binder components. It was also possible that the MFR would plateau after an initial drop in viscosity, in a similar fashion to batch mixing prior to shear degradation.

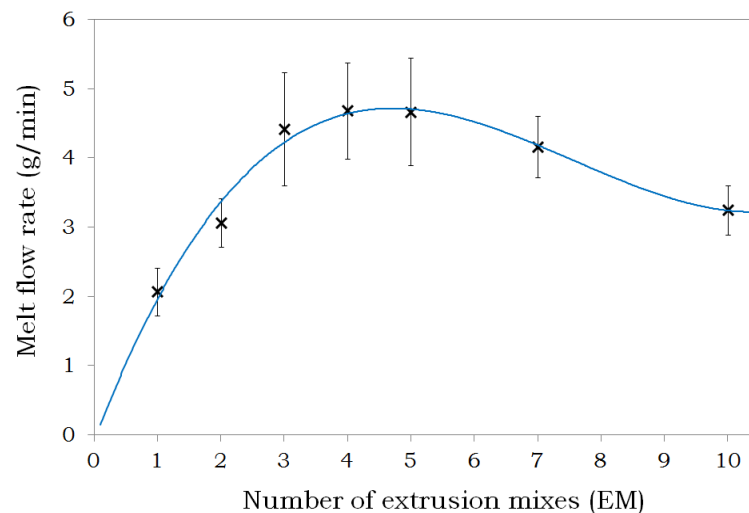


Figure 76: Melt flow rate for extrusion mixed feedstock.

The TGA results for the EM feedstocks showed degradation onset and rate of change to be the same for all samples. There was some evidence of inhomogeneity with a low number of extrusion passes (EM(1,2)) but this averaged out over a number of samples. The binder content removed was similar ( $u_B = (13.1 \text{ to } 13.8) \%$ ) to the theoretical value ( $u_B = 13.2 \%$ ).

### 6.2.2. Press moulding

SEM examination of the moulded samples (Figure 77) showed binder agglomerates that disrupted packing uniformity of the powders. This affects not only the moulded state, but when the binder is removed the powders do not rearrange and voids remain. It was not clear whether the agglomeration was due only to insufficient mixing, limitations of chemical solubility or a combination of both. It has been shown for certain binder systems that complete mixing may not be completed in under 60 minutes [194]. EM4 (Figure 77 b) had uniform distribution with reduction of agglomerates indicating sufficient mixing [195]. EM10 (Figure 77 c) supported the theory that attributed high viscosity to shear degradation and loss of the lower viscosity binder components through extended mixing. Binder poor areas, evident on the part surface, contributed to the low MFR and were attributed to loss of the PEG (Figure 77). It is also possible that miscibility and contraction during cooling created the binder poor regions.

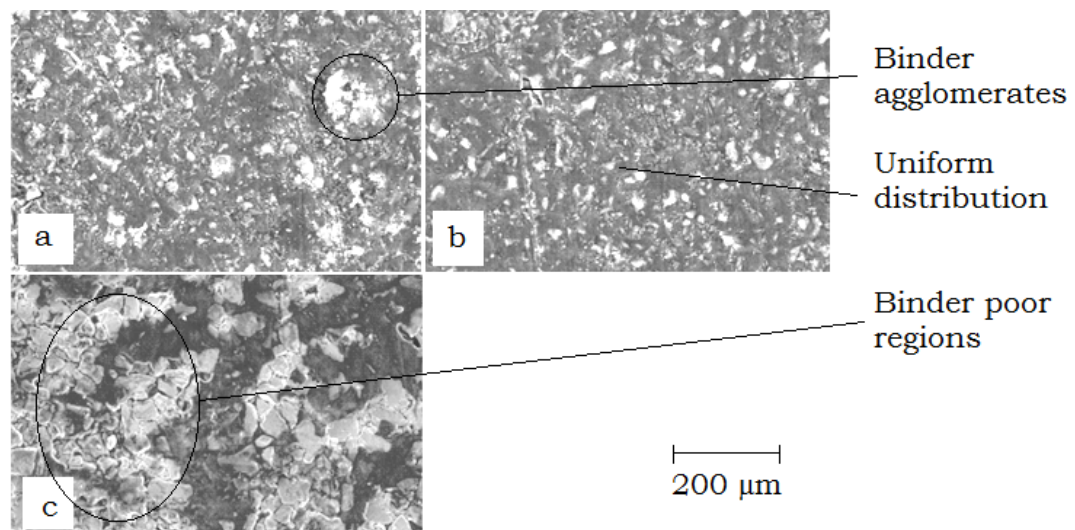


Figure 77: Surface of the green parts, a) EM1, b) EM4 and c) EM10.

The binder was formulated to allow removal from a moulded part as a gradual process to reduce slumping, distortion and cracking. The average relative density of the feedstock samples remained the same as the number of passes increased. The overall average greenpart density for all samples ( $\rho_{ave} = 64.4 \%$ ) was  $\sim 5 \%$  lower than the theoretical greenpart density ( $\rho_{ave} = 69.1 \%$ ) calculated from the individual component density and mass fractions. The variation may be the result of insufficient wetting and the possibility of interfacial gaps between the particles and the binder. Literature suggests good bonding between particles and binder is required, it would however increase the likelihood of particle surface contamination. In the absence of good bonding clean surfaces will enable optimum sintering, avoid fracture mode separation of particles and increase necking between particles, which is critical to consolidation. In other words, the binder would perform better having weak bonds with the particles providing that uniformity of feedstock component distribution was maintained.

Dimensional change of the greenparts was measured using TMA (Figure 78). It allowed assessment of expansion between components and how this may affect particle packing and particle - particle proximity. Greenparts were heated to the SD temperature ( $t = 50 \text{ }^\circ\text{C}$ ), followed by an isothermal period and cooling. Expansion of part thickness during heating was followed by contraction through the isothermal period. In turn this was followed by reduction in thickness corresponding to the cool down period ( $t = (50 \text{ to } 30) \text{ }^\circ\text{C}$ ). Maximum change occurred during the isothermal period and minimum change when returned to the starting temperature ( $t = 30 \text{ }^\circ\text{C}$ ). The contraction was due to relaxation and softening of the binder which allowed for particle rearrangement that would not occur in the physical confines of the mould.

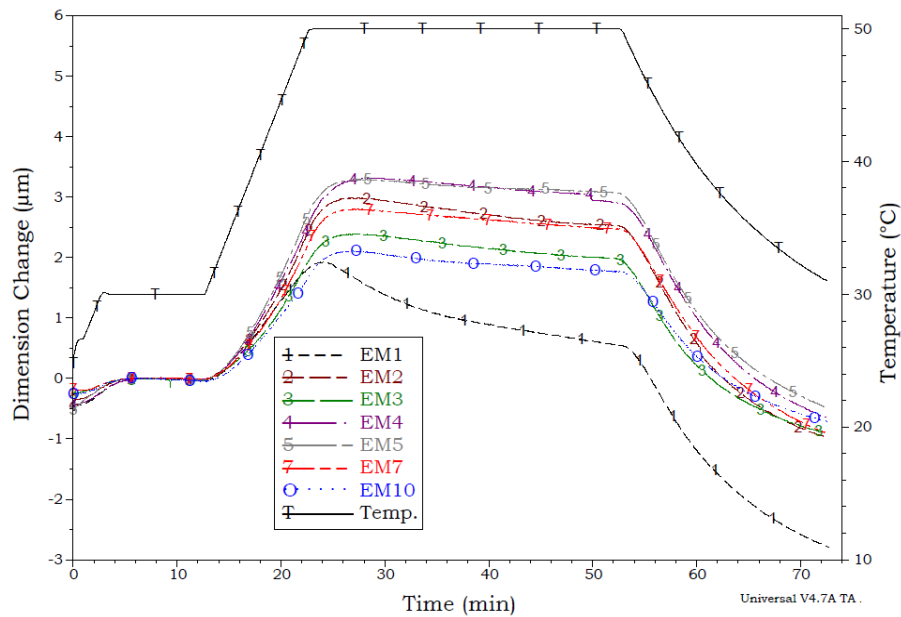


Figure 78: TMA expansion curves for moulded parts overtime, temperature profile also shown.

The maximum and minimum dimensional changes did not follow any trend but a slightly higher dimensional change was seen during the isothermal period for EM(2 to 4) ( $\Delta x = 0.43 \mu\text{m}$ ) as opposed to EM(5 to 10) ( $\Delta x = 0.32 \mu\text{m}$ ). The EM1 specimen showed greater dimensional change ( $\Delta x = 1.4 \mu\text{m}$ ) due to expansion of binder agglomerates not dispersed into the feedstock. Non-recoverable dimensional change was seen for all parts as the temperature returned to the starting temperature ( $t = 30 \text{ }^\circ\text{C}$ ) and corresponded to the isothermal relaxation (EM1 ( $\Delta x = 2.8 \mu\text{m}$ ), EM(2 to 4) ( $\Delta x = 0.83 \mu\text{m}$ ), EM(5 to 10) ( $\Delta x = 0.67 \mu\text{m}$ )). No difference was seen between samples, with the exception of EM1, further confirming non-uniformity due to insufficient mixing.

### **6.2.3. Debinding**

Solvent debinding is a counter-flow process driven by the hydrophilic nature of the PEG and the concentration gradient set up between the PEG in the part and the water. The ability of water to remove PEG from the greenpart is initially governed by the permeability of the outer surface. As water diffuses into the part diluted PEG molecules disperse back into the water until the solubility limit is reached. In this work the amount of PEG in the SD ranged from (0.5 to 4.5) g/L, well above the water solubility limit for the PEG8 (700 g/L) and PEG20 (500 g/L).

The permeability of water into the parts was dependent not only on the binder components but also on their chemical interactions. The non-polar and highly hydrophobic wax being immiscible in water could retard debinding, whereas, PEG is highly soluble. If PEG was encapsulated in either the wax or polymer removal would not be possible.

The solvent debound (SD) parts (Figure 79 (a to c)) showed that binder agglomerate size decreased (50 to 30)  $\mu\text{m}$  as the number of extrusions increased, indicative of continuing distributive mixing. After thermal processing, voids in the form of non-uniform spacing between particles, where seen to have formed even in the EM10 sample (Figure 79 (d to f)). Particle movement during thermal processing may create voids within a brownpart as the binder softens the particles reorient themselves. As the binder was removed capillary forces moved particles bringing them into contact. Also a reduction of the overall surface energies of adjacent particles can enable particles to overcome the Vander-Waal forces between them to create voids. Defects such as this will not self-repair during sintering as the distance between particles would not be sufficient to close voids unless some liquid phase was created.

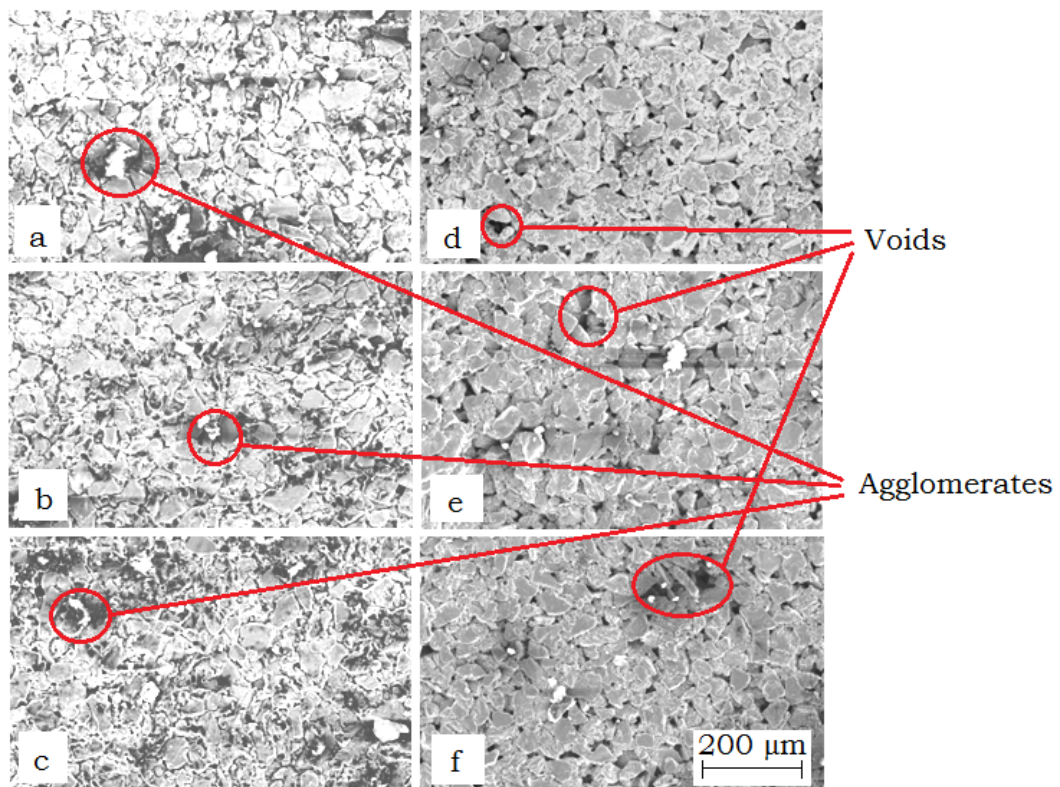


Figure 79: Solvent debound a) EM1, b) EM4 and c) EM10, and solvent/ thermal debound d) EM1, e) EM4 and f) EM10, parts.

#### 6.2.4. Particulate interactions and compact handling

As debinding proceeds particle to binder interactions change and the handling strength also changes. To investigate this greenpart and greypart specimens were tested using DMA. The brownparts were too brittle to be loaded into the apparatus. Only handling between debinding processes was simulated as handling at higher temperatures is unlikely to occur ( $t = (35 \text{ to } 40) \text{ }^\circ\text{C}$ ).

All specimens had the same modulus differential (Figure 80) with a clear difference between the green and greyparts. The greyparts had lower overall values and less deviation between samples indicating that the reduction was due to the interactions being dominated by the PEG. It was clear from the higher values for the greenparts that the PEG improved bonding between components in the compact. No trend was evident from the results however there was an indication that the parts with the lower EM number had consistently lower modulus in both AM and SD condition.

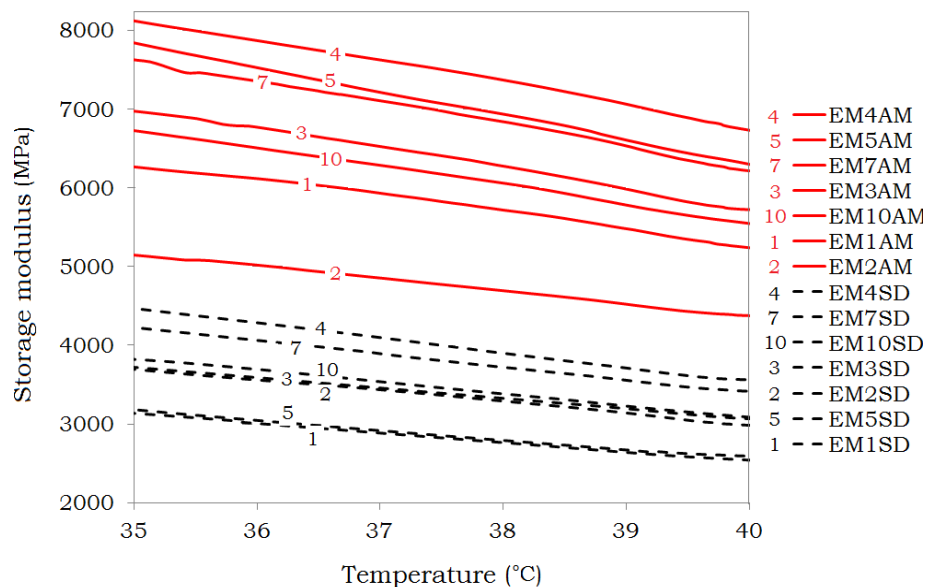


Figure 80: DMA plots from testing of greenpart (AM) and greypart (SD) specimens.

In summary there was no systematic trend seen with relation to the degree of mixing. There were indications that the lesser mixing reduced particle encapsulation and restricted melt flow and that higher mixing produced binder loss and restricted melt flow.

#### **6.2.5. Injection moulding and part processing.**

The titanium feedstock investigated in the previous section was extruded three times prior to injection moulding to form thin, stepped and thick greenparts. During moulding of MIM feedstock the flow enables a preferential arrangement of the particles that conforms to the shape of the cavity. The interaction of particles and binder during moulding determines how well the greenpart shape is retained when removed from the mould. In this work the parts retained their moulded shape and had good handling strength after debinding. This was evidence of bonding between particles, such as mechanical interlocking, that was not related to the continuous nature of the binder. This does not however preclude the fact that the interactions may change during the debinding process due to chemical or thermal reactions.

Investigation of particle arrangement and bonding was done using thermal mechanical analysis (TMA) to measure expansion and strain within parts. The expansion coefficients of polymers ( $\alpha = (100 \text{ to } 200) \times 10^{-6} \text{ }^\circ\text{C}^{-1}$ ) and waxes ( $\alpha = (150 \text{ to } 1500) \times 10^{-6} \text{ }^\circ\text{C}^{-1}$ ) are much higher than for titanium ( $\alpha = 8.5 \times 10^{-6} \text{ }^\circ\text{C}^{-1}$ ) [185]. Therefore strain during moulding and debinding was dominated by the binder as the greenparts and greyparts showed expansion followed by contraction (Figure 81, Table 32). The maximum dimensional change for the greenparts ( $\epsilon = 2100 \text{ } \mu\text{m}/\text{m}$ ) was two times that of the greyparts and correlated with reductions in binder fraction ( $\varphi_B = 0.4$  and  $0.2$ ). Therefore keeping SD temperatures as low as possible will benefit and maintain mechanical interlocking.

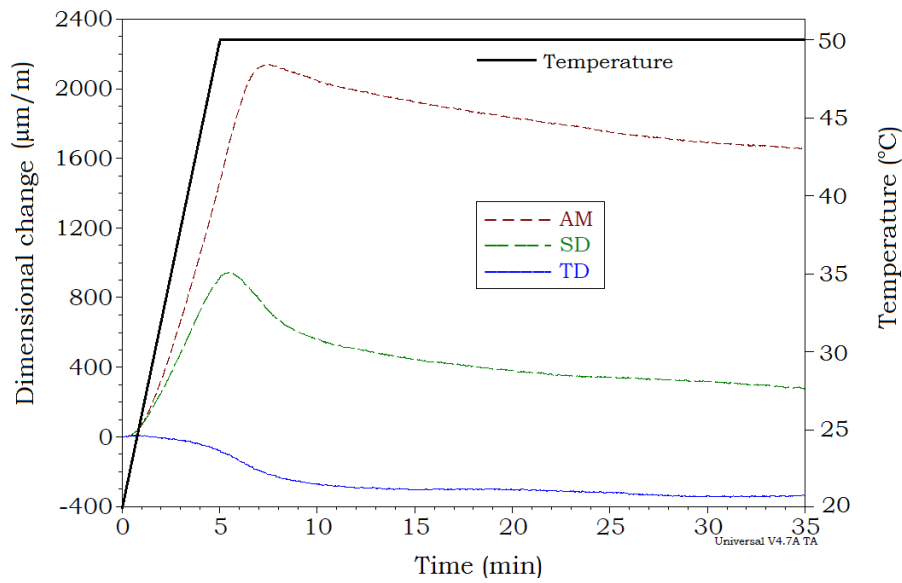


Figure 81: TMA plots for dimensional change during part heating.

Table 32: Dimensional change from TMA ( $\epsilon$ ) ( $t = (25 \text{ to } 50) \text{ }^\circ\text{C}$ ).

| $\mu\text{m}/\text{m}$ | Maximum | Post iso-thermal | Relaxation | Relaxation gradient |
|------------------------|---------|------------------|------------|---------------------|
| Greenpart              | 2150    | 1650             | 500        | 400                 |
| Greypart               | 950     | 300              | 650        | 250                 |
| Brownpart              | 0       | -350             | 350        | 50                  |

The SD process removed 50 % of the total binder phase in agreement with a 44 % dimensional change ( $\epsilon = (1700 \text{ to } 950) \mu\text{m/m}$ ). Waxes may not show linear expansion behaviour and are known to change inconsistently with temperature [185]. A similar correlation was seen for the storage modulus values with 47 % reduction from AM to SD samples ( $E' = (5700 \text{ to } 3000) \text{ MPa}$ ).

As seen in previous chapters mass loss during debinding occurred progressively based on the individual components and the process. Thermal response was previously shown with one melting peak observed, for PEG and wax, and SD still able to remove PEG suggesting that these did not form a miscible blend. The greypart (Figure 82, SD) showed a similar trend but without the large endothermic trough, confirming that the PEG was removed. The remaining endothermic trough at ( $t = 82 \text{ }^\circ\text{C}$ ) was caused by melting of the BW and CW. The brownpart (Figure 82, TD) showed no endothermic peaks confirming removal of the PEG and waxes during TD debinding.

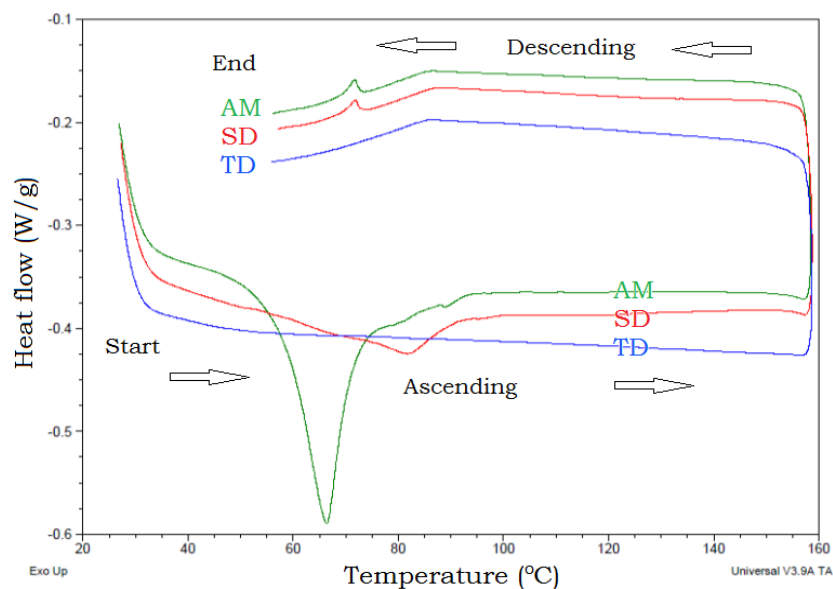


Figure 82: Ascending and descending heat flow curve of TiCP greenpart (AM), greypart (SD) and brownpart (TD).

The surface of greenparts and greyparts (Figure 83 a, b) appeared similar although there was a reduction in the overall amount of binder and noticeable channels between and around some of the particles. The brownparts (Figure 83 c) showed an absence of binder on the particle surfaces and the particles were easily distinguishable.

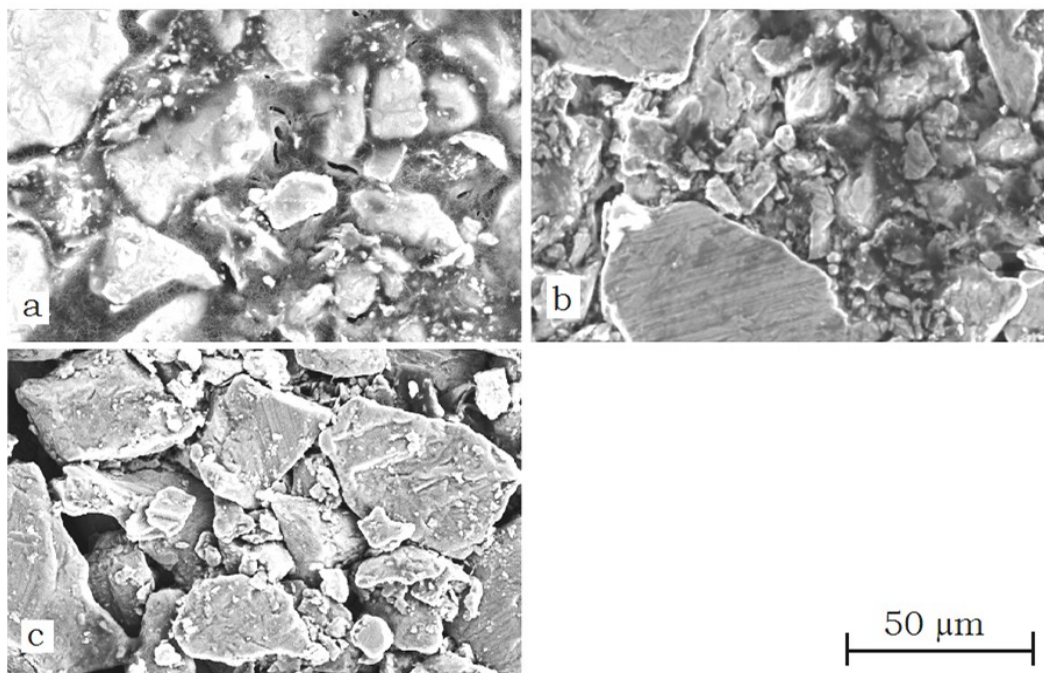


Figure 83: SEM images a) greenpart, b) greypart, c) brownpart.

To reduce/eliminate changes to interparticle distance that cause disruption to the moulded geometry the feedstock binder fraction will need to be reduced below the void fraction of the Ti powders. The ability to do this will require particle encapsulation suitable for retention of feedstock flowability and sufficient slip between the powders, mould walls and/ or machine surfaces. Shrinkage during thermal debinding may bring the particles closer together but the forces that initiated mechanical interlocking may be compromised.

### 6.2.6. Debinding

It was evident from the part mass that the theoretical fraction of binder components and powder was not realised in the greenparts. Accordingly the actual mass of PEG and wax for removal differed from the anticipated level. It was seen that the binder was removed from the thinparts but it was not possible during SD (24 h) and TD (4 h) to totally remove the binder from the thickparts.

Moulding of the step part showed similar mass discrepancy as the thin and thick parts. In order to determine correlation between SD rate and remaining binder components, long-time solvent debinding with continuing measurement was done. As shown in Figure 84 the dissolution rate decreased with increasing time, as expected.

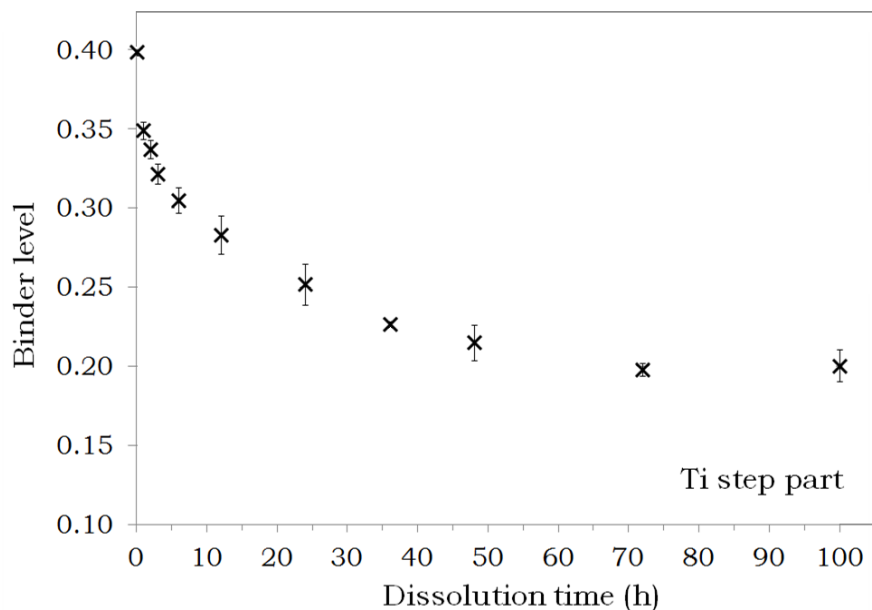


Figure 84: Binder removal by dissolution for the step part.

Part to part mass deviation may be due to feedstock inhomogeneity, powder/binder separation during moulding, irregularities with the debinding system, loss of particulates or part

geometry. The low deviation was essential as uniformity is very important to ensure part density and final dimensional tolerances can be met. The longtime solvent debinding proved to be suitable for the total removal of the water soluble component. This was based on the true mass of the samples and not the theoretical values which showed to be unachievable for the greenparts.

When cracking and surface deformation appeared from TD it was consistent in its form and location; central in the thick parts and central to each step in the step part (Figure 85). Defects in consistent locations indicate the cause was not related to feedstock inhomogeneity. The cause more likely related to moulding, the location of the gate and the flow behaviour of the feedstock filling the cavity. Changing this was beyond the scope of this study, however, means of eliminating separation defects were suggested in Chapter Three and applied in the following Chapter.

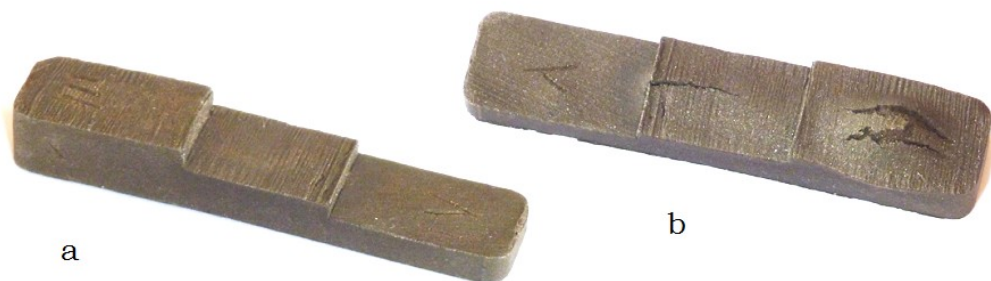


Figure 85: TD step parts a) without defects and b) with defects.

As the binder, powder fraction and debinding parameters were kept constant it can be stated that binder removal was a function of sectional thickness and part geometry. Particle loss from the compacts would also have a considerable effect on the final part, especially when the part size is small.

### 6.2.7. Sintering

The thin and thick parts were sintered under flowing argon, the thinparts had uniform linear shrinkage in all axes ( $\epsilon \approx 15\%$ , Figure 86 c), with no defects, a clean contaminant free surface and density of  $\sim 93\%$ . The parts with defects that had manifest during debinding retained the defects (Figure 86 (d, e)).



Figure 86: Thinpart a) green, b) brown, c) sintered and defects that remained during sintering d) thinpart and e) thickpart

Cut and polished samples seen during EDS (Figure 87, Table 33) showed the elemental composition was uniform. The polished outer surface (Figure 87 a) showed silicon traces in the pores and greater consolidation of the particles than the polished inner section. No contaminants were found in the bulk titanium indicating that carbon diffusion did not take place.

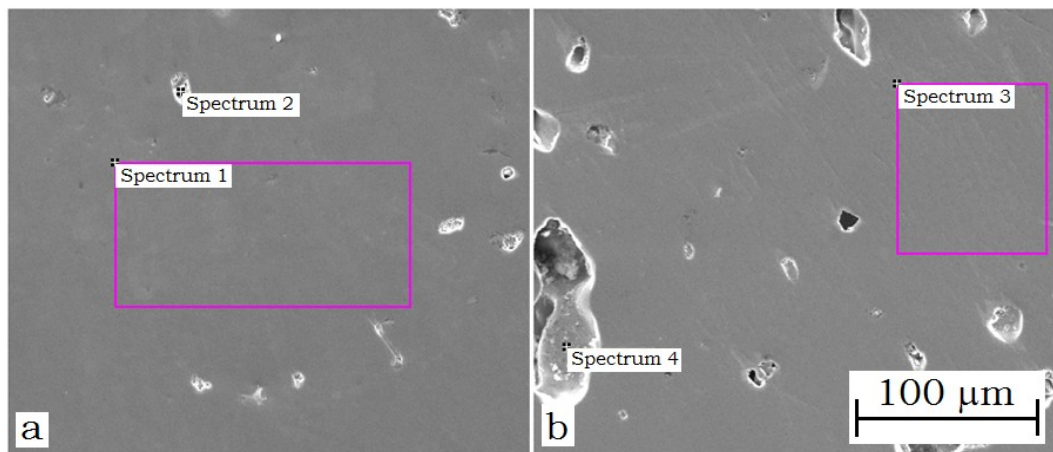


Figure 87: SEM image from the outer surface of thinpart, a) bulk Ti and b) internal porosity.

Table 33: Elemental values from EDS spectrum ( $w_E$  (%), Figure 87).

| Spectrum | C    | Ti     | Si   |
|----------|------|--------|------|
| 1        | 0    | 100.00 | 0    |
| 2        | 0    | 99.45  | 0.55 |
| 3        | 0    | 100.00 | 0    |
| 4        | 7.20 | 92.80  | 0    |

The XRD analysis showed evidence that carbon and oxygen were at levels high enough to form oxides and carbides (Figure 88).

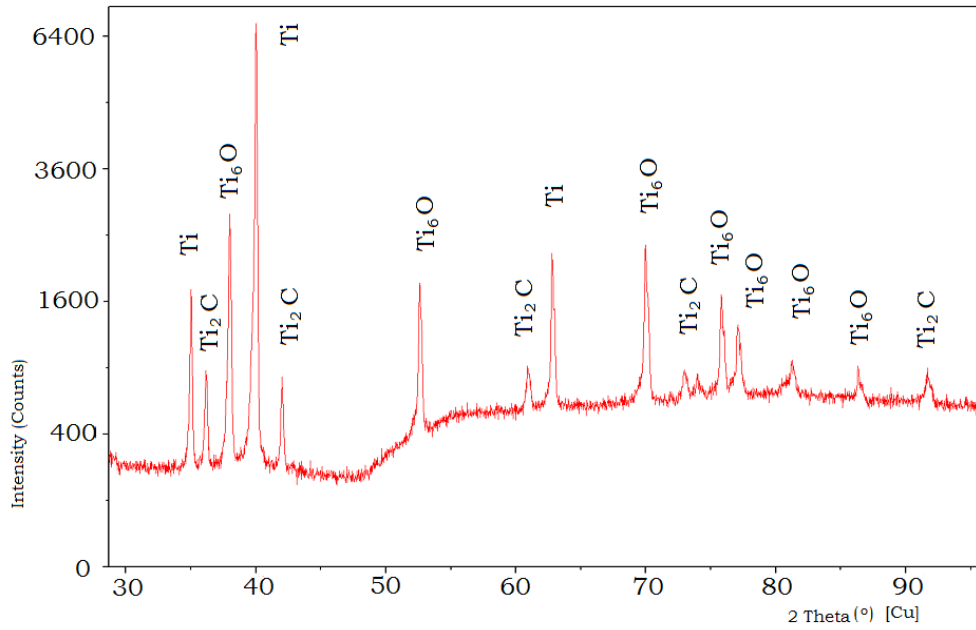


Figure 88: XRD map of the thin titanium part shows high oxygen and carbon levels.

The microstructure of the thin part was highlighted after etching with Kroll reagent. (Figure 89 a, b). Pores at the surface and internally in the parts were primarily about the grain boundaries but were also seen within the grains. Porosity appears uniform although the internal pores are smaller and greater in number than the outer surfaces.

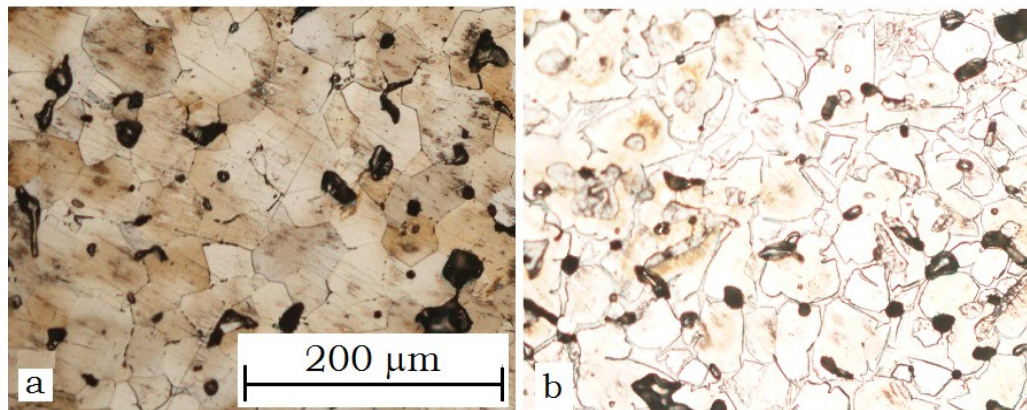


Figure 89: Microstructure of sintered Ti part etched with Kroll reagent, a) polished outer surface and b) polished internal surface.

The thickpart images showed (Figure 90 a) some twinning within the mainly alpha grains ( $d = (30 \text{ to } 80) \mu\text{m}$ ) indicative of hydride formation. The formations shown from another area (Figure 90 b) are the alpha grains with contamination likely from the trace carbon and iron determined from EDS.

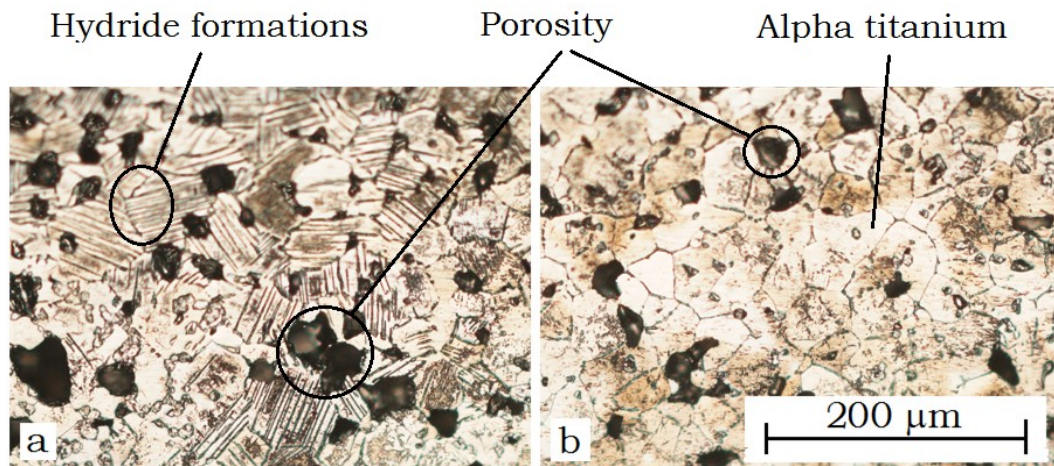


Figure 90: Cross section of thickpart etched with Kroll reagent.

The cracking (Figure 91) manifest during TD was due to slip bands and binder separation, or weld lines from jetting. Both of these phenomena are dynamically formed due to inconsistent flow during moulding. The cracking (Figure 91) fans out and was seen to be aligned with the point of injection (ingate).

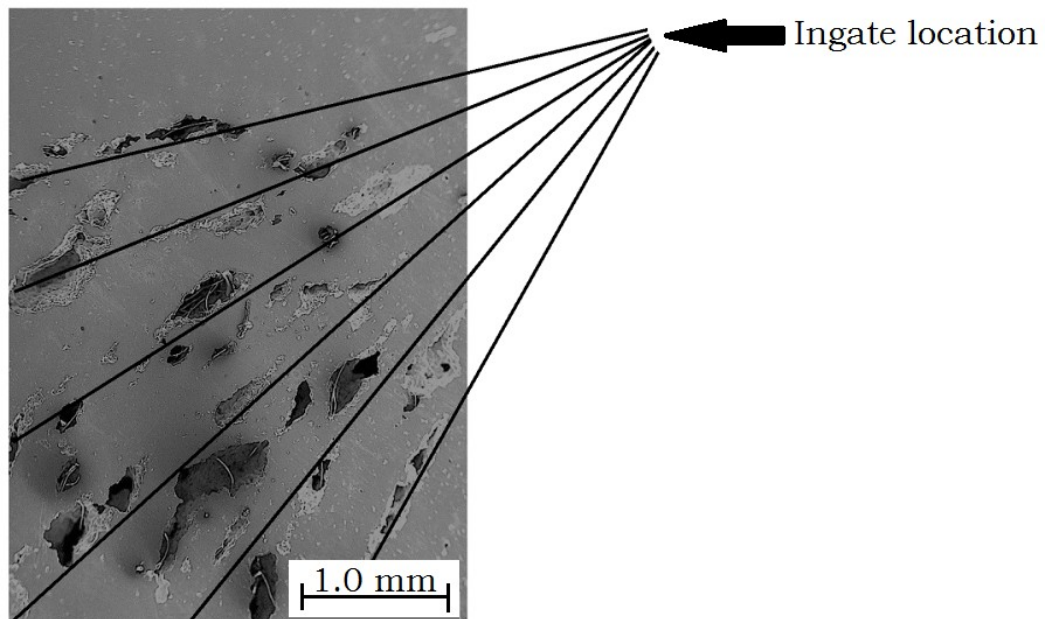


Figure 91: Defect seen after sintering only evident in the brownpart.

Slip bands are a function of feedstock separation and may be considered due to poor feedstock formulation and too high shear rates. This will be exasperated by tool design where the position of runners and gates become critical. Jetting is also a form of separation where the feedstock melt deviates from its intended path due to sectional changes causing rapid pressure drop that splits the flow front [196]. This can be overcome by increasing mould temperature [1], changing the cavity design, the in-gate location or part geometry. As seen in Chapter Three separation was also overcome by increasing the powder loading.

The step parts were sintered in the ACME vacuum furnace (5 °C/min, 1300 °C, 180 min,  $2 \times 10^{-3}$  mbar) and had good clean surfaces with the distinct titanium lustre (Figure 92). The defects that manifest in the thermal debinding were not able to self-repair therefore accurate density measurement was difficult (Figure 92 b). As above these defects were considered to be due to low powder loading and deficiencies in tool design which promoted separation and non-uniform feedstock flow. This in turn affected debinding with some binder agglomerates creating high internal pressures due to non-uniform expansion during heating.



Figure 92: Sintered Part a) without and b) with defects.

### 6.3. Conclusions

Extrusion mixing of the feedstock showed a preferential distribution of the particles to the outer surface of the extrudate. This was in agreement with a higher resistance to flow between individual particles than between the extrusion surfaces of barrel, screw and die. The melt flow indexer results also confirmed this.

No correlation was found between mixing duration using the extruder and that of the torque rheometer. This was attributed to the turbulent flow using the torque rheometer and the laminar flow through the extrusion die head.

TMA testing showed that dimensional change was not affected by uniformity of the feedstock however it was clear that the amount of binder has direct affect on interparticular distances. It will therefore benefit particle interactions to keep processing temperatures low to reduce disruption to the moulded geometry where the volume is greater than that required to fill the space about the particles.

The ability to debind the Ti greyparts by low temperature thermal debinding is possible. The variables to be considered are part thickness, mass and overall volume.

Although the binder formulated for titanium alloy was successful for mixing, moulding and processing of titanium parts. Defects that manifest during debinding would not self repair during sintering.

## **Chapter Seven: Summary and solution**

It was shown in the previous Chapters that of the four main MIM processing steps (feedstock production, moulding, debinding and sintering) each are essential to ensuring a successful part is produced. Of the four steps the main deficiencies that were shown to affect the feedstock were component uniformity and particle binder interactions. For moulding, mould design and particle loading were shown to be critical. The debinding process required sufficient strength of the greenpart, greypart and brownpart to enable handling and placement. Sintering showed that removal of decomposition products (control of elemental levels) and maintaining an inert furnace atmosphere was essential.

In this chapter the conclusions from the previous chapters were applied to the fabrication of acetabular cup parts.

### **7.1. Experimental**

#### **7.1.1. Materials**

No new materials were introduced in this chapter:

- Linear low density polyethylene (LLDPE) and Polypropylene (PP).
- Polyethylene glycol 8000 (PEG8) and Polyethylene glycol 20000 (PEG20).
- Carnauba wax (CW) and Refined beeswax (RBW).
- Pure titanium (TiCP).

### 7.1.2. Equipment

No new equipment was introduced in this chapter:

Feedstock mixing was done in the batch mixer (BM) and pelletising was done using the ThermoLab co-rotating twin screw extruder (TSE). Viscosity measurement was done using the Shimadzu capillary rheometer (CFT 500D). The Dr Boy 50T2 injection moulder was used for moulding the samples with the acetabular cup mould. Solvent debinding used the SD3 debinding kit ( $V = 21$  L) in conjunction with the Contherm convection oven for drying the greenparts ( $t = 50$  °C) and also for low temperature thermal debinding (TD3,  $t = 250$  °C). Comparison of the LTTD was done by TGA using the TA Instruments SDT2960. Elemental oxygen, hydrogen and nitrogen levels were measured by the inert gas fusion-infrared absorbance method (LECO TCH600). Elemental analysis was also done using the Panalytical Empyrean series 2 XRD with Hyscope software. Visual inspection was by optical microscopy methods (Olympus BX60, Wild M3B) as well as imaging by SEM and EDS (ZEISS EVOMA25). The ACME high temperature sinter furnace (Model ZSJ-35/35/70), was used for final sintering of the brownparts. The A&D electronic balance (EJ-410) with density determination kit allowed density measurement.

### 7.1.3. Methodology

The binder and Ti feedstock previously formulated, was used in this investigation with an increased powder loading. The feedstock components were weighed into a bag and hand blended ( $\phi_P = 0.65$ ). The blend was then compounded in the batch mixer (BM1,  $t = 10$  min,  $t = 170$  °C) to produce 1 kg of feedstock. After compounding the feedstock was granulated before extrusion and pelletising using the TSE ( $\omega = 50$  r/min,  $t = 170$  °C).

The Shimadzu capillary rheometer was used to test melt flow. A sample of the feedstock was pre-heated before application of the load ( $m = 2.0$  g,  $t = 170$  °C,  $t = 180$  s). Viscosity corrections were made using the results from multiple die configurations and loads (Table 34) with the CFT application software.

Table 34: Shimadzu capillary rheometer load and die parameters.

| Capillary |        | Load $F$ (N) |     |     |     |
|-----------|--------|--------------|-----|-----|-----|
| D (mm)    | L (mm) | 105          | 305 | 405 | 455 |
| 2.0       | 2.0    | ✓            | ✓   | ✓   | ✓   |
| 2.0       | 5.0    |              |     |     | ✗   |
| 3.0       | 3.0    | ✗            |     |     | ✗   |

Acetabular cups were moulded using the Dr Boy 50T2. The greenparts were measured, marked and weighed.

SD was done in the same manner as the previous feedstock, by placing the greenparts in circulating water (SD3,  $t = 50$  °C,  $t = (0$  to 600) h) to remove the PEG. At specified times parts were removed from the water, dried ( $t = 50$  °C,  $t = 24$  h) and weighed to measure binder mass loss.

LTTD involved slow heating rates (TD3, Figure 51,  $\beta = 1$  °C/min) to control expansion of the waxes ( $t = 100$  °C) and polymers ( $t = 175$

°C). This was followed by an isothermal period to remove the wax components ( $t = 250$  °C,  $t \leq 100$  h).

The ACME furnace was used to sinter the parts ( $\beta = 5$  °C/min,  $t = 1340$  °C,  $t = 180$  min). First gas flow using industrial grade argon ( $\dot{V} = 10$  L/min,  $t = (20$  to  $800)$  °C) and then vacuum condition ( $t = (800$  to  $1340)$  °C,  $p = 2 \times 10^{-3}$  mbar) followed by further gas flow during cooling ( $\dot{V} = 20$  L/min).

The sintered parts were inspected on the outer and inner surfaces as well as through the parts using radiography. Samples were sectioned and analysed using optical light microscopy and SEM. EDS was used to confirm metal chemistry, i.e. C, Ti, Al and V content. The micro-structure was inspected using samples treated with Kroll's reagent (100 mL distilled water, 2 mL HF, 4 mL HNO<sub>3</sub>,  $t = 60$  s) and optical microscopy.

Sectioned and polished parts were analysed by XRD with power settings 45 kV at 40 mA through a copper electrode. Scanning from position (20 to 100) °2 $\theta$ , using a step size of 0.026 °2 $\theta$ , scan step time of 17.340 s in continuous scanning mode. Peak identification was done using the Highscope software.

Oxygen, hydrogen and nitrogen levels were measured using the inert gas fusion-infrared absorbance method (LECO TCH600).

## **7.2. Results and discussion**

### **7.2.1. Feedstock melt flow**

In Chapter Three separation defects were observed (Figure 31) that could be eliminated by increasing the powder loading. Other benefits include less binder and therefore less potential contamination as well as a reduction in shrinkage during sintering.

As with the previous feedstocks the greenpart mass was lower than the theoretical values ( $m < 3.5 \%$ ,  $\sigma = 0.5$ , Table 35). The increased powder loading ( $w_P = (0.60 \text{ to } 0.65)$ ) had no appreciable effect on viscosity (Figure 93). This was further supported during injection moulding with the feedstock filling the mould with no visible shape loss or defects. The greenparts were easily ejected and were able to be handled without damage.

Table 35: Mass averages for greenpart (AM), greypart (SD), brownpart (TD) and sintered part (S).

| g ( $\sigma$ ) | AM            | SD            | TD            | S          |
|----------------|---------------|---------------|---------------|------------|
| Theory         | 131.67        | 123.89        | 119.37        | 117.30     |
| Actual         | 126.95 (0.50) | 119.80 (0.58) | 116.12 (0.58) | 111 (0.41) |

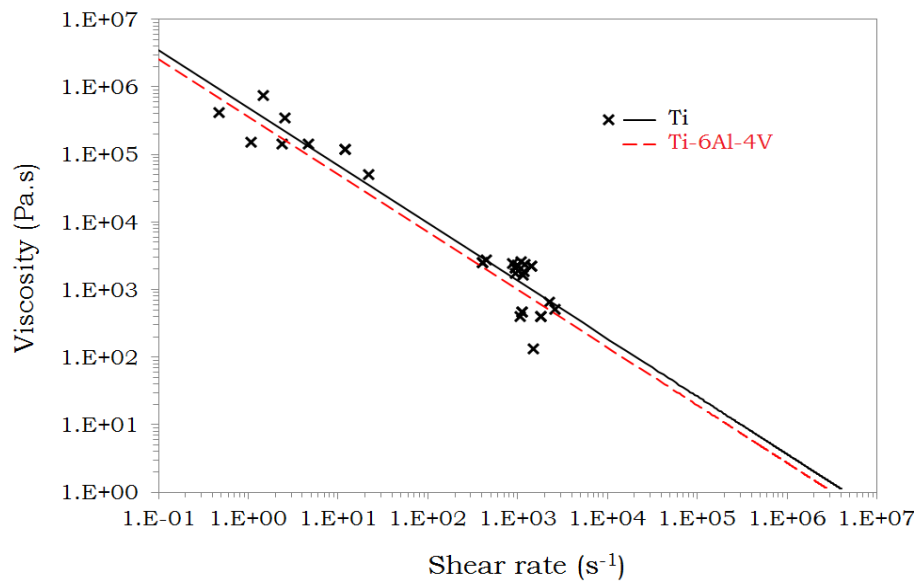


Figure 93: Corrected viscosity and shear rate for the Ti ( $\varphi_P = 0.65$ ) and Ti64 ( $\varphi_P = 0.6$ ) feedstock made with the same binder.

### 7.2.2. Debinding

PEG removal from the greenparts had the same mass loss response as the Ti64 greenparts in Chapter Five. Analysis of the SD data showed that changes in mass loss could be related to changes in the mechanism of debinding. Initially the process was dissolution dominated followed by a transition period, ending with a diffusion controlled process (Figure 94).

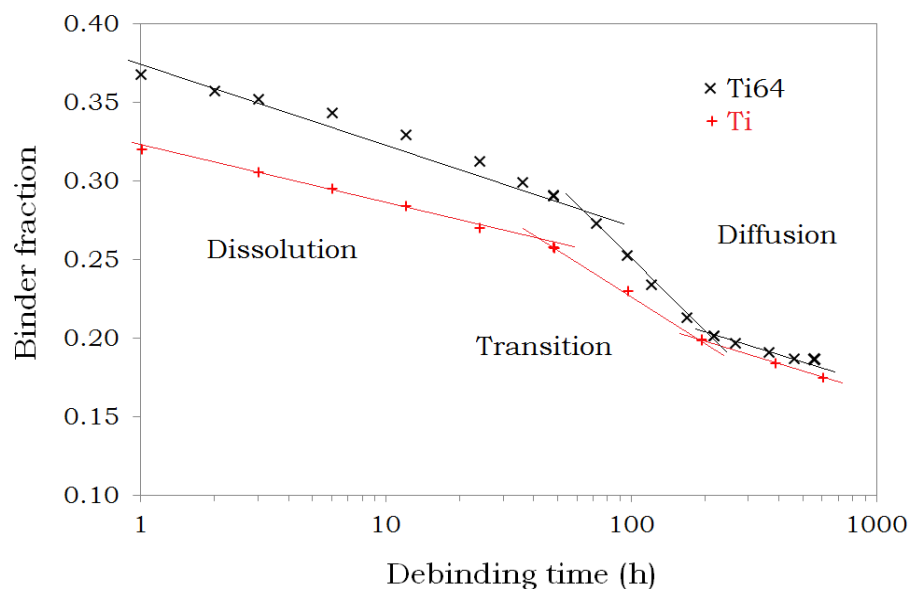


Figure 94: The debinding mechanisms for solvent debinding changes as the level of binder changes.

The data from Figure 94 showed similar rate constants for all mechanisms as the binder composition was the same (Table 36). The differences in the duration of each mechanism related to the amount of binder, the powder loading and the particle size. The increase in duration for the Ti greenpart during diffusion was attributed to the increase in the available channels between particles within the part and the subsequent reduction in the size of the channels. Any increase in processing duration will be offset by the elimination of defects thereby improving part quality.

Table 36: Solvent debinding rate analysis.

|      |                    | Dissolution | Transition | Diffusion |
|------|--------------------|-------------|------------|-----------|
| Ti   | $k_r$ ( $h^{-1}$ ) | 0.0012      | 0.0004     | 0.00006   |
|      | t (h)              | 48          | 144        | 408       |
|      | $\phi_B$           | 0.093       | 0.059      | 0.024     |
| Ti64 | $k_r$ ( $h^{-1}$ ) | 0.0013      | 0.0005     | 0.00006   |
|      | t (h)              | 72          | 144        | 242       |
|      | $\phi_B$           | 0.127       | 0.072      | 0.014     |

Low temperature thermal debinding (LTTD) was investigated using TGA to determine efficacy of debinding (Figure 95, Table 37). The maximum possible binder to be removed from the greypart was the sum of the waxes and polymers ( $w_B = 5.26\%$ ). Binder removal was initially at a higher rate than that seen for Ti64, this was attributed to improved thermal conductivity as a result of the higher particle loading. The residual binder mass in the greypart reached a steady level ( $w_B = 5.5\%$ ) and no longer changed after 72 h. This indicated that removing the targeted component by LTTD would be possible. Being higher than the theoretical binder level ( $w_B = 5.3\%$ ) would be due to incomplete removal of the PEG during solvent debinding.

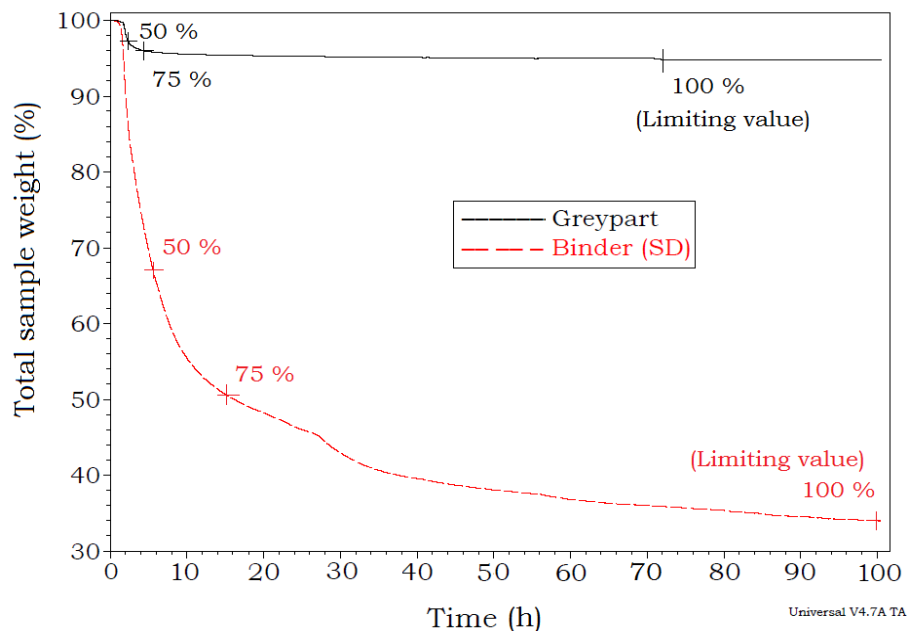


Figure 95: TGA weight loss plot for low temperature thermal debinding shows thermal stability occurs sooner for the feedstock.

Table 37: TGA data for low temperature process ( $t = 250\text{ }^\circ\text{C}$  in air).

|                        |             |      |      |       |
|------------------------|-------------|------|------|-------|
| Binder removal (%)     |             | 50   | 75   | 100   |
| Time at isothermal (h) | Binder (SD) | 5.5  | 15.5 | 100.0 |
|                        | Greypart    | 2.2  | 4.2  | 72.0  |
| Weight $w_B$ (%)       | Binder (SD) | 33.0 | 50.0 | 66.0  |
|                        | Greypart    | 2.8  | 4.1  | 5.5   |

Binder removal during LTTD was attributed to two main mechanisms supported by the debinding plot (Figure 96). Initially as the temperature increased, the binder melts and expands causing pressure increase within the greypart. Providing an open pore structure had formed during SD the internal pressure and subsequent viscosity decrease enables binder to flow out of the part. When the pressure of the oven was below the vapour pressure of the binder, evaporation occurred and the binder vapours were removed with the sweep gas. Once the pressure within the part dropped, below the vapour pressure of the binder, melt flow ceased and the mechanism was driven by the concentration gradient between the binder vapour and the atmosphere in the oven.

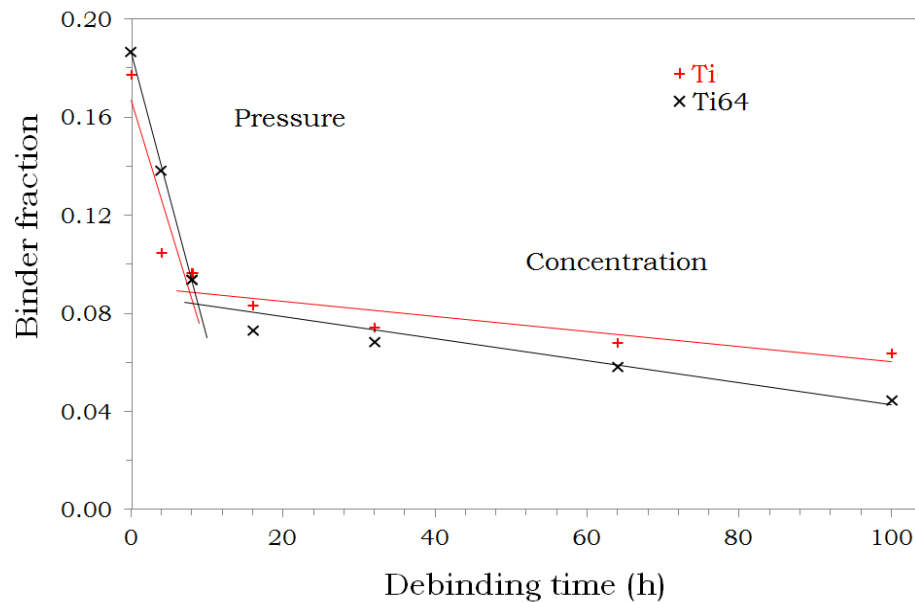


Figure 96: Debinding mechanisms for LTTD shown as pressure driven and concentration driven.

The LTTD data showed strong correlation between the Ti and the Ti64 feedstocks with regard to the rate constants (Figure 96, Table 38). Unlike SD the duration of each mechanism was the same for both Ti and Ti64, indicating the binder volume to interparticle volume ratio within the part dictated the removal rate. After solvent debinding and LTTD negligible shrinkage occurred and therefore debinding within each part was a constant volume process. As compact porosity increased, the rate of binder removal would increase if totally dependent on particulate spacing. This did not occur indicating that the removal rate depended on the size of the component molecules being removed especially during the concentration driven diffusion phase.

Table 38: Thermal debinding rate analysis.

|      |                    | Pressure | Concentration |
|------|--------------------|----------|---------------|
| Ti   | $k_r$ ( $h^{-1}$ ) | 0.0101   | 0.0003        |
|      | t (h)              | 8        | 92            |
|      | $\phi_B$           | 0.088    | 0.023         |
| Ti64 | $k_r$ ( $h^{-1}$ ) | 0.0116   | 0.0004        |
|      | t (h)              | 8        | 92            |
|      | $\phi_B$           | 0.104    | 0.040         |

This result was favourable to the increase in powder loading with no increase in process duration but the gain from reduced shrinkage and predicted defect reduction.

### 7.2.3. Sintering

After sintering the Ti cups there was no cracking or separation at the surfaces and none of the shape distortions seen in Chapters Three or Four (Figure 97, Figure 31, Figure 45). The density ( $\rho = 4.36 \text{ g/cm}^3$ ) was  $\sim 96.9 \%$  of theoretical density, although this is low in respect of wrought material it is in line with acceptable values for MIM titanium [150, 197-200]. The low linear shrinkage factor at 1.12 supports the improvement expected for a higher powder loading compared to the value of 1.18 for the Ti64 ( $\phi_P = 0.6$ ) parts. This leads to less strain and therefore less residual stress within the parts.

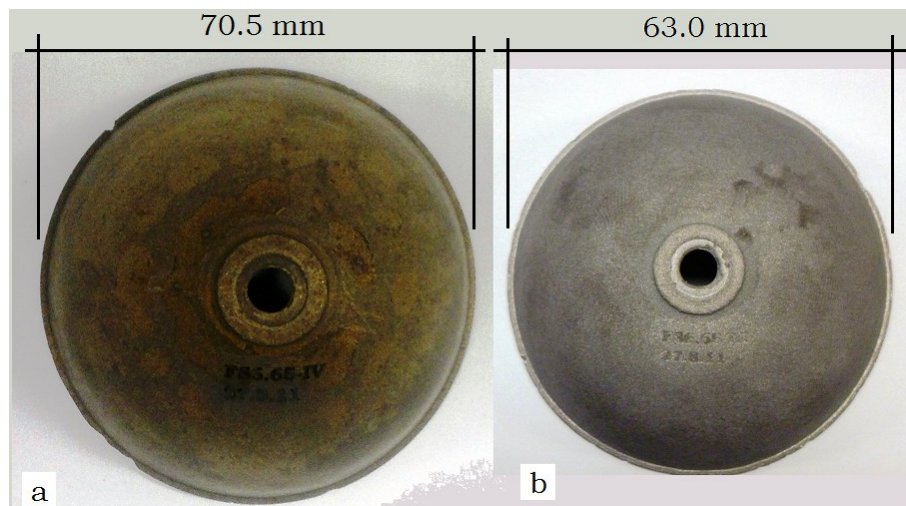


Figure 97: Ti cup a) brownpart and b) as sintered.

A single radiograph taken for the sintered cup showed no large defects and a reduction in shrinkage compared to the Ti64 cup (Figure 98). The energy settings for the X-ray instrument were lower ( $E = 90$  kV,  $t = 60$ s) in comparison to the settings previously used for the greenparts ( $E = 100$  kV,  $t = 60$ s).

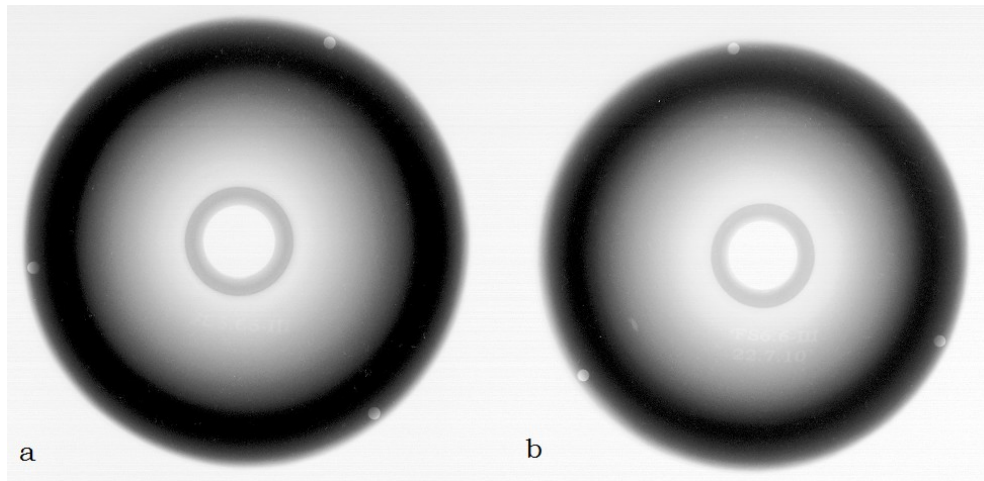


Figure 98: Radiographs of fully sintered cups a) Ti ( $u_p = 0.65$ ) and b) Ti64 ( $u_p = 0.60$ ).

In agreement with the density value porosity was observed in the SEM images. The EDS trace analysis results indicated carbon levels similar to the Ti64 parts ( $w_B = 2.88 \%$ , Figure 99 b). LECO analysis values (Table 39) for oxygen were outside the ASTM specification and greater than the as received powder for the Ti part. It can therefore be said that contamination was outside acceptable levels but had no noticeable effect on consolidation during sintering. This was attributed to the use of LTTD that saw reduction in the interstitial levels over conventional thermal debinding approach. It also indicated that the contamination levels were a result of insufficient sinter conditions.

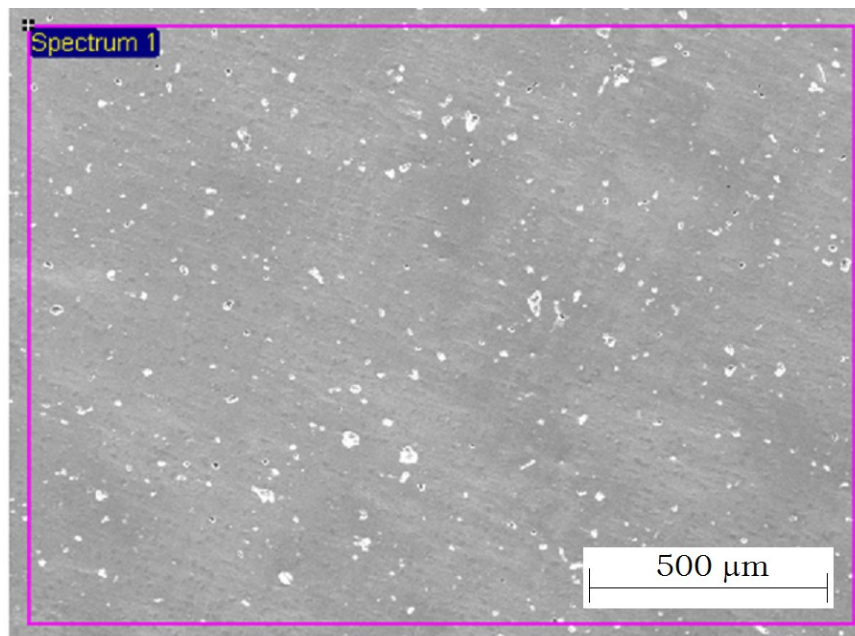


Figure 99: SEM/EDS image of sintered Ti cup part section.

Table 39: Elemental levels for the powder and sintered part.

| $w_E$ (%)                | C    | H     | N     | O     |
|--------------------------|------|-------|-------|-------|
| ASTM <sup>1</sup>        | 0.08 | 0.015 | 0.05  | 0.4   |
| As received <sup>2</sup> | N/A  | 0.045 | 0.023 | 0.35  |
| Ti Cup part <sup>3</sup> | N/A  | 0.019 | 0.078 | > 1.0 |

<sup>1</sup> Standard values from ASTM B348 Grade 4 titanium [173].

<sup>2</sup> Powder suppliers data [201].

<sup>3</sup> Values measured using LECO.

The XRD analysis detected peaks for oxides and carbides of titanium as well as some nitride formation confirming that identified by EDS (Figure 100).

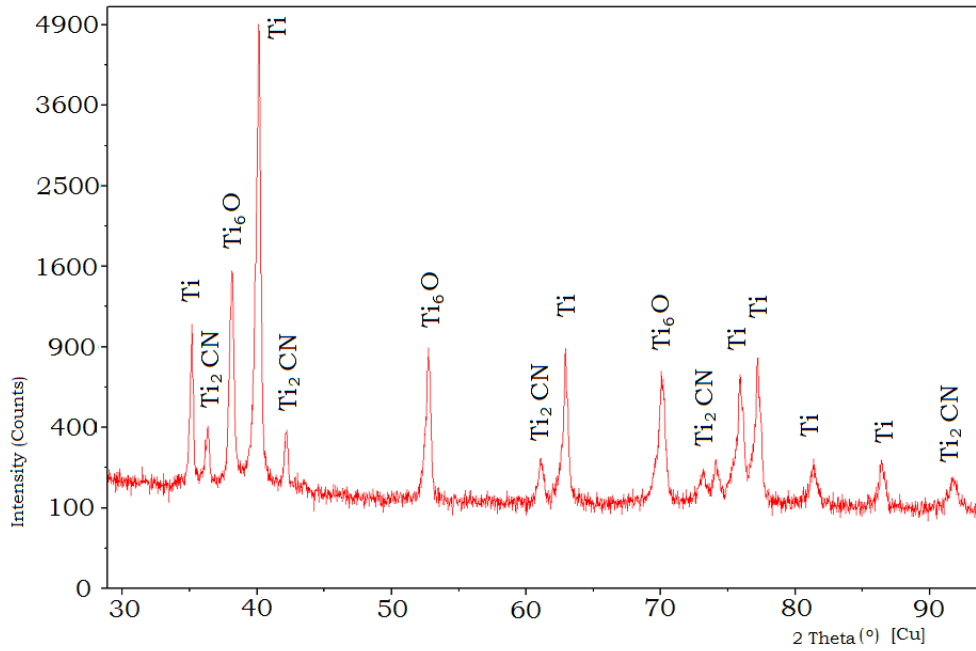


Figure 100: XRD line spectra for the sintered cup with carbides, nitrides and oxides of titanium identified.

Further investigation of the sintered Ti was done using samples prepared with Kroll's etchant (Figure 101). The etched samples showed a near alpha titanium matrix of equiaxed grains ( $d = (30 \text{ to } 50) \mu\text{m}$ ) with secondary phase formations. The microstructure was strongly influenced by the carbon and oxygen, known to give alpha phase stability, similar to near alpha alloys. The reduction of hydrogen, from the as received powder supported the acicular formation, at the inner and outer sections, due to intergranular beta stabilising. Moisture entering the furnace with the sweep gas also contributed to the acicular hydride structures.

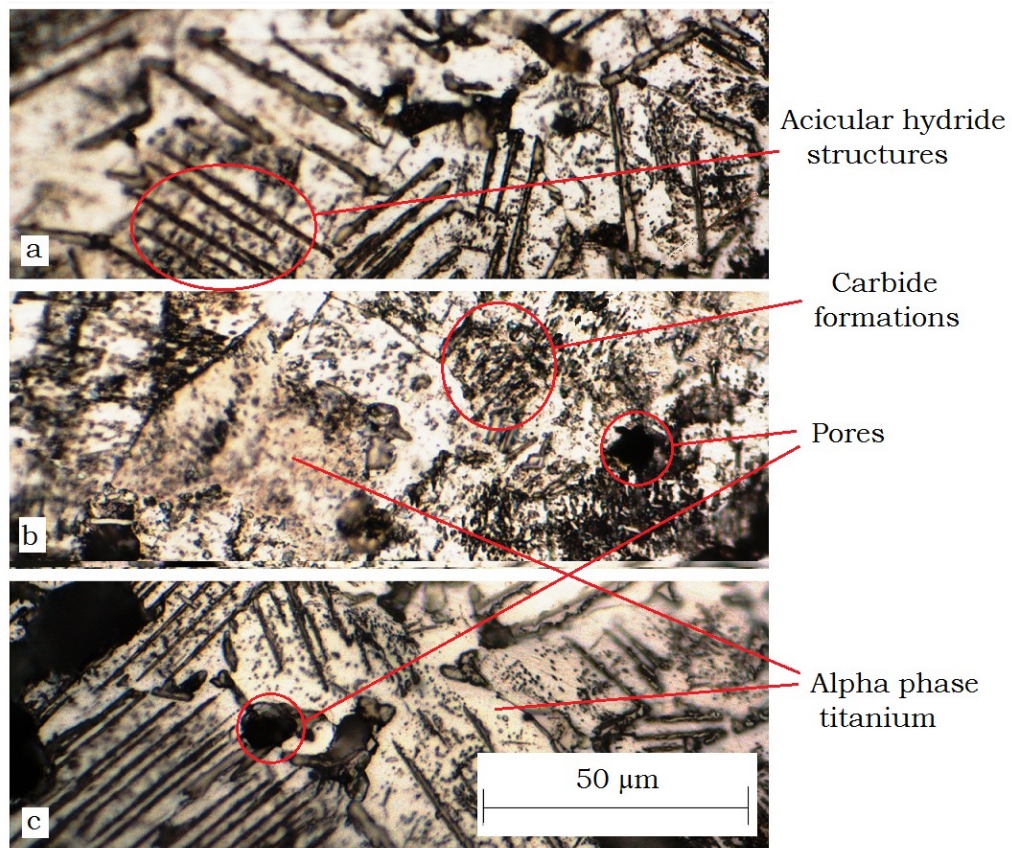


Figure 101: Microstructure of alpha phase Ti matrix with carbide and acicular formations a) inner b) centre and c) outer section.

Pure Ti has an alpha phase atomic microstructure that changes with high cooling rates and the presence of increased levels of

interstitial elements. At temperatures above 1000 °C the typical alpha crystal structure transforms to beta phase and, providing the cooling rate will allow it, the alpha phase will return during cooling [202].

Overall the microstructure for the sintered Ti parts indicated that the sinter conditions were not ideal. This was attributed in part to the use of industrial grade argon sweep gas. While industrial argon gas was specified to have  $\leq 10$  ppm moisture and  $\leq 10$  ppm oxygen [203], it is not measured at the cylinder and wide variations are known to occur. Also the sweep gas flowed for 3 h during the beginning of the sinter cycle and then for a further 6 h during cooling at  $\dot{V} = (10 \text{ to } 20) \text{ L/min}$  therefore introducing a large volume of those elements. However even scientific Zero Grade Argon gas has  $\leq 5$  ppm moisture and  $\leq 5$  ppm oxygen [204], and although they do monitor variation and certify each cylinder it is still a high volume of potential contaminants. Although this was a limitation of the furnace it highlights the need for inline gas purifiers and driers in conjunction with high purity sweep gases.

There were also concerns over the design of the sweep gas retort system with poorly optimised flow paths and no specific channelling of the flow gas across the part surfaces which is considered necessary for efficient removal of the decomposition products.

### **7.3. Conclusions**

By applying the findings of the research undertaken in this thesis an optimised process enabled the formulation and subsequent processing of titanium parts by injection moulding and sintering.

The developed binder system was successfully mixed with a high volume of irregular shape HDH TiCP powders ( $\phi_p = 0.65$ ,  $d < 45$

$\mu\text{m}$ ) to produce a feedstock with good uniformity and particle binder interactions.

The feedstock was easily injection moulded to form greenparts with excellent handling strengths and shape retention that were free of any defects.

Dissolution ( $k_r = 0.0012 \text{ h}^{-1}$ ) was the fastest mechanism for PEG removal during solvent debinding and diffusion the slowest ( $k_r = 0.00006 \text{ h}^{-1}$ ). At the completion of SD 99 % of the PEG, equal to 17.8 % of the total part volume, was removed to produce a uniform structure of open channels to assist removal of the remaining binder during TD.

Low temperature thermal debinding ( $t = 250 \text{ }^\circ\text{C}$ ) was suitable for removing the binder from this feedstock allowing reduced interstitial contamination and improved microstructure uniformity.

The final sinter process was successful in producing titanium parts with density comparable to that of MIM standards. The higher powder loading ( $\varphi_p = 0.65$ ) eliminated the separation defects previously seen, it produced clean surfaces with none of the shape distortions seen in earlier formulations.

## **Chapter Eight: Conclusion and recommendations**

Within the Oceania region, serious academic investigation into metal injection moulding (MIM) only started about ten years ago with industry development shortly after. Commercial activity has been underway four to five years and start-up companies in New Zealand (NZ) only in the last three years. In NZ, barriers to commercial activity (technical expertise, suitability of equipment, process knowledge, customer expectations and licensing costs [10]) are even greater than they were in Europe, Asia and the Americas thirty years ago. This has been due to a lack of expertise and the associated technologies from which MIM emerged, especially the lack of an established powder metallurgy industry.

Fabrication of titanium parts by MIM was investigated in four key processing steps; the first is to production of a feedstock, the second to form (mould) the required part geometry, the third to remove the binder (debind) and the final consolidation (sinter) step. Each step was shown to be essential in ensuring a defect free part with acceptable material characteristics.

The main factors seen to affect feedstock quality were binder component and particle distribution uniformity and particle-binder interactions. The selection of binder components was done to address specific roles in the feedstock, but also with environmental and safety aspects in mind. Polyethylene glycol (PEG) reduced overall feedstock viscosity, improved particle wetting and aided shape retention after moulding. Being water soluble PEG also eliminated the use of toxic solvents in debinding. Natural waxes aided dispersion, lubricated and improved part release during moulding as well as being safe to handle. The low melt

temperatures also aided their removal during thermal debinding, especially important for residue elimination. However, the use of a high volume fraction of wax had a negative effect on the strength of the greenparts. Thermal mechanical analysis (TMA) showed that dimensional change was not affected by uniformity of the feedstock; however it was clear that the amount and molecular weight (MW) of binder had a direct affect on interparticular distances. Keeping processing temperatures low reduced disruption to the moulded geometry, benefitted particle bonding and helped retention of handling strength.

Using varying MW of the three main binder components improved the efficacy of debinding by minimising disruption of the particle packing and part shape. By optimising the component ratios in the feedstock, for melt flow and pellet formation, defect free greenparts with uniform particle distribution were produced. Although this was confirmed using radiography, defects were found after debinding which linked to the mixing process. Extrusion mixing of the feedstock showed a preferential distribution of the particles to the outer surface of the extrudate during the initial stages of mixing. This was in agreement with a higher resistance to flow between individual particles than between the extrusion surfaces of barrel, screw or die.

The binder system formulated here was suitable for hydride dehydride (HDH) powders of both titanium alloy and pure titanium metal. Increased powder loading ( $u_p = (0.60 \text{ to } 0.65)$ ) had no appreciable effect on viscosity and it enabled a feedstock with good uniformity and pellet formation.

Mould design and particle loading were seen to be critical during injection moulding. Initially, the binder formulated for titanium alloy was successful for mixing, moulding and processing of titanium parts. It was also found that defects could be initiated during moulding due to problems with the feedstock and tooling

that were not apparent until debinding and that these would not self repair during sintering. While surface defects were readily identified, internal defects were monitored by the use of X-ray radiography and highlighted cracks and separation defects in the greenpart. The results were limited by the size and orientation of defects as the fine resolution required to identify defects required multiple imaging by varying radiation energy. Considering the complexity of the acetabular cup part radiography was unsuitable for discerning density distribution. Radiography results also lead to the conclusion that success with part moulding does not ensure uniformity of the greenparts.

Solvent debinding followed by thermal debinding reduced the mass of residual binder compared to thermal debinding only. There was also a strong correlation seen between low handling strength within the greenpart and defects such as low density and cracking of the part after sintering. The use of low temperature thermal debinding ( $t = 250\text{ }^{\circ}\text{C}$ ) enabled removal of the wax component below the temperatures known to facilitate impurity diffusion and elemental compound formation i.e. oxides, carbides. The ability to debind the greyparts by low temperature thermal debinding was possible although variables such as part thickness, mass and overall volume must be considered. It was also shown that low temperature thermal debinding enabled reduced interstitial contamination.

Sintering as the final step in the MIM process is dependent on the performance of the feedstock during moulding and debinding, and the handle-ability of the brownparts. The processing atmosphere during sintering was critical and having a binder free brownpart was not the sole criteria for eliminating impurities in the final part. The sinter furnace atmosphere must also remain free from contamination to eliminate diffusion back into the parts. This can be mitigated using a sweep gas during the initial stages of

sintering; however, it became apparent that the design and efficacy of the sweep gas system was also critical. Not only was sufficient capacity for the removal of binder decomposition products needed but also the ability to limit the pickup of interstitial elements from the sweep gas itself during the extended duration at the sintering temperatures.

The combination of optimised titanium feedstock and the use of a low temperature thermal debinding technique produced a well consolidated MIM part of relatively large dimensions. The parts were seen to have uniform microstructure with density comparable to that of MIM standards. In difference to the literature, a high powder loading ( $\phi_p = 0.65$ ) of irregular shape HDH powders was used and shown to be readily mouldable. The higher powder loading also eliminate separation defects and shape distortions evident using lower amounts of powder.

Further investigation will be necessary to enhance the value of Ti MIM to NZ industry. Firstly, to support feedstock development, a study of extrusion mixing over the range of shear stress and shear rate typical for injection moulding is needed. A rheological study of the feedstock is also needed to understand the changing flow regimes between the injection moulder and the mould cavity.

With respect to the sintering of titanium, quantitative studies of the elemental pickup of the powders and subsequent parts are needed. This must take into account the effects of the argon gas available in NZ and the support structures used during sintering.

## References:

1. German, R. and A. Bose, *Injection Molding of Metals and Ceramics*. 1997, Princeton: Metal Powder Industries Federation.
2. Schwartzwalder, K., *Refractory body and method of making the same*, in [www.google.com/patents](http://www.google.com/patents), U.S.P. Office, Editor. 1938, General Motors: United States.
3. German, R., *Final Report; on the Workshop on Scientific Issues for Medical and Dental Applications of Micro/Nano Powder Injection Molding – Molding, Sintering, Modeling, and Commercial Applications*. 2009: Lake Buena Vista (Orlando), Florida, USA.
4. Bellamy, H.T., *Production of molded metallic articles*, in [www.google.com/patents](http://www.google.com/patents), U.S. Patents, Editor. 1946: United States.
5. Kryachek, V.M., *Injection Moulding (Review)*. Powder Metallurgy and Metal Ceramics, 2004. **43**(7-8).
6. Williams, N., *Parmatech: The MIM industries first commercial producer, and still going strong*. Powder Injection Moulding International, 2010. **4**(2).
7. ATW, C. *Parmatech Business Profile*. 1973 31 October 2011]; Available from: <http://www.parmatech.com/parmatech/profile.html>.
8. German, R., *Powder injection moulding and what the designer needs to know*. Metal Powder Report, 2003.
9. Cornwall, R.G. and R.M. German, *Powder Injection Molding - World Markets and Technologies*, in *Euro PM2004*. 2004: Vienna, Austria.
10. Grant, D. and B. Breeding, *MIM in NZ*, P. Ewart, Editor. 2009: Hamilton.
11. IEEE/ASTM, *American National Standard for Metric Practice*. 2011, Institute of Electrical and Electronics Engineers: New York. p. 78.

12. Heaney, D. and R. German, *Advances in the Sintering of Titanium Powders*, in *Euro PM2004*. 2004.
13. Williams, N., *Metal Injection Moulding in Italy: A review of Early Development and Current Activity*. Powder Injection Moulding International, 2010. **4**(3).
14. Pitzer, E.W., *Method of improving fluid properties of finely divided materials*, in [www.google.com/patents](http://www.google.com/patents), U.S. Patents, Editor. 1958, Phillips Petroleum Co: United States.
15. Adames, J.M., *Characterization of Polymeric Binders for Metal Injection Molding (MIM) Process*, in *Polymer Engineering*. 2007, The University of Akron: Akron, OH.
16. Ferri, O.M., T. Ebel, and R. Bormann, *High cycle fatigue behaviour of Ti-6Al-4V fabricated by metal injection moulding technology*. *Materials Science and Engineering A*, 2009. **504**: p. 107-113.
17. Schwartz, S., P. Quirnbach, and M. Kraus, *Solvent Debinding Technology for a Continuous 316L MIM Production*, in *PIM Compilation II. Molding, Debinding, Sintering*, MPIF, Editor. 2007, Metal Powder Industries Federation: Princeton, NJ.
18. Schofalvi, K., *Low Contamination Binders for Reaction Sensitive Alloy Applications*, in *PIM Compilation I. Powders, Binders and Feedstocks*, MPIF, Editor. 2007, Metal Powder Industries Federation: Princeton, NJ.
19. Herranz, G., et al., *Development of new feedstock formulation based on high density polyethylene for MIM of M2 high speed steels*. *Powder Metallurgy*, 2005. **48**(2).
20. Seagle, S.R., *The state of the USA titanium industry in 1995*. *Materials Science and Engineering A*, 1996. **213**.
21. ITA. *Titanium Facts*. 2007 [cited 2010; Available from: [www.titanium.org](http://www.titanium.org)].
22. German, R., *Conceptual Optimization of Titanium Powder Injection Molding*, in *Advances in Powder Metallurgy & Particulate Materials*, M. Bulger and B. Stebick, Editors. 2010, Metal Powder Industries Federation: Hollywood, Florida. p. 11.
23. Kobryn, P., *Casting of Titanium Alloys*. 1996, Wright Laboratory. p. 112.

24. Liang-jian, C., et al., *Porous titanium implants fabricated by metal injection molding*. Transactions of Nonferrous Metals Society of China, 2009. **19**: p. 6.
25. Boyer, R., *Attributes, Characteristics and Applications of Titanium and its Alloys*. Journal of Materials, 2010. **62**(5): p. 4.
26. McCracken, C., C. Motchenbacher, and D. Barbis, *Review of Titanium Powder-Production Methods*. International Journal of Powder Metallurgy, 2010. **46**(5): p. 19 - 26.
27. Capus, J., *MIM Titanium – price is still the issue*. Metal Powder Report, 2010(May/ June 2010).
28. EHK Technologies, *Summary of Emerging Titanium Cost Reduction Technologies*. 2004: Vancouver, WA.
29. Ebel, T., et al., *Metal Injection Moulding of Advanced Titanium Alloys*, in *Advances in Powder Metallurgy & Particulate Materials - 2011*, MPIF, Editor. 2011, PowderMet 2011: San Francisco, California.
30. Froes, S., *Powder Metallurgy Abroad Advances in Titanium Metal Injection Molding*. Powder Metallurgy and Metal Ceramics, 2007. **46**(5-6): p. 8.
31. Froes, S., *Developments in titanium P/M*. 2003, University of Idaho: Moscow, Idaho.
32. Froes, S., *Getting better: big boost for titanium MIM prospects*. Metal Powder Report, 2006: p. 4.
33. JPMA, *2011 Report for MIM Market*. 2011, Japan Powder Metallurgy Association: Tokyo.
34. Kryachek, V.M., D.A. Levina, and L.I. Chernyshev, *Powder Metallurgy Abroad, Developmental Trends in European Powder Metallurgy*. Powder Metallurgy and Metal Ceramics, 2007. **46**(11-12).
35. Whychell, D., *The Effect of Powder Particle Size and Alloying Technique on Distortion in MIM Parts*, in *PIM Compilation II. Molding, Debinding, Sintering*, MPIF, Editor. 2007, Metal Powder Industries Federation: Princeton, NJ.
36. Ahn, S., et al., *Effect of powders and binders on material properties and molding parameters in iron and stainless steel powder injection molding process*. Powder Technology, 2009. **193**: p. 162-169.

37. Heaney, D.F., *Qualification Method For Powder Injection Molded Components*. P/M Science & Technology Briefs, 2004. **6**(3).
38. Gai, G., et al., *Particle shape modification and related property improvements*. Powder Technology 2008. **183**: p. 115-121.
39. Li, Y., X.M. Chou, and L.M. Yu, *Dehydrogenation debinding process of MIM titanium alloys by TiH<sub>2</sub> powder*. Powder Metallurgy, 2006. **49**(3).
40. Oberg, E., et al., *Machinery's Handbook*. 29 ed, ed. C. McCauley. 2012, New York, NY: Industrial Press Inc.
41. Guha, S., *MER introduces golf clubs using superfine powders*. Metal Powder Report 1997.
42. Herranz, G., et al., *Metal injection moulding of bronze using thermoplastic binder based on HDPE*. Powder Metallurgy, 2007. **50**(2).
43. Haack, J., et al., *The Processing of Biomaterials for Implant Applications by Powder Injection Moulding*. Powder Injection Moulding International, 2010. **4**(2).
44. Jackson, C., *The Process*, in *Perspectives in Powder Metallurgy. New Methods for the Consolidation of Metal Powders*, H. Hausner, K. Roll, and P. Johnson, Editors. 1967, Plenum Press.
45. Myers, N., R. Baijal, and P. King, *Sintering of PIM Fe-2Ni-0.8C*, in *PIM Compilation II. Molding, Debinding, Sintering*, MPIF, Editor. 2007, Metal Powder Industries Federation: Princeton, NJ.
46. Kainer, K., et al., *From titanium to magnesium: processing by advanced metal injection moulding*. Powder Metallurgy, 2012. **55**(4): p. 7.
47. Kim, Y., et al., *Application of metal injection molding process to fabrication of bulk parts of TiAl intermetallics*. Journal of Material Science, 2007. **42**: p. 6.
48. Menard, K.P., *Dynamic Mechanical Analysis; A practical introduction*. Second ed. 2008, Boca Raton: CRC Press.
49. Tam, K.C., et al., *Metal injection molding: effects of the vinyl acetate content on binder behavior*. Journal of Materials Processing Technology, 1997. **67**: p. 120-125.

50. Knight, P.C., *Structuring agglomerated products for improved performance*. Powder Technology, 2001. **119**: p. 14-25.
51. Ahn, S., et al., *Integrated filling, packing and cooling CAE analysis of powder injection moulding parts*. Powder Metallurgy, 2008. **51**(4): p. 10.
52. EPMA. *MIM (Metal Injection Moulding)*. 2009 [cited 2009 18/06/2009]; Available from: <http://www.epma.com/mim-metal-injection-moulding>.
53. German, R.M., *Powder Injection Moulding*. 1990: Metal Powder Industries Federation. 521.
54. Dreger, D.R., *INJECTION MOLDING MOVES INTO METALS*. Machine Design, 1975. **47**(24): p. 80-81.
55. Rivers, R.D., *Method of Injection Molding Powder Metal Parts*, in [www.google.com/patents](http://www.google.com/patents), U.S.P. Office, Editor. 1978, Cabot Corporation: United States.
56. Weich, J., R. E., *Manufacture of parts from particulate material*, in [www.google.com/patents](http://www.google.com/patents), U.S.P. Office, Editor. 1980, Parmatech Corporation: United States.
57. Weich, J., R. E., *Particulate Material Feedstock, use of said Feedstock and Product*, in [www.google.com/patents](http://www.google.com/patents), U.S.P. Office, Editor. 1986, Fine Particle Technology Corporation: United States.
58. Weich, J., R. E., *Method for removing binder from a green body.*, in [www.google.com/patents](http://www.google.com/patents), U.S.P. Office, Editor. 1983, Parmatech Corporation: United States.
59. Billiet, R.L., *Method of Making Articles from Sinterable Materials*, in [www.google.com/patents](http://www.google.com/patents), U.S.P. Office, Editor. 1989, Solid Micron Materials: United States.
60. Benson, J., W. Richter, and H. Chikwanda, *Rheological assessment of titanium MIM feedstocks*. The Journal of The Southern African Institute of Mining and Metallurgy, 2011. **111**: p. 4.
61. Vyal', E.Y. and A.M. Laptev, *Exchange of Experience Use of Certain Binders to Increase the Strength of Green Compacts*. Powder Metallurgy and Metal Ceramics, 2005. **44**(11-12).
62. Shibo, G., et al., *Mechanical Properties and Microstructure of Ti-6Al-4V Compacts by Metal Injection Molding*. Trans. Nonferrous Met. Soc. China, 2004. **14**(6): p. 1055-1061.

63. Shibo, G., et al., *Powder injection molding of Ti-6Al-4V alloy*. Journal of Materials Processing Technology, 2006. **173**: p. 310-314.
64. Chuankrerkkul, N., P.F. Messer, and H.A. Davies, *Flow and void formation in powder injection moulding feedstocks made with PEG/PMMA binders Part 1 – Experimental observations*. Powder Metallurgy, 2008. **51**(1).
65. Chuankrerkkul, N., P.F. Messer, and H.A. Davies, *Flow and void formation in powder injection moulding feedstocks made with PEG/PMMA binders Part 2 – Slip band model*. Powder Metallurgy, 2008. **51**(1).
66. Imam, M. and F. Froes, *Low Cost Titanium and Developing Applications*. Journal of Materials, 2010. **62**(5): p. 4.
67. Liu, Y., et al., *Design of powder metallurgy titanium alloys and composites*. Materials Science and Engineering A, 2006. **418**: p. 25-35.
68. Morelli, E. and J. Bidaux, *Processing of Titanium-Based Materials from Low Cost Titanium Hydride Powders: PIM and Tape Casting*, in *Advances in Powder Metallurgy & Particulate Materials - 2011*, MPIF, Editor. 2011, PowderMet 2011: San Francisco, California.
69. Moxson, V., O. Senkov, and F. Froes, *Innovations in Titanium Powder Processing*. Journal of Materials, 2000. **52**(5): p. 3.
70. Malvern, *Optimize rheology to increase dispersion / colloidal / emulsion stability, in 10 ways to...* Malvern, Editor. 2009: Worcestershire. p. 9.
71. Malvern, *Control Rheology by Changing Particle Properties' (Size, Zeta potential and shape)*, in *10 ways to...* Malvern, Editor. 2009: Worcestershire. p. 10.
72. Fletcher, J. and A. Hill (2007) *Making the connection - particle size, size distribution and rheology*. ChemEurope White paper.
73. Imam, M. and F. Froes, *TMS 2010 Symposium: Cost-Affordable Titanium III* Journal of Materials, 2010. **62**(5): p. 2.
74. Atre, S.V., et al., *Process simulation of powder injection moulding: identification of significant parameters during mould filling phase*. Powder Metallurgy 2007. **50**: p. 76-85.
75. Park, S., et al., *Rheological and thermal debinding behaviors in titanium powder injection molding*. Metallurgical and

Materials Transactions A: Physical Metallurgy and Materials Science, 2009. **40**(1): p. 215-222.

76. Manas-Zloczower, I., ed. *Mixing and Compounding of Polymers. Theory and Practice*. 2 nd ed. 2009, Carl Hanser Verlag: Munich. 1158.
77. James, P.J., *Discovering the PIM process*. Manufacturing Engineer, 1989. **68**(9): p. 40, 42-44.
78. Shah, J. and R.E. Nunn, *Rheology of Metal Injection Molding Feedstock*. Powder Metallurgy International, 1987. **19**(6): p. 38-40.
79. Patterson, B.R., R.J. Waikar, and M.T. Young. *Several Aspects of P/M Injection Molding*. in *1986 Annual Powder Metallurgy Conference Proceedings*. 1986. Boston, MA, USA: Metal Powder Industries Federation.
80. Hens, K.F. and D. Lee. *Process analysis of injection molding with powder products*. in *Proceedings of the 1991 Powder Metallurgy Conference and Exhibition, June 9, 1991 - June 12, 1991*. 1991. Chicago, IL, USA: Publ by Metal Powder Industries Federation.
81. Cao, M.Y., B.O. Rhee, and C.I. Chung. *Usefulness of the viscosity measurement of feedstock in powder injection molding*. in *Proceedings of the 1991 Powder Metallurgy Conference and Exhibition, June 9, 1991 - June 12, 1991*. 1991. Chicago, IL, USA: Publ by Metal Powder Industries Federation.
82. Benson, J.M., W. Richter, and H.C. Chikwanda. *Rheological assessment of titanium MIM feedstocks*. 2011. P.O. Box 61127, Marshalltown, 2107, South Africa: South African Institute of Mining and Metallurgy.
83. Lauffer, M.A., *Experimental Facts Pertaining to the Relationship between Viscosity, Molecular Size, and Molecular Shape*, in *The Symposium on Viscosity, Molecular Size, and Molecular Shape*. 1942: Brooklyn Polytechnic Institute. p. 26.
84. Barriere, T., B. Liub, and J.C. Gelin, *Determination of the optimal process parameters in metal injection molding from experiments and numerical modeling*. Journal of Materials Processing Technology, 2003: p. 636-644.
85. Kwon, T.H. and S.Y. Ahn, *Slip characterization of powder/binder mixtures and its significance in the filling process analysis of powder injection molding*. Powder Technology, 1995. **85**: p. 45-55.

86. Bicerano, J., J.F. Douglas, and D.A. Brune, *Model for the Viscosity of Particle Dispersions*. Journal of Macromolecular Science, Part C: Polymer Reviews, 1999. **39**(4): p. 561 - 642.
87. Chhabra, R.P. and J.F. Richardson, *Non-newtonian flow and applied rheology*. 2 ed. Engineering Applications. 2008, Oxford: Butterworth-Heinemann.
88. Einstein, A., *A New Method of Determining Molecular Dimension*. Annalen der Physik, 1906. **19**: p. 289 - 306.
89. Einstein, A., *Correction to my Paper on Determination of Molecular Dimension*. Annalen der Physik, 1911. **34**: p. 591 - 592.
90. Maron, S.H. and P.E. Pierce, *Application of ree-eyring generalized flow theory to suspensions of spherical particles*. Journal of Colloid Science, 1956. **11**(1).
91. Ahn, S., et al., *9.C. Metal Powder Injection Molding*, in *ASM Handbook*. 2008. p. 43.
92. Douglas, J.F. and E.J. Garboczi, *Intrinsic Viscosity and the Polarizability of Particles having a Wide Range of Shapes*, in *Advances in Chemical Physics*, I. Prigogine and S. Rice, Editors. 1995, John Wiley & Sons, Inc. p. 85 - 153.
93. Bangs, S., *Injection Molding Expands P/M Forming Capability*. Precision Metal, 1975. **33**(12): p. 32-34.
94. Ceramics, M.A., *Metal Injection Moulding Design Guide*, in *Criteria for optimizing MIM process and cost effective products*, M.A. Ceramics, Editor. 2005, Morgan Advanced Ceramics: New Bedford, MA USA.
95. General Electric Co, *GE Engineering Thermoplastics Injection Molding Processing Guide*, G. Plastics, Editor. 1998 GE Plastics: Pittsfield, MA. p. 52.
96. Maetzig, M. and H. Walcher, *Strategies for injection moulding metals and ceramics*, in *PIM Compilation II. Molding, Debinding, Sintering*, MPIF, Editor. 2002, Metal Powder Industries Federation: Princeton, NJ. p. 33 - 42.
97. Nor, N., et al., *Injection Molding Parameter Optimization of Ti-6Al-4V Powder Mix With Palm Stearin and Polyethylene for Highest Green Strength Using Taguchi Method*, in *International Conference on Advanced Materials and Processing Technologies*, F. Chinesta, Y. Chastel, and M. Mansori, Editors. 2010, American Institute of Physics. p. 7.

98. Schlieper, G., *Back to basics: From the injection moulding machine to the debinding oven*. Powder Injection Moulding International, 2010. **4**(3).
99. German, R., *Metal Injection Molding A Comprehensive MIM Design Guide*. 2011, Princeton, NJ: Metal Powder Industries Federation.
100. Bono, R.W., *New Methodology of Resonant Inspection Applied to Metal Injection Moulded Parts*. Powder Injection Moulding International, 2010. **4**(2).
101. Wohlfromm, H., *Catamold Feedstock for Powder Injection Molding: Processing - Properties - Applications*. 2002, BASF. p. 8.
102. DrBoy, *1.1 Technical data*, M. T2, Editor. 2000, Dr Boy: Germany. p. Technical machine manual.
103. Hannah, J. and M. Hillier, *Applied Mechanics*. Third ed. 1995, Harlow: Longman Scientific & Technical. 448.
104. Suri, P., et al., *Numerical analysis of filling stage during powder injection moulding: effects of feedstock rheology and mixing conditions*. Powder Metallurgy, 2004. **47**(2).
105. Bilovol, V., et al., *The effect of constitutive description of PIM feedstock viscosity in numerical analysis of the powder injection moulding process*. Journal of Materials Processing Technology, 2006. **178**: p. 194 - 199.
106. ASTM, *E176 Standard Terminology of Fire Standards*, in *ASTM International Standards*: West Conshohocken, PA.
107. Bailey, J., et al., eds. *Properties and Behavior of Polymers*. Vol. 1. 2011, John Wiley & Sons, Inc.: Hoboken, New Jersey. 755.
108. Facaros, G., *Removal of lubricants and binders from sinterable powder components* in [www.google.com/patents](http://www.google.com/patents), U.S. Patents, Editor. 1975, General Electric Company: United States.
109. Ewart, P.D., et al., *Encapsulation of titanium powders during binder removal from a metal injection moulded part*. Advances in Powder Metallurgy & Particulate Materials, 2011.
110. Thian, E.S., et al., *Ti-6Al-4V/HA composite feedstock for injection molding*. Materials Letters, 2002. **56**.

111. Schlieper, G., *Back to basics: Sintering and furnace technology for metal injection moulding*. Powder Injection Moulding International, 2009. **3**(1).
112. Li, Y., X. Chou, and L. Yu, *Dehydrogenation debinding process of MIM titanium alloys by TiH<sub>2</sub> powder*. Powder Metallurgy, 2006. **49**(3).
113. Grohowski, J. and J. Strauss, *Effect of Atmosphere Type on Thermal Debinding*, in *A collection of technical literature on Powder Injection Moulding*, MPIF, Editor. 2007, Metal Powder Industries Federation: Princeton, NJ.
114. Lee, H., G. Shu, and K. Hwang, *Effect of Particle Size on the Debinding of PIM Parts*, in *PIM Compilation II. Molding, Debinding, Sintering*, MPIF, Editor. 2007, Metal Powder Industries Federation: Princeton, NJ.
115. Beg, D., *Powder Injection Moulding (PIM) Process*. 2009, University of Waikato: Hamilton, New Zealand. p. 24.
116. Shengjie, Y., et al., *Simulation of Thermal Debinding*, in *PIM Compilation II. Molding, Debinding, Sintering*, MPIF, Editor. 2007, Metal Powder Industries Federation: Princeton, NJ.
117. Krug, S., *Reaction and Transport Kinetics of a Water-Soluble MIM Binder System*. PolyMIM Publications online, 2008: p. 12.
118. Westcot, E., C. Binet, and R. German, *In situ Monitoring of the Dimensional Changes and Mechanisms During Solvent Debinding*, in *PIM Compilation II. Molding, Debinding, Sintering*, MPIF, Editor. 2002, Metal Powder Industries Federation: Princeton, NJ. p. 10.
119. Ishmail, M., et al., *Study of evolution of Pore Structure during Water Leaching using PEG-PMMA Binder System*, in *A collection of technical literature on Powder Injection Moulding*, MPIF, Editor. 2007, Metal Powder Industries Federation: Princeton, NJ.
120. Atre, S. and R. German, *Quantitative Analysis of Thermal Debinding*, in *PIM Compilation II. Molding, Debinding, Sintering*, MPIF, Editor. 2007, Metal Powder Industries Federation: Princeton, NJ.
121. Schwartz, S., P. Quirnbach, and M. Kraus, *Solvent Debinding Technology for a Continuous 316L MIM Production*, in *A collection of technical literature on Powder Injection Moulding*, MPIF, Editor. 2007, Metal Powder Industries Federation: Princeton, NJ.

122. D20, A.C., *D5226-98(2003) Standard Practice for Dissolving Polymer Materials*, in *ASTM International Standards*. 2003: West Conshohocken, PA.
123. Eroglu, S. and H.I. Bakan, *Solvent debinding kinetics and sintered properties of injection moulded 316L stainless steel powder*. Powder Metallurgy, 2005. **48**(4).
124. Bakan, H.I., et al., *Study of processing parameters for MIM feedstock based on composite PEG-PMMA binder*. Powder Metallurgy, 1998. **41**(4).
125. Hidalgo, J., et al., *Rheological And Thermal Behavior Of Powder Injection Moulding (PIM) Feedstocks Fabricated With Binder Systems Based On Waxes*, in *PM2010 World Congress*, A. Bose, Editor. 2010. p. 6.
126. Grohowski, J. and J. Strauss, *Effect of Atmosphere Pressure on Thermal Debinding Behavior*, in *PIM Compilation II. Molding, Debinding, Sintering*, MPIF, Editor. 2007, Metal Powder Industries Federation: Princeton, NJ. p. 105 - 111.
127. LaVoie, L., *Titanium Powder Injection Molding*, in *PIM Compilation III. Secondary Processing and Materials Properties*, MPIF, Editor. 2007, Metal Powder Industries Federation: Princeton, NJ.
128. Jee, C., et al., *Experimental and molecular dynamics studies of the thermal decomposition of a polyisobutylene binder*. Acta Materialia, 2006. **54**: p. 11.
129. Enneti, R., *Thermal Analysis and Evolution of Shape Loss Phenomena During Polymer Burnout in Powder Metal Processing*, in *Engineering Science and Mechanics*. 2005, The Pennsylvania State University. p. 149.
130. Foreman, J., S. Sauerbrunn, and C. Marcozzi, *Exploring the Sensitivity of Thermal Analysis Techniques to the Glass Transition*. 1997, TA Instruments, Inc.: New Castle. p. 15.
131. Sauerbrunn, S. and P. Gill, *Decomposition Kinetics using TGA*. 1997, TA Instruments, Inc.: New Castle.
132. Thomas, L., *Practical Benefits of Using Heat Capacity Versus Heat Flow Signals*. 2001, TA Instruments, Inc.: New Castle. p. 6.
133. Rawlinson, C., *Differential Scanning Calorimetry "Cooking with Chemicals"*, in *Poisons, Pills and Potions*. 2006, MMS Conferencing & Events Ltd: Daventry, Midlands, UK.

134. Grohowski, J. and J. Strauss, *Effect of Atmosphere Type on Thermal Debinding*, in *PIM Compilation II. Molding, Debinding, Sintering*, MPIF, Editor. 2007, Metal Powder Industries Federation: Princeton, NJ. p. 137 - 144.
135. TAINstruments, *Thermal Solutions, Determination of Polymer Blend Composition*, in *Thermal Analysis & Rheology*. 2001, TA Instruments, Inc.: New Castle. p. 4.
136. Herranz, G., et al., *Effect of Binder Composition on Rheological Behaviour of M2-HSS Powder-Polymer Mixtures for PIM Tec*, in *PIM Compilation I. Powders, Binders and Feedstocks*, MPIF, Editor. 2007, Metal Powder Industries Federation: Princeton, NJ.
137. Petcavich, B., *Water Soluble Binders for Large Volume MIM Production*, in *PIM Compilation I. Powders, Binders and Feedstocks*, MPIF, Editor. 2007, Metal Powder Industries Federation: Princeton, NJ.
138. Robinson, S., *Debinding Metal and Ceramic MIM Components in Batch Furnaces using Vacuum/Controlled Atmospheres*, in *PIM Compilation II. Molding, Debinding and Sintering*, MPIF, Editor. 2007, Metal Powder Industries Federation: Princeton, NJ.
139. Grohowski, J. and J. Strauss, *Effect of Atmosphere Pressure on Thermal Debinding Rate Behavior*, in *PIM Compilation II. Molding, Debinding, Sintering*, MPIF, Editor. 2007, Metal Powder Industries Federation: Princeton, NJ.
140. Banerjee, S. and C. Joens, *Sintering Atmospheres for Powder Metal Injection Molded (MIM) Titanium Alloys*, in *MIM2011*, MIMA, Editor. 2011: Orlando, Florida.
141. Ebel, T., et al., *Metal Injection Moulding of Titanium and Titanium-aluminides*, in *Powder Metallurgy of Titanium*, M. Qian, Editor. 2012, Trans Tech Publications: Brisbane, Australia. p. 357.
142. Ergul, E., H. Gulsoy, and V. Gunay, *Effect of sintering parameters on mechanical properties of injection moulded Ti-6Al-4V alloys*. Powder Metallurgy, 2009. **52**(1): p. 65 - 71.
143. German, R., *Sintering Theory and Practice*. 1996: John Wiley
144. German, R., *Powder Injection Molding of Titanium Medical Devices and Implants*, in *International Conference on Injection Molding of Metals, Ceramics and Carbides*, M.I.M. Association, Editor. 2011, Metal Powder Industries Federation: Orlando, Florida.

145. Grohowski, J., B. Sherman, and J. Strauss, *Processing of Titanium by Metal Injection Moulding*, in *PIM Compilation III. Secondary Processing and Material Properties*, MPIF, Editor. 2007, Metal Powder Industries Federation: Princeton, NJ. p. 9.
146. Limberg, W., et al., *Doctor's orders? Less oxygen = more life for titanium MIM*. Metal Powder Report, 2005(March): p. 4.
147. Shengjie, Y., *Titanium Powder Injection Moulding*, in *Advances in Powder Metallurgy & Particulate Materials - 2011*, MPIF, Editor. 2011, PowderMet 2011: San Francisco, California.
148. Williams, B., *Challenges for MIM titanium parts*. Metal Powder Report, 2003.
149. Pospisil, J., et al., *Degradation and aging of polymer blends I. Thermomechanical and thermal degradation*. Polymer Degradation and Stability, 1999. **65**: p. 10.
150. ASTM, *B817 Standard Specification for Powder Metallurgy (PM) Titanium Alloy Structural Components*, in *ASTM International Standards*. 2008, ASTM International: West Conshohocken, PA. p. 4.
151. Gerling, R., et al., *Metal injection moulding of gamma titanium aluminide alloy powder*. Materials Science and Engineering A, 2006. **423**: p. 262-268.
152. Ibrahim, R., et al., *Injection Molding of Titanium Alloy Implant for Biomedical Application using novel Binder System based on Palm Oil Derivatives*. American Journal of Applied Sciences, 2010. **7**(6): p. 4.
153. Takizawa, T., H. Kanazawa, and H. Izui, *Effect of deoxidising agents on sinterability and mechanical properties of B<sub>4</sub>C/Ti-6Al-4V*, in *PM2012 Yokohama*, H. Miura and A. Kawasaki, Editors. 2012, Japan society of powder and powder metallurgy: Yokohama. p. 6.
154. Tokita, M., et al., *Development of large sized three dimensional Ti-6Al-4V alloy for industrial application by spark plasma sintering (SPS) method*, in *PM2012 Yokohama*, H. Miura and A. Kawasaki, Editors. 2012, Japan society of powder and powder metallurgy: Yokohama.
155. Jia, M., D. Zhang, and B. Gabbitas, *Comparison of blended elemental (BE) and mechanical alloyed (MA) powder compact forging into Ti-6Al-4V rocker arms*, in *Powder Metallurgy of Titanium*, M. Qian, Editor. 2012, Trans Tech Publications: Brisbane, Australia. p. 7.

156. Qian, M., *Cold compaction and sintering of titanium and its alloys for near-net-shape or pre-form fabrication*. International Journal of Powder Metallurgy 2010. **46**(5): p. 16.
157. Zhang, D., *Powder Metallurgy*, in *Materials Processing and Production*. 2003, UoW: Hamilton.
158. German, R., *Coarsening in Sintering: Grain Shape Distribution, Grain Size Distribution, and Grain Growth Kinetics in Solid-Pore Systems*. Critical Reviews in Solid State and Materials Sciences, 2010. **35**: p. 43.
159. Banerjee, S. and C. Joens, *A Comparison of Techniques for Processing Powder Metal Injection Molded 17-4 PH Materials*. 2008.
160. Myers, N. and R. German, *Binder Selection for PIM of Water Atomised 316L*, in *PIM Compilation I. Powders, Binders and Feedstocks*, MPIF, Editor. 2007, Metal Powder Industries Federation: Princeton, NJ.
161. Chuankrerkkul, N., et al., *Powder Injection Moulding of WC-Co Hardmetal Components using a PEG/PMMA Composite Binder System*, in *PIM Compilation I. Powders, Binders and Feedstocks*, MPIF, Editor. 2007, Metal Powder Industries Federation: Princeton, NJ.
162. Chuankrerkkul, N., et al., *The Effect of PEG/PMMA Composite Binder System on the Powder Injection Moulding of WC-Co Hardmetal Composites*, in *PIM Compilation I. Powders, Binders and Feedstocks*, MPIF, Editor. 2007, Metal Powder Industries Federation: Princeton, NJ.
163. MPIF, in *PIM Compilation II. Molding, Debinding, Sintering*, MPIF, Editor. 2007, Metal Powder Industries Federation: Princeton, NJ. p. 166 - 311.
164. ASTM, *E1641 Standard Test Method for Decomposition Kinetics by Thermogravimetry*, in *ASTM International Standards*. 2012, ASTM International: West Conshohocken, PA. p. 6.
165. Roura, P. and J. Farjas, *Analytical solution for the Kissinger equation*. Material Research, 2009. **24**(10).
166. Kissinger, H.E., *Reaction kinetics in thermal analysis*. Analytical Chemistry, 1957. **29**.
167. Charrier, J., *Polymeric materials and processing: plastics, elastomers and composites*. 1990, Munich, Vienna, New York: Hanser. 633.

168. Islam, M.S., *The Influence of Fibre Processing and Treatments on Hemp Fibre/Epoxy and Hemp Fibre/PLA Composites*, in *Materials and Process Engineering*. 2008, University of Waikato: Hamilton. p. 268.
169. Jorge, H., *Compounding and Processing of a Water Soluble Binder for Powder Injection Moulding*, in *School of Engineering*. 2008, University of Minho. p. 213.
170. Suri, P., et al., *Homogeneity of Powder-Binder mixtures: A Microstructural Model*, in *PIM Compilation I. Powders, Binders and Feedstocks*, MPIF, Editor. 2007, Metal Powder Industries Federation: Princeton, NJ.
171. Gutmann, V. and G. Resch, *Lecture Notes on Solution Chemistry*. 1995, Singapore: World Scientific Publishing Co. Pte. Ltd.
172. Cox, B.G., *Modern Liquid Phase Kinetics*. Oxford Chemistry Primers, ed. R.G. Compton. 1994, Oxford: Oxford University Press.
173. ASTM, *B348 Standard Specification for Titanium and Titanium Alloy Bars and Billets*, in *ASTM International Standards*. 2011, ASTM International: West Conshohocken, PA. p. 8.
174. Kang, S.L., *Sintering densification, grain growth & microstructure*. 2005, Oxford: Elsevier. 265.
175. Prasad, A., *A Quantitative Analysis of Low Density Polyethylene and Linear Low Density Polyethylene Blends by Differential Scanning Calorimetry and Fourier Transform Infrared Spectroscopy Methods*. *Polymer Engineering and Science*, 1998. **38**(10).
176. Prausnitz, J., R. Lichtenthaler, and E. de Azevedo, eds. *Molecular thermodynamics of fluid-phase equilibria*. Third ed. Prentice Hall international series in the physical and chemical engineering sciences, ed. N. Amundson. 1999, Prentice Hall PTR: Upper Saddle River.
177. Kang, T., et al., *Modeling and simulation of metal injection moulding (MIM)*, in *Handbook of metal injection moulding*, D. Heaney, Editor. 2012, Woodhead Publishing: Cambridge.
178. Krug, S. and S. Zachmann, *Influence of sintering conditions and furnace technology on chemical and mechanical properties of injection moulded 316L*. *Powder Injection Moulding International*, 2009. **3**(4).

179. Enneti, R., et al., *Review: Thermal Debinding Process in Particulate Materials Processing*. Materials and Manufacturing Processes, 2012. **27**: p. 17.
180. Williams, N., *'Thermal only' binder system for Powder Injection Moulding (PIM) offered by Japan's Atect Corp*. Powder injection moulding international, 2010. **4**(1).
181. Kulkarni, K. and W. Mossner, *Response of Commercially Available MIM Feedstocks to various First Stage Debinding Methods*, in *PIM Compilation II. Molding, Debinding, Sintering*, MPIF, Editor. 2007, Metal Powder Industries Federation: Princeton, NJ. p. 173 - 184.
182. Shimadzu, *CFT-500D/100D Shimadzu Flowtester Capillary Rheometers*, in *C228-E006A*, Shimadzu Corporation: Japan.
183. Okuchaba, B.J., *Development of a Model to Calculate Mechanical Specific Energy for Air Hammer Drilling Systems*, in *Department of Petroleum Engineering*. 2008, The University of Texas A&M. p. 51.
184. ThermoPRISM, *Instruction manual for Thermo PRISM TSE-16-TC twin screw extruder for thermoplastic compounding*. 2002, Thermo PRISM: Staffordshire, England.
185. Craig, R., J. Eick, and F. Peyton, *Properties of Natural Waxes Used in Dentistry*. Journal of Dental Restoration, 1965. **44**.
186. Baril, E., et al., *Powder Injection Molding (PIM) for low cost manufacturing of intricate parts to net shape*, in *NATO-Research and Technology Organisation-Specialists Meeting-Cost Effective Manufacture via Net Shape Processing*. 2006, NRC Publications Archive (NPArc). p. 12.
187. Marquez, A., J. Quijano, and M. Gaulin, *A calibration technique to evaluate the powerlaw parameters of polymer melts using a torque rheometer*. Polymer Engineering and Science, 1996. **36**(20): p. 2566-2563.
188. Buskirk, P., *Using your plasticorder measuring head to determine melt viscosity*. 1990, Brabender GmbH: Duisburg.
189. Einstein, A., *On the Movement of Small Particles Suspended in Stationary Liquids Required by the Molecular-Kinetic Theory of Heat*. Annalen der Physik, 1905. **17**: p. 549 - 560.
190. Parfitt, G. and H. Barnes, *The dispersion of fine particles in liquid media*, in *Mixing in the process industries*, N. Harnby, M. Edwards, and A. Neinow, Editors. 2000, Butterworth-Heinemann: Woburn, MA. p. 19.

191. Domenech, T., E. Peuvrel-Disdier, and B. Vergnes, *The importance of specific mechanical energy during twin screw extrusion of organoclay based polypropylene nanocomposites*. Composites Science and Technology, 2013. **75**: p. 7 - 14.
192. Imam, M., F. Froes, and K. Housley, *Titanium and Titanium Alloys*, in *Kirk-Othmer Encyclopedia of Chemical Technology*, K. Othmer, Editor. 2006, John Wiley & Sons, Inc. p. 41.
193. Olsen, T., *Model MP 987 Extrusion Plastometer (Melt Indexer)*, in *Instruction Booklet*. 1987: Willow Grove, PA.
194. Merz, L., et al., *Feedstock Development for Nitride Ceramics in Micro-PIM Based on SiN<sub>4</sub> and TiN*, in *PIM Compilation I. Powders, Binders and Feedstocks*, MPIF, Editor. 2007, Metal Powder Industries Federation: Princeton, NJ.
195. Suri, P., S. Atre, and R. German, *Effect of Mixing on the Rheology of Alumina Feedstocks*, in *PIM Compilation I. Powders, Binders and Feedstocks*, MPIF, Editor. 2007, Metal Powder Industries Federation: Princeton, NJ.
196. Fenner, R.T., *Principles of Polymer Processing*. 1980, New York: Chemical Publishing Co. 176.
197. PolyMIM, *Product specification – polyMIM® Titan grade 2*, in *Data sheet*. 2013, PolyMIM GmbH: Bad Sobernheim.
198. PolyMIM, *Product specification – polyMIM® Ti6Al4V*, in *Data sheet*. 2013, PolyMIM GmbH: Bad Sobernheim.
199. ASTM, *F2885 Standard Specification for Metal Injection Molded Titanium-6Aluminum-4Vanadium Components for Surgical Implant Applications*, in *ASTM International Standards*. 2011, ASTM International: West Conshohocken, PA. p. 5.
200. ASTM, *F2989 Standard Specification for Metal Injection Molded Unalloyed Titanium Components for Surgical Implant Applications*, in *ASTM International Standards*. 2012, ASTM International: West Conshohocken, PA. p. 5.
201. Clark, J., *Certified Analysis*, in *Microsoft Excel*, T.p.-m.C. HDH, Editor. 2010: Red Lion, PA.
202. Vander Voort, G.F., *Microstructure of Titanium and its Alloys*. 2000, Buehler Limited: Lake Bluff.
203. BOC, *Argon Welding Grade, Compressed*. 2014, The Linde Group.
204. BOC, *Argon Zero Grade*. 2014, The Linde Group.

